A model-based analysis of meteorological processes important for North African dust emission

Stephanie Fiedler

Submitted in accordance with the requirements for the degree of:
Doctor of Philosophy

The University of Leeds
School of Earth and Environment

April 2014

DECLARATION OF INTELLECTUAL PROPERTY

The candidate confirms that the work submitted is her own, except where work has formed part of jointly authored publications has been included. The contribution of the candidate and the other authors to this work has been explicitly indicated below.

The majority of chapter 2 and parts of chapter 3 contain figures, tables and text passages from my publication Fiedler et al (2013a)[1], Copyright 2014 John Wiley & Sons, Inc. This material is reproduced with permission of John Wiley & Sons, Inc (pers. comm. Paulette Goldweber, Wiley, 2014). The candidate solely analysed the data and wrote the text with advice from P. Knippertz and comments from all co-authors during the manuscript preparation. The nocturnal low-level jet detection algorithm was initially designed in collaboration with K. Schepanski. The candidate solely did the debugging, further development including code extensions and application. The dust emission calculation in this paper was produced by B. Heinold with the model from I. Tegen. Chapter 1 contains figures from Heinold et al (2013)[2], Copyright 2014 John Wiley & Sons, Inc. The candidate solely applied the nocturnal low-level jet detection algorithm, provided this data and provided comments during the manuscript preparation.

Figures and text passages from the revised versions of my publication Fiedler et al (2013b)[3] distributed under the Creative Commons Public License (http://creativecommons.org/licenses/by/3.0/) form the majority of chapter 4 and parts of chapter 3. The candidate solely wrote the manuscript with advice from P. Knippertz and comments from co-authors, developed and applied the method to filter cyclones and combine tracks with dust emission and analysed the data. K. Schepanski provided the original depression tracks and B. Heinold helped with the dust emission calculation with the model from I. Tegen.

---

[1] Fiedler, S., Schepanski, K., Heinold, B., Knippertz, P., Tegen, I., 2013: Climatology of nocturnal low-level jets over North Africa and implications for modeling mineral dust emission, J. Geophys. Res.- Atmos.,118, 6100–6121, doi:10.1002/jgrd.50394.

[2] Heinold, B., Knippertz, P., Marsham, J.H., Fiedler, S., Dixon, N. S., Schepanski, K.,Laurent, B., Tegen, I., 2013: The role of deep convection and nocturnal low-level jets for dust emission in summertime West Africa: Estimates from convection-permitting simulations, J. Geophys. Res.- Atmos.,118, 4385–4400, doi:10.1002/jgrd.50402.

[3] Fiedler, S., Schepanski, K., Knippertz, P., Heinold, B., Tegen, I., 2013: How important are cyclones for emitting mineral dust aerosol in North Africa?, Atmos. Chem. Phys. Discuss., 13, 32483–32528, doi:10.5194/acpd-13-32483-2013.

The candidate confirms that appropriate credit has been given within the thesis where reference has been made to the work of others. This copy has been supplied on the understanding that it is copyright material and that no quotation from the thesis may be published without proper acknowledgement.

© 2014, The University of Leeds and Stephanie Fiedler

The right of Stephanie Fiedler to be identified as Author of this work has been asserted by her in accordance with the Copyright, Designs and Patents Act 1988.

ACKNOWLEDGEMENTS

First of all I would like to thank my supervisors Peter Knippertz (now at Karsruhe Institute of Technology, Germany) and Andrew Ross (University of Leeds, United Kingdom) for their advise on my PhD research. Your willingness to let me work freely and to provide support where needed made my PhD time a great experience. I would also like to express my thanks to Kerstin Schepanski and Bernd Heinold (now at Leibniz Institute for Tropospheric Research, Germany) for the productive collaboration. Your interest and feedback was motivating throughout and made even tough work enjoyable. Further I would like to thank Ken Carslaw and John Marsham (University of Leeds, United Kingdom), Ina Tegen (Leibniz Institute for Tropospheric Research, Germany), Nicolas Bellouin (University of Reading, United Kingdom), Gill Martin and Stephanie Woodward (UK Met Office, United Kingdom) for feedback on my work.

My warmest thanks to Daniel and my parents for supporting me patiently during the entire PhD time. A big thank you to my friends for the wonderful memories of the UK.

I would like to thank Nicolas Bellouin (University of Reading, United Kingdom) for providing HadGEM2-ES data; Bernd Heinold (Leibniz Institute for Tropospheric Research, Germany) for dust emission calculations and teaching me to run the model; Kirsty Pringle (University of Leeds, United Kingdom) for HadGEM3-A data as well as ECMWF and the UK Met Office for access to ERA-Interim data. Further many thanks to Martin Todd (University of Sussex, United Kingdom) for PIBAL observations at Chicha from the BoDEx campaign; Kerstin Schepanski (Leibniz Institute for Tropospheric Research) for satellite observation data; the AMMA radiosondes program and Mathieu Nuret (Meteo France, France) for quality controlled radiosondes at Agadez, Tombouctou and Niamey; the Fennec project for observation data from the central Sahara (NERC grant NE/G017166/1), in particular ONM of Algeria and Mauritania, Jean-Blaise Ngamini and Janvier Bentefouet (Aero Equip and Conseil) for radiosondes measurements at Zouerat and Bordje Badji Mokhtar as well as NCAS (National Centre for Atmospheric Science) and FGAM (Facility for Ground-Based Atmospheric Measurement) for SODAR and LIDAR measurements. I would also like to thank Irina

Sandu (European Centre for Medium-Range Weather Forecasts, United Kingdom) for explaining the physical parameterization of the boundary layer in ERA-Interim and Barbara Brooks (University of Leeds, United Kingdom) for advising on SODAR and LIDAR uncertainties.

This PhD thesis is funded by a scholarship from the European Research Council as part of the "Desert Storms" project (ERC grant: 257543).

ABSTRACT

Dust aerosol is abundant and important in the Earth system due to its influence on the radiation balance, the hydrological cycle, human health and ecosystems. Reducing the currently large uncertainties in dust effects requires realistic simulations of the lifecycle of dust aerosol which depends on the time, location and amount of dust emission. Emission estimates from models show a large variety, the reduction of which requires a systematic evaluation of dust-emitting winds. Different processes are known, but their relative importance was previously poorly quantified. This work investigates dust-emitting winds in North Africa based on single meteorological processes which helps guiding future model development.

Based on 32 years of ERA-Interim data and a dust model, the emission amounts associated with nocturnal low-level jets (NLLJs), atmospheric depressions and mobile, long-lived cyclones are estimated climatologically for the first time. The results highlight NLLJs as an important driver for dust emission, particularly in the Bodélé Depression during winter. Associated maxima in mid-morning emission underline the importance of temporally high-resolved winds for dust modelling. ERA-Interim systematically underestimates NLLJ core wind speeds, likely due to artificially increased mixing in stable boundary layers. Derived emission frequencies over the Bodélé Depression agree well with observations, but differ elsewhere.

Atmospheric depressions, often in the form of heat lows and lee depressions, occur frequently and coincide with the majority of dust emission. Few depressions develop into mobile and long-lived cyclones which coincide with particularly intense events. The largest emission fractions associated with cyclones are found in northeast Africa during spring, primarily at day with a small emission reduction by soil moisture. Smaller West African areas show similar fractions, likely associated with near-surface signatures of African Easterly Waves.

Comparing results derived from ERA-Interim against the Earth system model of the UK Met Office shows considerable disagreement in NLLJ core wind speeds and dust emissions. In depth analysis underlines the urgency for model development that improves the synoptic-scale conditions and the stable boundary layer. Such model improvements

hold the potential to advance the scientific understanding of dust aerosol in the Earth system.

Contents

5 Evaluation of dust emission in the Earth system model from the UK Met Office 135

List of Figures

List of Tables

List of Abbreviations

ABL	Atmospheric Boundary Layer
AEJ	African Easterly Jet
AEW	African Easterly Wave
AOD	Aerosol Optical Depth
AR5	Fifth Assessment Report of IPCC
BBM	Bordj Badji Mokhtar
BoDEx	Bodélé Dust Experiment
CMIP5	Coupled Model Intercomparison Project Phase Five
DSA	Dust Source Activation
ECMWF	European Centre for Medium-Range Weather Forecasts
GACM	Global Aerosol-Climate Model
IPCC	Intergovernmental Panel of Climate Change
ITCZ	Intertropical Convergenze Zone
ITD	Intertropical Discontinuity
LLJ	Low-Level Jet
LT	Local Time
MCS	Mesoscale Convective System
MERRA	Modern-Era Retrospective Analysis for Research and Applications
MSG	Meteosat Second Generation
MSLP	Mean sea level pressure
NCEP	National Centers for Environmental Prediction
NLLJ	Nocturnal Low-Level Jet
PIBAL	Pilot Balloon
SABL	Saharan Atmospheric Boundary Layer
SEVIRI	Spinning Enhanced Visible and Infrared Imager
UTC	Universal Time Coordinated

CHAPTER 1

Motivation and Background

One of the largest uncertainties in our understanding of the climate system is the role of aerosols. Aerosol may affect climate directly through scattering and absorption of radiation (e.g. Lohmann & Feichter, 2005), semi-directly by cloud burn-off (Ackermann et al, 2000) and indirectly by aerosol-cloud-effects (cloud albedo, top height and lifetime, Albrecht, 1989; Pincus & Baker, 1994; Twomey, 1974). Possible aerosol effects also include changes of the photo-synthetically active radiation spectrum on land vegetation (Mercado *et al.*, 2009) as well as altered surface albedo (Flanner *et al.*, 2007). Aerosol may have a net cooling effect on the global mean near-surface temperature thereby counteracting the warming through anthropogenically increased green house gas (GHG) concentrations. This implies that the effect of GHGs might be partially masked, particularly in regions of high aerosol burden. Despite possibly important climate sensitivity to aerosol, particularly on regional scales, the Intergovernmental Panel of Climate Change (IPCC) acknowledges in their fifth assessment report (AR5) that studies disagree on the magnitude and sign of the climate response to aerosol changes resulting in an overall low confidence in our current scientific understanding (Boucher *et al.*, 2013).

The reasons for the gaps in our knowledge of understanding aerosols in the climate system are attributed to different aspects. Firstly, the presence of aerosols is spatially and temporally variable making their observation and modelling a challenging task. Secondly, their atmospheric life cycle and possible climate effect depend on the meteorological character of the air and the underlying surface (Stevens & Feingold, 2009). Thirdly, aerosols may interact and trigger chemical reactions producing new aerosols of different characteristics than the precursors. A detailed understanding of influences and possible feedback mechanisms between aerosols and the climate system would require a global dense network for joint observation of aerosol and meteorological conditions. Our current knowledge based on direct observation is largely based on case studies under specific meteorological regimes and thus incomplete (Stevens & Feingold, 2009).

Numerical modeling is used to compensate some of the shortcomings of the observational network for aerosol investigations. In contrast to observations, atmospheric models can provide global information for investigating the role of aerosols in the climate system over long time periods. Validation studies, however, demonstrate the limitation of atmospheric models to reproduce aerosol observation. Evaluation of global aerosol climate models from the intercomparison projects AEROCOM indicates uncertainty of 30−70 % for the global annual mean aerosol direct effect (Quaas *et al.*, 2009).

According to AR5 of the IPCC (Boucher *et al.*, 2013) processes involved in emission of natural aerosol are one of the key aspects causing the large model spread in the climate sensitivity to aerosol. Atmospheric dust constitutes a large fraction of the aerosol mass. Dust has important effects on the radiation balance, the hydrological cycle, ecosystems and human health. Despite the implication of mineral dust, our understanding of the future development of dust aerosol concentrations is poor. Previous work show both increases and decreases of the mineral dust concentrations under a changing climate (Carslaw *et al.*, 2010, and references therein). The future development of the wind speed and the vegetation cover have been highlighted to be important (Carslaw *et al.*, 2010). For instance, a vegetation decline can be driven by a rainfall deficit and agricultural use. The vegetation die-back may in turn lead to a larger bare soil fraction but may also decrease the surface roughness so that the momentum transport to the surface is larger. Such complex interactions and feedbacks require an Earth system model for studies on mineral dust in context of climate change. Validation of such models underline their variety and deviations from observed climate (e.g. Collins *et al.*, 2011; Huneeus *et al.*, 2011). One of the reasons can be the parameterisation of sub-grid scale processes that are crucial in all stages of the life cycle of dust aerosol and their impact in the Earth system. A systematic analysis of processes involved in the life cycle of dust aerosol holds the potential to improve the model simulations and to advance our scientific understanding.

This PhD thesis addresses the emission of mineral dust aerosol in North Africa, the largest dust source on Earth (e.g. Engelstaedter *et al.*, 2006; Tegen & Schepanski, 2009), from where dust aerosol can be transported towards America and Europe (e.g. Ben-Ami *et al.*, 2009; Kaufman *et al.*, 2005; Koren *et al.*, 2006; Moulin *et al.*, 1998; Winstanley, 1972). The atmospheric concentration of mineral dust depends strongly on the location, time and amount of dust emission. State-of-the-art atmospheric models applied to dust aerosol over North Africa show a large diversity of their emission amount (Colarco *et al.*, 2010; Evan *et al.*, 2014; Huneeus *et al.*, 2011; Laurent *et al.*, 2008; Schmechtig *et al.*, 2011). Realistic simulations of dust emission depend on the representation of both soil properties and meteorological processes generating sufficiently large near-surface winds for mobilizing soil particles (Gillette & Passi, 1988; Reinfried *et al.*, 2009; Shao *et al.*, 1993). The dust emission depends herein usually non-linearly on the wind speed (e.g. Kok, 2011; Marticorena & Bergametti, 1995; Tegen *et al.*, 2002). Several studies underline that misrepresentations of the wind speed in a model has a particularly strong impact on dust emission (Knippertz & Todd, 2012; Schmechtig *et al.*, 2011).

The present work contributes to our understanding of the relative importance of meteorological processes generating sufficiently large wind speeds for dust emission in North Africa and their current representation in atmospheric models. While different meteorological processes are known to cause dust-emitting wind speeds, their relative importance from a climatological perspective is poorly quantified (Cuesta *et al.*, 2009; Knippertz & Todd, 2012). Amongst other atmospheric phenomena, these include nocturnal low-level jets, atmospheric depressions and mobile cyclones which are the subject of the present work. These dust-emitting processes are investigated with the help of innovative detection tools applied to ERA-Interim re-analysis from the European Centre for Medium-Range Weather Forecasts (ECMWF, Dee *et al.*, 2011) and a dust emission model (Tegen *et al.*, 2002). This approach enables the first climatological estimate of their relative importance for North African dust emission amounts. The detailed insights in the NLLJ, a layer of relatively high wind speed in a few hundred metres above the ground during the night, as driver of dust emission over North Africa and the newly developed tool for their automatic identification are used to compare the representation of this mechanism in ERA-Interim to the global Earth system model from the UK Met Office. The following sections review the literature to give an overview of dust aerosol as part of the Earth system as well as processes for dust emission and relevant physical parameterisations in atmospheric models. At the end the aims of this thesis are defined in more detail.

1.1 Mineral Dust in the Earth System

Atmospheric dust may affect meteorological conditions and therefore the climate by interaction with radiation (Haywood *et al.*, 2003; Sokolik & Toon, 1996), cloud-microphysics (Karydis *et al.*, 2011; Lohmann & Feichter, 2005) and precipitability (Rosenfeld *et al.*, 2001). The direct radiative effect can be as much as 50 $\mathrm{Wm^{-2}}$ in the monthly mean, the missing representation of which may cause substantial forecast errors in numerical weather prediction models (Haywood *et al.*, 2005). Allan *et al.* (2011) show that a long-wave radiation bias of 20 $\mathrm{Wm^{-2}}$ in the UK Met

Office forecasting model over summertime North Africa is removed when the radiation effect of dust aerosol is represented. In addition to influences on the radiation budget, dust impairs the air quality with impacts on human well-being and health (e.g. De Longueville *et al.*, 2010; Griffin, 2007; Griffin *et al.*, 2001, and references therein). Dust may also function as fertilizer for near and far-away terrestrial and oceanic ecosystems through iron transport (e.g. Jickells *et al.*, 2005; Mahowald *et al.*, 2005; Okin *et al.*, 2004).

Several feedback mechanisms involving dust aerosol have been proposed. Zhao *et al.* (2010) use the model WRF-CHEM to study the aerosol climate sensitivity over Africa and highlight the importance of aerosol feedbacks on the regional climate. Fertilizing of marine ecosystems through dust-transported iron is proposed to cause possible feedbacks in the climate system by changing the surface albedo and altering the carbon cycle, e.g. due to plankton blooms (Jickells *et al.*, 2005; Schulz *et al.*, 2012; Shao *et al.*, 2011). Dust aerosol may also influence the atmospheric flow through its radiation feedback on the vertical stratification (Schmechtig *et al.*, 2011). A modelling study with the integrated forecast system from ECMWF shows the removal of a model bias for the location and intensity of the African Easterly Jet when changes to the aerosol climatology are included in the model (Tompkins *et al.*, 2005). Feedbacks of dust aerosol on the dust emission process are suggested by different model studies, although the signs and magnitudes differ (Heinold *et al.*, 2007; Miller *et al.*, 2004; Stanelle *et al.*, 2010). Mahowald & Luo (2003) proposes that changing near-surface winds and source regions under different climatic conditions alters the atmospheric dust loading. Their modelling study suggests an emission decrease by 20 % under the future climate scenario A1 when the dust sources are kept constant and an even larger decrease of up to 60 % when changing dust sources are included in the model. The uncertainty of estimating dust aerosol concentrations under a changing climate is, however, large due to the assumptions made and requires further research (e.g. Isaksen *et al.*, 2009; Mahowald & Luo, 2003).

Despite the importance of dust aerosol in the Earth system, estimates of the dust emission amount from North Africa based on satellite retrievals (e.g. Engelstaedter *et al.*, 2006; Schepanski *et al.*, 2009) and model simulations (e.g. Ginoux *et al.*, 2001; Huneeus *et al.*, 2011; Shao *et al.*, 2011; Tegen *et al.*, 2002) show a large diversity. Based on satellite products for aerosol optical properties off the African coast, the annual mean emission of dust is 130−1600 Tg per year (Engelstaedter *et al.*, 2006). In contrast to satellite estimates, model calculations for the North African dust emission amount range between 400 Tg and 3000 Tg per year (Cakmur *et al.*, 2004; Duce, 1995; Huneeus *et al.*, 2011; Schepanski *et al.*, 2009; Shao *et al.*, 2011; Tanaka & Chiba, 2006; Zender *et al.*, 2004). These estimates correspond to 40−70 % of the global dust emission under present climate conditions, making North Africa the dominant dust source on Earth (Engelstaedter *et al.*, 2006; Schepanski *et al.*, 2009; Tanaka & Chiba, 2006). The year-to-year variability of the annually averaged North African dust emission is estimated to be 585−759 Tg per year for 1996−2001 following Laurent *et al.* (2008). In addition to large natural variability, the physical parameterisation of sub-grid scale processes required in coarse resolution models is an important reason for model diversity. The atmospheric life cycle of dust aerosol and its impacts is likely affected by improvements of the representation of processes for dust emission which is described in the next section.

1.2 Dust emission

Dust emission from North Africa is favoured by large areas with fine sediments and several atmospheric mechanisms that generate winds sufficiently large for dust mobilization (Engelstaedter *et al.*, 2006). Loose sediments are geomorphologically formed by soil destabilization caused by mechanical disruption, wetting and subsequent drying with clay shrinking as well as soil expansion and contraction by heat (Ginoux *et al.*, 2001). Looking at small-scale atmospheric factors for dust mobilization shows that the effect of wind on grains is twofold (Warner, 2004). Firstly, the air motion over the grain at the ground causes a decrease in the pressure at the top, while the one at the bottom remains unchanged. In result of the vertical pressure gradient an upward motion of the particle is forced. Secondly, the frictional drag of the wind forces the dust particle to move in the direction of the wind. These forces created by the wind stream are countered by particle-size dependent forces related to the grain weight, the packing, the cohesion and adhesion (Marticorena & Bergametti, 1995; Warner, 2004). The latter two forces refer to molecular bounding between single particles that are either of the same or different types. These include Van der Waals, electrostatic, capillary and chemical binding forces. Packing of soil particles determines the effect of the wind shade of larger particles on dust emission. The grain weight determines the sedimentation velocity such that large sand grains have short lifetimes.

The presence of water in the top soil can have an impact on the erodibility, especially for soils with a high clay content due to their ability to form aggregates (Cornelis & Gabriels, 2003; Fécan *et al.*, 1999). The annual mean precipitation does usually not exceed 200 mm in most areas in the inner Sahara (Engelstaedter *et al.*, 2006). Since rainfall supplies soil moisture close to the surface, moisture

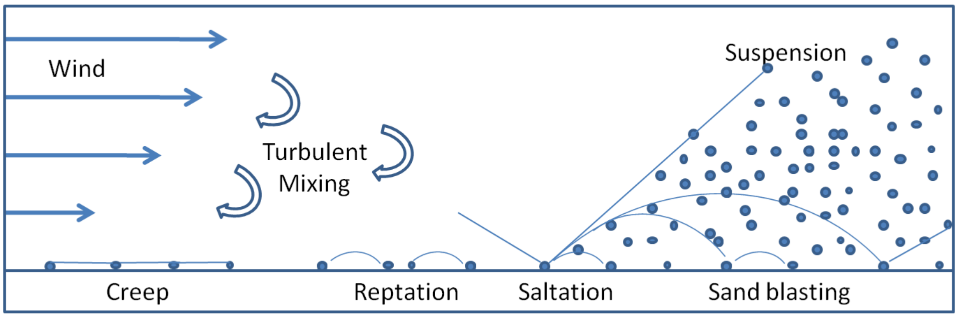

Figure 1.1: *Schematic diagram of particle trajectories during dust mobilization. After Warner (2004).*

in the top-soil is usually not a limiting factor in the hot-arid climate types (Kottek *et al.*, 2006) of the central Saharan desert. Some areas like oases and mountains, however, show different climates (Warner, 2004). The highest mountain ranges are the Atlas Mountains (4165 m) in Morocco, the Hoggar Masif (2918 m) in Algeria, the Aïr Mountains (2310 m) in Niger as well as the Tibesti (3415 m) and Ennedi (1450 m) Mountains in Chad. These areas as well as regions along the margins of the desert may receive much larger, but typically localized rainfalls (e.g. Warner, 2004). Laurent *et al.* (2008) show that soil moisture limits dust emission at the northern margins of the continent. Similarly dust emission shows a correlation to the rainfall deficit in the Sahel along the southern margin of the Sahara, although the effect of higher soil moisture on dust emission here may be rather indirect through the growth of vegetation that increases the surface roughness and in turn weakens wind speeds for dust emission (Chiapello *et al.*, 2005).

As soon as the aerodynamic force overcomes the forces holding particles within the surface crust, soil particles are available for emission. As a rule of thumb particles with 0.04−0.4 mm diameters are most efficiently mobilized (Warner, 2004). Particles with diameters of more than 0.1 μm require more energy to be released from the surface and have shorter atmospheric lifetimes due to the larger gravitational force. Particles smaller than 0.1 μm tend to form larger particles through aggregation. Their availability for aeolian transport is reduced due to the larger inter-particle forces (Ginoux *et al.*, 2001). The direct wind-driven emission of these mineral dust particles is therefore inefficient. Indirect effects must be responsible for the release of large mineral dust amounts from the ground surface as explained in the following.

1.2.1 Soil grain trajectories

In general, mobilized particles follow different trajectories as indicated in Figure 1.1. These are namely creep, reptation and saltation (Warner, 2004). Creeping particles are usually larger than 2 mm and roll over the surface without loosing ground contact (Marticorena & Bergametti, 1995). Saltation describes the repeated bouncing of particles with typical diameters of 60 to 2000 μm within a near-surface layer (Marticorena & Bergametti, 1995). If the bouncing particle undergoes a single jump the process is called reptation (Warner, 2004). When saltating particles impact on the surface (saltation bombardment), their momentum is partly transferred to other soil grains at the ground. The impact may destroy soil aggregates so that smaller particles are released from the surface crust.

When the energy transfer of saltating particles is large enough to overcome forces holding particles at the surface, the saltation bombardment triggers the emission of particles of different sizes. This process is known as sandblasting and causes the most intense dust emission events (Laurent *et al.*, 2008). The particle size, form and weight, and the wind field control the height of the particle trajectories that define the saltation layer depth, typically 1 m (Marticorena & Bergametti, 1995). Measurements summarized by Warner (2004) suggest maximum saltation layer depths of up to 3 m, but most of the saltating grains occur within the lowest 2 cm. Especially particles larger than 6 μm have short atmospheric life times as they settle on the surface by gravitation quickly (Tegen & Fung, 1994). It is interesting to highlight that particles with diameters larger than 2 μm may represent 98 % of the dust mass distribution but only 12 % of the dust number distribution (Foret *et al.*, 2006). The largest number of particles is found for smaller particle sizes. These fine particles, dust with diameters smaller than 0.06 μm, can be further lifted in the atmospheric boundary layer by turbulent mixing (Marticorena & Bergametti, 1995; Warner, 2004). The vertical dust emission flux is defined by these dust particles suspended in air (Marticorena & Bergametti, 1995).

The momentum transfer between the atmosphere and the surface is mainly maintained by turbulent fluxes. In the Prandtl layer, accounting for roughly 10 % of the entire atmospheric boundary layer (ABL) depth (Holton, 2004), the wind friction velocity u_* describes the turbulent momentum flux for eddies in the x-z-plane $\overline{w'u'}$ (e.g. Etling, 2008) by:

$$u_*^2 = \left|\overline{w'u'}\right| . \tag{1.1}$$

Within the Prandtl layer, the vertical variations of the vertical flux of momentum $\overline{w'u'}$, and therefore the friction velocity, are small (Etling, 2008). Assuming the

Coriolis and pressure gradient forces are negligible allows to relate the turbulent momentum transfer to the near-surface wind shear $\partial\overline{u}/\partial z$ (e.g. Etling, 2008) by

$$u_*^2 = K_m \frac{\partial \overline{u}}{\partial z}. \tag{1.2}$$

The turbulent exchange coefficient or eddy viscosity K_m is commonly described by the mixing length theory that assumes eddy diameters as directly proportional to the distance from the surface (e.g. Holton, 2004). Under neutral stratification the logarithmic wind profile follows:

$$\overline{u}(z) = \frac{u_*}{\kappa} ln\left(\frac{z}{z_0}\right). \tag{1.3}$$

The mean wind speed $\overline{u}(z)$ at a specific height z thus depends on the friction velocity u_*, the von Karman constant κ ≅0.4, and the roughness length z_0. The roughness length is defined in the Prandtl layer as the height where the mean wind speed $\overline{u}$ is zero which is strongly influenced by the orography and the surface coverage. The process of saltation can be interpreted as part of the surface roughness, as it acts as a momentum sink for the atmosphere (Marticorena & Bergametti, 1995). The friction velocity describes the turbulent transfer of momentum and can be approximated by an empirical relationship which uses the drag coefficient c_d (Etling, 2008):

$$u_* = \sqrt{c_d}\overline{u}(z = 10m). \tag{1.4}$$

The drag coefficient accounts for the state of the ABL and increases with decreasing stability. This relationship implies that both wind speed and friction velocity are dependent so that both variables are suitable to describe dust emission. While the logarithmic wind relationship is valid for neutral condition, it is also applicable for non-neutral conditions by applying empirical corrections from the Monin-Obukhov similarity theory. Wind speeds during extreme stability conditions, however, may be affected by uncertainties of 10$-$20 % (Folken, 2006). Qualitatively speaking, the near-surface wind speed is lower (higher) and its vertical gradient is larger (smaller) than the logarithmic wind profile in case of more stable (unstable) stratifications. The increase of the mean wind speed with height implies that saltating grains lifted into the Prandtl layer are increasingly accelerated with height.

1.2.2 Dust sources

Dust emission occurs in distinct regions that are typically covered by no or sparse vegetation such as grass or shrubs. Dominant North African sources for fine sediments are typically ancient lake basins and paleo rivers, mostly dating back to the Holocene and situated in orographic depressions (Ghienne *et al.*, 2002). This motivated the usage of topographic depressions as preferential sources in global models (Stier *et al.*, 2005; Tegen & Schepanski, 2009; Tegen *et al.*, 2002). Not only ancient lakes provide loose material for deflation but also smaller alluvial sources in complex terrain (Schepanski *et al.*, 2013). Potential dust sources may therefore be best described by observations. Since the network of ground observation is sparse, the satellite product for dust source activation frequency from Schepanski *et al.* (2009) is a good alternative. In this thesis, dust sources are defined when at least two events have been observed between March 2005 and February 2010 in this product following Heinold *et al.* (2013) and Fiedler *et al.* (2013a).

For illustrating the geographical position of the most active dust sources in North Africa, Figure 1.2 shows the annually averaged occurrence frequency of dust source activation (DSA) derived from satellite observations (Schepanski *et al.*, 2009, 2012, 2007). The distribution of DSA frequencies highlights that almost the entire of North Africa north of 10° N may act as dust source (Figure 1.2). The Bodélé Depression in Chad stands out as a particularly important dried out lake bed with fine clay and silt sediments from the perspective of both the North African and global dust load (Laurent *et al.*, 2008; Washington & Todd, 2005). This source may be active throughout the year, but emission events are most frequent during winter (e.g. Schepanski *et al.*, 2009). Previous work shows that dust aerosol originating in this area can be transported as far as South America in winter (Koren *et al.*, 2006).

A larger but less productive source region is situated in Western Africa covering large parts of Mali and Mauritania (e.g. Engelstaedter *et al.*, 2006; Laurent *et al.*, 2008; Schepanski *et al.*, 2009). This source region stretches across 900 km and is primarily active in summer (e.g. Knippertz, 2008). Further source regions are found between the Atlas Mountains and southern Algeria, in the Libyan Desert, and the Nubian Desert covering parts of Egypt and Sudan, and also between western Tunisia and central Algeria (Engelstaedter *et al.*, 2006; Knippertz, 2008; Laurent *et al.*, 2008). Dust sources in the eastern Sahara are primarily active between March and May (Laurent *et al.*, 2008; Schepanski *et al.*, 2009). The simulation by Schmechtig *et al.* (2011) suggests that this dust source produces amounts of comparable magnitude to the maximum over summertime West Africa and may last for a longer time period of January to June. Their results also show dust sources close to the Mediterranean Sea which are most active at the beginning of the year. The activation of dust sources depends on the meteorological conditions that change in the course of the year. Driving meteorological mechanisms for dust emission

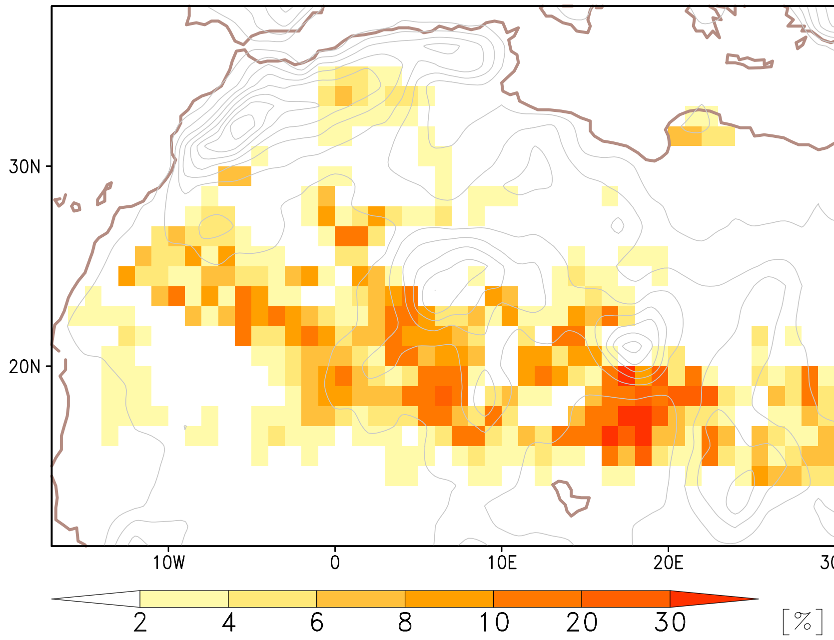

Figure 1.2: *Observation of dust source activation (DSA). Shown is the annual mean DSA occurrence frequency identified from false-color images from the Meteosat Second Generation (MSG) Spinning Enhanced Visible and Infrared Imager (SEVIRI) by Schepanski* et al. *(2012) with permission of K. Schepanski (TROPOS, Leipzig, 2014). Grey contours show the orographic height from ERA-Interim re-analysis in steps of 200 m.*

are reviewed after introducing the physical parameterisation of dust emission in the following subsection.

1.2.3 Dust emission parameterisation

Dust emission is a sub-grid scale phenomenon in weather and climate models so that it needs to be parameterised. Different physical parameterisation schemes for the description of the dust emission flux exist. An early attempt by Gillette & Passi (1988) describes the vertical dust emission flux F_v by:

$$F_v = \alpha u_*^n \left(1 - \frac{u_{*,t}}{u_*}\right), \qquad u_* > u_{*,t}. \tag{1.5}$$

Here, $u_{*,t}$ is the threshold wind friction velocity for emission onset at which forces lifting soil particles are in balance with forces keeping the particle in the soil crust and moving it towards it. Soil observation data are required to specify the empirical coefficient α, the exponent n of which varies between three and five, but is often assumed as four (Shao *et al.*, 2011).

A more recent and sophisticated parameterisation using detailed information on soil properties is the one by Marticorena & Bergametti (1995) that is also the basis of the model by Tegen *et al.* (2002) and Woodward (2001) used in this work.

These schemes relate the total vertical dust emission flux F_v to the saltation flux F_h by $F_v = \alpha F_h$. The sandblasting efficiency α is an empirical value derived from observations for different values of the soil clay content η following (Marticorena & Bergametti, 1995):

$$\alpha = \frac{F_v}{F_h} = a_1 exp\left(a_2\eta - a_3\right). \tag{1.6}$$

The saltation flux, also termed horizontal dust emission flux, is often described as a cubic function of the wind friction velocity (e.g. Kok, 2011; Marticorena & Bergametti, 1995; Tegen *et al.*, 2002; Woodward, 2001). In the case of Marticorena & Bergametti (1995) the horizontal dust flux is calculated for several particle sizes D_p and written as:

$$F_h = C\frac{\rho_a}{g}u_*^3\left(1 + \frac{u_{*,t}(D_p)}{u_*}\right)\left(1 - \frac{u_{*,t}^2(D_p)}{u_*^2}\right), \qquad u_* > u_{*,t}. \tag{1.7}$$

Dust emission may be suppressed if the soil moisture in the upper 10$-$30 cm crust reaches a model specific value approaching the field capacity (Tegen *et al.*, 2002). The uppermost millimetres of the soil, however, dry quickly under high-wind regimes and allow dust emission, despite saturated conditions in most soil layers beneath (Gillette, 1999). This argument is used to tune the influence of the soil moisture on the calculated saltation flux. The soil moisture effect may be represented by the factor C in the saltation flux.

This dust emission parameterisation by Marticorena & Bergametti (1995) describes the saltation flux implicitly. Other schemes, e.g. Shao (2001) and Alfaro & Gomes (2001), calculate dust emission for different dust sizes by saltation bombardment and aggregate disruption by sand particles explicitly (Shao *et al.*, 2011). These schemes are computationally more expensive so that implicit schemes like the one by Marticorena & Bergametti (1995) are commonly used in weather and climate modelling for dust application.

Threshold velocity

The threshold friction velocity $u_{*,t}$ in Equations 1.5 and 1.7 controls the onset of dust emission. It is a function of the particle size and soil properties, e.g. the aggregate size depending on the chemical composition, the roughness length depending on non-erodible obstacles and the erodible fraction of the grid box (Laurent *et al.*, 2008). Following Marticorena & Bergametti (1995), the threshold friction velocity is described by:

$$u_{*,t} = A\sqrt{\left(\frac{\rho_p g D_p}{\rho_a}\right)}. \tag{1.8}$$

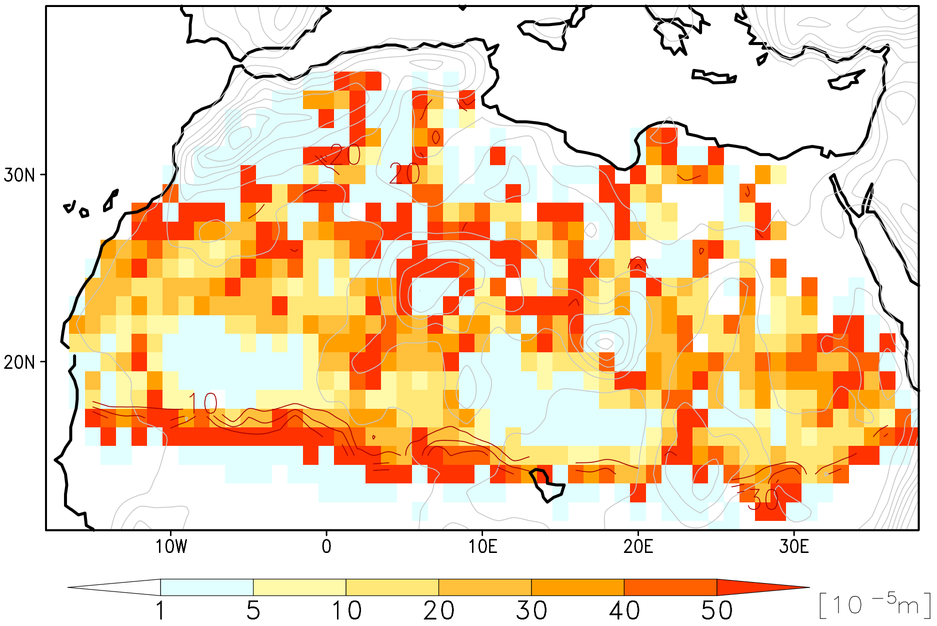

Figure 1.3: *Roughness length and dust sources. Shown are the roughness length for September (shaded) from Prigent* et al. *(2005) in potential dust sources derived from SEVIRI satellite data (e.g. Schepanski* et al.*, 2007) and the absolute difference of the roughness length between September and March in steps of 10·10^{-5} m (brown contours). Grey contours show the orography in steps of 200 m.*

Here, the threshold depends on the particle diameter D_p, the gravitational acceleration g, a scaling parameter A, the densities of the air ρ_a and of the particle ρ_p.

The effect of the roughness length is incorporate in the threshold friction velocity (Engelstaedter *et al.*, 2006; Tegen & Schepanski, 2009) by drag partition. This means that the roughness length acting on the atmospheric flow, z_0, is divided into a fraction from non-erodible obstacles and from the erodible soil bed, z_{0s}. Non-erodible elements act as a sink of atmospheric momentum so that less soil particles may be mobilized. As a result larger roughness lengths of non-erodible elements increase the threshold friction velocity.

The roughness length z_0 from Prigent *et al.* (2005) used in the model by Tegen *et al.* (2002) is shown for September in Figure 1.3. The roughness length is generally small in topographic depressions with typical values of 0.001 cm (Schepanski *et al.*, 2007). Loose sediments and no or sparse vegetation are ideal prerequisites for dust emission in such areas (Ginoux *et al.*, 2001; Marticorena & Bergametti, 1995; Tegen *et al.*, 2002). The effect of growing vegetation as non-erodible elements on the roughness length is visible at the end of the rainy season in September, when the roughness length in the Sahel is larger than in March (Figure 1.3). This effect can be taken into account by monthly varying roughness lengths. The calculated dust emission fluxes with these roughness lengths, however, misses some dust sources identified by the satellite product, so that all potential dust sources in the calculations in this thesis are set to 0.001 cm, the typical value for a soil bed (pers. comm. B. Heinold, University of Leeds and now at TROPOS, Leipzig, 2012).

Experimental studies indicate a minimum of the threshold friction velocity for particle sizes around 80μm with an increase above due to gravitational forces and below caused by molecular forces (Iversen & White, 1982; Tegen *et al.*, 2002). In North Africa, the spatially averaged threshold wind speeds for dust mobilization are around 8 ms^{-1} with a spatial variance from 5 ms^{-1} to 12.5 ms^{-1} (Chomette *et al.*, 1999; Tegen *et al.*, 2002). The threshold wind velocities in the Bodélé Depression are about 10 ms^{-1} (Koren & Kaufmann, 2004). Different atmospheric processes generating dust-emitting wind speeds above those threshold velocities are known and reviewed in the following section.

1.2.4 Uncertainties

Simulations of dust emission from different models show a large variety affecting the entire lifecycle of dust aerosol and its impacts. Comparing dust emission estimates from various studies (e.g. Fiedler *et al.*, 2013a; Laurent *et al.*, 2008; Schmechtig *et al.*, 2011; Tegen *et al.*, 2004; Woodward, 2001) reveales that the solution for African emission is diverse for both weather forecast and climate models. The Northern Africa-Middle East-Europe Node of the “Sand and dust storm warning advisory and assessment system” (SDS-WAS)[*] of the World Meteorological Organization illustrates the model diversity in daily forecasts from nine different national weather services. A set of global aerosol-climate models is used by Huneeus *et al.* (2011) to perform the intercomparison project AEROCOM for the year 2000. Their results indicate that North African emission in climate applications varies by a factor of six. Likewise, a large uncertainty is likely in CMIP5 models as suggested by Evan *et al.* (2014).

Understanding the reasons for the variety in dust emission is a complex problem due to different aspects: (1) Physical parameterisations of dust emission differ. For instance, parameters are used to tune the model to observed conditions. (2) Different treatments of soil properties, particle size distributions and locations of preferential dust sources can alter the simulations (Laurent *et al.*, 2008; Menut *et al.*, 2005, 2013; Schepanski *et al.*, 2013). (3) Interactions and feedbacks in Earth system models can complicate the interpretation and improvement of the simulations. For instance, a coupled land-vegetation component in an atmosphere model

---

[*] http://sds-was.aemet.es/forecast-products/dust-forecasts/compared-dust-forecasts, as of April 2014

can lead in case of a rainfall deficit to a vegetation decrease which can imply larger dust sources and wind speed (e.g. Woodward, 2001). (4) The wind speed distribution differs amongst models and compared to observations. Accurately representing wind speed in dust models is understood as an important factor due to the non-linear dependency (e.g. Knippertz & Todd, 2012; Schmechtig *et al.*, 2011). If meteorological processes generating dust-emitting winds are misrepresented, the associated dust emission is also affected. Known dust-emitting processes are reviewed the next section.

1.3 Meteorological conditions for dust storms in North Africa

The processes involved in dust emission can be classified by their typical length and time scale that are schematically depicted in Figure 1.4. The production of loose sediments by weathering and soil formation characteristically act on long time scales and could be extended to millions of years for the formation of mountains. Climate change is also acting on time periods of decades to hundreds of years and beyond, influencing both geo-physical processes like the formation of deserts as well as atmospheric conditions. In contrast to these large scales, winds for dust emission may last for a few hours or may be characterized by short fluctuation of seconds to minutes. Typical African weather patterns involved in generating these winds act on time scales of minutes to days, e.g. the breakdown of nocturnal low-level jets (NLLJs) and changes of synoptic-scale conditions. Weather conditions for dust storms are described in the following.

Synoptic-scale features dominate the overall weather conditions and influence dust mobilizing phenomena on smaller scales indicated in Figure 1.5. For instance, large-scale subsidence in a high pressure system causes clear skies and the associated high net surface radiation leads to the development of deep atmospheric boundary layers (ABL, Cuesta *et al.*, 2008). The synoptic-scale conditions are discussed first (Section 1.3.1) followed by processes acting on smaller scales, namely cold pool formation due to deep convection and processes in the ABL including the NLLJ (Sections 1.3.2-1.3.4).

1.3.1 Synoptic-scale flow and cyclones

Harmattan

The general circulation of the atmosphere determines the seasonal changes of the synoptic pattern over North Africa. Figure 1.6 shows the seasonal mean sea

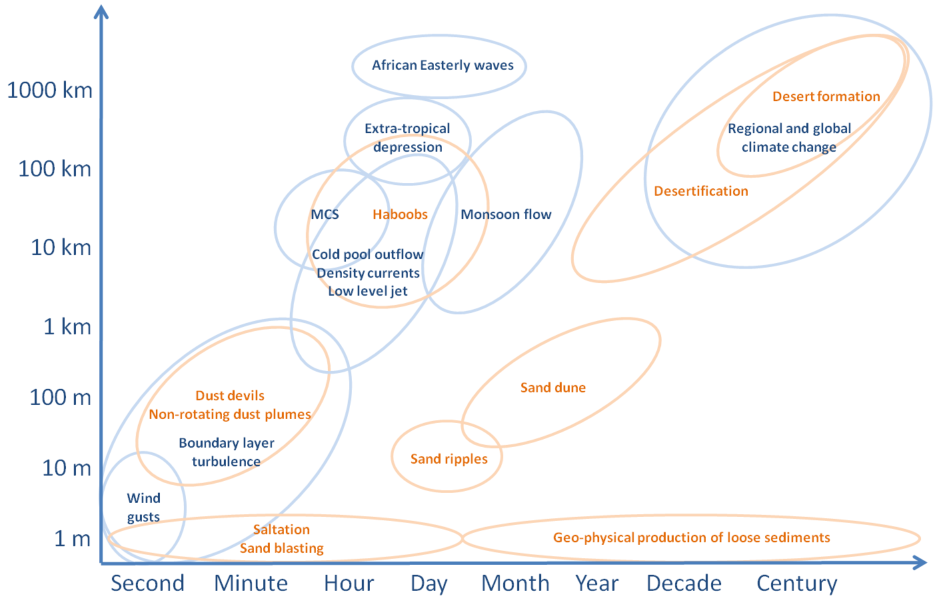

Figure 1.4: *Schematic diagram of scales. Shown are characteristic temporal and spatial scales of processes involved in dust emissions in the atmosphere (blue) and the soil (orange), based on Shao* et al. *(2011)*

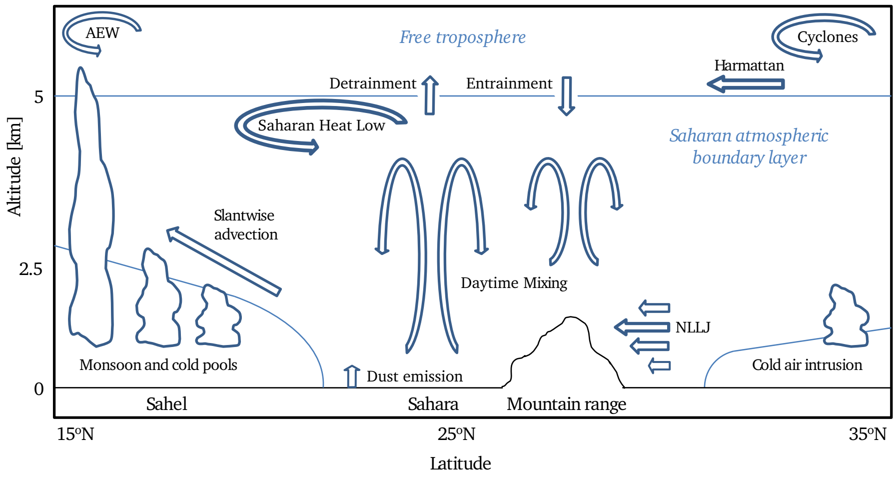

Figure 1.5: *Schematic summary of meteorological processes for North African dust emission. Arrows indicate atmospheric flow non-quantitatively. After Cuesta* et al. *(2009).*

level pressure and the mean winds at 850 hPa. In winter, anticyclonic (cyclonic) conditions prevail over the north (south) of the continent (Figure 1.6a). Associated with this pattern are prevailing north-easterly trade winds, known as Harmattan in North Africa. These winds can cause dust emission and, in extreme cases, long and fast propagating dust fronts (Knippertz & Fink, 2006; Slingo *et al.*, 2006).

Harmattan winds are caused by the northern-hemisphere Hadley cell, the origin of which is described in the following. In the annual mean, the net radiation budget near the equator is more positive than further poleward. In consequence of the net energy gain, the air masses warm and expand more in low latitudes. The different expansion leads to a higher pressure near the equator at upper levels compared to further poleward. The meridional pressure gradient increases with height and drives a compensating south-westerly flow, due to the deflection to the right by the Coriolis force on the northern hemisphere, typically between 0° and about 30° N. The associated poleward mass transport leads to an increase of mass in the atmospheric column in higher latitudes. In result the near-surface pressure increases and forms a low-level high. At the same time, the divergence near the equator at upper levels causes a decrease of the pressure near the surface. The resulting low-level pressure gradient results in the north-easterly Harmattan winds the direction of which is again determined by a balance between the pressure gradient, the friction and the Coriolis force. For continuity reasons, compensating vertical motions arise. During the large-scale subsidence, air masses warm dry-adiabatically and stabilize the lower troposphere. This process can be strong enough to create a trade wind inversion. The hot-arid air masses in the low-level high gradually transition to moister and cooler characteristics towards the equator. This results in initially shallow convection and then deeper convection towards the equator. At the same time the trade inversion height increases from higher to lower latitudes and diminishes near the Inter Tropical Convergence Zone (ITCZ), defined as the zone of maximum tropospheric water content (Fink, 2006). Here, large-scale ascending motion favours the development of deep convection.

Along with the seasonal change of maximum insolation, the ITCZ migrates and affects both strength and extent of the northern-hemisphere Hadley cell. The ITCZ reaches its southernmost position over the Gulf of Guinea (long-term climatological mean) during winter (Fink, 2006). During this season north-easterly Harmattan winds prevail over most of North Africa. In August, the ITCZ is situated furthest north at 11° N (Fink, 2006). At this time of year, the northern hemisphere Hadley cell is weaker and the Saharan heat low develops over West Africa (Figure 1.6b)

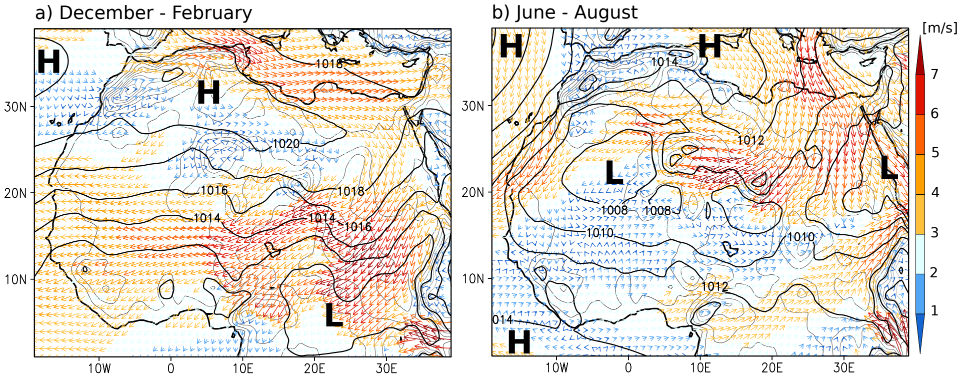

Figure 1.6: *Mean synoptic conditions for North Africa. Shown is the seasonal mean sea level pressure in steps of 2 hPa (black contours) as well as the seasonal mean wind speed (color) and direction (vector) at 850 hPa for (a) December to February and (b) June to August based on ERA-Interim re-analysis for 1981–2010. Thin grey contours show the orography in steps to 200 m.*

Saharan heat low

The mean position of the Saharan heat low is 20° N and 0° (Lavaysse *et al.*, 2009; Nicholson, 2000) and shown in Figure 1.6b. The depression forms in response to strong solar irradiation, the location of which changes in the course of year. In North Africa the heat low moves from positions near the equator in the east between November and March towards West Africa between April and October (Lavaysse *et al.*, 2009). The Saharan heat low during summer is typically quasi-stationary over several days to weeks (Lavaysse *et al.*, 2009; Todd *et al.*, 2013) and coincides with high concentrations of dust aerosol (e.g. Knippertz & Todd, 2010).

Horizontal pressure gradients along the margins of the heat low can be large enough for generating dust storms (Hannachi *et al.*, 2011; Winstanley, 1972) which may include the NLLJ mechanism (Section 1.3.4). Idealized simulations by Racz & Smith (1999) show that the pressure minimum and the upward motion in a heat low is strongest in the late afternoon, when surface heating establishes a well mixed boundary layer. The drag of the daytime turbulence leads to converging winds in the centre of the low. In contrast to the day, nighttime conditions lead to a weakening of the frictional constraint for the acceleration of the flow. In response, the low-level winds follow a more cyclonic rotation around the low during the night. These low-level winds may appear in the form of NLLJs that are discussed in Section 1.3.4. Weakened low-level convergence and cooling at night causes the pressure in the heat low centre to rise to its largest value during the morning. A typical diurnal amplitude of a heat low is about 1–10 hPa (Racz & Smith, 1999). The heat low strongly affects the positions of the intertropical discontinuity (ITD), where the northeasterly Harmattan winds and the southeasterly monsoon winds converge.

Intertropical discontinuity

The ITD describes the leading edge of the West African monsoon (Lavaysse *et al.*, 2009) between May and September. Here, the near-surface north-easterly Harmattan and the south-westerly monsoon winds converge (Knippertz & Todd, 2010; Peters & Tetzlaff, 1988). Both a jump in the dewpoint temperature and the convergence of the wind field mark the front at low levels. The ITD can show wave patterns and changes its position from 20° N in northern hemisphere summer to 7° N during winter (Fink, 2006). Maxima of the monsoon rainfall amount occur south of the ITD with a most northern position at 15° N (Nicholson, 2000). South of the ITD, favourable conditions for deep convection, namely a usually conditionally unstable stratification and large-scale ascending motion, result in large rainfall and may also generate convective dust storms known as haboobs (Section 1.3.2)

Dust emission along the ITD is suggested as a dust-emitting mechanism in West Africa by Bou Karam *et al.* (2008) but may be particularly important for dust transport. Knippertz (2008) presents a case study on the efficient southward transport of dust north of the ITD. The undercutting of the Saharan air layer by the relatively cool monsoon air forces slantwise advection of the often dust-loaded Saharan air about the ITD (Figure 1.5). This up-gliding along the front may force further dust uplift to elevated levels (Cuesta *et al.*, 2009) where dust aerosol may be transported over long distances (Marsham *et al.*, 2008a).

African Easterly Waves

[*] During the monsoon period, African Easterly Waves (AEWs) form at the southern side of the African Easterly Jet (AEJ) at 700 hPa along 10° N (Burpee, 1972). The AEJ results from the horizontal temperature contrast between the hot Saharan air poleward and the cooler air masses equatorward of the AEJ. Burpee (1972) suggests that the wind shear at the AEJ is the origin of wave-like disturbances. More recent work suggests deep convection (e.g. Mekonnen *et al.*, 2006; Thorncroft *et al.*, 2008) and extra-tropical influence (Leroux *et al.*, 2011) as trigger of AEWs. The main genesis region of AEWs remains controversial and ranges from 10° E to 40° E (Burpee, 1972; Mekonnen *et al.*, 2006; Thorncroft & Hodges, 2000;

---

[*] Text passages in the present section on African Easterly Waves are from my publication currently under review for the second stage in the Journal Atmospheric Chemistry and Physics with the intended title “How important are atmospheric depression and mobile cyclones for emitting mineral dust aerosol in North Africa?” following my publication “How important are cyclones for emitting mineral dust aerosol in North Africa?”, 13, 2013, pp. 32483−32528, in Atmospheric Chemistry and Physics Discussions distributed under the Creative Commons Public License (http://creativecommons.org/licenses/by/3.0/).

Thorncroft *et al.*, 2008, and references therein) from where they propagate westwards with the mean flow. AEWs occur about every three to five days between June and September with a peak activity at the beginning of August (Burpee, 1972; Jones *et al.*, 2003). At 850 hPa, AEW signatures occur both north and south of the AEJ axis at 10° N and 20° N (Mekonnen *et al.*, 2006). They are most frequently found in West Africa with up to six events between May and October around 20° N and 10° W (Thorncroft & Hodges, 2000).

AEWs are linked to variability of dust mobilization and concentration over West Africa although the diurnal cycle seems similarly important (Luo *et al.*, 2004). Jones *et al.* (2003) suggest that AEWs maintain 20 % of dust uplift into the atmosphere. However, the most important meteorological processes for dust emission over West Africa remain controversial. Several studies (Knippertz & Todd, 2010; Laurent *et al.*, 2008; Schepanski *et al.*, 2009; Schmechtig *et al.*, 2011) address the dust emission maximum in summer for different time periods (1996−2001, 2006−2008, 1979−1992, and 2006, respectively). Marsham *et al.* (2008b) relate the central Western Sahara dust maximum to more frequent haboobs triggered by the monsoon flow. Knippertz (2008) and Schepanski *et al.* (2009) point to the breakdown of NLLJs causing dust-emitting near-surface winds. Prevailing dust emission due to the convective boundary layer are concluded by Engelstaedter & Washington (2007). Knippertz & Todd (2010) argue that dust emission associated with AEWs is driven by embedded haboobs and NLLJs (Section 1.3.2 and 1.3.4) which leads to large dust concentrations over West Africa as follows. A few days in advance of the maximum concentration, an extra-tropical wave interacts with an AEW causing low-level northerlies to the west and southerlies to the east of an AEW trough. Advection of moist air into the Sahara behind the AEW trough may lead to the development of moist convection with the formation of haboobs (Section 1.3.2). Suspended dust in the propagating density current is subsequently advected northward, where further uplift by dry convection occurs. As the AEW propagates westward, the wind direction turns to northerly directions which re-advects the dusty air towards the south. The background dust concentration may be further increased by emission over West Africa, the driving mechanisms of which likely involve the breakdown of NLLJs in the morning hours (Knippertz & Todd, 2010). AEWs are also important for atmospheric transport of dust aerosol (Jones *et al.*, 2003) and are linked to tropical cyclone formation (e.g. Hopsch *et al.*, 2007; Landsea *et al.*, 1992). Dust aerosol may interact with radiation leading to a feedback on the amplitude of AEWs (Jones *et al.*, 2004).

Sudano-Saharan depressions

[*] Another migrating depression type in low-latitudes than AEW signatures is the Sudano-Saharan depression the concept of which is described in classical literature and has recently been revised (Schepanski & Knippertz, 2011, and references therein). These depressions form in the central Sahara, usually southwest of the Tibesti Mountain. They initially migrate westwards before turning anticyclonicly over West Africa to track eastwards over northern parts of the continent. Analysis of 20 years of ECMWF ERA-Interim re-analysis suggests that Sudano-Saharan depressions are rare and too shallow to cause sufficiently high wind speeds for significant amounts of dust emission (Schepanski & Knippertz, 2011).

Cyclones

[†] Extra-tropical cyclones affect northern margins of the African continent (e.g. Alpert & Ziv, 1989; Hannachi *et al.*, 2011; Winstanley, 1972). The core of these cyclones can either lie over the continent itself or further north in the Mediterranean region (e.g. Maheras *et al.*, 2001; Schepanski & Knippertz, 2011). Several studies suggest that cyclones can cause dust storms (Bou Karam *et al.*, 2010; Hannachi *et al.*, 2011; Knippertz *et al.*, 2009a; Schepanski & Knippertz, 2011; Schepanski *et al.*, 2009), although a case study by Knippertz & Fink (2006) for the exceptionally strong and continental-scale dust storm in March 2004 gives evidence that a cyclone only produces one part of the associated dust emission. The remaining dust mobilization is linked to strong northeasterly Harmattan winds. These Harmattan surges manifest themselves by an increased horizontal pressure gradient between the post cold frontal ridge and the prevailing low pressure over the continent. Both the cyclone and the Harmattan surge are caused by a wave in upper tropospheric levels. While the trough is typically associated with the cyclone, the ridge behind causes the strengthening of anticyclonic conditions over wide areas of the north, which

---

[*] Text passages and figures in the present section on Sudano-Saharan depressions are from my publication currently under review for the second stage in the Journal Atmospheric Chemistry and Physics with the intended title “How important are atmospheric depression and mobile cyclones for emitting mineral dust aerosol in North Africa?” following my publication “How important are cyclones for emitting mineral dust aerosol in North Africa?”, 13, 2013, pp. 32483−32528, in Atmospheric Chemistry and Physics Discussions distributed under the Creative Commons Public License (http://creativecommons.org/licenses/by/3.0/).

[†] Text passages and figures in the present section on Cyclones are from my publication currently under review for the second stage in the Journal Atmospheric Chemistry and Physics with the intended title “How important are atmospheric depression and mobile cyclones for emitting mineral dust aerosol in North Africa?” following my publication “How important are cyclones for emitting mineral dust aerosol in North Africa?”, 13, 2013, pp. 32483−32528, in Atmospheric Chemistry and Physics Discussions distributed under the Creative Commons Public License (http://creativecommons.org/licenses/by/3.0/).

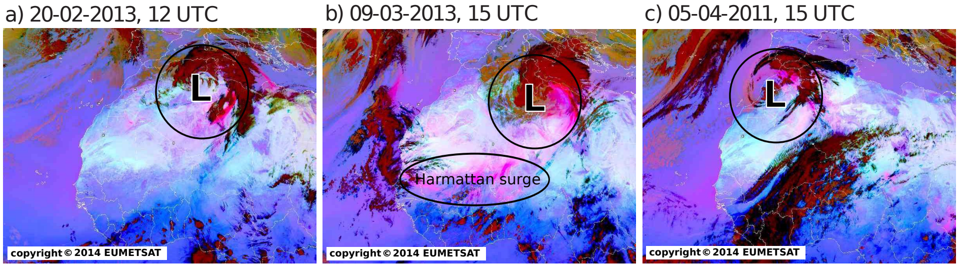

Figure 1.7: *Observations of cyclones and associated dust aerosol over North Africa. Shown are false-colour images from MSG-SEVIRI (e.g. Schepanski* et al.*, 2009, 2012, 2007) indicating mineral dust aerosol (pink) and clouds (red and black). Circles and ellipse mark the cyclone-affected area with a radius of 10° and dust emission associated with a Harmattan surge, respectively. Figure from Fiedler* et al. *(2013b).*

increases the northeasterly Harmattan winds. Harmattan surges may reach continental scale and cause dust emission, typically involving the NLLJ mechanism, as far south as the Bodélé Depression and the West African Sahel (Knippertz & Todd, 2010, and references therein). The dust may then be transported towards the Sahel, Atlantic Ocean and beyond. Klose *et al.* (2010) show that about half of dust suspended over the Sahel may be linked to a pressure pattern typical of Harmattan surges: a low over the Arabian Peninsula and the Azores High expanding eastwards into the continent. The mass of dust emission associated with cyclones has not been estimated before.

Figure 1.7 shows false colour images derived from thermal and infrared radiation measurements from the "Spinning Enhanced Visible and Infrared Imager" (SEVIRI) of the geostationary Meteosat Second Generation (MSG) satellite (e.g. Schepanski *et al.*, 2009, 2007). The typical horizontal extent of these cyclones, visible by the curling cloud band (red) and indicated by a circle around the cyclone centre, is on the order of 10°. Dust aerosol is visible near the cloud band, but parts of it are likely obscured by clouds. On 9 March 2013, dust emission also occurs over southern West Africa (Figure 1.7b), highlighted by an ellipse. These emissions are not directly related to the cyclone but likely driven by a Harmattan surge associated with the post frontal ridge (e.g. Knippertz & Fink, 2006; Knippertz & Todd, 2012, and references therein).

Previous work on cyclones influencing North Africa focuses on the meteorological analysis in the Mediterranean basin. Alpert *et al.* (1990) use five years of analysis data from the ECMWF for analysing Mediterranean cyclones statistically. A longer time period of 18 years of ECMWF re-analysis is exploited by Trigo *et al.* (1999) for cyclone tracking. The contributing factors of cyclogenesis in the Mediterranean region is investigated later by Trigo *et al.* (2002). Maheras *et al.* (2001) present a 40-year climatology of surface cyclones based on re-analysis from the

National Centers for Environmental Prediction (NCEP) and underline the variability of both the position and the core pressure of cyclones with the time of day. Since the method does not have a criterion for cyclone migration, the climatology by Maheras *et al.* (2001) includes heat lows and orographic depressions. NCEP data is also used for a springtime climatology of cyclones north of 20° N for 1958–2006 (Hannachi *et al.*, 2011). Hodges *et al.* (2011) compares cyclone climatologies derived from state-of-the-art re-analysis showing spatial differences of track densities and cyclone intensity.

All of these studies highlight distinct regions that are prone to frequent cyclogenesis. These are over the Aegean Sea, the Gulf of Genoa and the Black Sea (Trigo *et al.*, 2002). Regions of frequent cyclogenesis in northern Africa lie to the south of the Atlas Mountains, and east of the Hoggar Mountains (Alpert & Ziv, 1989; Maheras *et al.*, 2001; Schepanski & Knippertz, 2011; Trigo *et al.*, 1999; Winstanley, 1972). Cyclones may further form or intensify over Libya, also termed Sharav or Khamsin cyclones (e.g. Alpert & Ziv, 1989) which are thought to be the main driver for dust transport towards the eastern Mediterranean (Moulin *et al.*, 1998; Winstanley, 1972). Classically the term “Sharav” is used for heat waves in Israel, for which cyclones from Africa are one of the meteorological conditions (Winstanley, 1972). Most of the cyclones in the Mediterranean basin form between December and May, when the temperature contrast between land and sea is largest.

Cyclogenesis in Northwest Africa occurs east of an upper level trough where positive vorticity advection supports the formation of a depression near the surface. These troughs advect cool air masses at their western side towards the Sahara and transport Saharan air northwards at their eastern side (e.g. Knippertz & Fink, 2006; Maheras *et al.*, 2001). Their interaction with orography can lead to cyclogenesis on the lee side of mountain ranges. In North Africa, the position of lee cyclogenesis is typically the southern side of the Atlas Mountains (e.g. Schepanski & Knippertz, 2011; Trigo *et al.*, 2002). Migrating lee cyclones usually follow east- to northeastward trajectories with propagation speeds around $10\,\mathrm{ms}^{-1}$ (e.g. Alpert & Ziv, 1989; Alpert *et al.*, 1990; Bou Karam *et al.*, 2010; Hannachi *et al.*, 2011). They can advect hot, dry and dusty air towards the eastern Mediterranean, but may also bring rainfall (Winstanley, 1972) with flood risk in Israel (Kahana *et al.*, 2002). Unusually deep cyclones over the western Mediterranean that move from Algeria northwards are documented for winter that can cause high impact weather (Homar & Stensrud, 2004; Homar *et al.*, 2002, 2007). Suspended dust in the warm sector is frequently transported towards Europe, known as Sirocco or Khamsin (Warner, 2004).

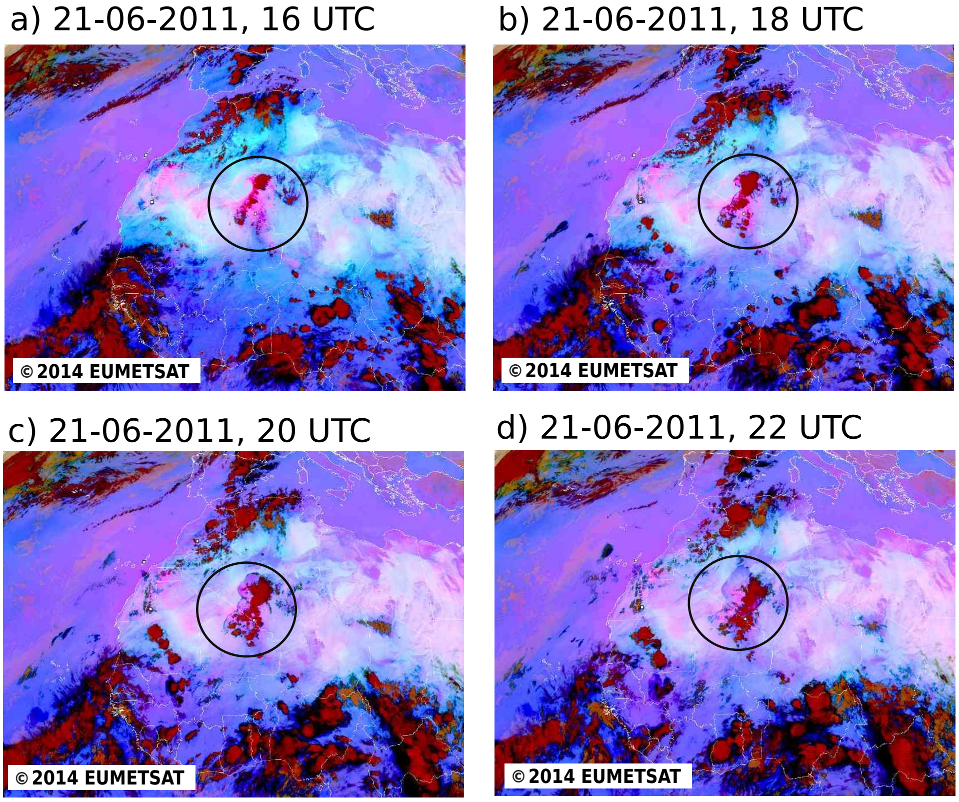

Figure 1.8: *Observation of deep convection and dust. Shown are false-color images from MSG SEVIRI of a haboob over Algeria and Mali (highlighted by circle) at 21 June 2011 indicating mineral dust aerosol (pink) and clouds (red) (e.g. Schepanski* et al.*, 2007) (a) at 16 UTC, (b) 18 UTC, (c) 20 UTC and 22 UTC.*

1.3.2 Cold pool outflows - haboobs

Synoptic-scale conditions may be favourable for the formation of deep moist convection, which generate density currents in the form of cold pools as driver for dust storms in North Africa (e.g. Flamant *et al.*, 2007; Heinold *et al.*, 2013; Knippertz *et al.*, 2009b; Marsham *et al.*, 2011). The generation of a cold pool is initiated by a convective downdraft. In-cloud water droplets grow and begin to fall, once the hydrometeors gain more weight than the updraft is able to balance. The sinking hydrometeors drag the surrounding air downward potentially further enhanced by: (1) mid-level entrainment of sub-saturated surrounding air that leads to evaporation of cloud droplets and melting of in-cloud ice, and (2) the evaporation or melting of falling hydrometeors below the cloud base. Both processes require heat, resulting in a cooling and associated increase of the air density. The vertical velocity of the downdraft may reach $5-10\,\mathrm{ms^{-1}}$, even to up to $20\,\mathrm{ms^{-1}}$ (Knippertz *et al.*, 2009b). Favourable conditions for intense downdrafts are a deep dry-adiabatic mixed layer, small hydrometeor sizes and a high in-cloud content of precipitable water and ice (Knippertz *et al.*, 2009b).

The downdraft from the convective cell diverges and spreads horizontally once it gets close to the ground. While horizontally propagating the current undercuts and lifts the Saharan air in the ABL (Flamant *et al.*, 2007). The horizontal propagation speed depends on the density current height and the temperature gradient between the current and the environment (e.g. Knippertz *et al.*, 2009b). Temperature contrast to their environment may by at least 7 K and winds associated to cold pools are often strong and gusty with typically $15-25\,\mathrm{ms}^{-1}$ (Knippertz *et al.*, 2009b). These winds can mobilize dust particles, typically near the leading edge of the cold pool (Flamant *et al.*, 2007; Knippertz *et al.*, 2009b).

The dust emission event over source regions associated with the gust front of a cold pool outflow is known as a haboob (Arabic *haboob* for strong wind, Miller *et al.*, 2008). These dust walls may cross horizontal distances of 100 km from the convective cell with typical durations of several hours (Flamant *et al.*, 2007; Knippertz *et al.*, 2009b; Miller *et al.*, 2008; Sutton, 1925). Since they are preceded by deep moist convection they are most frequently observed during the afternoon and evening hours (Flamant *et al.*, 2007; Peters & Tetzlaff, 1988).

Haboobs can be associated with meso-scale convective systems (MCSs). Figure 1.8 shows the development of convective cells along a squall line over Algeria and Mali for 21 July 2011 as an example illustrating the temporal delay of convection and the dust lifted by the haboob. During summer, haboobs frequently occur in association with the West African monsoon (e.g. Bou Karam *et al.*, 2008). In addition to dust emission, cold pool outflows may dynamically lift air parcels to their level of free convection. This means that potentially more convective cells are triggered, often organized along the convex front line of the cold pool (Fink, 2006).

Cold pool outflows are, however, not limited to West Africa, but are also observed in regions south of the Atlas Mountains, Algeria and other semi-arid areas worldwide (Knippertz *et al.*, 2009b; Miller *et al.*, 2008; Sutton, 1925). Particularly the frequency of density currents close to the Atlas Mountain in late summer is notable (Emmel *et al.*, 2010; Knippertz *et al.*, 2007, 2009b; Schepanski *et al.*, 2009). Here, orographic effects of the Atlas on the prevailing moist westerly flow in combination with elevated heating favours the formation of clouds near the mountain tops. Relatively warm and sub-saturated air masses are found in the lee of the mountain range, where cloud droplets blown out of the cloud and falling precipitation evaporate. The associated cooling increases the density of the air mass so that it descends and follows the orographic gradient (Knippertz *et al.*, 2007; Reinfried *et al.*, 2009; Schepanski *et al.*, 2009). These haboobs are associated with a mean increase of the near-surface wind speed of typically $8\,\mathrm{ms}^{-1}$ and prevailing northerlies to north-easterlies (Emmel *et al.*, 2010).

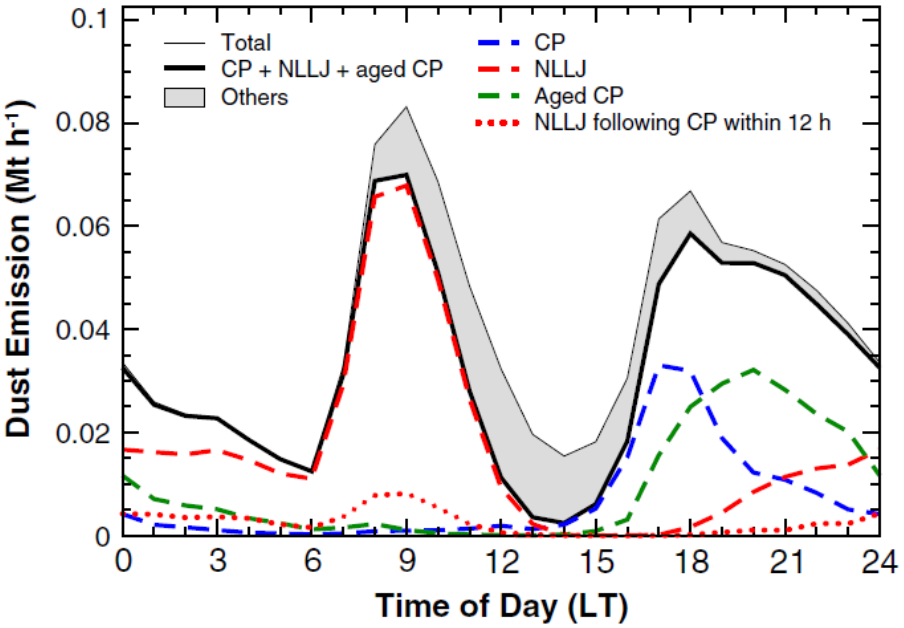

©2013. American Geophysical Union. All Rights Reserved.

Figure 1.9: *Mean diurnal cycle of dust emission over West Africa. Shown are hourly mean emissions associated with NLLJs and haboobs (blue) from a convection-permitting simulation of 4 km horizontal resolution for 26 July to 2 September 2006. Reprint of Figure 8 from Heinold* et al. *(2013) with permission of John Wiley & Sons.*

Haboobs are suggested to be the dominant generation mechanism for dust emission in the afternoon and early night (Heinold *et al.*, 2013; Schepanski *et al.*, 2009). The occurrence of dust activation in the afternoon seen in satellite products, however, is small compared to the morning DSA frequencies (Schepanski *et al.*, 2009). Kocha *et al.* (2013) suggest that satellite observation of the aerosol optical depth may miss a substantial fraction because of clouds. Based on a model simulation over West Africa for August 2006, Heinold *et al.* (2013) suggest that only 10 % of afternoon dust emission occurs under clear sky conditions. Figure 1.9 shows the diurnal cycle of dust emission from this simulation with explicit convection (Heinold *et al.*, 2013). These results suggest that a substantial part of the afternoon and nighttime dust emission is associated with cold pools.

1.3.3 Structure of the Saharan boundary layer

The lowest layer of the troposphere with a typical vertical extend of 100 m to a few kilometres from the ground is known as the ABL. Here, the daily variations of the radiation budget and surface friction affect the dynamical behaviour of the atmospheric flow.

The daytime ABL is characterized by turbulence which is driven by both wind shear and surface heating (dry convection). The turbulent eddies cover a wide

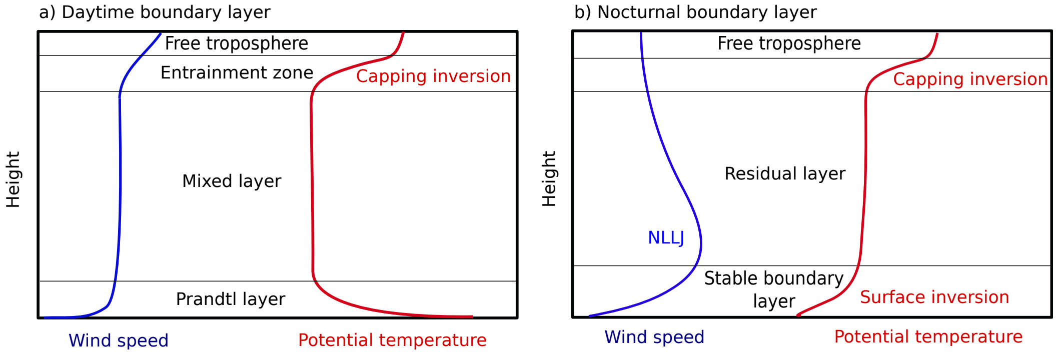

Figure 1.10: *Schematic diagram of ABL structure. Shown are vertical profiles of the horizontal wind speed and the potential temperature in (a) the daytime and (b) the nocturnal ABL, after Shao (2008) and Stull (1988).*

spectrum of size and shape, and reach typical vertical velocities of $1-2\mathrm{ms}^{-1}$ (Stensrud, 2007), which is usually larger than synoptic-scale vertical motion. About half of the boundary layer is characterized by large eddies with horizontal extensions of 1.5 times the boundary layer depth (Stensrud, 2007).

The vertical structure of the ABL is characterized by its stratification described by the vertical gradient of the potential temperature (e.g. Etling, 2008). The typical vertical profiles of the potential temperature along with the mean horizontal wind speed at day and night are schematically depicted in Figure 1.10. During daytime, the potential temperature decreases with height near the surface (Figure 1.10a), which favours vertical fluxes of heat, moisture and momentum. In contrast, an increase of the potential temperature with height is found in the the entrainment zone between the boundary layer and the free troposphere (Figure 1.10a). This capping inversion suppresses or weakens vertical exchange. Entrainment at the ABL top may contribute to growth or shrinking of the ABL, in addition to surface heating and cooling as the main driving processes for the ABL structure. Daytime heating and turbulent mixing results in an increasing ABL depth in the course of the day.

The Saharan ABL (SABL) is characterized by a relatively large surface sensible heat flux generating deep dry convection so that the daytime SABL is amongst the deepest in the world. It can reach depths of up to 6 km (Gammo, 1996) and can be capped by a strong inversion at its top in summer (Marsham *et al.*, 2008a). Regional and seasonal differences are important to mention. For instance surface heterogeneities, e.g. different surface cover and complex terrain (Figure 1.5), cause differential heating which leads to locally increased surface fluxes and therefore deeper SABLs (Cuesta *et al.*, 2009).

The SABL structure has important implications for dust emission. The daytime mixing layer is characterized by relatively large mean near-surface wind speeds and frequent wind gusts caused by dry convection (e.g. Stull, 1988). Consequently more frequent and intense dust emission events are expected during the day. The largest emission fluxes likely occur when the boundary layer depth is sufficiently deep to reach levels of large wind speeds in the free troposphere. This may be the case at mid-day or in the afternoon depending on the rate of growth of the SABL and the synoptic-scale conditions.

Dry convection in the daytime ABL is suggested to cause up to 30 % of the dust emission based on observation and modelling studies (Koch & Renno, 2005; Marsham *et al.*, 2008a; Takemi *et al.*, 2006). Koch & Renno (2005) suggest a major contribution to dust emissions by dust devils and non-rotating convective plumes. These phenomena occur under a moderate near-surface wind shear, weak mean winds and a relatively large vertical temperature gradient (Ansmann *et al.*, 2008). These conditions suggest that dry convective plumes may dominate dust emission generation at mean wind speeds well below typical threshold velocities necessary for a saltation flux. Contrary to the day, nighttime cooling at the surface due to a negative net surface radiation balance may lead to the formation of a surface inversion (Figure 1.10b). These conditions are favourable for NLLJ formation which is discussed next.

1.3.4 Nocturnal low-level jets

[*] Low-level jets (LLJs) are wind speed maxima in the lower troposphere, as defined in the meteorological terminology database METEOTERM[†] run by the World Meteorological Organization. Different definitions for LLJs, NLLJs, and nocturnal jets in previous studies and meteorological glossaries show that there is no universal agreement on the terminology, a problem already raised by Stensrud (1996). For instance the definition for "nocturnal jets" by METEOTERM follows the idea of an inertial oscillation proposed by Blackadar (1957), while the American Meteorological Society more generally defines it as "Usually, a low-level jet that occurs at night."[‡]. The term LLJ is, herein, used for a wind speed maximum in the lower part of the troposphere in both glossaries.

Previous studies on LLJs, NLLJs and nocturnal jets can be summarized under this more general term LLJ. Most of them focus on LLJs in specific parts of the

---

[*] Text passages and figures in the present section 1.3.4 are based on my publication "Climatology of nocturnal low-level jets over North Africa and implications for modeling mineral dust emission", 118, 12, 2013, pp. 6101−6103 in Journal of Geophysical Research - Atmosphere, Copyright 2014 John Wiley & Sons, Inc., This material is reproduced with permission of John Wiley & Sons, Inc (pers. comm. Paulette Goldweber, Wiley, 2014).

[†] http://wmo.multicorpora.net/METEOTERM as of August 2013

[‡] http://amsglossary.allenpress.com/glossary as of August 2013

world, e.g. north-east Australia (May, 1995), the Nares Strait channel near Greenland (Samelson & Barbour, 2007), the USA (Banta *et al.*, 2003; Bonner, 1968; Hoxit, 1975; Whiteman *et al.*, 1997), Cabauw in the Netherlands (e.g. Baas *et al.*, 2009), the Persian Gulf (Giannakopoulou & Toumi, 2012), the Bodélé Depression in Chad (Washington & Todd, 2005; Washington *et al.*, 2006), and the Sahara (Schepanski *et al.*, 2009). Some work has been done on compiling a global distribution of LLJs. These include the qualitative review by Stensrud (1996) and the quantitative investigation of diurnally varying LLJs based on a 21-year re-analysis data set by Rife *et al.* (2010). The focus here is the LLJ that occurs at night. These NLLJs reside close to the top of the nocturnal surface inversion (Baas *et al.*, 2009; Blackadar, 1957; Gross, 2012). Studies for the Great Plain LLJ indicate that the jet is found in variable heights above the surface inversion top at night (Bonner, 1968; Whiteman *et al.*, 1997).

Formation

Different meteorological conditions can generate NLLJs. While some mechanisms have been identified for specific seasons and regions of North Africa (Parker *et al.*, 2005; Todd *et al.*, 2008; Washington & Todd, 2005), an assessment of the relative importance of the mechanisms for the entire of North Africa does not exist. The formation of NLLJs can be explained with the aid of different conceptual approaches.

The classical theory by Blackadar (1957) describes the NLLJ formation using the concept of an inertial oscillation, a process tied to a decoupling of the air flow from surface friction. One of the requirements is radiative cooling that stabilizes the surface layer (Figure 1.10b). The associated weaker dynamical friction due to reduced eddy viscosity enables an acceleration of the air aloft, a process primarily occurring over land at night. Blackadar (1957) assumes a complete frictional decoupling and a constant horizontal pressure gradient. Under these theoretical conditions the wind change is solely determined by the Coriolis force. The actual wind then oscillates around the geostrophic wind vector, leading to super-geostrophic speed and preventing a geostrophic adjustment (Stull, 1988). The actual wind speed in the core of the NLLJ is determined by both the initial ageostrophic wind at the time of decoupling and the geostrophic wind (Blackadar, 1957). While the geostrophic wind is driven by horizontal pressure gradients on the meso to synoptic scale, surface friction has a strong influence on the ageostrophic wind component. The oscillation period is a function of the Coriolis parameter f, which depends on the geographical latitude. The time of maximum enhancement of the wind speed occurs when the actual wind vector and the geostrophic wind vector are aligned,

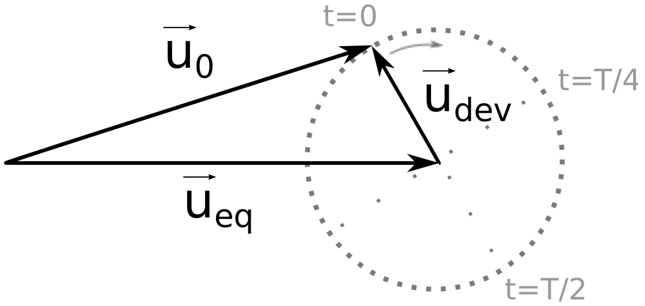

Figure 1.11: *Schematic diagram of the inertial oscillation. Shown are the equilibrium wind vector* $\vec{u}_{eq}$*, the wind vector at the beginning of the oscillation* $\vec{u}_0$ *and the wind vector describing the departure from the equilibrium wind* $\vec{u}_{dev}$*. Grey indicates points during the oscillation for different times* t *of the oscillation period* T*. Figure after Van de Wiel* et al. *(2010).*

which is between a quarter and a half of the oscillation period T. Half a period ($T/2 = \pi/f$) corresponds to 12 hours at 30° N and 17.5 hours at 20° N. Highest wind speeds and, therefore, potentially largest mineral dust emission are expected when the time of maximum enhancement of NLLJs agrees with the time of their breakdown. Even though the inertial oscillation is a simplified concept of a two-dimensional problem over flat terrain under neglection of any frictional effects, it is found to capture observed conditions in the United States reasonably well (Bonner & Paegle, 1970). An even better agreement with the variations of boundary layer winds is found, when the diurnal cycles of both the eddy viscosity and the geostrophic wind speed are included (Bonner & Paegle, 1970).

A recent revision of the classical inertial oscillation considers frictional effects in the nocturnal ABL by replacing the geostrophic wind with a more general equilibrium wind vector $\vec{u_{eq}} = (u_{eq}; v_{eq})$ (Van de Wiel *et al.*, 2010). The temporal evolution of the wind vector describing the departure from the equilibrium wind $\vec{u}_{dev} = (u - u_{eq}; v - v_{eq})$ for a stationary boundary layer is schematically depicted in Figure 1.11 and described by the equations (Van de Wiel *et al.*, 2010):

$$\frac{\partial\,(u - u_{eq})}{\partial t} = f\,(v - v_{eq}) \qquad \text{and} \qquad \frac{\partial\,(v - v_{eq})}{\partial t} = -f\,(u - u_{eq})\,. \tag{1.9a,b}$$

The analytical solution is a function of the equilibrium wind vector and the wind vector $\vec{u}_0 = (u_0; v_0)$ at time $t = 0$ given by (Van de Wiel *et al.*, 2010):

$$u - u_{eq} = (v_0 - v_{eq})sin(ft) + (u_0 - u_{eq})cos(ft) \tag{1.10a}$$

$$v - v_{eq} = (v_0 - v_{eq})cos(ft) - (u_0 - u_{eq})sin(ft). \tag{1.10b}$$

This solution describes an actual wind vector oscillating clockwise around the equilibrium wind (Figure 1.11). Oscillations at a given height are independent of the ones at other altitudes and undamped because of the assumed balance of the Cori-

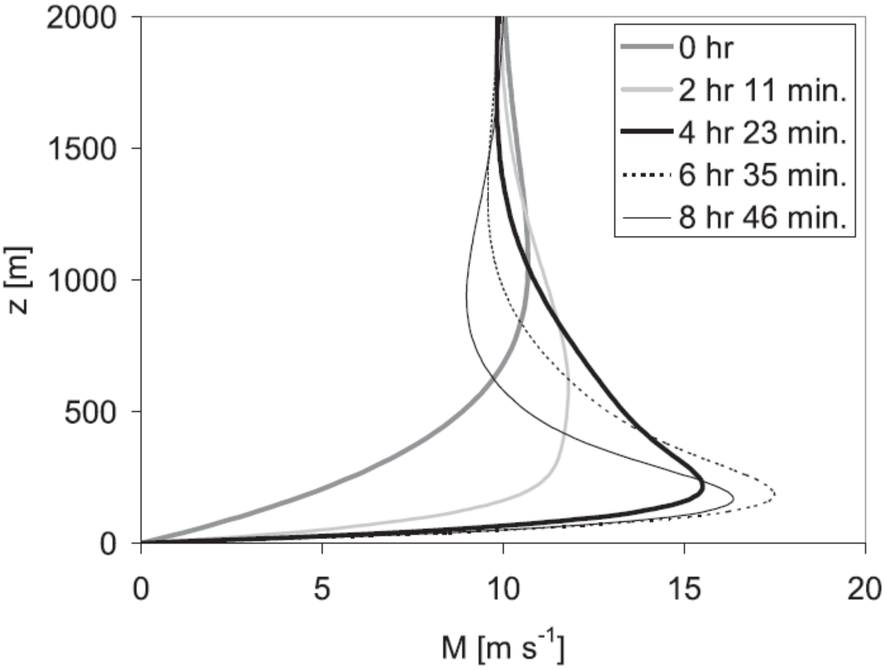

©American Meteorological Society. Used with permission.

Figure 1.12: *NLLJ formation by inertial oscillations. Shown are the vertical profiles of wind speed predicted by equations 1.10a and 1.10b with an Ekman wind profile for $\vec{u}_0$. Reprint of Figure 4 from Van de Wiel* et al. *(2010) with permission of American Meteorological Society (pers. comm. Jinny Nathans, 2014).*

olis and frictional force (Van de Wiel *et al.*, 2010). An equilibrium wind vector equal to the geostrophic wind results in the solution by Blackadar (1957). The equilibrium wind vector is not trivial to predict, but for simplicity an Ekman wind profile can be assumed for $\vec{u}_0$ which describes increasing and clockwise turning wind speeds in the lower part of the ABL (Van de Wiel *et al.*, 2010). With the Ekman profile typical NLLJ profiles are predicted by their theory (Van de Wiel *et al.*, 2010). Figure 1.12 shows the temporal development of the vertical profile with NLLJ formation from equations 1.10a and 1.10b.

Other NLLJ generating conditions include compensating air flows for low-level baroclinicity in regions of differential heating and cooling. Evidence from the Arabian Peninsula shows that baroclinicity can be a more important forming mechanism for LLJs than the inertial oscillation (Giannakopoulou & Toumi, 2012). In contrast to the concept of an inertial oscillation, LLJ formation due to baroclinic condition can occur during day and night. However, a nocturnal enhancement of the LLJ can nevertheless be expected due to the reduction of the eddy viscosity in the nocturnal ABL. For instance, Stensrud (1996) documents that the enhancement of LLJs at night can occur over regions with land-sea contrasts. Grams *et al.* (2010) describe the baroclinicly driven inflow of air from the Atlantic over parts of

West Africa and show a significant increase of the wind speed in the stably stratified air behind the sea-breeze front at night.

In addition to coastlines, baroclinic conditions may develop over complex terrain. After sunset the surface and subsequently the air above higher lying terrain cools more than in a valley. In response to the horizontal pressure gradient a downhill flow develops with a wind speed maximum close to the surface. These circulations over sloping terrain can generate LLJ profiles, a process first documented by Bleeker & Andre (1951). Schepanski *et al.* (2009) suggest that a relatively large number of NLLJs occur over mountainous regions in North Africa, pointing to baroclinicity over complex terrain as a driving mechanism.

Recently, the application of the NLLJ detection algorithm developed during this PhD thesis in a simulation with explicit convection revealed that aged cold pools are also sufficient for generating NLLJs (Heinold *et al.*, 2013). Figure 1.13 schematically depicts the formation process. The horizontal pressure gradient across the leading edge of an aged cold pool typically causes a wind speed maximum near the surface. When the aged cold pool migrates over a stably stratified surface layer, this may lead to the formation of a NLLJ.

Previous work further indicates that NLLJs are generated by larger-scale baroclinicity during the West African monsoon in the Sahel in northern hemisphere summer. Parker *et al.* (2005) describe these NLLJs at the southern margins of the Saharan heat low embedded in the monsoon air flow. Observations give evidence for the nocturnal acceleration of these LLJs (Abdou *et al.*, 2010; Bain *et al.*, 2010; Pospichal *et al.*, 2010) with largest core wind speeds in the morning (6−7 UTC at Niamey for 2006, Lothon *et al.*, 2008).

NLLJ structures also emerge as a dynamical response to orographic channeling (Samelson & Barbour, 2007; Schepanski *et al.*, 2009; Todd *et al.*, 2008; Washington & Todd, 2005; Washington *et al.*, 2006). Channeling may also cause LLJ structures throughout the day, but a diurnal cycle of the jet wind speed is nevertheless expected based on observational evidence over the Bodélé Depression, Chad (Todd *et al.*, 2008; Washington *et al.*, 2006). The results show a distinct diurnal cycle of the near-surface wind speed under both weak and strong large-scale forcing (Todd *et al.*, 2008). This indicates a diurnal variation in the eddy viscosity, which implies a reduction of frictional effects as conditions for a nocturnal acceleration of the LLJ. The diurnal amplitude of the near-surface wind speed is, herein, smaller under a large horizontal pressure gradient compared to a weaker background forcing. This can be linked to more frequent or more efficient shear-induced turbulence beneath the NLLJ. It is this interruption of the NLLJ development that keeps the NLLJs relatively short-lived under strong background flows. Both the weakening or intermittent

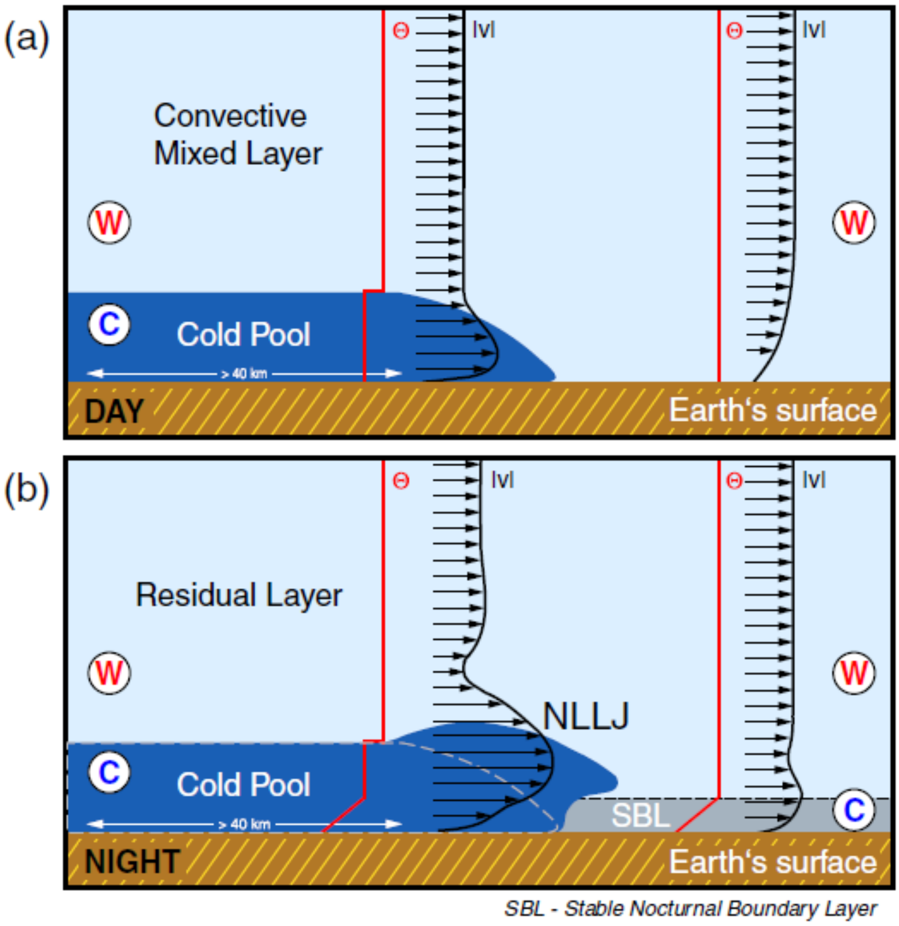

©2013. American Geophysical Union. All Rights Reserved.

Figure 1.13: *NLLJ formation by aged cold pools. Schematic depiction for the vertical cross section of (a) a haboob in the daytime boundary layer and (b) NLLJ formation due to the horizontal pressure gradient associated with an aged cold pool. Black (red) lines show a typical vertical profile of the horizontal wind speed (potential temperature). C (W) refer to relatively cold (warm) air. Reprint of Figure 10 from Heinold* et al. *(2013) with permission of John Wiley & Sons.*

erosion of the NLLJ by downward mixing of the momentum and the short time periods between mixing events for recovering from the momentum loss means that the nocturnal enhancement of a NLLJ under strong large-scale forcing is overall smaller. Less net momentum gain of the NLLJ implies that a potential increase in the near-surface wind speed from a sudden downward mixing event in the mid-morning is relatively small. This process keeps the amplitude of the diurnal cycle in both the NLLJ and the near-surface level relatively small when the background flow is strong.

Impact on Dust Aerosol

The effect of NLLJs on mineral dust aerosol is twofold. On the one hand, NLLJs efficiently transport uplifted dust (Kalu, 1979). On the other hand, the downward mixing of NLLJ momentum by turbulence increases the near-surface wind speed and potentially leads to mineral dust emission in source areas (Heinold *et al.*, 2011; Schepanski *et al.*, 2009; Todd *et al.*, 2008). This downward mixing of momentum from the NLLJ is schematically depicted in Figure 1.14. The associated peak winds and dust emission during the mid-morning can be larger than mid-day values in wide areas across North Africa (Crouvi *et al.*, 2012; Schepanski *et al.*, 2009). Figure 1.15 shows examples from SEVIRI observations of increased dust aerosol during the mid-morning over the Bodélé Depression. It is interesting that relatively higher near-surface wind speed for 4−7 LT than at 9−15 LT has been documented in an early study over the Sudan, for which theodolite measurements were made twice a day in 1935 and 1936 at Khartoum (Farquharson, 1939). High wind speeds during the mid-morning are further observed at Niamey, Niger, and Nangatchori, Benin (Abdou *et al.*, 2010; Lothon *et al.*, 2008).

Turbulence mixes the NLLJ momentum towards the surface (graphically depicted as eddies in Figure 1.14). Lothon *et al.* (2008) show observational evidence for this downward mixing from West Africa. A turbulent flow is caused by vertical wind shear and by surface heating leading to a reduced static stability (Lenschow & Stankow, 1979; Van de Wiel *et al.*, 2003, and references therein). A useful concept for describing the onset of turbulence in an atmospheric flow, and thereby the timing of downward mixing of momentum from a NLLJ, is the Richardson number. The gradient Richardson number is defined as (Stull, 1988):

$$Ri = \frac{\frac{g}{\overline{\theta_v}} \frac{\partial \overline{\theta_v}}{\partial z}}{\left(\frac{\partial \overline{u}}{\partial z}\right)^2 + \left(\frac{\partial \overline{v}}{\partial z}\right)^2}. \tag{1.11}$$

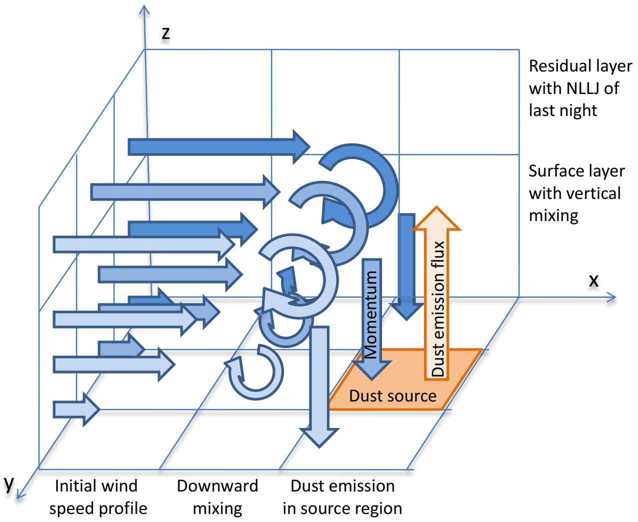

Figure 1.14: *Schematic depiction of the NLLJ mechanism for dust emission. Shown is the downward mixing of NLLJ momentum during the morning hours as proposed by the literature. Turbulent mixing transports momentum towards the surface, which leads to dust emission in source areas, when the specific threshold velocity is exceeded. For details see Section 1.3.4. Figure from Fiedler* et al. *(2013a) with permission of John Wiley & Sons, Inc.*

Ri is a function of the gravitational acceleration g and the vertical gradients in the mean virtual potential temperature $\overline{\theta_v}$, in the mean zonal and mean meridional wind components $\overline{u}$ and $\overline{v}$, respectively. This dimensionless number is defined as the ratio of the static stability and the vertical wind shear. Turbulence occurs when the Richardson number is below a critical threshold, e.g. in a situation of a large vertical wind shear in weakly stable conditions. Banta *et al.* (2003) show that the critical bulk Richardson number beneath a NLLJ over flat terrain describes the onset of turbulent kinetic energy production for values smaller than 0.4. Continuous turbulence is observed for moderately stable situation characterized by Richardson numbers smaller than 0.25$-$0.3. Intermittent turbulence occurs for more stable situations with Richardson numbers larger than 0.3 (Banta *et al.*, 2003).

The downward mixing of NLLJ momentum has been suggested as an important mechanism for generating near-surface peak winds, and dust emission in North Africa during the mid-morning (e.g. Abdou *et al.*, 2010; Knippertz, 2008; Marsham *et al.*, 2011; Schepanski *et al.*, 2009; Washington & Todd, 2005). A quantification in terms of dust source activation (DSA) frequency suggests that 65 % of the dust emission events in the entire of North Africa are linked to the morning breakdown of NLLJs, a result which is based on the time of DSA from satellite observations

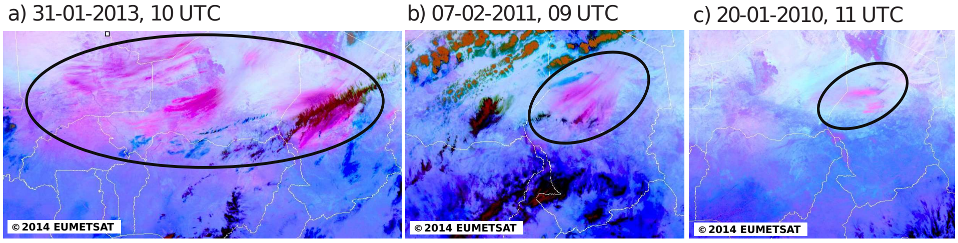

Figure 1.15: *Observation of dust aerosol likely associated with the breakdown of NLLJs. Shown are false-color images derived from MSG SEVIRI indicating mineral dust aerosol (pink, highlighted by ellipse) and clouds (red).*

for March 2006 to February 2008 (Schepanski *et al.*, 2009). NLLJs occur on 50 % of all nights during winter along an almost cross continental band between 10° N and 20° N based on wind speed differences between wind speeds at two near-surface pressure levels (Schepanski *et al.*, 2009). At the same time dust sources are most frequently activated between 6 and 9 UTC with a clear spatial maximum over the Bodélé Depression and in the eastern Sahara in winter (Schepanski *et al.*, 2009). The time of day and analysis of both ERA-40 re-analysis and a regional climate model simulation indicate that NLLJs generate the necessary near-surface winds for these dust emission events. In summer, NLLJs occur more frequently between 15° N to 30° N. At the same time, the dust emission frequency increases in West Africa and near topographic elevations, where both frequent NLLJs and the availability of fine sediments generated by fluvial erosion may build favourable conditions (Schepanski *et al.*, 2009, 2013). Heinold *et al.* (2013) investigate the emission amounts associated with NLLJs with the aid of the NLLJ identification tool developed in this thesis. Figure 1.9 suggests that most of the simulated morning emission in August 2006 is associated with NLLJs. However, a $20-30$ year climatology of the NLLJ breakdown, and an estimate of the associated amount of emitted dust for different seasons has not been quantified yet.

1.3.5 Boundary layer parameterisation

The vertical momentum transport in the ABL is a crucial factor for simulating near-surface wind speeds for dust emission. The Reynolds stress term, describing the turbulent momentum transport, needs to be parameterised. Linearisation and temporal averaging the Boussinesque equations of atmospheric motion results in a description by mean variables and unknown perturbations. While the former are predicted by the model, the latter need to be specified for solving the equation. Deriving further equations for the Reynolds stress would lead to a cascade of unknowns. To overcome this closure problem, the perturbations are parameterised

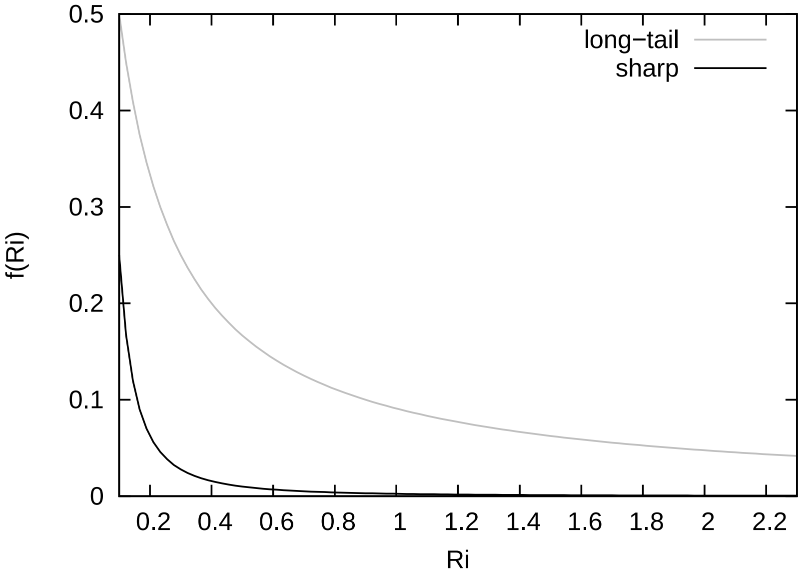

Figure 1.16: *Parameterisation for momentum mixing. Shown is the dependency of the long-tail and sharp function on the Richardson number above values of 0.1.*

by values of known mean variables. Different parameterisation schemes are suggested: (1) local closure schemes which relate the Reynolds stress to a variable at a nearby grid point and (2) non-local closure schemes relating the Reynolds stress to a variable at any number of grid points (Stensrud, 2007).

Closure schemes

The most common first-order closure scheme used for stably stratified boundary layers in state-of-the-art atmospheric models is based on the K-diffusion scheme (Brown *et al.*, 2008; Sandu *et al.*, 2013). The vertical turbulent flux $\overline{w'\psi'}$ of a given variable ψ with the vertical wind perturbation w' is related to the vertical gradient of its mean value multiplied by a turbulent exchange coefficient K (e.g. Stull, 1988):

$$\overline{w'\psi'} = -K\frac{\partial\overline{\psi}}{\partial z}. \tag{1.12}$$

The turbulent exchange coefficient K (also termed diffusivity) is parameterised as:

$$K = l^2\frac{\partial\overline{\psi}}{\partial z}f(Ri) \tag{1.13}$$

where l is the mixing length and the function $f(Ri)$ is the long-tail function (Figure 1.16):

$$f(Ri) = \frac{1}{1+10Ri^2} \tag{1.14}$$

with the Richardson number Ri (Brown *et al.*, 2008).

This long-tail function artificially increases the vertical mixing in stable boundary layers so that higher nocturnal near-surface winds are simulated than observed (Brown *et al.*, 2008, 2006; Sandu *et al.*, 2013). Such an approach is applied to balance other model errors so that an overall good forecast skill is maintained, e.g. regarding cyclones and near-surface temperatures, and justified by the currently missing representation of surface heterogeneities and sub-grid scale variability (e.g. Brown *et al.*, 2008; Sandu *et al.*, 2013). An upgrade over sea in the operational forecast configuration and over both land and sea in the climate configuration of the Unified Model HadGEM2-ES (e.g. Martin *et al.*, 2011) uses instead of the long-tail function the sharp function (Figure 1.16) given by:

$$f(Ri) = \begin{cases} (1-5Ri)^2 & 0 \leq Ri < 0.1 \\ \left(\frac{1}{20Ri}\right)^2 & Ri \geq 0.1 \end{cases} \tag{1.15}$$

which reduces the artificially enhanced mixing and thereby complies better with Monin-Obukhov similarity theory (Brown *et al.*, 2008).

A major shortcoming of such local closure schemes is the consideration of eddies produced by local gradients only. Daytime turbulent mixing, however, is associated with eddies which may stretch across the entire boundary layer depth. Under these conditions K-theory fails which can be explained with the aid of the vertical turbulent heat transport $\overline{w'\theta'}$. The daytime surface layer is characterized by decreasing potential temperatures with height close to the surface ($\partial\overline{\theta}/\partial z < 0$, Figure 1.10a). This means that the turbulent heat transport is directed upwards ($\overline{w'\theta'} > 0$, Equation 1.12). In the convective mixing layer, however, K-theory predicts no turbulent fluxes during the day ($\partial\overline{\theta}/\partial z \cong 0$, thus $\overline{w'\theta'} \cong 0$), which is inconsistent with observations. In the entrainment zone, the mean vertical heat transport is directed downwards ($\partial\overline{\theta}/\partial z > 0$, thus $\overline{w'\theta'} < 0$). Entrainment, however, incorporates both up- and downward motion. K-theory is therefore suggested to be used for boundary layers with small eddies only, conditions which can be found in the free troposphere and close to the surface (up to 200m; Blackadar, 1979). Daytime boundary layers are often parameterised by non-local closure schemes instead (e.g. Zhang & Zheng, 2004). Following (Stensrud, 2007), they may be classified into mixed layer schemes (Betts, 1973; Carson, 1973; Lilly, 1968), penetrative convection schemes (Blackadar, 1978; Estoque, 1968; Zhang & Anthes, 1982), nonlocal diffusion schemes (Hong & Pan, 1996; Troen & Mahrt, 1986) and others (Stull, 1993). Due to the large variety of these parameterisation schemes and the focus on nocturnal boundary layers, no review of them is presented here.

Effect of ABL parameterisation on wind speed

ABL parameterisation schemes perform differently. In a model study for the summertime USA under a weak synoptic-scale pressure gradient, the daily cycle of 10m-wind speed is not well captured, even though the 2m-temperature is well simulated (Zhang & Zheng, 2004). They found a general underestimation of the 10m-wind speed in all tested ABL schemes during daytime and an overestimation by some schemes at nighttime, although the mean vertical wind profile is reasonably well captured (Zhang & Zheng, 2004). Particularly the parameterisation of nocturnal boundary layers is difficult due to a number of reasons: (1) Nocturnal turbulence may be present in the form of intermittent or continuous mixing; (2) The nocturnal ABL is tightly coupled to other parameterised processes including radiative transfer, vegetation and soil properties; (3) The occurrence of drainage flows, gravity waves, fog and low-level stratus influence the nocturnal ABL, which are difficult to simulate themselves; (4) Heterogeneities of land use smaller than the grid resolution are difficult to represent (e.g. Holtslag *et al.*, 2013; Sandu *et al.*, 2013; Steeneveld *et al.*, 2006, 2008; Svensson *et al.*, 2011). In addition, the ABL can be used to balance other shortcomings of a model, e.g. the vertical exchange under stable stratification is artificially increased in order to maintain an overall good model performance at the synoptic scale (Sandu *et al.*, 2013). As a side effect, the NLLJ may be weaker and higher than observed (Sandu *et al.*, 2013). Higher vertical resolution is suggested to improve the diurnal cycle, in particular surface inversions and the NLLJ (Zhang & Zheng, 2004), but the results from other studies show little improvement for the NLLJ from the resolution alone (Schepanski *et al.*, 2014; Svensson *et al.*, 2011; Todd *et al.*, 2008). The daily cycle of the near-surface wind speed in the Bodélé Depression in a regional model is underestimated with all ABL schemes investigated, even when the model setup is tuned for the regional characteristics and more vertical levels are added close to the surface (Todd *et al.*, 2008). Using another regional model over West Africa and the NLLJ identification technique developed in this PhD research shows that both increased resolution and changes of the ABL parameterisation have overall small effects on the diurnal cycle of wind speed and the occurrence of NLLJs (Schepanski *et al.*, 2014).

In common practice, the underrepresented high end of the wind distribution can be compensated for by tuning the dust emission towards observations or re-analysis. For instance, the emission is changed such that the amount from dynamical downscaling of re-analyzed winds is matched. This can be done by lowering the threshold velocities for dust emission in grid boxes where the re-analysis predicts larger small-scale fluctuations than a global model (Cakmur *et al.*, 2004). However, re-analysis data are produced by atmospheric global models themselves. They assimilate observations in order to calculate a three-dimensional estimate of the past state of the atmosphere with the aid of a forecast system. Uncertainties from the model system and observations influence the accuracy of this estimate. In fact, Koren & Kaufmann (2004) show an underestimation of wind speeds along dust fronts in the Bodélé Depression in NCEP re-analysis data by a factor of two. Similarly, near-surface winds from ECMWF re-analysis are underestimated compared to local measurements from March 2005 (Bouet *et al.*, 2007). Also, Schmechtig *et al.* (2011) found a systematic underestimation of the high end of the wind speed distribution from the ECMWF operational analysis product for the Bodélé Depression and adapted the simulated winds to station observations by linear regression such that the intensity of dust events is tuned, while the frequency is kept constant. The effect of the changed wind speeds on the simulated dust emission from the Bodélé Depression is of the order of a factor of ten (Schmechtig *et al.*, 2011), which demonstrates the importance of accurate winds for dust emission.

1.4 Aims of this thesis

The atmospheric life cycle of dust aerosol and its impacts in the Earth system depend on the time, location and amount of dust emission. Estimates from atmospheric models for dust emission, most of which originates in North Africa, show a large variety. Both the physical parameterisation of the dust emission process and the soil (Section 1.2.3) as well as winds for emitting dust are sources of uncertainty (Section 1.3.5). The latter is, herein, important due to non-linear parameterisations of the emission flux as function of the wind speed (Section 1.2.3). A small error in wind speed therefore has a large impact on the calculated dust emission flux, but a systematic evaluation of meteorological mechanisms generating those winds does not exist. Different meteorological processes are known for generating dust-emitting winds. From a climatological perspective, their relative importance is, however, not well quantified (Section 1.3). Improving the simulation of important meteorological processes for dust-emitting winds over North Africa can contribute to decreasing the model spread in dust emission estimates and thereby holds the potential for reducing uncertainties in Earth system models. This would contribute to further increase our scientific confidence in future climate change projections.

This PhD work provides the first-ever systematic evaluation of meteorological processes for North African dust emission based on long-term data and innovative automatic identification. Firstly, the relative importance of NLLJs for the North

African dust emission amount is assessed, which has not been well quantified before (Section 1.3.4). Secondly, uncertainties are analysed regarding the NLLJ and the dust emission based on re-analysis data as previous studies indicate that these have limitations in representing 10m-winds (Sections 1.3.5). Thirdly, the importance of atmospheric depressions and mobile cyclones for North African dust emission which has been proposed in the literature (Section 1.3.1) is investigated for the first time. Moreover, the new climatology of NLLJs for dust emission is compared to the Earth system model of the UK Met Office. This helps identifying systematic model behaviour affecting North African dust emission and guide future model development.

The individual chapters address the following questions:

1. **Importance of NLLJs for emitting mineral dust aerosol**
    (a) When and where do NLLJs most frequently occur over North Africa?
    (b) Do they show spatio-temporal varying characteristics?
    (c) How do NLLJs affect the near-surface wind speed distribution?
    (d) How much of the total dust emission amount is associated with them?
    (e) What is the relative contribution from night-time and mid-morning emissions?
2. **Uncertainties of the baseline climatology**
    (a) What is the performance of ERA-Interim forecasts for simulating NLLJs and their characteristics?
    (b) How does the dust emission calculation compare against observational data sets?
    (c) What is the uncertainty of synoptic-scale dynamics from re-analysis products?
    (d) How large are differences of the total dust emission amount with winds from a set of re-analysis products?
    (e) What are the implications for model evaluation of dust emission?
3. **Mineral dust aerosol emission associated with atmospheric depressions and cyclones**
    (a) How often and where do atmospheric depressions and mobile cyclones most frequently form?

   (b) What are the lifetimes and migration distances of mobile cyclones?
   (c) How much dust emission is associated with cyclones and atmospheric depressions?
   (d) What is the role of embedded NLLJs in atmospheric depressions and cyclones?
   (e) How much dust emission is suppressed due to the presence of soil moisture?

4. **Evaluation of dust emission in HadGEM2-ES and HadGEM3-A**
   (a) Is the climatology of dust emission in a state-of-the-art Earth system model different to re-analysis?
   (b) How large is the effect of different wind speeds in the same dust emission model on the emitted amount?
   (c) What is the role of the NLLJ for dust emission in the Earth system model?
   (d) How does the synoptic-scale dynamics compare against re-analysis?
   (e) What are the implications for modelling mineral dust emission?

1.5 Research method and data

Achieving the aims of this thesis requires a systematic analysis of meteorological processes in context of dust emission. The investigation of dust-emitting processes from a climatological perspective, require long-term data with sub-daily resolution. Since such observations are sparse over North Africa, the thesis is based on several years of model data with at least 6-hourly resolution. An automated detection algorithm for NLLJs is developed (Section 2.2.2) and depressions tracks (Section 4.2.1) are used for investigating the importance of NLLJs, atmospheric depressions and mobile cyclones for North African dust emission. An overview on the data is given in the following section. Details on the different methods and the data are given in each of the thesis chapters.

1.5.1 Data

ERA-Interim forecasts and re-analysis data from ECMWF (Dee *et al.*, 2011, Details in Section 2.2.1) are used for the majority of the work. For validation, the re-analysis data sets from the National Center for Environmental Prediction (NCEP, Kalnay & Coauthors, 1996) and the “Modern-era Retrospective Analysis for Research and Applications” (MERRA, Rienecker *et al.*, 2011) from NASA are used. Based on

Model	Horizontal resolution	Levels	Time sampling	Time period
ERA-Interim re-analysis	1^o	60	6-hourly	1979−2010
ERA-Interim forecasts	1^o	60	3-hourly	1979−2010
MERRA re-analysis	$0.6x0.5^o$	72	hourly	1979−2010
NCEP re-analysis	2.5^o	28	00 UTC	June 2011
HadGEM2-ES	$1.875x1.25^o$	38	hourly	1980−2009
HadGEM3-A	$1.875x1.25^o$	85	hourly	2003−2007
HadGEM3-A nudged	$1.875x1.25^o$	85	hourly	2003−2007

Table 1.1: *Overview on model data*

results from ERA-Interim, the latest Earth system model HadGEM2-ES and the atmosphere only model version HadGEM3-A from the UK Met Office are evaluated (Bellouin *et al.*, 2011; Collins *et al.*, 2011; Martin *et al.*, 2011, Details Section 5.2.1). The characteristics of the model data used in this thesis are summarized in Table 1.1.

Since ERA-Interim does not provide dust emission, these are calculated with the dust emission model by Tegen *et al.* (2002). The uncertainty in comparing dust emission (Section 1.2.4) derived from ERA-Interim and calculated by the Earth system model HadGEM2-ES in Chapter 5 is reduced by using the winds of HadGEM2-ES to drive the dust emission model by Tegen *et al.* (2002). Details about the calculations are provided in the Chapters where they are relevant (Section 2.2.3, 4.2.2 and 5.2.2).

Wind observation is used for assessing the model performance of ERA-Interim in Chapter 3, namely radiosondes, pilot baloon, SODAR and LIDAR measurements (Section 3.2). Satellite observation of the dust source activation frequency by Schepanski *et al.* (2012) and observations during BoDEx (Washington *et al.*, 2006) is used for evaluating the dust emission calculation (Details in Section 3.2).

CHAPTER 2

Importance of Nocturnal Low-Level Jets for dust emission

2.1 Motivation

* Further improvements of simulating the mineral dust budget for weather forecast and climate applications require a systematic analysis of individual meteorological processes relevant for dust emission. Different meteorological processes have been identified as potential generators for dust-emitting peak winds near the surface. The understanding of the relative importance of these mechanisms is, however, incomplete (Chapter 1). One of the relevant meteorological processes is the downward mixing of momentum from the NLLJ (Chapter 1.3.4). While a frequent occurrence of NLLJs and their contribution to mineral dust emission in North Africa has been suggested qualitatively (Knippertz, 2008; Schepanski *et al.*, 2009; Washington & Todd, 2005), a climatological estimate of the phenomenon is missing.

This chapter presents a climatological assessment of NLLJs and their contribution to the dust emission amount from North Africa (Fiedler *et al.*, 2013a). A new automatic algorithm for detecting NLLJs in atmospheric models has been developed and applied to ECMWF ERA-Interim re-analysis and forecasts for 1979−2010 for this purpose, which is described along with the data in Section 2.2. The climatology of the NLLJ frequency, of the jet characteristics, of the dust emission, and the relative importance of NLLJs for dust emission are presented in Sections 2.3.1−2.3.3. A discussion of the findings and their implication for mineral dust modeling are given in Section 2.4. Section 2.5 draws conclusions from this chapter.

---

* Text passages and figures in the present chapter 2 are from my publication "Climatology of nocturnal low-level jets over North Africa and implications for modeling mineral dust emission", 118, 12, 2013, pp. 6100−6121 in Journal of Geophysical Research - Atmosphere, Copyright 2014 John Wiley & Sons, Inc., This material is reproduced with permission of John Wiley & Sons, Inc (pers. comm. Paulette Goldweber, Wiley, 2014).

2.2 Method

2.2.1 ECMWF ERA-Interim

The basis for the statistical investigation of NLLJs in North Africa is the ERA-Interim data from the European Centre for Medium-Range Weather Forecasts (ECMWF) for 1979−2010 (Dee *et al.*, 2011). The choice of ERA-Interim for the present work instead of radiosonde observations was based on (1) the sparse observation network, (2) the lack of long-term records over most of North Africa, and (3) too few radiosonde ascents per night. These shortcomings do not enable to capture the nocturnal development of NLLJs by observations in most areas of North Africa, especially in remote regions of the Sahara desert that are particularly interesting from the perspective of dust emission.

The six-hourly re-analysis provides instantaneous fields on a $1^\circ \times 1^\circ$ horizontal grid and 60 vertical levels, which are terrain following close to the surface and gradually adjust to pressure coordinates in the free troposphere. The re-analysis of the horizontal wind components, the air temperature, and the specific humidity are used for the NLLJ climatology. Temporally higher resolved data is beneficial for understanding the development and the breakdown of NLLJs as well as the associated mineral dust emission flux. In order to increase the temporal resolution of the diurnal cycle for process studies, three-hourly ERA-Interim forecasts are used. The present work uses the forecasts for +3 to +12 hours initialized at 00 UTC and 12 UTC. All variables from ERA-Interim forecasts are instantaneous values, except the 10m-wind gusts that are representative for the last three hours.

A crucial factor for simulating the NLLJ is the treatment of the ABL. The turbulent transport in stable ABLs in ERA-Interim is parametrized by a K-diffusion scheme (Beljaars & Viterbo, 1999; Louis *et al.*, 1982). Artificially higher values for the diffusion coefficient K from a long-tail function (Chapter 1.3.4) are used for stable ABLs in order to achieve a better overall performance of the numerical weather prediction system (Bechtold *et al.*, 2008; Sandu *et al.*, 2012). Undesired side effects are too smooth vertical profiles of meteorological variables in the nocturnal ABL, and comparably weak and higher residing NLLJs (Sandu *et al.*, 2012). Further improvements in the representation of stable ABLs in the ECMWF model is subject of ongoing research.

The increased turbulent mixing within inversion layers (Bechtold *et al.*, 2008) affects the time and amount of momentum transfer to the surface. The associated momentum loss at the NLLJ level decelerates or even erodes the jet in the course of the night. The NLLJ strength in ERA-Interim during the morning is, therefore, likely to be underestimated. This can have an impact on the simulated diurnal cycle of the near surface wind speeds, and the mineral dust emission. Nevertheless, reanalysis give the best estimate of the past state of the atmosphere. Observation records with comparable resolution and record length are not available for this part of the world.

2.2.2 Automated NLLJ detection

The different definitions of LLJ structures in previous studies is tightly connected to the applied identification methods. The variety of methods range from plain wind speed maximum analysis to more complex, physically motivated, and automated approaches. Each of the different techniques have their own advantages and disadvantages for the specific research interests. A short summary is given in the following.

Nocturnal jets are identified in radiosondes over north-east Australia by finding a wind speed maximum below 1,500 m above ground level (a.g.l.) that shows an increase of the wind speed over night and decays around sunrise (May, 1995). This approach is tailored towards inertial oscillations. Other studies more generally address NLLJs with more generous identification criteria. For instance, Banta *et al.* (2003) investigate NLLJs in observations averaged over fifteen minutes for ten nights over Kansas by choosing the lowest wind speed maximum in the vertical profile as the NLLJ. This approach does not consider a critical vertical wind shear above the NLLJ, which is useful for confining the NLLJ to a vertically narrow band as suggested by Stensrud (1996). While the confinement beneath the jet core is naturally given due to the effect of surface friction, a restriction of the vertical extent of the NLLJ above the nose is a useful addition for the identification.

A criterion for the decrease of wind speed above the NLLJ core is applied by a number of previous studies (e.g. Baas *et al.*, 2009; Bonner, 1968; Whiteman *et al.*, 1997). The study by Bonner (1968) determines NLLJs in two years of radiosondes observations across the United States by using four criterion sets of an absolute core wind speed of at least 12 ms^{-1} and a certain wind speed decrease above the LLJ nose. This classification scheme by Bonner (1968) has been used later by Whiteman *et al.* (1997) to study LLJs over the USA independent of the time of day. Baas *et al.* (2009) identified NLLJs when the maximum resides below 500 m, is at least 2 ms^{-1}, and 25 % faster than the following minimum. While this height range works well for typical mid-latitude ABLs over the Netherlands, observations from Africa show that NLLJs can reside in altitudes exceeding 500 m a.g.l. (Pospichal *et al.*, 2010; Rife *et al.*, 2010; Todd *et al.*, 2008).

Rife *et al.* (2010) use 21-years of re-analysis data to compile a global climatology of the “NLLJ index” defined as the wind speed at a fixed height of 500 m a.g.l. at mid-night that is larger than the wind speed twelve hours earlier and than the wind speed at 4000 m. Their spatial distribution of the “NLLJ index” indicates where diurnally varying LLJs are located, but does not provide the absolute wind speed and height of the jet core. Further, this approach does not take into account that the synoptic conditions may change in a twelve hour period. Re-analysis data have also been used to compile a mean NLLJ climatology over the Bodélé Depression in Chad based on pressure levels by Washington & Todd (2005). Schepanski *et al.* (2009) and Crouvi *et al.* (2012) use wind speed differences between standard pressure levels as indicator for NLLJs for entire North Africa. This approach does not provide the absolute wind speed and height of the NLLJ core and is not applicable over mountains.

The objective of the present work is to identify NLLJs that develop at night and potentially lead to mineral dust emission during the following morning (Section 1.3.4). Based on this research aim and following METEOTERM[*], NLLJs over North Africa are defined in this study as wind speed maxima in the nocturnal ABL that form above a stably stratified surface layer and have an appreciable vertical wind shear. This NLLJ definition is a more restrictive form of the relatively general term LLJ. The present work includes but is not limited to jets of super-geostrophic speed, as proposed by Blackadar (1957).

NLLJs are detected in the ECMWF ERA-Interim re-analysis and forecasts at all available times by using a newly developed automatic detection algorithm. Two desirable key characteristics of this algorithm are: (1) the terrain independent identification that enables determining the exact wind speed and height of the NLLJ core and (2) the consideration of the reduced frictional effects for the nocturnal acceleration in some distance to the surface. These features have not been combined in a single detection method for NLLJs before. The first characteristic is implemented by choosing data on the original model levels from ERA-Interim. Depending on the surface pressure, the depth of the three lowest model layers is 18−22 m, 27−33 m, and 39−48 m, which is assumed to provide a sufficient vertical resolution of the ABL. Using meteorological fields on model levels has the additional advantage of avoiding interpolation uncertainty. The second characteristic is achieved by requiring the presence of a surface inversion.

The main criteria of the detection algorithm in the present work are summarized in Figure 2.1. A NLLJ is identified as a wind speed maximum between the lowest model level and approximately 1,500 m a.g.l.

---

[*] http://wmo.multicorpora.net/METEOTERM as of March 2013

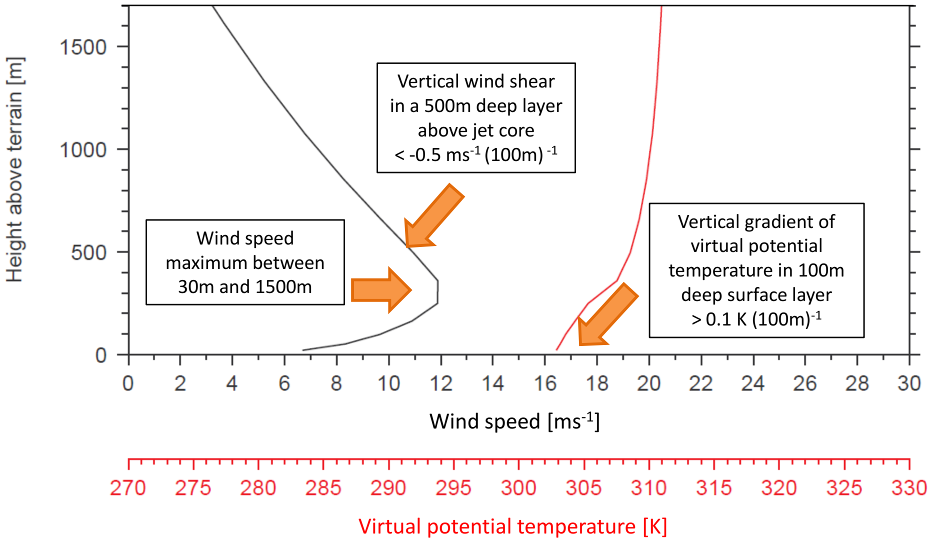

Figure 2.1: *Schematic diagram showing the criteria for the NLLJ detection. Shown is an example of the vertical profiles of wind speed and virtual potential temperature from six-hourly ERA-Interim re-analysis. Figure from Fiedler* et al. *(2013a) with permission of John Wiley & Sons, Inc.*

1. that is situated above a stably stratified surface layer of at least 100 m depth measured by a vertical gradient of the virtual potential temperature exceeding 0.001 Km^{-1},
2. and has a vertical wind shear stronger than - 0.005 s^{-1} in a 500m-deep layer above the jet core.

The first criterion reflects the reduced frictional effects in the nocturnal ABL as a necessary prerequisite for the formation of a NLLJ (Section 1.3.4). The choice of this rather weak stratification threshold enables intermittent and continuous turbulent mixing beneath the NLLJ (Section 1.3.4). Using a criterion for the vertical wind shear above the jet core confines wind maxima to vertically-narrow jets which is suggested by Stensrud (1996). This wind shear criterion implies a wind speed of at least 2.5 ms^{-1} in the jet core. The height range of up to 1,500 m is a generous definition of possible NLLJ heights (see Section 2.3.2) that is in agreement with the identification by Lothon *et al.* (2008). The NLLJ height corresponds to the upper boundary of the model grid box where the maximum wind speed is found and is calculated using the time-dependent surface pressure.

A night is defined as a “NLLJ night” if a NLLJ occurred between 18 and 6 UTC in the re-analysis. In order to analyse the evolution of NLLJs and the contribution to mineral dust emission after sunrise, NLLJs and additionally “NLLJ survivors” are detected in ECMWF forecasts. “NLLJ survivors” are defined as wind speed maxima which fulfil the criterion for the vertical wind shear three hours after the occurrence of a NLLJ or a previous NLLJ survivor.

The choice of the threshold values in the NLLJ detection algorithm is subjectively derived from ERA-Interim re-analysis. Possible uncertainties are assessed by sensitivity tests. The main findings are:

1. An increased threshold for the vertical gradient of the virtual potential temperature from 0.001 $\mathrm{Km^{-1}}$ to 0.01 $\mathrm{Km^{-1}}$ reduces the number of identified NLLJs by about 60 % in the annual and spatial mean. Dropping the criteria of the virtual potential temperature gradient leads to a spatially and annually small mean increase of 7 % of the NLLJ frequency at 0 UTC, but this increase is heterogeneously distributed across the continent. In this test, NLLJs at 0 UTC in regions of baroclinic conditions are pronounced, e.g. along the West African monsoon front and along coasts. The increase of detected LLJs is larger during the day when surface inversions are usually absent. Since reduced frictional effects at night are expected to enable a nocturnal acceleration of a LLJ (Section 1.3.4), but cases with turbulence beneath the NLLJ need to be included to investigate dust emission associated with NLLJs, the weak stability criterion of 0.001 $\mathrm{Km^{-1}}$ is chosen.

2. Reducing the mean vertical wind shear to -0.0025 $\mathrm{s^{-1}}$ in the 500m-deep layer increases the number of NLLJs across the domain by up to 80 %. In contrast requiring -0.005 $\mathrm{s^{-1}}$ in a shallower layer of 300 m decreases the number of jets by up to 50 %. Since the geographical structures of the NLLJ occurrence frequency is robust, the intermediate threshold seems to be a reasonable approach that successfully excludes NLLJs of a large vertical extent.

The result showing an almost unchanged areal extent of the NLLJ hot spots but fairly large frequency changes with different thresholds for the vertical wind shear is similar to findings from LLJ detections in other studies. For instance Bonner (1968) shows that the regions of most frequent LLJ occurrence over the United States remains similar but the actual number of identified jets varies by a factor of six when the threshold values for identifying NLLJs are changed. These tests clearly underline the sensitivity of the method to the choice of threshold values.

2.2.3 Dust emission

Since ERA-Interim does not have a prognostic aerosol scheme, mineral dust emission is calculated offline with the mineral dust emission model developed by Tegen *et al.* (2002). This dust emission calculation has been provided by B. Heinold (University of Leeds and now at TROPOS, Leipzig, 2011). The model is driven by 10m-wind speeds and the moisture content in the uppermost soil layer from ECMWF ERA-Interim forecasts. Soil particles are mobilized in a source, when the near-surface wind speed exceeds the particle-size-dependent threshold velocities (Section sub:dustemi). The dust emission model by Tegen *et al.* (2002) has been validated and is implemented in global and regional models (e.g. Heinold *et al.*, 2011; Zhang *et al.*, 2012).

Potential sources for mineral dust aerosol are prescribed by the map of DSA frequency (Section 1.2.2), where sources are identified from the MSG SEVIRI infrared dust index product (Schepanski *et al.*, 2009, 2012, 2007). A grid box of $1^\circ \times 1^\circ$ is defined as a potential dust source if at least two dust events were observed between March 2006 and February 2008. The surface roughness length of dust sources is set to a constant value of 10^{-3} cm as in Schepanski *et al.* (2007). The activation of dust sources is limited to non-saturated soils, expressed by soil moisture values below the field capacity. Dust sources, i.e. silt and clay soil types, are assumed to have a field capacity of 0.28 $\mathrm{m^3 m^{-3}}$. The sensitivity to this parameter has been tested and was found to be negligible in the Sahara, which is in agreement with previous literature (Laurent *et al.*, 2008). Dust emission is parametrized for four soil particle-size distributions, namely coarse sand ($500-1000\,\mu$m), fine and medium sand ($50-500\,\mu$m), silt ($2-50\,\mu$m), and clay ($0-2\,\mu$m). The relative content of the different populations has been derived from the global soil-texture data from the Food and Agriculture Organization (FAO) on a horizontal grid of 0.5°. The threshold 10m-wind speed is determined for each of the four particle size bins. This threshold 10m-wind speed for dust emission is not parameterised as a function of the NLLJ wind speed.

2.3 Results

2.3.1 NLLJ climatology

NLLJs are a frequent phenomenon in North Africa. In the annual and spatial mean, NLLJs are detected in 29 +/- 4 % (mean +/- standard deviation) of the nights in the ERA-Interim re-analysis for $1979-2010$ over North Africa. Figure 2.2 shows the seasonal cycle by the monthly mean frequency of NLLJ nights and the mean geopotential height at 975 hPa that is a strong control of wind speed at any fixed point with constant roughness. In January, NLLJs occur in 5-25 % of all nights between 20° N and 30° N (Figure 2.2a). South of 20°N, the NLLJ frequency reaches higher values, typically 25 % to 50 %. The most active regions show NLLJ frequencies of up to 80 %, namely the Bodélé Depression, the Vallée de Tarka, the Nubian desert, the Darfur region, and the Hoggar-Tibesti channel. These hot spots in terms of occurrence frequency, summarized as blue areas in Figure 2.3, remain active in February (Figure 2.2b), but decrease in their dominance in March (Figure 2.2c) before they disappear between April and September (Figures 2.2d−i). In the latter period, the NLLJ climatology shows hot spots in the western Sahel, and in areas along the Atlantic and the Mediterranean coast lines. Maxima during this time of the year, are summarized as orange areas in Figure 2.3. NLLJs in the western Sahel and Sudan occur in 40−65 % of the nights between April and September (Figures 2.2d−i). The overall maximum for April−September is found in the Atlantic ventilation hot spot, which is named after the advection of relatively cool maritime air to hot areas further inland. Here, the amount of NLLJ nights is comparable to the frequency in the Bodélé Depression for November−March (Figures 2.2k−l, and a−c). In contrast, NLLJs in the Mediterranean ventilation occur only during up to 60 % of the nights.

Specific environmental conditions, such as (1) orographic channelling and (2) low-level baroclinicity, may favour the development of NLLJs (Section 1.3.4). Previous studies suggest orographic channeling as driving mechanism for NLLJs over the Bodélé Depression (e.g. Todd *et al.*, 2008; Washington & Todd, 2005). A climatology of the wind direction and speed in the core of NLLJs is depicted as a wind rose for the Bodélé Depression in Figure 2.4a. Here, the majority (68 %) of the NLLJs are north-easterly between November and March. The narrow distribution around the prevailing wind direction indicates channeling of the north-easterly Harmattan winds between the Tibesti and Ennedi Mountains. This can be further supported by the horizontal gradient of the 975 hPa isohypses (Figures 2.2k−l, and a−c), which show a ridge upstream of the channel and a trough in the lee of the Mountains. The air is accelerated down-gradient and frequently forms NLLJs above the stably stratified surface layer at night. Half of the NLLJs in the Bodélé Depression hot spot are characterized by wind speeds of 12−20 $\mathrm{ms^{-1}}$. These core wind speeds agree well with the range of measured and simulated NLLJs in the area from Todd *et al.* (2008). In addition to the Bodélé Depression hot spot, orographic channeling of the Harmattan winds might also play a role between the Hoggar and the Tibesti Mountains.

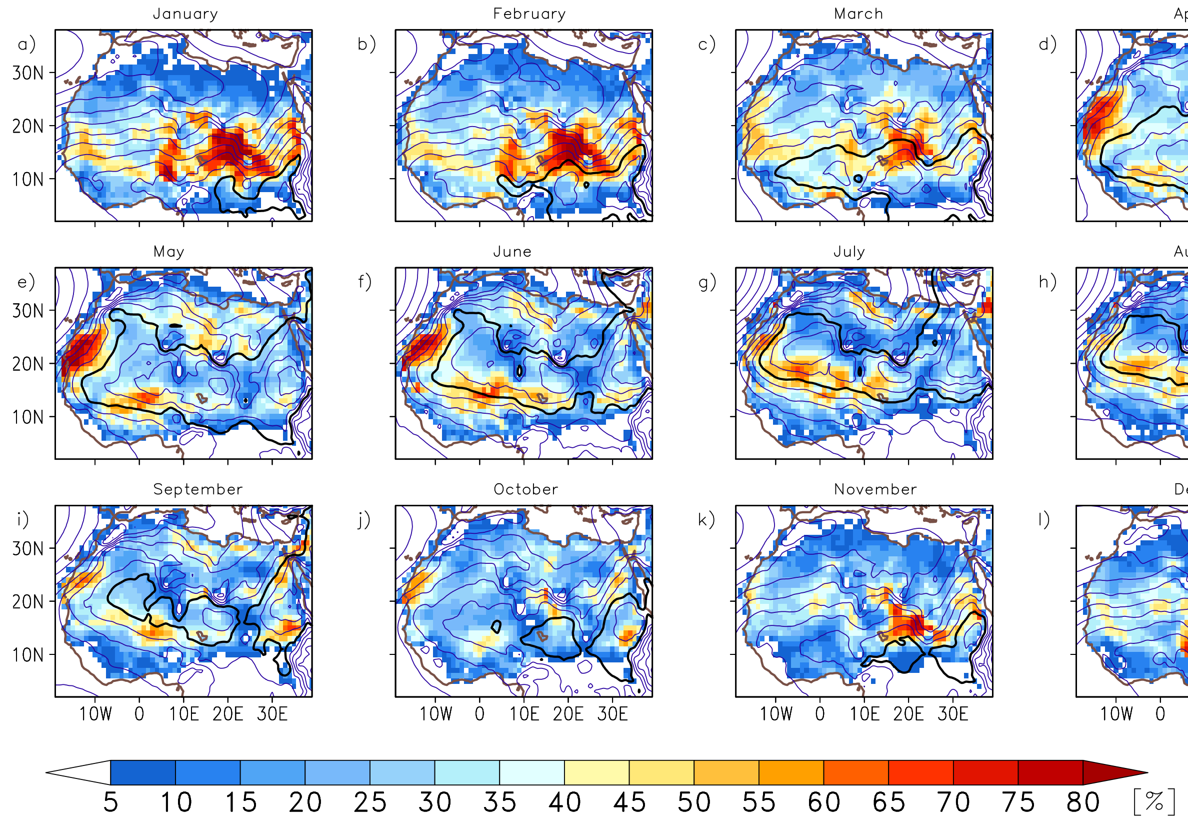

Figure 2.2: *Annual cycle of the frequency of NLLJ nights. Monthly mean occurrence of nights with a NLLJ (colours) and mean 975 hPa geopotential height at 0 UTC (contours) for (a) January, (b) February, (c) March, (d) April, (e) May, (f) June, (g) July, (h) August, (i) September, (j) October, (k) November, and (l) December, based on six-hourly ECMWF ERA-Interim re-analysis 1979–2010 and the new NLLJ detection algorithm. Geopotential heights are contoured in steps of 1 gpdm (thick contours correspond to 30 gpdm). Note that 975 hPa level is below model orography over parts of North Africa. Figure from Fiedler* et al. *(2013a) with permission of John Wiley & Sons, Inc.*

Another NLLJ forming in response to the effects of orography is the jet along the northern slopes of the Ethiopian Highlands described by Rife *et al.* (2010) and part of the Nubian desert hot spot in Figure 2.3. The spatial distribution of the NLLJ index by Rife *et al.* (2010) is not directly comparable to the NLLJ frequency presented here, but the results by Rife *et al.* (2010) enable calculating a frequency of non-zero NLLJ indices of 94 % in the Ethiopian NLLJ at 12.8° N and 34° E for January. The largest indices for the Ethiopian NLLJ by Rife *et al.* (2010) occur in the area 10−15° N and 30−38° E. Based on this spatial extend, the Ethiopian jet occurs in up to 70 % of the nights in the climatology for January presented here. The difference between the results is caused by the different methods for the NLLJ identification (Section 2.2.2).

Between April and September (Figures 2.2d−i), the location of NLLJ hot spots along the margins of the Saharan heat-low point to favourable conditions due to low-level baroclinicity. NLLJs are, here, embedded in the large-scale inflow from the Mediterranean, the Atlantic, and in the West African Monsoon flow over the western Sahel. The Atlantic ventilation hot spot coincides with an increased horizontal gradient of the 975 hPa isohypses (Figures 2.2d−i) between the Azores High and the northwestward expanding heat low. NLLJs are embedded in this inflow, most frequently between April and June (Figures 2.2d−f). Deflection of the air masses by the Atlas Mountains causes prevailing northerly NLLJs (Figure 2.4b). Half of the NLLJs have maximum core wind speeds of 8-16 ms^{-1}. The NLLJs between 15° N and 20° N have previously been described as part of the Atlantic inflow by Grams *et al.* (2010). The results of the present work indicate that the Atlantic ventilation extends even further north to the southern foothills of the Atlas Mountains. Similarly, low-level baroclinicity may cause the Mediterranean ventilation hot spot over northern Libya between May and September (Figures 2.2e−i). Here, the horizontal pressure gradient evolves between the ridge over the Mediterranean Sea, and the Saharan heat-low. NLLJs over the western Sahel follow the latitudinal migration of the heat-low along with the West African Monsoon. This result shows that the frequent formation of NLLJs along the margins of the Saharan heat low, previously proposed by observational studies for parts of West Africa (Abdou *et al.*, 2010; Bain *et al.*, 2010; Parker *et al.*, 2005; Pospichal *et al.*, 2010), is not limited to the southern margins of the heat low.

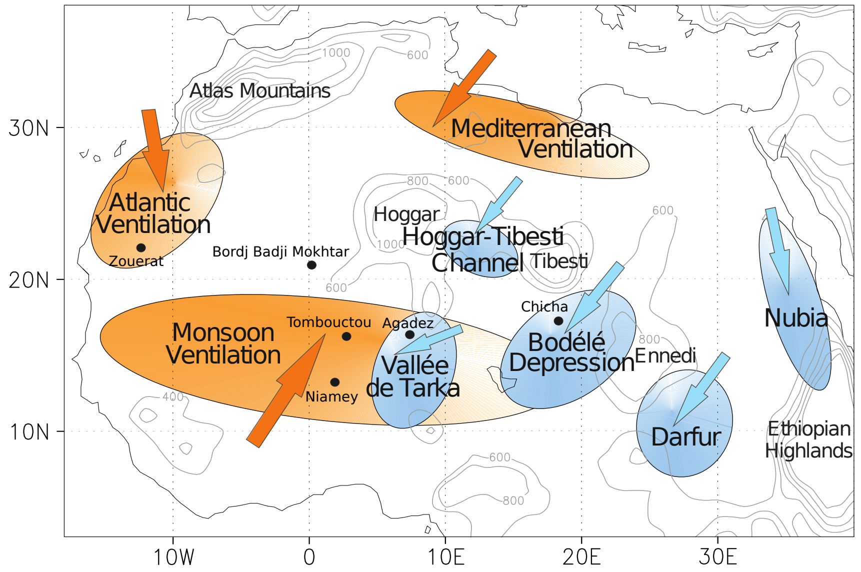

Figure 2.3: *Overview of NLLJ hot spots in North Africa for November–February (blue) and April–September (orange). Contours show the terrain height in steps of 200 m. The arrows indicate the prevailing wind direction for each hot spot. Geographical locations are indicated. Based on Figure from Fiedler* et al. *(2013a) with permission of John Wiley & Sons, Inc.*

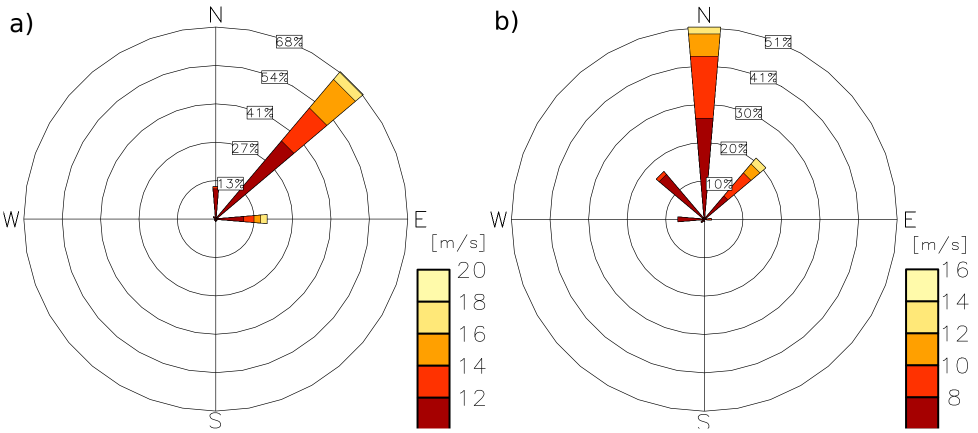

Figure 2.4: *Wind roses for NLLJs (a) in the Bodélé Depression hot spot for November–March and (b) in the Atlantic ventilation hot spot for April–June, based on six-hourly ECMWF ERA-Interim re-analysis 1979–2010. Regions are defined in Figure 2.5a. Figure from Fiedler* et al. *(2013a) with permission of John Wiley & Sons, Inc.*

2.3.2 Characteristics of NLLJs

Height and Core Speed

The detection algorithm enables a statistical assessment of the height and wind speed of NLLJs over North Africa. The median NLLJ height and core speed across North Africa is 350 m a.g.l. and 10 ms^{-1} in the annual statistics. In order to identify regional differences, seven sub-domains are defined (Figure 2.5a): three regions across the northern Sahara (N1, N2, and N3) and four sub-domains across the southern Sahara and Sahel (S1−S4). The geographical placement of the sub-domains is motivated by the sampling areas used by Schepanski *et al.* (2009). The lowest NLLJs are found in the Mediterranean ventilation regions N3 with a median of 300 m a.g.l. and a 99%-percentile of 620 m a.g.l., followed by N2 with 350 m a.g.l. as median height and a 99%-percentile of 670 m a.g.l. (Figure 2.5b). NLLJs over the Bodélé Depression, as part of S3, frequently reside at heights around 380 m a.g.l. (median) to up to 770 m a.g.l. (99%-percentile). The regional differences for the NLLJ core wind speeds are shown in Figure 2.5c. NLLJs are fastest in N1 and S3 with up to 18 ms^{-1} in the spatially averaged 99%-percentile, but the overall difference between the sub-domains is small.

The statistics of NLLJs in North Africa represent observed conditions reasonably well. Validating ERA-Interim against PIBAL observation at Chicha indicates that the statistic for the height of the NLLJ in S3 is well represented (Section 3). The core speed, however, is underestimated by 37 % averaged over the BoDEx period at Chicha. Todd *et al.* (2008) uses another re-analysis data set to determine a maximum core wind speeds of the NLLJ over the Bodélé Depression of 12 ms^{-1} at 17° N, 19° E, which is close to the upper quartile of the S3 sub-domain. Rife *et al.* (2010) finds core speeds of 12 ms^{-1} and a height of 400 m a.g.l. for the Ethiopian NLLJ, which is close to the upper quartile of the statistics for S4 of the present work. Upper air measurements at Khartoum by Farquharson (1939) show a NLLJ in a mean level of 305 m a.g.l. and an annual mean wind speed of 9 ms^{-1}. This observation lies close to the lower quartile of the computed NLLJ height and wind speed statistics of sub-domain S4 which covers but is not limited to the Sudan. Heights and wind speeds from AMMA radiosondes (Chapter 3) are well captured in S2 by ERA-Interim, but the high and fast jets are underrepresented in the statistics (Section 3). The typical heights of the NLLJ of 200−400 m from observations at Niamey (Abdou *et al.*, 2010; Lothon *et al.*, 2008) is well in agreement with the presented statistic for S2. The wind speeds are in the same range but tend to be underestimated in S2 compared to wind profiler observations at Niamey by Lothon *et al.* (2008).

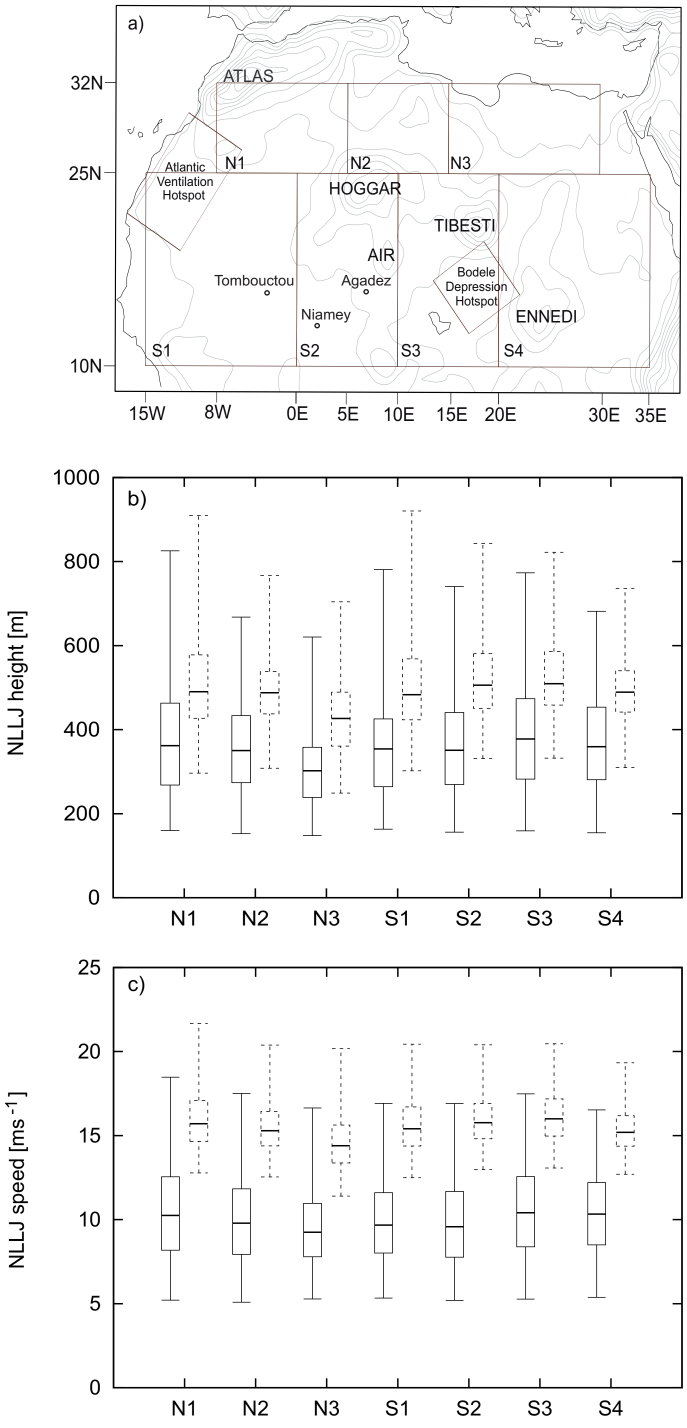

Figure 2.5: *Climatology of NLLJ characteristics. (a) Geographical location of the sub-domains (black boxes) and ERA-Interim model orography (grey) in 200 m steps. (b) Box-and-whisker plots for the core height and (c) core wind speed for all NLLJs (solid) and NLLJs emitting dust at the same time (dashed). Based on six-hourly ECMWF ERA-Interim re-analysis for 1979–2010. Figure from Fiedler* et al. *(2013a) with permission of John Wiley & Sons, Inc.*

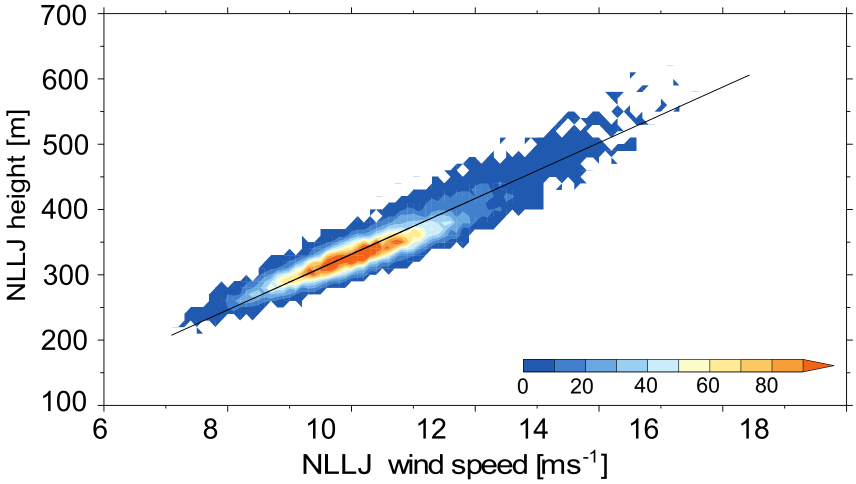

Figure 2.6: *Scatter plot for NLLJ core heights against wind speeds. Shown are values at 0 UTC over North Africa from the six-hourly ERA-Interim re-analysis for 1979–2010. Colours indicate the number of data pairs in the bin. Linear regression (solid line) is given by f(x) = -95.1 + 42.7 x with a Pearson correlation coefficient* R^2 *= 0.98. Figure from Fiedler* et al. *(2013a) with permission of John Wiley & Sons, Inc.*

Core height and wind speed of NLLJs shows a linear relationship (Figure 2.6). This finding is robust and not sensitive to single sub-domains or seasons. At the same geographical latitude and for the same geostrophic wind speed, NLLJs can be expected to develop faster core wind speeds over longer roughness lengths. Variations of the background pressure gradient, the surface roughness and the geographical latitude can, therefore, cause the spread around the linear regression. Figure 2.6 shows further that most NLLJs have intermediate heights of 300–350 m a.g.l. and wind speeds of 9–11 ms^{-1}. Fewer jets are observed at the lower and upper end of the distribution. Assuming calm conditions at the ground and a constant stratification, a strong NLLJ closer to the surface is more likely to become dynamically unstable, so that the NLLJ momentum is transferred to lower levels by turbulence. Stronger NLLJs close to the surface are therefore less likely to be detected in the temporally coarse resolution data. The less frequent occurrence of strong NLLJs at higher altitudes can be linked to a dependency of the jet height on the depth of the surface inversion layer (Baas *et al.*, 2009; Blackadar, 1957) and the strength of the geostrophic wind (Gross, 2012). The growth of the surface inversion can be disturbed by turbulent mixing in the course of the night, which will be further explored in the following section.

Nocturnal Evolution

Shear-induced turbulence beneath a NLLJ affects ABL characteristics with implications for the diurnal cycle of mineral dust emission. ECMWF ERA-Interim forecasts are used for investigating the nocturnal evolution of NLLJ characteristics with higher temporal resolution.

Figure 2.7a shows the nocturnal evolution of the fraction of grid boxes that have a NLLJ or a NLLJ survivor. At 18 UTC, NLLJs are found in 10 % of the grid boxes over North Africa, which is defined as an area covering all seven sub-domains plus the edges: 15° W−35° E and 10° N−32° N. Jets at this time of day are predominantly found in the east of the domain (not shown). As the night progresses, the number of grid boxes with NLLJs increases and reaches the maximum of 80 % at 3 UTC. The subsequent decrease of the number of NLLJ grid boxes is linked to the onset of the NLLJ breakdown in the east, where 6 UTC is after local sunrise. NLLJs survive in 30 % of all North African grid boxes at 9 UTC, and 5 % at 12 UTC, the latter of which are limited to the western boundaries of North Africa. The NLLJ statistic at 15 UTC is not shown due to the small sampling size at this time of day.

It is worth noting, that the presented diurnal cycle is influenced by the difference between UTC and local time (LT). Local times across North Africa range from approx. UTC + 2 in the east to UTC - 1 in the west. In eastern regions 9 UTC corresponds to 11 LT which is too late for the expected NLLJ breakdown at 9 LT. In fact, 11 LT in the west (12 UTC) clearly shows an abrupt reduction in the number of NLLJ survivors. Here, 9 UTC corresponds to 08 LT which can be too early for the NLLJ breakdown. This means that the peak in the near-surface wind speed is not captured in all areas. The associated mineral dust emission is, therefore, likely to be underestimated.

The temporal development of the NLLJ core height and wind speed is shown in Figures 2.7b−c. Between 18 UTC and 21 UTC, the median NLLJ height decreases from 400 m a.g.l. to 300 m a.g.l. while the median core wind speed increases from 9 ms^{-1} to 10 ms^{-1}. The wind speed increase indicates an acceleration of NLLJs. Decreasing spatial mean heights of the NLLJ are linked to generally shallow inversion layers at the beginning of the new NLLJ generation across large areas at 21 UTC. The NLLJ formation at 18 UTC is limited to S4 in all months and S3 between December and February, where the NLLJs reside relatively high (not shown).

The nighttime development between 21 UTC and 6 UTC shows an increase of both the core height and the number of NLLJ grid boxes, which points to an ongoing NLLJ evolution. However, the NLLJ wind speed does not show the expected acceleration in the course of the night. This hints at downward mixing of momentum due to shear-induced turbulence during the night. If the static stability is not high enough for balancing the vertical wind shear, turbulence transfers momentum to lower levels. The associated loss of momentum at and beneath the NLLJ nose decelerates the jet or even erodes the wind speed maximum. New NLLJs may start

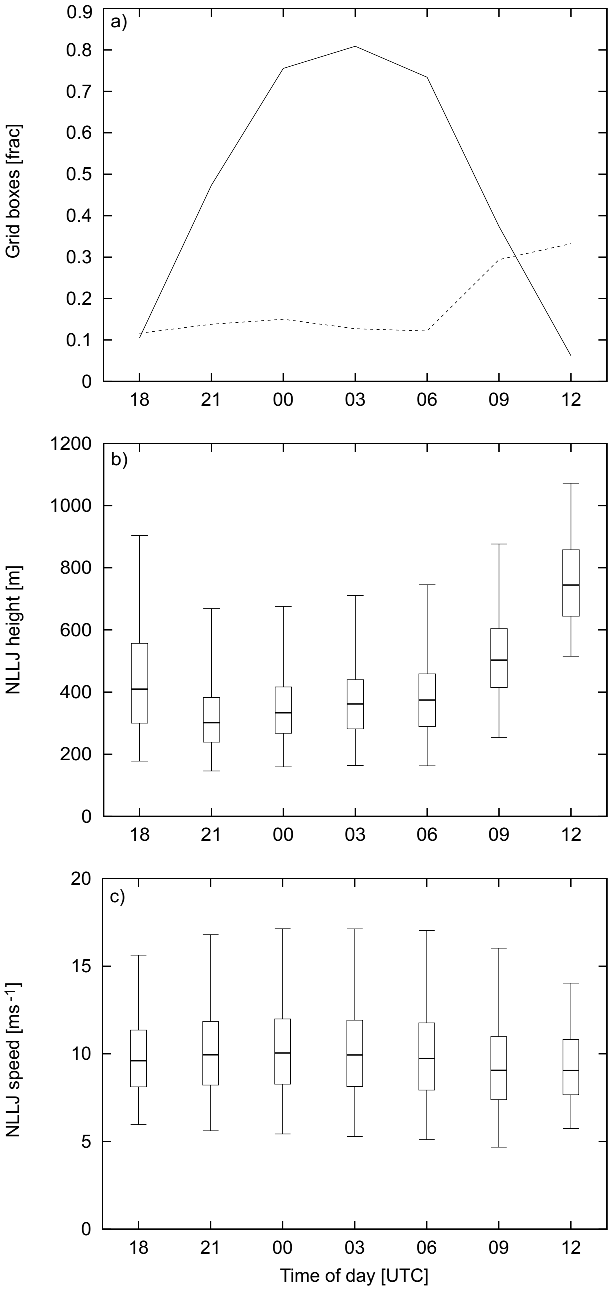

Figure 2.7: *Temporal development of NLLJs and NLLJ survivors over North Africa. (a) Nocturnal cycles of the mean fraction of grid boxes with a NLLJ (solid) and DSA (dashed), box-and-whisker plots showing 99%-, 75%-, 50%-, 25%- and 1%-percentiles of (b) the NLLJ core height and (c) core wind speed as function of time in UTC. Based on three-hourly ECMWF ERA-Interim forecasts for 1979–2010. Figure from Fiedler* et al. *(2013a) with permission of John Wiley & Sons, Inc.*

to form where they have been eroded earlier in the night. Both the weakening of pre-existing NLLJs and the beginning of new NLLJ formations explains the missing increase of the jet wind speed in the statistic. The decreasing number of grid boxes with a NLLJ after 3 UTC suggests that NLLJs are eroded and that less new NLLJ form towards the end of the night. The increasing height of NLLJs during the night can be linked to the depth of the surface inversion (Baas *et al.*, 2009; Blackadar, 1957). The inversion depth depends on both the cooling rate, determined by the net radiation budget at the surface, and the entrainment of air from the residual layer, under constant environmental conditions. Entrainment can be efficient during shear-driven turbulence beneath a NLLJ near the top of the surface layer (Van de Wiel *et al.*, 2010). It is this entrainment due to the vertical mixing beneath the NLLJ that can increase the inversion depth and therefore lift the NLLJ core to higher altitudes.

The median NLLJ core wind speed decreases and the height increases after 6 UTC. In combination with a decreasing number of grid boxes with NLLJs or NLLJ survivors, this development illustrates the expected breakdown and erosion of NLLJs during the following mid-morning. Dust emission due to the downward mixing of NLLJ momentum occurs when the increase in the 10m-wind speed is sufficiently high to exceed the threshold for dust mobilization.

Characteristics during Emission

The distributions of the NLLJ core wind speed and height are different during dust emission events as has been calculated by the offline dust emission model (Figures 2.5b-c). Dependent on the sub-domain, the median NLLJ speed and height during dust emission ranges from $14-16\,\mathrm{ms}^{-1}$, and $430-510$ m a.g.l., respectively. The distributions of the dust-emitting sub-sample of NLLJs are shifted to the upper quartile of the distributions of the enclosing NLLJ sample in all sub-domains. In some regions, even the 25%-percentile of wind speed of dust-emitting NLLJ is shifted to the upper quartile of the background climatology. This shift reflects the necessity of low-level wind speeds exceeding the threshold value for dust emission onset. The 1 % percentile of core wind speed of dust-emitting NLLJs has values of $12-13\,\mathrm{ms}^{-1}$ at relatively low levels of $250-350$ m, which can be interpreted as the threshold NLLJ characteristics for mineral dust emission.

2.3.3 Dust emission amount associated with NLLJs

The near-surface winds from the ECMWF ERA-Interim forecasts generate a total annual dust emission flux of 428 +/- 46 Tg for $1979-2010$ over North Africa. This

Time of year	Region			
	Bodélé Depression	North Sahara	West Sahara	North Africa
December−February	24	57	10	124
March−May	14	104	13	174
June−August	2	26	39	87
September−November	8	18	8	42
Annual	48	205	70	428

Table 2.1: *Estimate of mean mineral dust emission in Tg based on ECMWF ERA-Interim forecasts and the offline dust model by Tegen* et al. *(2002) for 1979−2010. Table from Fiedler* et al. *(2013a) with permission of John Wiley & Sons, Inc.*

dust emission amount lies within the computed dust emission range of 130−1600 Tg per year over North Africa from previous studies (Engelstaedter *et al.*, 2006, and references therein). The most recent assessments of the mean annual dust emission in North Africa are: 2077 Tg per year for 2006 estimated by Schmechtig *et al.* (2011), 670 +/- 60 Tg per year for 1996−2001 by Laurent *et al.* (2008), and 400−2200 Tg per year from the AeroCom model intercomparison for 2000 (Huneeus *et al.*, 2011). Most dust aerosol from North Africa is emitted during northern hemisphere spring with 41 %, followed by winter with 29 %, summer with 20 %, and fall with 10 % of the annual emission flux. Spatially integrated dust emission fluxes over North Africa and different sub-domains are shown in Table 2.1. The choice of the three sub-domains is, here, motivated by dominant dust sources in terms of emitted mass.

Seasonal Climatology

Seasonal and spatial variations of the mineral dust emission are shown in Figure 2.8. From December to February (Figure 2.8a), a maximum of dust emission is found over the Bodélé Depression with typical dust emission values around 50 gm^{-2}. The seasonal mean over the area from 15° N−19° N and 15° E−20° E is 24 Tg (Table 2.1). The dust emission amount from this source decreases as the year progresses to 14 Tg for March−May down to a minimum of 2 Tg in June−August. Between September and November, the seasonal mean dust emission increases again to 8 Tg.

Regions along the northern margins of the Sahara desert have the highest mineral dust emission of around 50 gm^{-2} between March and May compared to mostly 6-30 gm^{-2} in the rest of the year (Figure 2.8b). In northern hemisphere spring, the

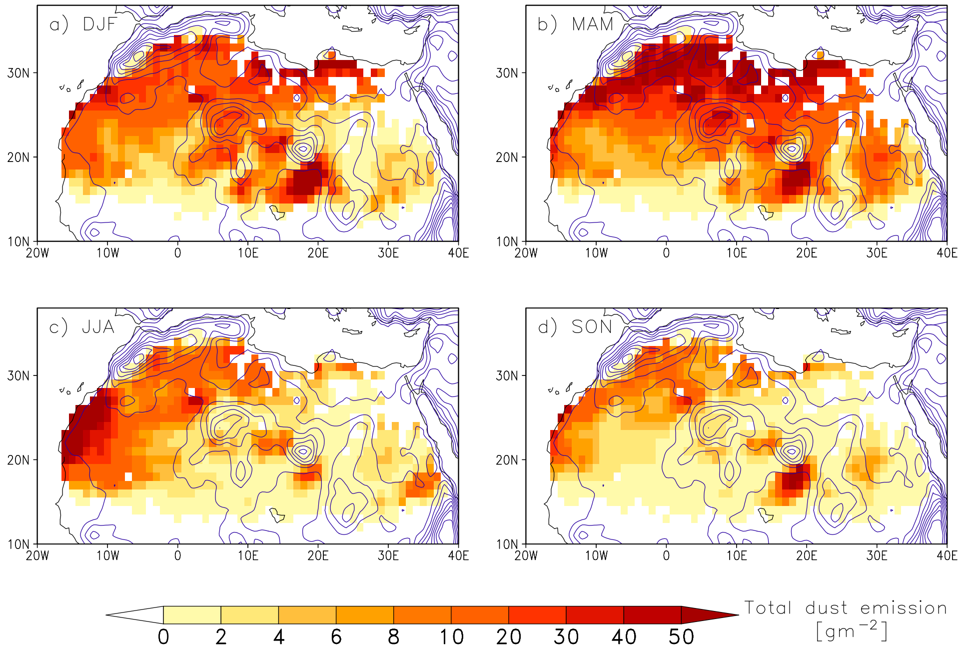

Figure 2.8: *Dust emission climatology. Seasonal mean dust emission for (a) December–February, (b) March–May, (c) June–August and (d) September–November, based on three-hourly ECMWF ERA-Interim forecasts for 1979–2010. Contours show the terrain height in steps of 200 m. Figure from Fiedler* et al. *(2013a) with permission of John Wiley & Sons, Inc.*

dust emitted in the area from 25° N–35° N and 10° W–25° E contributes 104 Tg or 25 % of the annual total dust emission budget of North Africa. The dominant dust sources between June and August are found in western North Africa with values between 20 gm^{-2} and 50 gm^{-2} (Figure 2.8c). Here, 39 Tg of dust aerosol is emitted in the seasonal mean over the region covering 20° N–28° N and 18° W–10° W. The three dominant dust sources contribute 73–81 % of the seasonally averaged dust emission over North Africa (Table 2.1). The relative importance of individual sources for dust emission varies seasonally.

The new NLLJ detection algorithm in the present work enables for the first time a calculation of the relative contribution of NLLJs to the dust emission amount in a quantitative manner. Other dominant meteorological drivers for generating peak winds and, therefore, dust emission are assumed to be negligible during the occurrence of a NLLJ or a NLLJ survivor. The validity of this assumption is assessed by the statistical analysis of 10m-wind speeds at times when a NLLJ event is detected and when no NLLJ is present. Figure 2.9 shows the frequency distribution of both the instantaneous 10m-wind speed and the 10m-wind gusts during the mid-morning spatially averaged over North Africa. It is the mid-morning when the largest impact of NLLJ momentum on the near-surface wind speed and dust emission is expected (Section 1.3.4). During the occurrence of NLLJs and NLLJ survivors the 10m-wind

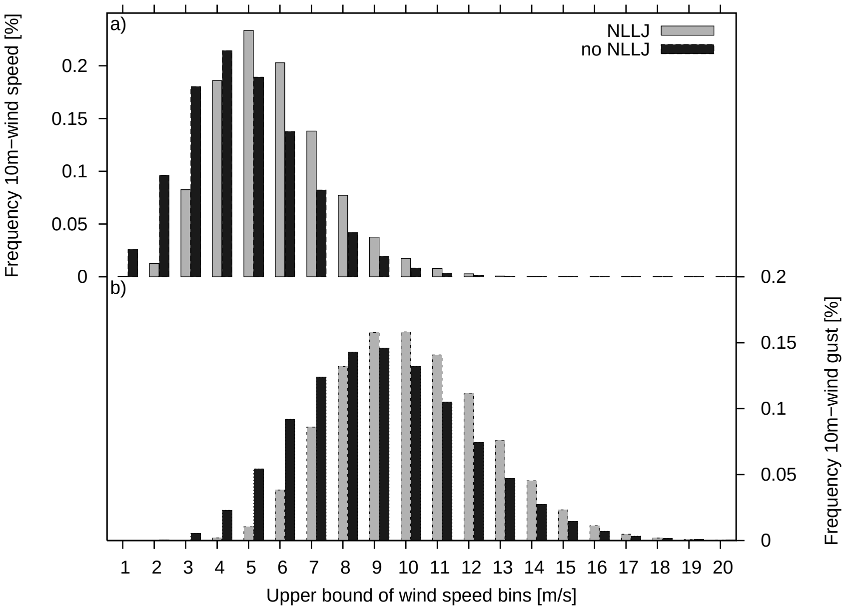

Figure 2.9: *Frequency distribution of the 10m-wind speed during the mid-morning. Spatially averaged frequency distribution over North Africa of (a) the instantaneous 10m-wind speed at 6 UTC and 9 UTC and (b) the 10m-wind gusts at 9 UTC and 12 UTC when a NLLJ or a NLLJ survivor has been detected (grey), and when no NLLJ structure has been identified (black), based on three-hourly ECMWF ERA-Interim forecasts for 1979–2010. Figure from Fiedler* et al. *(2013a) with permission of John Wiley & Sons, Inc.*

speed and the gustiness shows a distinct shift towards higher wind speeds compared to the distribution when no NLLJ is simultaneously detected. This result from the frequency distribution can be interpreted as the linkage between the occurrence of a NLLJ and dust emission, since the latter is a function of the 10m-wind speed.

It is interesting to note that the upward shift of the wind speed characteristics during the presence of a NLLJ or a NLLJ survivor during the mid-morning is largest in bins of medium wind speeds, 5–9 ms^{-1} for the 10m-wind speed and 9–14 ms^{-1} for the gustiness, respectively (Figure 2.9). The tail of the frequency distributions shows only small differences between NLLJ and no-NLLJ cases. This finding points towards a similar importance of NLLJs and other meteorological processes for the generation of the highest peak winds between 6 and 12 UTC. One of these processes can be a strong large-scale forcing that regularly transfers momentum to the surface. Even under these conditions, NLLJs can insert a diurnal variation of the near-surface wind speed but cause a smaller diurnal amplitude (Section 1.3.4). The frequent vertical mixing under strong background flows with an associated disruption of the nocturnal LLJ enhancement and the occurrence of other meteorological processes generating peak winds explain the rather small difference between NLLJs and other events for generating wind speeds at the upper end of the wind

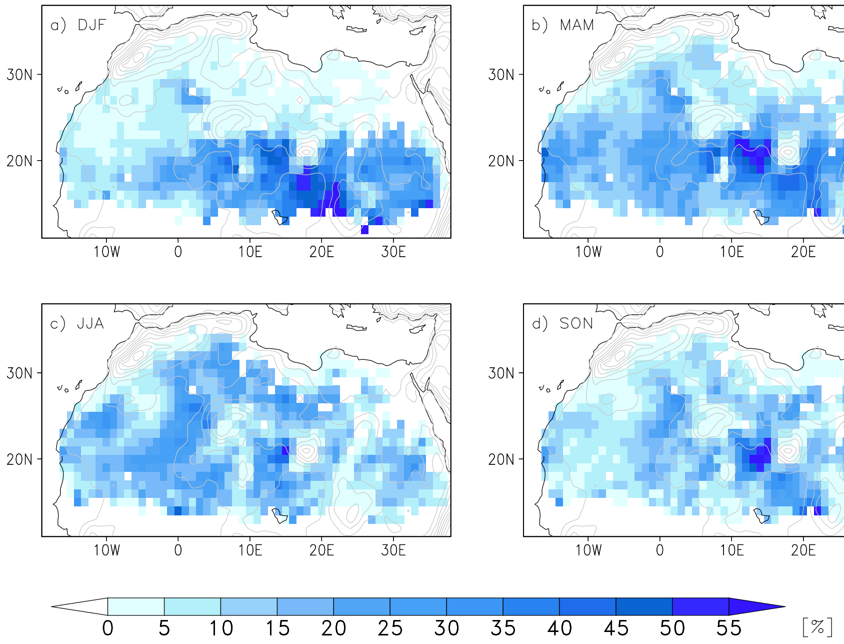

Figure 2.10: *Seasonal mean NLLJ contribution to dust emission for (a) December–February, (b) March–May, (c) June–August and (d) September–November, based on three-hourly ECMWF ERA-Interim forecasts for 1979–2010. Contours show the terrain height in steps of 200 m. Figure from Fiedler* et al. *(2013a) with permission of John Wiley & Sons, Inc.*

distributions.

The coherence of increased 10m-wind speeds during NLLJ events is used in the following to estimate the NLLJ contribution to dust emission which is based on the simultaneous occurrence of dust emission and a NLLJ or a NLLJ survivor. In the annual and spatial mean over North Africa, 15 % of dust is emitted when NLLJ momentum mixing occurs. The seasonal mean climatology of the NLLJ contribution to dust emission in Figure 2.10 shows distinct regional characteristics. Between December and February, the NLLJ contribution is largest south of 20° N and east of 0° (Figure 2.10a). The expected peak of the NLLJ contribution to dust emission over the Bodélé Depression is well reproduced with up to 60 % of the dust generated by NLLJs. This region remains distinctive in the climatology for March to May with 30–40 % NLLJ contribution (Figure 2.10b), but the largest contribution of around 50 % is now shifted to areas south of the Hoggar-Tibesti channel. At the same time, the relative importance of NLLJs over the western Sahel increases to values of 10–35 %. From June to August, NLLJs contribute more substantially to dust emission north of 20° N with regional maxima of up to 35 % over Algeria, Mali, Mauritania, and Libya (Figure 2.10c). Between September and November, the relative importance of NLLJs decreases in most regions in the north and west. In contrast, an increase of the NLLJ contribution to dust emission is found south of the Hoggar-Tibesti channel, over the Bodélé Depression, and over Nubia, where NLLJs contribute regionally 30−50 % to the dust emission (Figure 2.10d).

Diurnal Cycle

The diurnal cycle of the NLLJ contribution to dust emission is analyzed to understand the relative importance of NLLJ momentum for nighttime and morning dust emission. One perspective on the diurnal variations is given by the number of grid boxes with active dust emission in Figure 2.7a. The spatial mean number of dust-emitting grid boxes increases from 10 % during the night to up to 30 % in the mid-morning. The timing is consistent with the expected mechanisms for NLLJ momentum mixing, namely turbulence in the course of the night and the breakdown of NLLJs during the mid-morning. This suggests a mean relative importance of the NLLJ breakdown of up to 30 % in terms of DSA frequencies without accounting for the dust emission amount. The diurnal cycle of DSA based on satellite observation, however, shows nighttime emission of 1−5 % and morning DSA frequencies of 65 % (Schepanski *et al.*, 2009). This suggests an overestimation of nighttime and underestimation of morning DSA frequencies of the dust emission compared to the satellite observation, although the length of the time periods for the two climatologies differ. The relatively high nighttime DSA is in agreement with the too strong mixing in the ABL at night (Section 2.3.2).

In order to analyse the annual and diurnal cycle of the NLLJ contribution in more detail, the approach based on the dust emission amount is used in the following. Figures 2.11 and 2.12 show the spatial mean annual cycle of the three-hourly dust emission at the top and the contribution of NLLJs to dust emission at the bottom for each of the seven sub-domains given in Figure 2.5a. Whether NLLJs are a key driver for dust emission in specific regions can be concluded from considering (1) a phase comparison of the annual cycles of mineral dust emission and NLLJ contribution, (2) the total amount of dust emission, and (3) the frequency of NLLJs.

Northern Sub-domains

In the northern sub-domains, the spatial mean dust emission is largest in N1 (Figure 2.11a) and N2 (Figure 2.11b). The largest spatial mean dust emission is simulated during mid-day, up to 4 $\mathrm{gm^{-2}}$ at 12 UTC and 5 $\mathrm{gm^{-2}}$ at 15 UTC, respectively. N3 has smaller mid-day maxima of dust emission with values around 2 $\mathrm{gm^{-2}}$ for 12 UTC. Maxima at 09 UTC in March and May have values of 1−2 $\mathrm{gm^{-2}}$ (Figure 2.11a−c). Nighttime emission is substantially smaller with maximum values around 0.5 $\mathrm{gm^{-2}}$ for 21 UTC and 0 UTC.

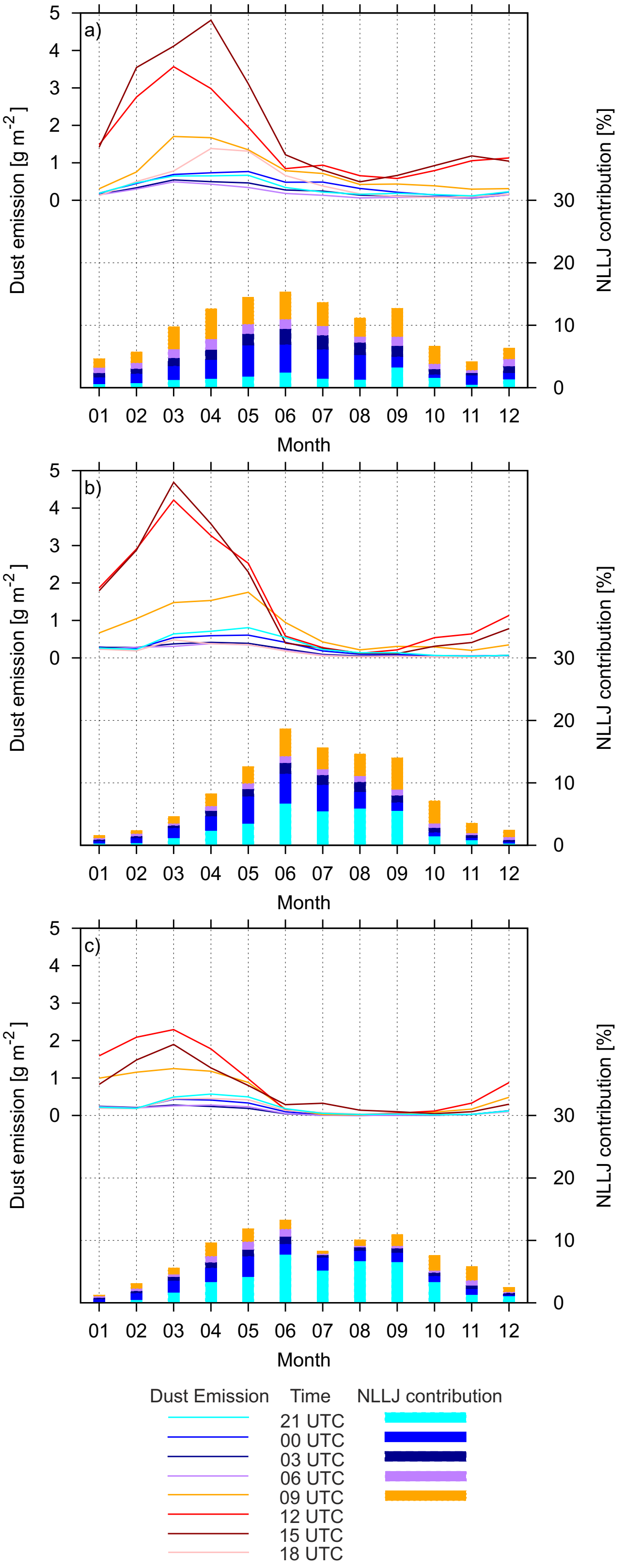

Figure 2.11: *Contribution of NLLJs to mineral dust emission. Annual cycle of the monthly mean dust emission (lines) and the monthly mean of the relative contribution of NLLJs to the total dust emission (bars) at different times of the day (colours) as spatial mean per subdomains (a) N1, (b) N2, and (c) N3 based on three-hourly ECMWF ERA-Interim forecasts for 1979–2010. Regions are defined in Figure 2.5a. Figure from Fiedler* et al. *(2013a) with permission of John Wiley & Sons, Inc.*

NLLJ and NLLJ survivors generate 1−19 % of the total dust emission flux in the spatial mean (Figure 2.11a−c). Maximum contributions of 10−19 % are found in N1 for March−September (Figure 2.11a), in N2 for May−September (Figure 2.11b), and N3 for April−June and August−September (Figure 2.11c). The overall maximum in the northern domains is 19 % in N2 for June (Figure 2.11b). Here, NLLJ contributions remain high with values larger than 10 % until September, which coincides well with the more frequent occurrence of NLLJs along the northern margins of the Saharan heat low in these months (Section 2.3.1).

N2 and N3 have larger values of the NLLJ contribution to dust emission at 21 UTC than at 9 UTC in most months, which points to turbulent mixing at night (Figures 2.11b−c). The total dust emission fluxes at night are, however, small. Furthermore, the annual cycle of dust emission is not in phase with the NLLJ contribution cycle, and the large mid-day dust emission are not related to the breakdown of NLLJs. This indicates other processes as driving mechanisms along the northern margins of the Sahara. A potential underestimation of the NLLJ strength in the model (Sandu *et al.*, 2012), the temporal resolution, and the uncertainty in the NLLJ detection algorithm are likely to have a small impact on this result.

Southern Sub-domains

Maxima of the spatial mean dust emission at single hours are generally smaller in the southern sub-domains than the northern ones. For example, S1 and S2 emit 0.5−1 $\mathrm{gm^{-2}}$ dust at 12 and 15 UTC between January and March. S1 has a secondary maximum in July, when the spatial mean dust emission reaches values of 0.4−1 $\mathrm{gm^{-2}}$ at all times of the day (Figure 2.12a). Both western sub-domains have comparably small emission fluxes of up to 0.5 $\mathrm{gm^{-2}}$ at 9 UTC (Figure 2.12a−b). In contrast, the dust emission in S3 is largest at 9 UTC throughout the year and reaches maximum values around 2 $\mathrm{gm^{-2}}$ between January and March (Figure 2.12c). The diurnal cycle of dust emission in S4 is similar to S3, but produces peaks of only up to 0.5−0.7 $\mathrm{gm^{-2}}$ at 9 UTC (Figure 2.12d).

The NLLJ breakdown appears generally more important for dust emission in the southern sub-domains (Figure 2.12). The spatial mean contribution varies between 5 % and 28 %. More than 20 % is found in S1 and S2 for April (Figure 2.12a−b), in S3 for November−May (Figure 2.12c), and in S4 for November−April (Figure 2.12d). In S2, S3, and S4, maxima of the mineral dust emission flux at 9 UTC coincide well with peak contributions from the NLLJ breakdown.

The phases of the annual cycles correspond well in S3 and S4, where clear regional NLLJ maxima are identified. At the same time, the mineral dust emis-

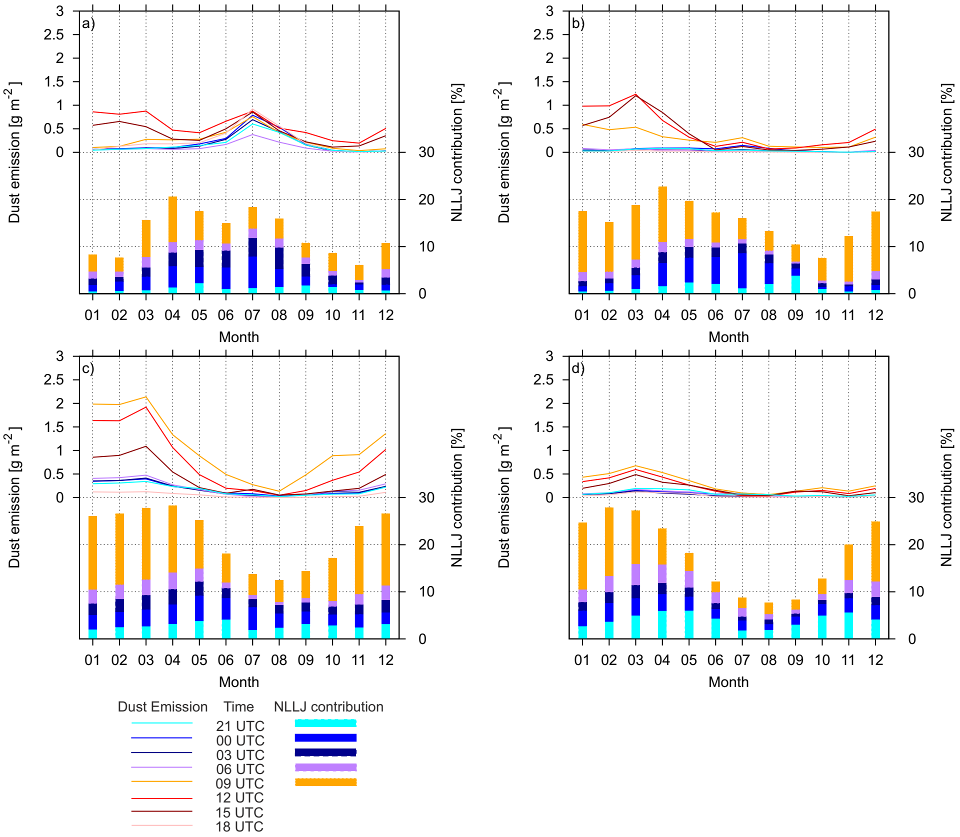

Figure 2.12: *As Figure 2.11 for sub-domains (a) S1, (b) S2, (c) S3 and (d) S4. Note the different scale for the dust emission. Figure from Fiedler* et al. *(2013a) with permission of John Wiley & Sons, Inc.*

sion and the relative contribution to the total dust emission show clear mid-morning maxima at 9 UTC. This suggests NLLJs as an important driver for dust emission in the southeastern sub-domains, which is in agreement with other studies (Schepanski *et al.*, 2009; Washington & Todd, 2005). In contrast, the annual cycles of the contribution of NLLJs and dust emission in S1 are not in phase. The driving meteorological processes here and for the northern sub-domains will be discussed further in Section 2.4.

2.4 Discussion

2.4.1 NLLJs as a driver for dust emission

The present chapter estimates the dust emission amount associated with NLLJs. The simultaneous occurrence of NLLJs and dust emission is frequent in southeastern areas of North Africa including the Bodélé Depression, which is in agreement with the literature (Schepanski *et al.*, 2009; Washington & Todd, 2005). S1, however, shows no agreement in the annual cycle of dust emission and NLLJ contribution, but comparably large dust emission amounts between June and September. Here, the West African Monsoon system determines the meteorological conditions. Different peak-wind generating processes have been suggested, but the key drivers for dust emission remain controversial (Section 1.3.1). The results of the present work suggest a $5-35\,\%$ contribution from NLLJs along the margins of the Saharan heat-low to West African dust emission during the monsoon season. Uncertainty due to the three hourly resolution that misses 9 LT remains in this area.

NLLJs are not a major generator of dust emission for most source areas north of 25° N suggested by a relatively small NLLJ frequency in most months, a small total contribution, and a shift in the phases of the annual cycles for the dust emission fluxes and the NLLJ contribution. The small NLLJ contribution to dust emission north of 25° N is in agreement with the geographical distribution of DSA frequency during the morning from Schepanski *et al.* (2009). An underestimation of the NLLJ contribution during the morning due to the weakening of jets by turbulence at night appears unlikely, as the dust emission amount is substantially larger at 12 UTC and 15 UTC when the NLLJ breakdown can not be the driving mechanism. Other processes have to generate the dust-emitting peak winds in this case. Fronts associated to cyclones along the northern margins of the Sahara and in the Mediterranean region (e.g. Alpert *et al.*, 1990) are proposed as a dust-emitting process in the north during this time of year which will be analysed in Chapter 4.

2.4.2 Implications for dust modeling

Satellite observations suggest that dust emission peaks in the mid-morning and decreases in the afternoon (Schepanski *et al.*, 2009). The morning peak has been associated with the breakdown of NLLJs. The dust emission maximum of NLLJs is expected around 9 LT, when the vertical mixing in the convective ABL erodes the nighttime surface inversion over a certain depth. The six-hourly re-analysis data does not include this time since 6 UTC corresponds to about 5−8 LT and 12 UTC to 11−14 LT across North Africa. This has the following implications for dust emission modeling:

1. Calculating offline dust emission with temporally coarse (several hours) resolution data may not simulate realistic results due to the importance of meteorological processes at intermediate times.
2. Results for the total dust emission and the dust emission associated with NLLJs in North Africa are likely to be underestimated when the offline simulation is based on ECMWF re-analysis alone.

The present work uses three-hourly data for dust emission simulations in North Africa, which fills the gap at 9 UTC (8−11 LT) to some extent. It has been shown that the DSA frequency and the amount of mineral dust emission increases in most North African regions in the mid-morning based on the ECMWF ERA-Interim forecasts. The satellite based DSA frequency by Schepanski *et al.* (2009) documents less frequent dust emission events at night by a factor of 16−84 dependent on their defined region. The nocturnal DSA in the present work is only three times smaller than the DSA during the mid-morning. At the same time, the contribution of NLLJ momentum for 21−3 UTC in terms of dust emission amount is surprisingly large. The magnitude of dust emission due to nocturnal mixing is comparable to the emission from the morning breakdown in four of seven sub-domains. Whether the nighttime emissions are realistic needs to be assessed by comparing with long-term observational data. An estimate of the diurnal cycle of the dust emission amount from observation is not given in the literature.

2.4.3 Limitations

Limitations of the present work arise from the relatively coarse temporal and spatial resolution as well as the physical parameterisations of both dust emission and the near-surface wind speed in the nocturnal ABL. Relevant variables for the NLLJ climatology for dust emission are validated in the following Chapter 3. Further uncertainties are due to the sensitivity of the detection algorithm to the chosen threshold values for the strengths of the surface inversion and the vertical wind shear above the jet core (Section 2.2). It is essential to acknowledge the chosen NLLJ definition for interpreting the presented results. The robustness of the NLLJ contribution to dust emission shall be evaluated with a sensitivity test of the detection algorithm applied to the ERA-Interim forecasts in the following. Although a vertically narrow layer of high wind speed has been defined as a criterion for the NLLJ definition, the shape of the NLLJ is not necessarily relevant for the associated dust emission. Especially under relatively strong large-scale forcing, NLLJs may not show a strong wind speed decrease above the NLLJ core. In order to test how the shape influences the NLLJ contribution to mineral dust emission, the vertical wind shear criterion is switched off. The result shows that the spatial mean contribution of NLLJ structures to dust emission increases by a factor two to three due to more identified jets in the test. The annual cycle and the relative importance of different times of the days, however, are not substantially affected. This finding gives confidence in the presented results for the NLLJ contribution to dust emission, but the absolute amount of NLLJ contribution to dust emission need to be treated with caution.

2.5 Conclusions

In this chapter, a quantitative NLLJ climatology was produced for North Africa, based on ECMWF ERA-Interim data for 1979−2010. Detailed characteristics of the wind speed maxima and the contribution of the downward mixing of their momentum to mineral dust emission were analyzed in a climatological sense. The work is based on a newly developed automatic NLLJ detection algorithm. A wind speed maximum between the lowest model level and 1,500 m a.g.l. is detected as a NLLJ, if the surface layer is stably stratified and the vertical wind shear above the jet core exceeds a certain threshold.

The results emphasize a frequent NLLJ occurrence of 29 % in the annual and spatial mean over North Africa. NLLJ frequencies of up to 80 % are found in NLLJ hot spots. Here, low-level baroclinicity and orographic channeling are suggested to favour their formation. Baroclinicity has been identified as favourable condition for the NLLJ hot spots along the margins of the heat-low between April and September. A NLLJ hot spot due to mountain channelling is the Bodélé Depression between November and March. Typical median heights and wind speeds of NLLJs in ERA-Interim are 350 m a.g.l. and 10 ms^{-1}, respectively.

NLLJs are a source of momentum for mineral dust emission in North Africa. The downward mixing of NLLJ momentum by nocturnal turbulence and the morning breakdown is associated with 15 % of North African dust emission annually and spatially averaged. Up to 60 % of the total dust emission can be associated with NLLJs, dependent on the region and the time of year. Breakdowns of the NLLJ are particularly important for dust emission in the southeast of North Africa at the beginning of the year. The peak contributions of NLLJs to mineral dust emission around 9 LT over North Africa underline the importance of using wind speed data of sufficient temporal resolution in a dust emission model. Six-hourly wind speeds do not capture the mid-morning maximum over North Africa. Uncertainties of the results remain due to the sensitivity of the NLLJ detection algorithm to the threshold values, physical parameterisations, temporal and spatial resolution. The following Chapter 3 presents a validation of the results.

Other meteorological processes than the vertical mixing of NLLJ momentum appear to be relatively more important for dust emission west of 10° E and generally north of 25° N. The main driving meteorological condition for dust emission in the western Sahara remains controversial, but the present work suggests seasonal mean NLLJ contributions to the mineral dust emission of 5−35 %. Extra-tropical cyclones are suggested as driving mechanisms for dust emission along the northern margins of the Sahara desert that will be addressed in Chapter 4 (Fiedler *et al.*, 2013b).

The new automated detection algorithm for NLLJs presented here will be used for evaluating the wind speed maxima and associated dust emission in HadGEM2-ES in Chapter 5. It contributes to identifying model systematic behaviour which helps guiding future model development for improved dust emission amounts.

CHAPTER 3

Validation of the baseline climatology

3.1 Motivation

The new NLLJ climatology and associated dust emission in Chapter 2 is based on the ERA-Interim re-analysis and forecasts for 1979−2010. It is known that weaknesses in the boundary layer parameterisation for stable stratification affecting NLLJs remain, the improvement of which is subject of ongoing research (e.g. Holtslag *et al.*, 2013; Sandu *et al.*, 2013). Despite shortcomings of ERA-Interim, this data is chosen to compile the baseline climatology for process analysis and model evaluation since the upper-air observation network is sparse and lacks continuous long-term observations over most of North Africa. Any attempt to study NLLJs in a climatological sense requires wind observation in the lowest 1500 m of the troposphere in the diurnal cycle for a time period of 20−30 years. Radiosondes are not launched sufficiently frequent over such long time periods in most remote areas of the Saharan desert, which are especially interesting from the perspective of dust emission. A long-term analysis of NLLJs based on observations for the entire of North Africa as well as a systematic validation of the vertical profile of wind speed in ERA-Interim are therefore not possible. In the following, the vertical profile of wind speed in ERA-Interim and observations are compared at different North African locations to indicate how the model system performs. In addition to the validation with radiosondes at single stations a set of re-analysis products is used to evaluate the uncertainty in the best estimate of the past state of the atmosphere in North Africa.

3.2 Method

For the purpose of wind speed validation in ERA-Interim forecasts, observations from three field campaigns in North Africa have been chosen that are summarized in Table 3.1. These are quality controlled radiosondes from the African Monsoon Multidisciplinary Analysis (AMMA, Parker *et al.*, 2008; Redelsperger *et al.*, 2006), pilot balloons (PIBAL) from the Bodélé Dust Experiment (BoDEx, Todd *et al.*, 2008;

Data type	Project	Time period	Locations
Radiosondes	AMMA	2006	Tombouctou, Agadez, Niamey
Radiosondes	Fennec	2011	Bordj Badji Mokhtar, Zouerat
Pibal balloon	BoDEX	March 2005	Chicha
SODAR, LIDAR	Fennec	June 2011	Bordj Badji Mokhtar

Table 3.1: *Overview on observation data for the vertical profile of wind speed from field campaigns used in this chapter. Geographical locations of the stations are indicated in Figure 2.3.*

Washington *et al.*, 2006), as well as radiosondes, SODAR and LIDAR from the Fennec field campaign (Allen & Washington, 2014; Marsham *et al.*, 2013b; Todd *et al.*, 2013). SODAR (LIDAR) measurements allow to derive information on the wind speed by using Doppler radial velocities from different directions. These velocities are derived from the shift in the frequency of an acoustic (optical) signal of objects in relative motion to each other. In the case of SODAR, the temperature gradient leads to the reflection of sound towards the receiver. For LIDAR, aerosol scatters light of the emitted laser beam towards the receiver. An important difference is the spatial representation of the sample which is much smaller for LIDAR both vertically and horizontally (pers. comm. B. Brooks, University of Leeds, 2013). All atmospheric soundings provide observations of wind speeds at night including NLLJs. The stations used for validation are Tombouctou, Agadez, Niamey, Bordj Badji Mokhtar (BBM), Zouerat and Chicha (Table 3.1), the geographical locations of which are shown in Figure 2.3. The higher temporal resolution of some of these observations over limited time periods even enables a comparison of the temporal development of the wind profile in the course of the night. The results of the validation of NLLJ characteristics with AMMA radiosondes and the qualitative comparison with PIBAL measurements are published in Fiedler *et al.* (2013a).

The different characteristics of the wind speed from observations and the numerical model system needs to be considered for the comparison. Wind speed data in ERA-Interim represents a spatial mean value for grid boxes with an edge length of roughly 100 km horizontally and of the order of 50−100 m vertically in the lowest 1500 m. Contrary, the measured wind speed from a radiosonde is an instantaneous value at a point, the position of which varies horizontally with height. In order to keep uncertainties to a minimum, radiosonde stations have been identified as suitable for the model validation if the surroundings are sufficiently horizontally homogeneous. In addition to the spatial differences between a radiosonde and the

		Observation	
		yes	no
Forecast	yes	a *(hit)*	b *(false alarm)*
	no	c *(miss)*	d *(correct negative)*

Table 3.2: *Contingency table with notation for event classification. The total number of counted events is the sample size n. Following Jolliffe & Stephenson (2003).*

model, the vertical resolution as well as the temporal mismatch of the radiosondes and the model cause uncertainty. Radiosonde profiles are selected that were launched close to the three-hourly model data. For instance soundings between 22.30 UTC and 01.30 UTC are used for comparison at mid-night from the model. Measurement uncertainty of the wind from instrument accuracy and swinging of the radiosonde beneath the balloon are likely smaller than the uncertainty from the resolution differences.

Each of the selected profiles has been manually examined for the occurrence of a NLLJ profile. If a NLLJ is found in the observation, it is matched to the corresponding profile from ERA-Interim in the grid box enclosing the station. Here, no automatic detection has been applied for identifying NLLJs, because the threshold values from the model study are not directly transferable to the more fluctuating values from a radiosonde ascent, which has been tested by Allen & Washington (2014). Given the small number of suitable radiosondes data, it is felt to be more appropriate to do the NLLJ identification in the radiosondes by eye instead of developing and testing a new set of threshold values for the automated detection algorithm. A NLLJ profile is here solely defined by the characteristic wind speed maximum in the lowest 1500 m. The low-level stability is not examined on a case-by-case basis but a stable stratification near the surface can be assumed as the majority of profiles at Agadez and Tombouctou show an increase of the virtual potential temperature with height close to the surface.

A contingency table as in Table 3.2 is used for measuring the categorical forecast skill of ERA-Interim to produce NLLJ events. On the basis of the contingency table a range of different measures for the accuracy of the forecasts are defined (e.g. Jolliffe & Stephenson, 2003). The hit rate H is the ratio of events correctly forecasted to the sample size:

$$H = \frac{a+d}{n}, H \in [0,1]. \tag{3.1}$$

An *H* value of one indicates a perfect forecast. The probability of detection *POD* is the ratio of the events correctly forecasted to the number of events observed:

$$POD = \frac{a}{a+c}, POD \in [0,1]. \tag{3.2}$$

POD does not take false alarms into account, so that a system overpredicting events could have a high *POD*. Therefore the false alarm ratio *FAR* is also considered. *FAR* is defined as the fraction of false alarms to the number of forecasted events:

$$FAR = \frac{b}{a+b}, FAR \in [0,1] \tag{3.3}$$

In contrast to *POD* and *H*, a perfect forecast has a *FAR* of zero. The skill of the forecasts are measured with two more complex scores. The Hanssen and Kuipers discriminant *HK* is given as:

$$HK = \frac{ad-bc}{(a+c)(b+d)}, HK \in [-1,1]. \tag{3.4}$$

A random forecast has a *HK* of zero, a forecast worse than one created by random chance negative values and a perfect forecast one. This measure is independent of the frequency of events in the sense of having larger values for rare and frequent events. The Heidke score *HSS* determines the hit rate as a result of random chance:

$$HSS = \frac{(a+d) - \frac{1}{n}((a+b)(a+c)+(b+d)(c+d))}{n - \frac{1}{n}((a+b)(a+c)+(b+d)(c+d))}, HSS \in (-\infty,1]. \tag{3.5}$$

The interpretation of the value is similar to that of *HK*, where positive values indicate skill of the forecast (e.g. Jolliffe & Stephenson, 2003).

Since the radiosonde information gives a benchmark at single locations over rather short time periods only, an intercomparison of different re-analysis data is used for assessing possible uncertainties on the synoptic scale. The mean sea level pressure (MSLP), temperature and geopotential height at 850 hPa from the current re-analysis ERA-Interim (Dee *et al.*, 2011) and the previous product ERA-40 (Uppala *et al.*, 2005) from ECMWF, the Modern-Era Retrospective Analysis for Research and Applications (MERRA Rienecker *et al.*, 2011) from NASA and the re-analysis from NCEP/NCAR (Kalnay & Coauthors, 1996) are used for comparison of synoptic-scale conditions for case studies at Zouerat. The intercomparison of the MSLP is extended thereafter to a climatology intercomparison for the whole overlapping time period of 1979$-$2001 from ERA-Interim, ERA-40 and MERRA re-analysis. Systematic differences of pressure patterns alter the horizontal pressure gradient which changes the geostrophic wind as the first-order driver of wind speed. The 10m-wind speed from ERA-Interim re-analysis and short-range forecasts (12 hours) are also compared. Differences of the large-scale flow between short-range forecasts and re-analysis are expected to be small (Milton *et al.*, 2008).

The validation of the dust emission amount is not possible due to a lack of quantitative observations of the emitted mass. In order to assess the credibility of the climatology of dust emission in Fiedler *et al.* (2013a), two simulations with the dust emission model by Tegen *et al.* (2002) are used driven by near surface wind speeds from ERA-Interim forecasts and MERRA re-analysis, respectively. Here, soil moisture is not taken into account in order to investigate the pure effect of differences in the atmospheric dynamics on dust emission. This approach is justified since the comparison of the dust emission amount with ERA-Interim in this section compared to the experiment used in Fiedler *et al.* (2013a) shows that soil moisture does not suppress dust emission in most areas of North Africa. A suppressing effect of moisture is limited to areas at the margins of the Sahara (Chapter 1). Absolute differences between both dust emission fields are calculated as MERRA minus ERA-Interim. Model results from MERRA are interpolated to the coarser horizontal grid of ERA-Interim while conserving the total dust mass. The mean difference *DIFF* of meteorological fields are calculated for the two models $M_1(t,i)$ and $M_2(t,i)$ for all times $t = [1,T]$, $t \in N$ at each grid points $i = [1,N]$, $i \in N$ by

$$DIFF = \frac{1}{T}\sum_{t=1}^{T}\left[M_1\left(t,i\right) - M_2\left(t,i\right)\right]. \tag{3.6}$$

The chosen times t in the statistics are a selection of all times for annual statistics and subsets of different months for seasonal differences, respectively. Spatially averaged seasonal differences are also shown in this chapter. Root mean square differences are calculated as spatial average by

$$RMSD = \sqrt{\frac{1}{N}\sum_{i=1}^{N}\left[M_1\left(t,i\right) - M_2\left(t,i\right)\right]^2}. \tag{3.7}$$

and based on data subsets for different seasons. Spatial and temporal correlation coefficients are calculated with the routines *fldcor* and *timcor* from *CDO*[*], respectively. *Fldcor(t)* correlates two data sets $M_1(t,i)$ and $M_2(t,i)$ over all grid points i separately at each time t while *timcor(i)* correlates the data over all times t at each grid point i separately.

---

[*] Climate Data Operators, https://code.zmaw.de/projects/cdo as of April 2014

		Radiosonde	
		yes	no
ERA-Interim	yes	217	10 (13)
	no	9 (10)	6 (12)

Table 3.3: *Contingency table for NLLJ events at Agadez launched around mid-night between 20 January 2006 and 10 October 2006. Note that few nights are missing in the record period so that 242 profiles are used in total. Ten radiosonde profiles show some ambiguity, i.e. are not pronounced enough to derive a NLLJ speed, and are therefore included in the statistics shown in brackets.*

3.3 Case studies

3.3.1 Seasonal NLLJ characteristics

AMMA radiosondes at Agadez

[*] The representation of NLLJ characteristics in the course of the year is tested with quality controlled radiosondes launched during AMMA. The longest record of radiosonde profiles around 0 UTC is available at Agadez in Niger (16° N, 7° E, Figure 2.3) for January−October 2006. This data set is exploited for testing the forecast skill of ERA-Interim for producing NLLJ events. Table 3.3 shows the contingency table for Agadez. Some of the profiles show some ambiguity and are added to the statistics in brackets. The hit rate is 0.92 (0.91) for the short-range forecasts of NLLJ occurrence. HSS is 0.42 (0.47) indicating that the hit rate is not a result of random chance. The probability of detection is 0.96 (0.96) while the false alarm ratio is 0.04 (0.06). These values indicate a good forecast performance for NLLJ events. The HK score is 0.28 (0.44), also pointing to some skill for forecasting NLLJ events. The small sample size limited to one station and year, however, does not allow to generalize this finding for the forecasting skill for NLLJs by ERA-Interim. Especially taking into account that the occurrence of NLLJs is a frequent event in both the model and the observation, the statistical assessment of the forecasting skill is rather uncertain.

In addition to the occurrence frequency of NLLJs, their height and speed need to be evaluated due to the importance for dust emission (Fiedler *et al.*, 2013a). The analysis of these characteristics is undertaken at Agadez and extended to profiles measured at Tombouctou in Mali (16° N, 3° E, Figure 2.3) for August−October 2006

---

[*] Text passages and figures in the present section 3.3 are based on my publication "Climatology of nocturnal low-level jets over North Africa and implications for modeling mineral dust emission", 118, 12, 2013, pp. 6105−6108 in Journal of Geophysical Research - Atmosphere, Copyright 2014 John Wiley & Sons, Inc., This material is reproduced with permission of John Wiley & Sons, Inc (pers. comm. Paulette Goldweber, Wiley, 2014).

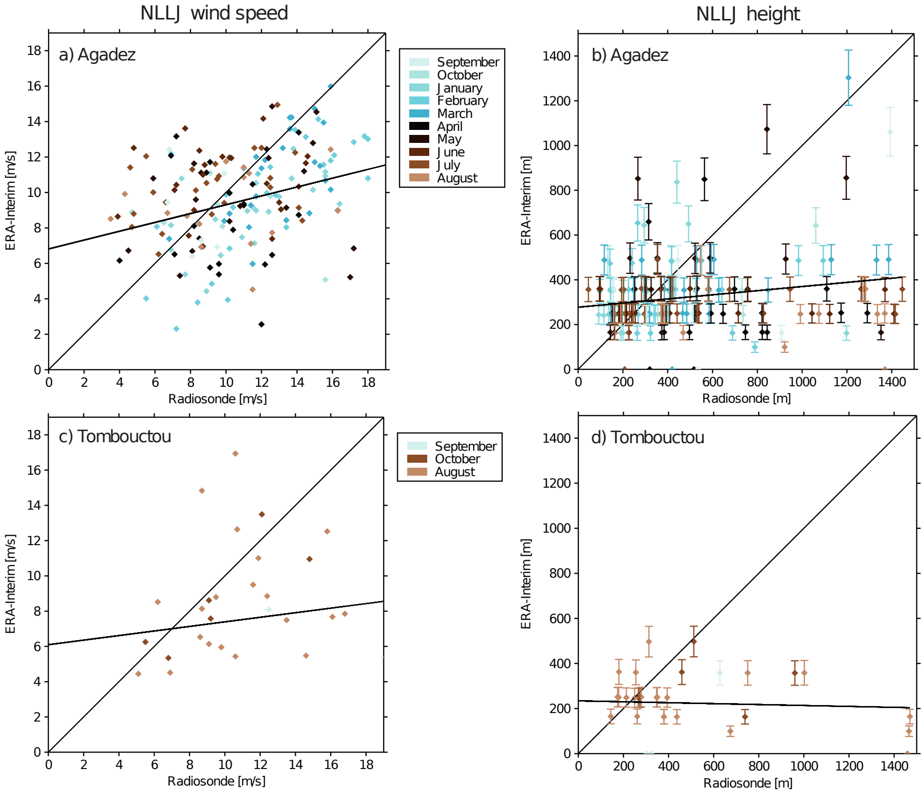

Figure 3.1: *Scatter plots of NLLJs in ERA-Interim in different months. Column on the left shows the NLLJ wind speed for (a) Agadez and (c) Tombouctou and on the right the NLLJ height with error bars indicating the calculated model layer thickness for (b) Agadez and (d) Tombouctou, based on mid-night data in 2006 from radiosondes launched during AMMA and ERA-Interim forecasts initialized at 12 UTC on the previous day. Figure and caption from Fiedler* et al. *(2013a) with permission of John Wiley & Sons, Inc.*

(Fiedler *et al.*, 2013a). Figure 3.1a–b shows the wind speed and height in the jet core from ERA-Interim forecasts against radiosonde measurements for the longer record at Agadez. The wind speed in the NLLJ core at Agadez shows a relatively large spread of data points with more points indicating an underestimation of the wind speed by the model (Figure 3.1a). Especially core wind speeds larger than 9 ms^{-1} tend to be too weak in ERA-Interim. Although the seasonal dependency is not strongly pronounced and the sample relatively small, NLLJ wind speeds in ERA-Interim tend to be more often underestimated than overestimated between September and March while the wind speed in the remaining year is roughly equally often too weak and too strong. The former time period coincides with the occurrence of a NLLJ hot spot around Agadez when northeasterly Harmattan winds prevail (Figure 2.2, Chapter 2).

The scatter diagram for the calculated height of NLLJs in Figure 3.1b shows that the expectation for typical heights below 1500 m is verified by the observations at Agadez. Data points for the height, however, show a rather large spread with a tendency for underestimation of the NLLJ height by ERA-Interim when the observed height exceeds 300 m. A changing performance skill by season can, herein, not be concluded. The validation of ERA-Interim at Agadez indicates that particularly strong and high NLLJs may be underrepresented in the model statistic although the data sample is small. These large wind speeds in the NLLJ core have been shown to be important for dust emission (Chapter 2).

AMMA radiosondes at Tombouctou

Other stations need to be analyzed to test whether the tendency for underestimation of NLLJ wind speed and height at Agadez by the model is an exception (Fiedler *et al.*, 2013a). AMMA radiosondes from Tombouctou enable comparison of the NLLJ characteristics at another location, although the time period is shorter (Fiedler *et al.*, 2013a). Figures 3.1c−d show scatter diagrams for the wind speed and height of NLLJ cores for August−October 2006, the first two months of which coincide with a NLLJ hot spot over the region (Figure 2.2). The spread of the data points is smaller than at Agadez, but this can be caused by the overall smaller number of data points at Tombouctou. Both the height and wind speed in the jet core tend to be underestimated by the model for values larger than 200 m and 7 ms^{-1}, respectively. The underestimation by the model at Tombouctou is in agreement with the findings for Agadez and suggests a rather systematic underestimation by the model. This finding is in agreement with the artificially increased mixing in the stable boundary layer of ERA-Interim (Sandu *et al.*, 2013). The resulting momentum loss at the NLLJ level reduces the wind speed in the core of the NLLJ.

3.3.2 The temporal development of NLLJs

The comparison of NLLJ characteristics from ERA-Interim against radiosondes launched during AMMA in 2006 suggest an underestimation when the jets reside higher than 200−300 m and are faster than 7−9 ms^{-1}. It can be speculated that the acceleration of the NLLJ in the course of the night is not well represented due to the artificially increased vertical mixing in the model (Chapter 2). In the following, this aspect is further analyzed with the diurnal cycle based on shorter but temporally higher resolved observation data sets. Such data is available at four different locations in West Africa during June of 2006 from AMMA (Fiedler *et al.*, 2013a) and 2011 from Fennec. During June the region is under the influence of the Saharan heat low where NLLJs form frequently (Chapter 2).

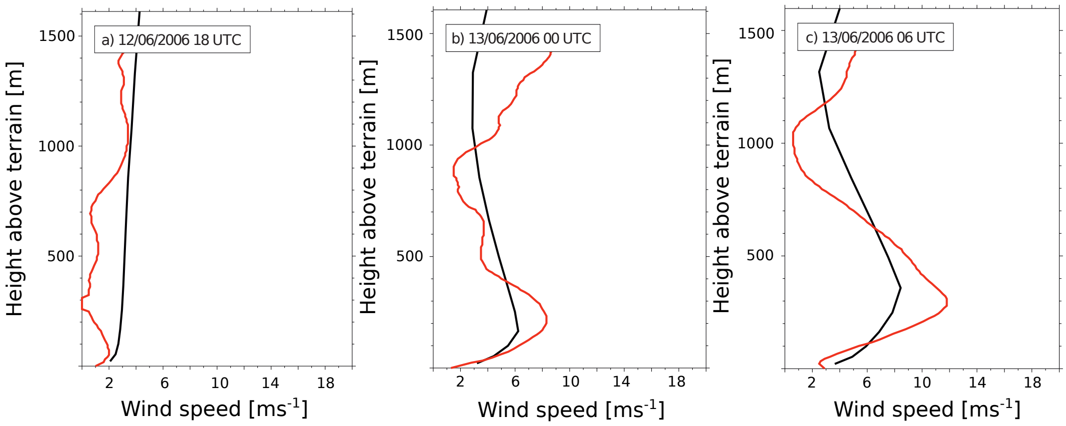

Figure 3.2: *Vertical profile of horizontal wind speed at Niamey. Shown are (a) 12 June 2006 at 18 UTC, (b) 13 June 2006 at 0 UTC and (c) 13 June 2006 at 6 UTC based on radiosondes (red) and ERA-Interim forecasts (black). Figure and caption from Fiedler* et al. *(2013a) with permission of John Wiley & Sons, Inc.*

AMMA radiosondes at Niamey and Agadez

Figure 3.2 shows the development of a NLLJ at Niamey, Niger (13° N, 2° E) for the night of 12–13 June 2006 that is well reproduced by ERA-Interim (Fiedler *et al.*, 2013a). The exact height and speed, however, is not accurately forecasted. While the observations suggest a wind speed of 11 ms^{-1} in the jet core at 6 UTC, the model has a core wind speed of only 8 ms^{-1}. This example also indicates that the difference between the radiosondes observation and the model grows in the course of the night. Whether this is created by chance or possibly a systematic behaviour is analyzed by comparing the height and speed of the NLLJ core at Niamey and Agadez during June 2006 next.

The scatter diagram of the NLLJ wind speeds and heights from the model against the radiosondes at Agadez and Niamey is shown in Figure 3.3 (Fiedler *et al.*, 2013a). Similar to earlier findings, the validation at Niamey also suggest that particularly high and fast NLLJs tend to be underestimated, namely above 400 m and 6 ms^{-1} (Figure 3.3c–d). Although the sampling size is not large enough for drawing a statistically robust conclusion, the data suggest that the underestimation of wind speed in the jet core is growing with time. This would imply that the necessary acceleration of the jet in the course of the night is not well simulated by ERA-Interim. However, the underestimation of the height of the NLLJ does not show a comparable temporal dependency. Also the scatter diagram for Agadez for June 2006, shown in Figure 3.3a–b, further supports that there is no clear diurnal dependency of the over- and underestimation. Nevertheless, the data at Agadez and Niamey support the finding that fast and high NLLJs are underestimated by ERA-Interim. The underestimation is likely caused by the overestimated vertical

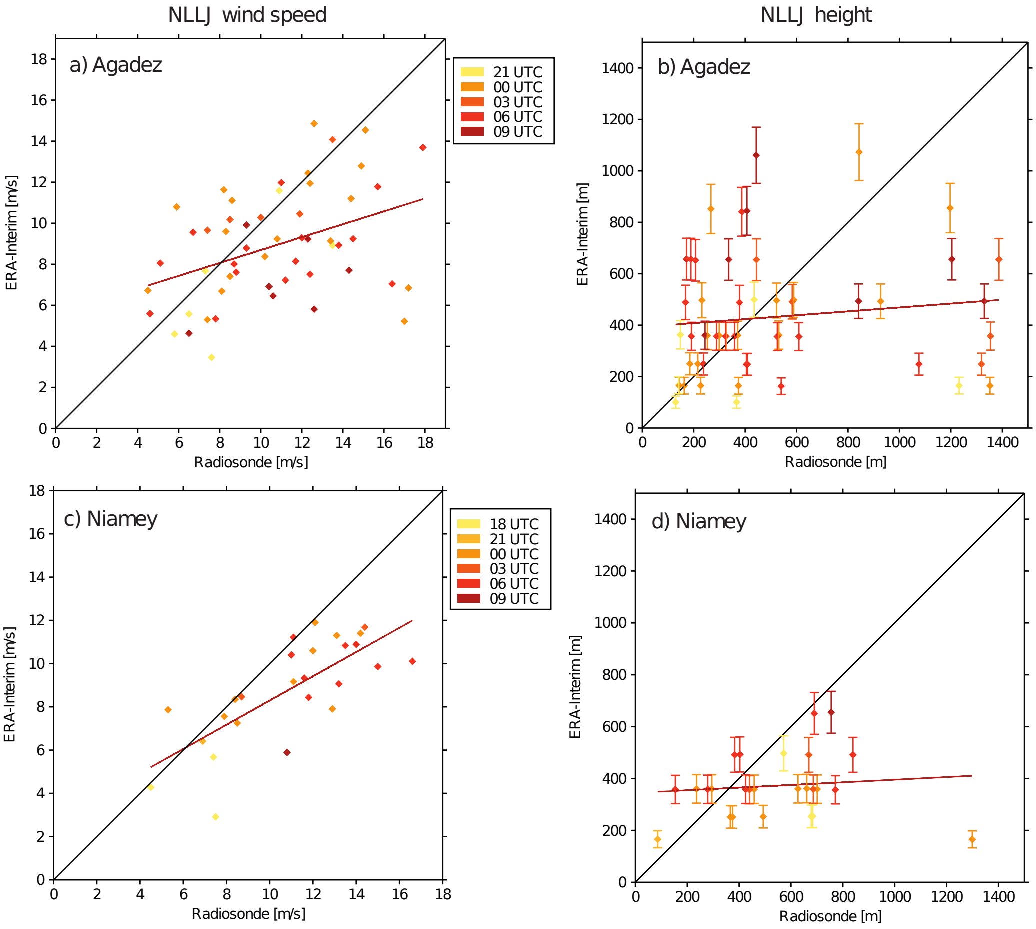

Figure 3.3: *Scatter plots of NLLJs in ERA-Interim for different times in June 2006. Column on the left shows the NLLJ wind speed for (a) Agadez and (c) Niamey and on the right the NLLJ height with error bars indicating the calculated model layer thickness for (b) Agadez and (d) Niamey, based on radiosondes launched during AMMA and ERA-Interim forecasts in June 2006. Figure and caption from Fiedler* et al. *(2013a) with permission of John Wiley & Sons, Inc.*

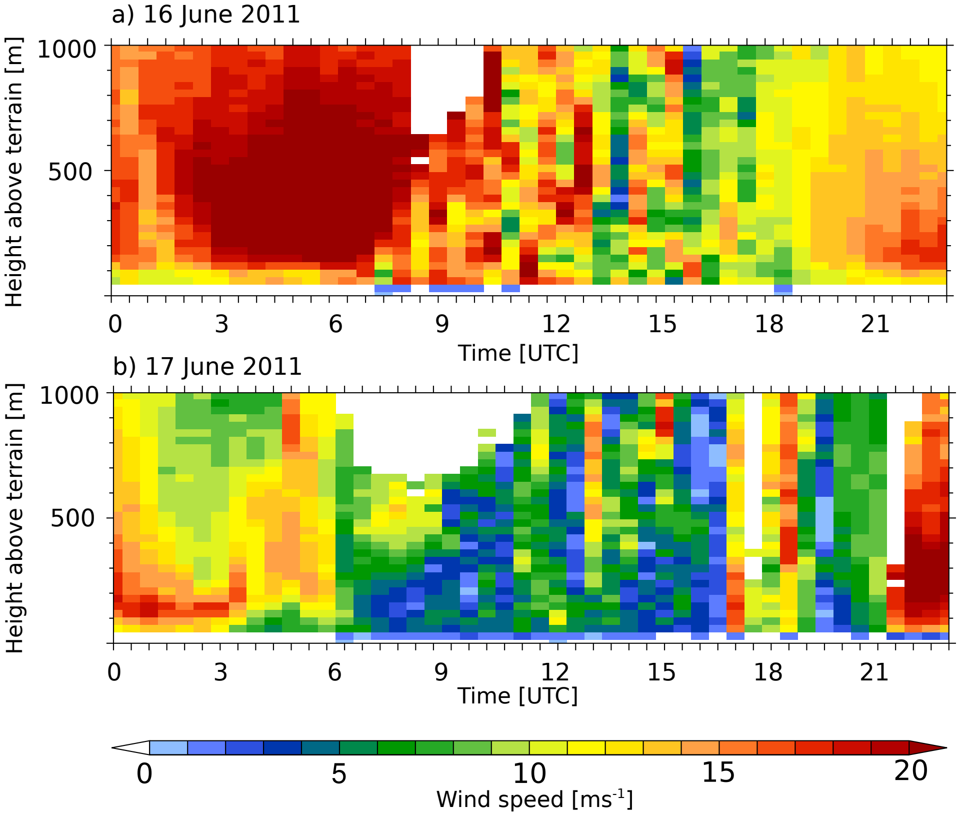

Figure 3.4: *LIDAR profiles at BBM. Shown is the time series of the vertical profile of the horizontal wind speed at BBM during Fennec at 16 and 17 June 2011 measured by LIDAR.*

mixing in stable boundary layers (Sandu *et al.*, 2013).

Fennec radiosondes at Bordj Badji Mokhtar

An interesting aspect influencing the development of NLLJs are haboobs that have been observed during the Fennec field campaign in 2011 (e.g. Marsham *et al.*, 2013b). Haboobs have been identified as a generating mechanism for NLLJs (Heinold *et al.*, 2013), but are currently not parameterised in ERA-Interim. Examples for the temporal development of NLLJ profiles during the occurrence of an haboob and one during the absence of haboobs are shown in Figure 3.4 and 3.5 from LIDAR and SODAR observations at BBM (21° N, O°, Figure 2.3), respectively. The morning of 16 June 2011 is free of the influence of haboobs. The wind speed profile from LIDAR shows a 700 m deep layer with wind speeds exceeding 20 ms^{-1} (Figure 3.4). This NLLJ mixes momentum towards the surface in the course of the night with near-surface winds around 9 ms^{-1} as seen by the SODAR instrument (Figure 3.5). Downward mixing is more efficient during the following morning and increases the wind speed near the ground between 6.30 and 9.30 UTC to values of $12-15\,\mathrm{ms}^{-1}$.

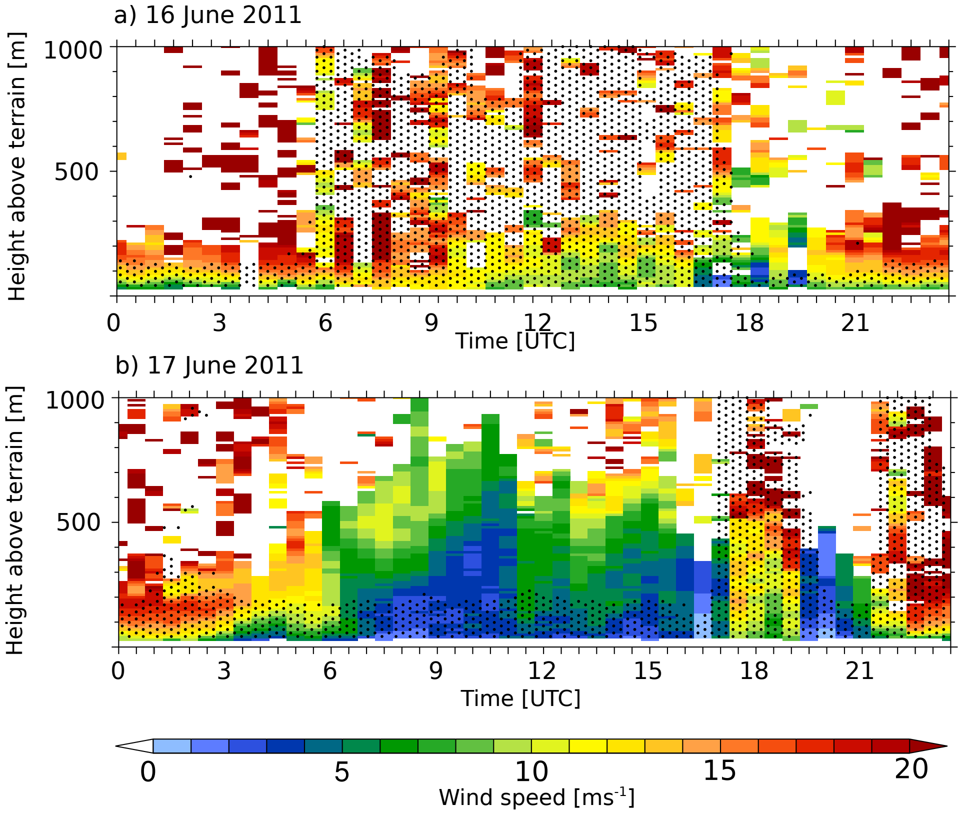

Figure 3.5: *As Figure 3.4 but measured by SODAR. Dotted areas indicating backscatter ratio larger than 15 that are assumed to give reliable results (pers. comm. J. Marsham and B. J. Brooks, University of Leeds, 2013).*

During the following night an haboob passes and influences the station observations. The associated NLLJ is weaker with a peak wind speed of 18−19 ms^{-1} (Figure 3.4). The downward mixing of the jet momentum to the surface is, however, more efficient than during the previous night. Nighttime wind speeds near the surface reach values around 11 ms^{-1} between 1 and 3 UTC (Figure 3.5). Since the vertical wind shear below the NLLJ is smaller in this night, the temperature inversion near the surface is likely weaker during the haboob leading to more mixing. The associated momentum loss weakens the NLLJ with wind speeds smaller than 14 ms^{-1} after 3 UTC. During the morning of 17 June 2011, a NLLJ with values smaller than 12 ms^{-1} remains that is associated with maximum near-surface wind speeds of around 9 ms^{-1} at 6 UTC.

The NLLJ wind speeds and heights from the radiosonde observations during the influence and absence of haboobs at BBM are shown in the scatter diagram in Figures 3.6a−b. Haboobs are a relatively frequent phenomenon at this station, the times of which have been provided by J. Marsham (University of Leeds, 2013) and are highlighted by colour in the figure. Three of four NLLJs coinciding with a haboob passage are too weak and occur at too high altitudes in ERA-Interim, suggesting that the model forecasts NLLJs when real conditions are determined by haboobs. NLLJs form after the occurrence of a haboob driven by the horizontal pressure gradient along the leading edge of an aged and lifted cold pool (Heinold *et al.*, 2013). This mechanism is not parameterised in ERA-Interim leading to a larger underestimation of the NLLJ height and speed than during times without haboob influence. This suggests that the horizontal pressure gradient associated to the aged cold pool is important for NLLJ formation, but is currently missing in atmospheric model with parameterised convection. Contrary, NLLJ speeds are better represented by ERA-Interim during the absence of haboobs, but the largest wind speeds above 10 ms^{-1} are still underestimated. In these cases the artificially increased vertical mixing in stable boundary layers likely causes the underestimation of NLLJ characteristics. This finding is in agreement with the validation results for the other stations discussed above.

Fennec radiosondes at Zouerat

Observations at Zouerat, Mauritania (22° N, 12° W, Figure 2.3) are used to test whether the evaluation of NLLJs at BBM are similar at this location. Figures 3.6c−d show the scatter diagrams of NLLJ characteristics at Zouerat which is less frequently influenced by haboobs. Todd *et al.* (2013) document the days when haboobs affect the measurements at the station that are highlighted in Figure 3.6c−d,

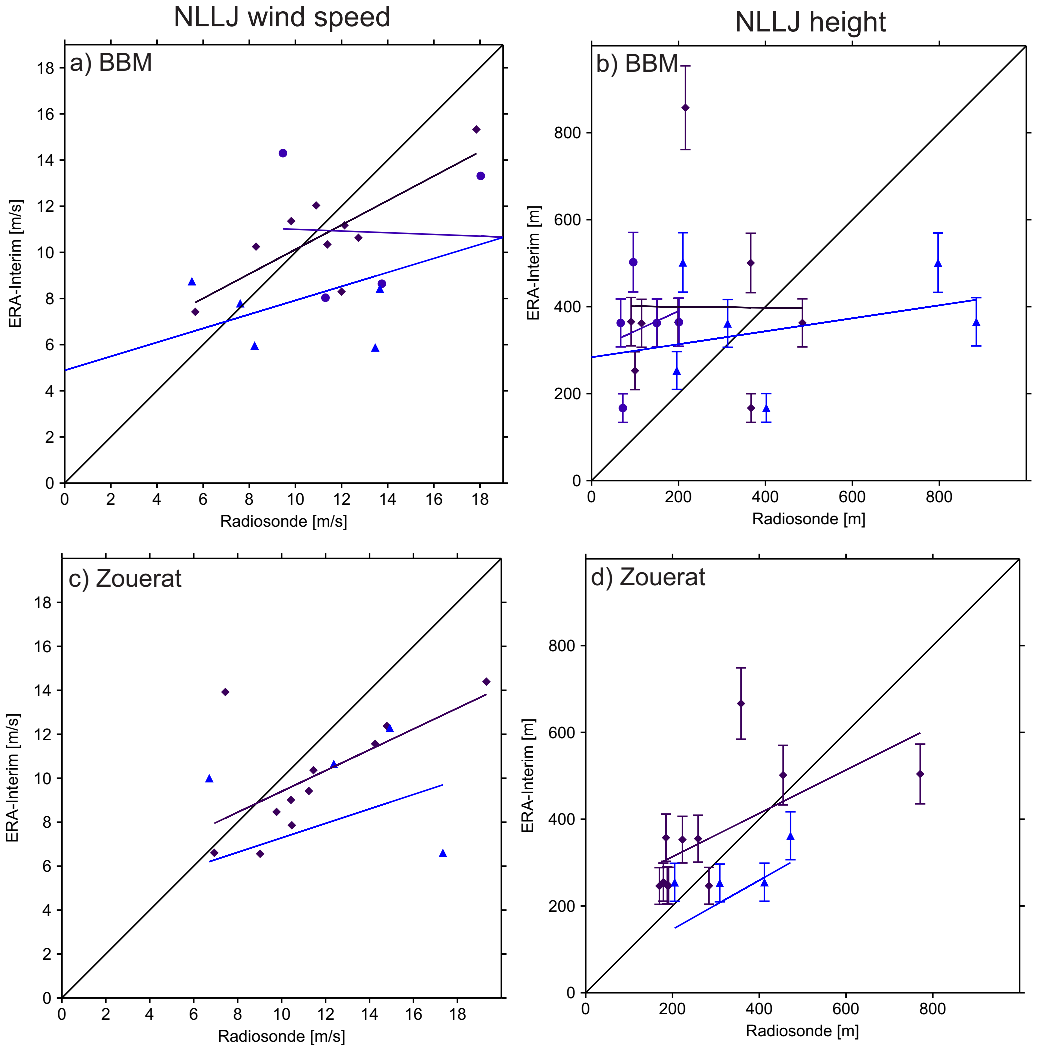

Figure 3.6: *Scatter plots of NLLJs in ERA-Interim in June 2011. Column on the left shows the NLLJ wind speed for (a) Bordj Badji Mokhtar and (c) Zouerat and on the right the NLLJ height with error bars indicating the calculated model layer thickness for (b) Bordj Badji Mokhtar and (d) Zouerat, based on data from mid-night in June 2011 from radiosondes launched during Fennec and ERA-Interim forecasts. Colour and shape indicate cases with simultaneously observed haboobs (Circle/Purple), after an observed haboob (Triangle/Blue) and free of haboob passage (Square/Black).*

but direct passages of haboobs are not observed. The speed of the NLLJs is mostly underestimated by ERA-Interim. As at BBM, the model performance for NLLJ simulations is better during the absence of haboob influence while the largest wind speeds are underestimated in agreement with the validation at the other stations.

Zouerat is located in one of the identified NLLJ occurrence hot spots (Figure 2.2) motivating more detailed evaluation of the model performance at this location in individual nights, here 9−11 June 2011. This weather episode is characterized by the change between two large-scale pressure patterns, namely the shift from the maritime phase to the heat low phase (Todd *et al.*, 2013). The maritime phase of the first night has an eastward displaced heat low visible in the geopotential height at 975 hPa in Figure 3.7a−b. The following night is characterized by the northwestward extension and deepening of the heat low that leads to a decrease of the geopotential height at 975 hPa over wide areas of West Africa (Figure 3.8a−b). The subsequent episode is the heat low phase where the flow is determined by an anomalously westward displaced Saharan heat low and the Azores High lying anomalously far west (Todd *et al.*, 2013). The strength of the heat low weakens in the course of both nights implying a slackening of the horizontal gradient of the geopotential height (Figures 3.7a−b and 3.8a−b). This phenomenon is well known for heat lows from idealized modelling (Racz & Smith, 1999) showing a connection to surface cooling at night. This cooling is especially strong in both nights at Zouerat due to a relatively large outgoing long-wave radiation flux that is enabled by cloud free conditions and low aerosol concentrations, seen in the SEVIRI product (Figure 3.7d and 3.8d). The associated development of surface temperature inversions (Todd *et al.*, 2013) weakens the effect of surface friction on the air flow as an ideal pre-requisite for the formation of NLLJs.

Figure 3.7c shows the NLLJ development at Zouerat for the first night, 9−10 June 2011. ERA-Interim forecasts a NLLJ that gradually accelerates at a constant height of 350 m to a maximum of 10 ms^{-1} at 6 UTC. The radiosonde, however, shows a stronger NLLJ that occurs earlier in the night and resides in lower levels, namely a core wind speed of 11 ms^{-1} at 200 m a.g.l. at 0 UTC. At 6 UTC, this NLLJ is largely eroded with a core wind speed of 7 ms^{-1} (Figure 3.7c). It is possible that the NLLJ continued accelerating after mid-night leading to a larger wind speed in its core before becoming dynamically unstable and transferring momentum to the ground that is not captured by the observations. ERA-Interim therefore underestimates the core wind speed by at least 1 ms^{-1} and overestimates the height of the jet by 150 m in the maritime phase, although the uncertainty from the model layer thickness needs to be taken into account. The resulting vertical wind shear at 6 UTC between the jet level and the surface is underestimated by a factor of two.

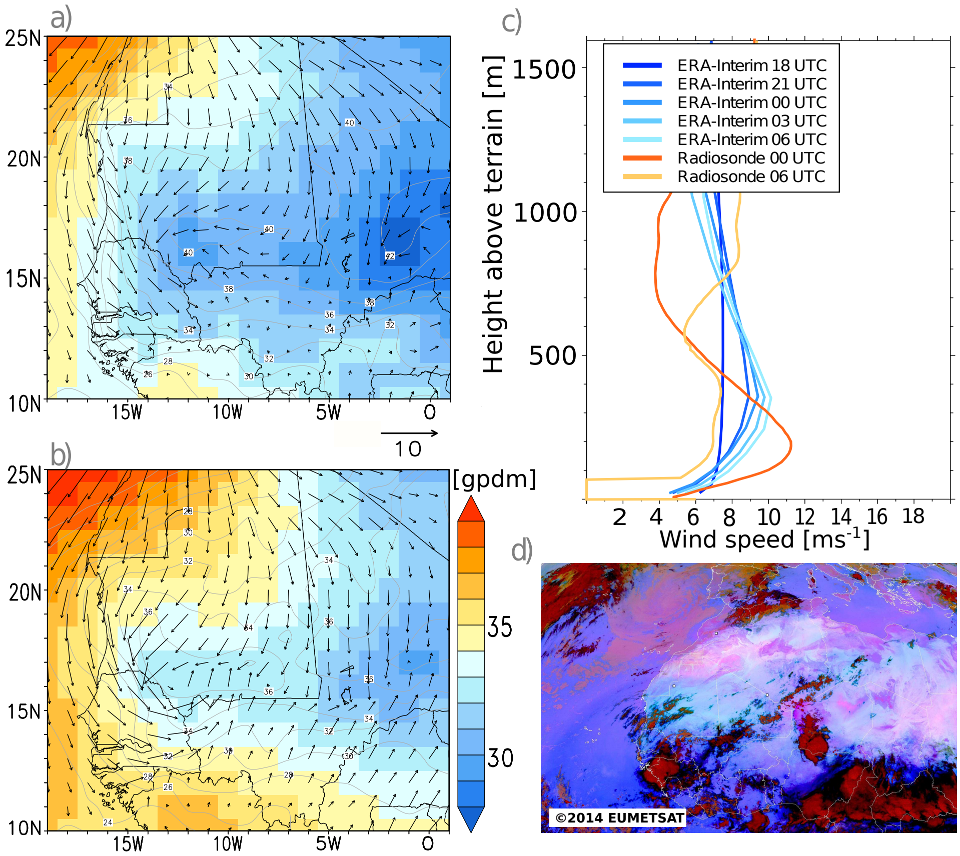

Figure 3.7: *Meteorological condition for 9–10 June 2011 at Zouerat (22° N, 12° W). Geopotential height (shaded) and wind vectors at 975 hPa for (a) 09 June 2011 at 18 UTC, (b) 10 June 2011 at 0 UTC from ERA-Interim forecasts and (c) vertical profile of the wind speed based on Fennec radiosonde and ERA-Interim forecast for different times. The forecasts are initialized for 09 June 2011 at 12 UTC. (d) MSG SEVIRI satellite observation for 10 June 2011 at 0 UTC.*

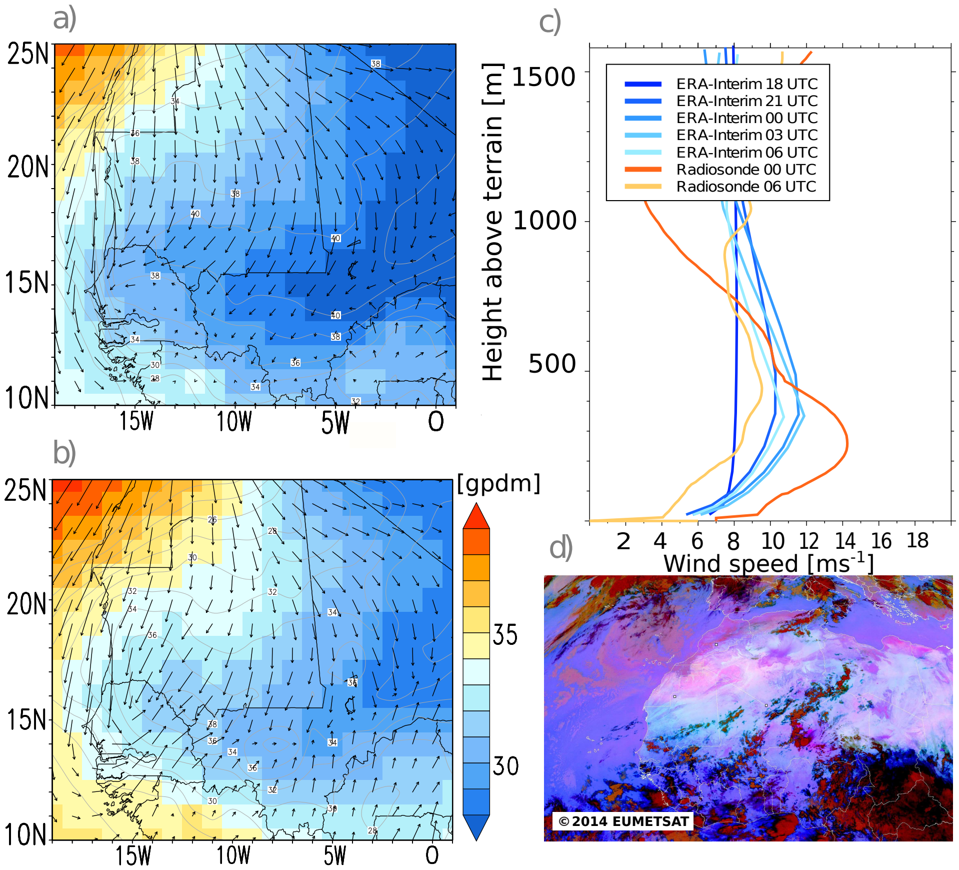

Figure 3.8: *As Figure 3.7 but for 10–11 June 2011.*

The observed NLLJ in the following night, 11 June 2011, is stronger with 14 $\mathrm{ms^{-1}}$ at 0 UTC (Figure 3.8c). The most likely reason is the increased horizontal pressure gradient compared to the previous night. ERA-Interim forecasts a NLLJ, but underestimates the maximum wind speed by around 3 $\mathrm{ms^{-1}}$ at both 0 UTC and 3 UTC. The height of the modelled NLLJ is the same as in the previous night but is now closer to the observed value of 250 m a.g.l. at 0 UTC and lies within the uncertainty of the vertical resolution of the model. Interestingly, the simulated jet speed is overestimated but at a similar height at 6 UTC. As in the previous night the overestimation is 1 $\mathrm{ms^{-1}}$ at 6 UTC, which implies a larger vertical wind shear in the model at this time. The overestimation of the core wind speed and the associated vertical wind shear at 6 UTC is surprising as the artificially increased vertical mixing implies an underestimation of the wind speed during the following morning. A possible reason is that the momentum from the NLLJ has not yet been mixed downwards in the model but has been eroded in reality. Simulating the transition between the two large scale pressure patterns in this night may cause uncertainty so that another case during the well-established heat low phase is studied in the following.

The NLLJ at Zouerat of the night from 15 to 16 June 2011 occurs under prevailing northerlies (Figure 3.9). Relatively strong cooling due to the absence of clouds and relatively low aerosol optical depth (Todd *et al.*, 2013) as well as a relatively large horizontal gradient in the geopotential height over West Africa enable the development of a strong NLLJ. The jet reaches a core wind speed of 19 $\mathrm{ms^{-1}}$ at 450 m a.g.l. at 0 UTC and 20 $\mathrm{ms^{-1}}$ at 550 m a.g.l. at 6 UTC (Figure 3.9c). ERA-Interim reproduces the nighttime maximum of 19 $\mathrm{ms^{-1}}$ at 500 m a.g.l. but later at 3 UTC than observed which is in agreement with the artificially increased mixing slowing the acceleration. The core wind speed at 6 UTC is underestimated with 16 $\mathrm{ms^{-1}}$. It is plausible that a large vertical wind shear along with the increased vertical mixing in the model leads to an earlier momentum transfer to the surface than would be observed. Whether the jet is underestimated at the time of re-coupling in the morning and therefore provides less momentum for downward mixing and dust emission, can not be concluded with the coarse temporal resolution.

NLLJ wind speeds from the radiosondes at 0 UTC are not reproduced by ERA-Interim at any of the available times during two out of three nights. The core height of NLLJs tends to be overestimated and constant during the night although the height differences are similar to the vertical resolution of the model. The artificially increased vertical mixing during stable stratification in ERA-Interim (Sandu *et al.*, 2013) is likely an important cause of this mismatch. Further improvement of the representation of stable boundary layers is subject of ongoing research. In addition to the parametrization of the stable boundary layer, the large-scale conditions of

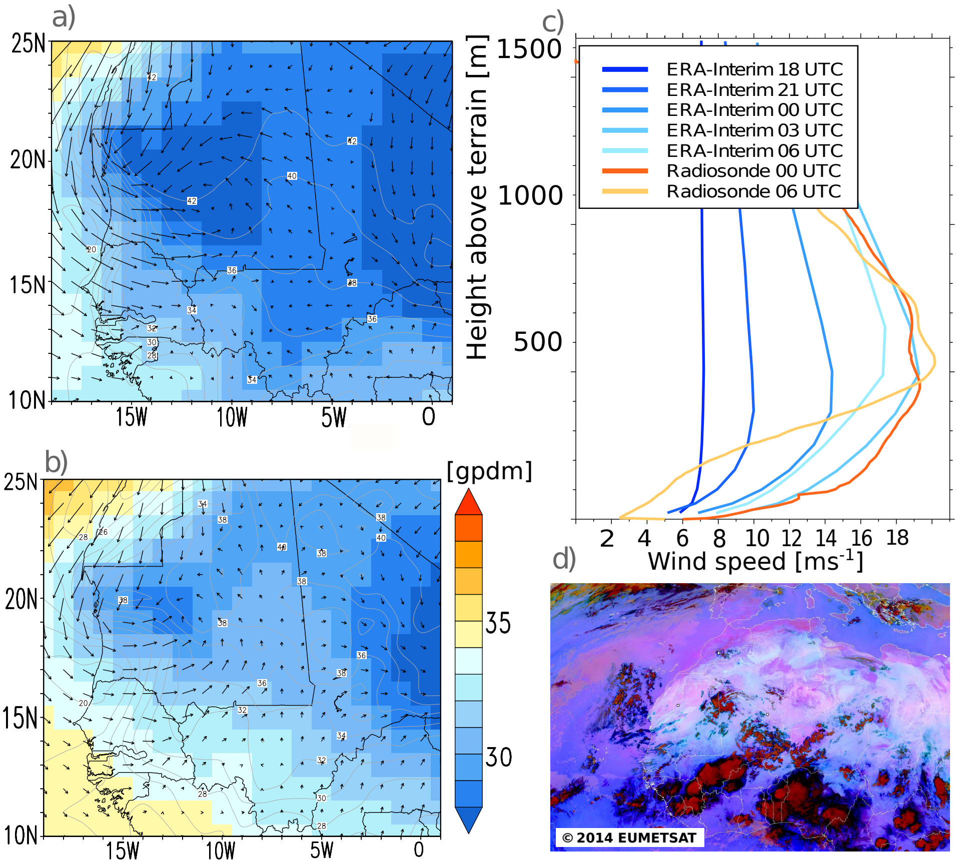

Figure 3.9: *As Figure 3.7 but for 15–16 June 2011.*

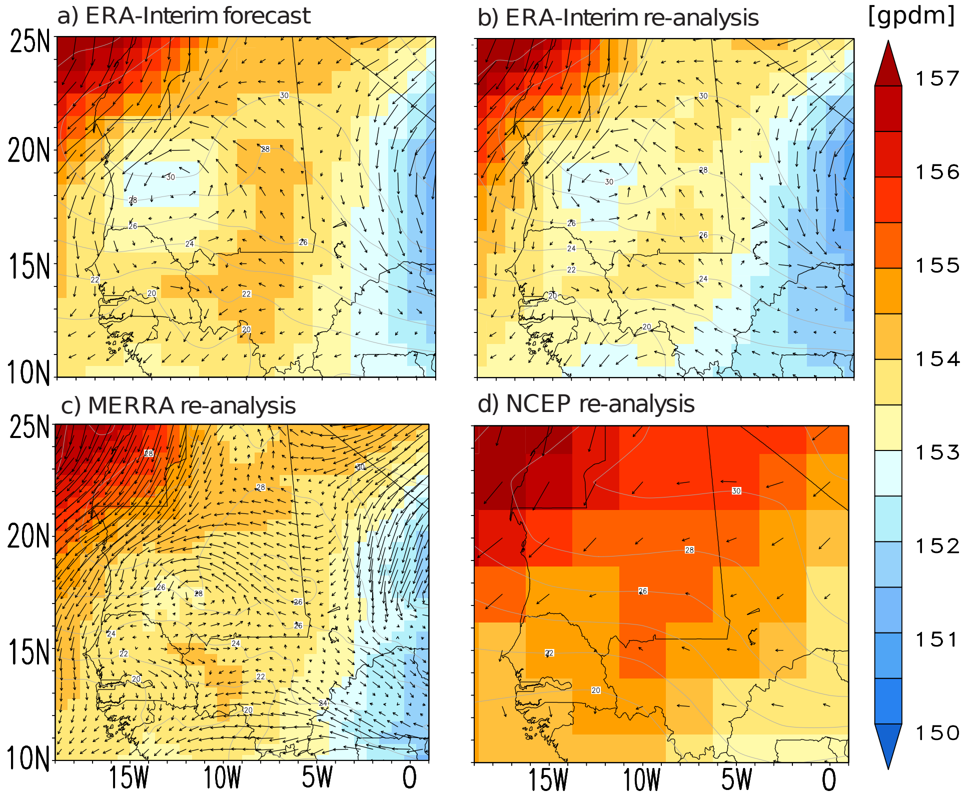

Figure 3.10: *Synoptic-scale condition for 16 June 2011 around Zouerat (22° N, 12° W). Shown are the geopotential height (shaded), air temperature (contours) and wind vectors at 850 hPa for 16 June 2011 at 0 UTC from (a) ERA-Interim 12 hour forecasts, (b) ERA-Interim re-analysis, (c) MERRA re-analysis and (d) NCEP re-analysis.*

ERA-Interim forecasts could further contribute to the uncertainty that is analyzed at Zouerat next.

Synoptic-scale conditions at Zouerat

The case studies at Zouerat illustrate that the NLLJ wind speed is faster during the presence of a stronger geostrophic wind. Since the horizontal gradient of the geopotential height is a strong control of the wind, any uncertainty in the synoptic-scale conditions in ERA-Interim may contribute to a mismatch of NLLJs compared to observations. Different patterns of the geopotential height and the MSLP in different re-analysis products give a rough estimate of regions where the wind speed has a relatively large uncertainty.

Figure 3.10 shows the geopotential height at 850 hPa for the night of 15–16 June 2011 from ERA-Interim forecasts and re-analysis, as well as MERRA and NCEP re-analysis. The forecasts from ERA-Interim is closest to the re-analysis product from the same numerical model at 0 UTC, but the geopotential height is consistently lower by 1 gpdm in the analysis. Comparing ERA-Interim to the re-analysis products of MERRA and NCEP, shown in Figure 3.10c–d, reveals that

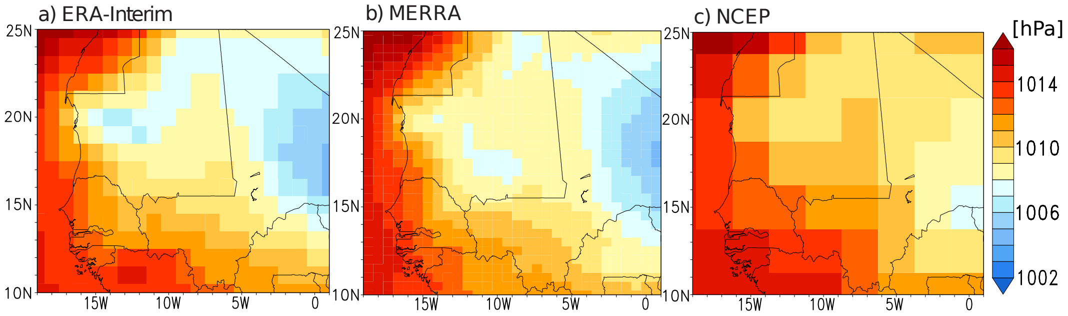

Figure 3.11: *MSLP for 16 June 2011 around Zouerat (22° N, 12° W). Shown are values at 0 UTC from (a) ERA-Interim re-analysis, (b) MERRA re-analysis and (c) NCEP re-analysis.*

the general pattern of the geopotential height and the air temperature at 850 hPa in ERA-Interim agree reasonably well with MERRA re-analysis (Figures 3.10a–c), which has a higher spatial resolution (Decker *et al.*, 2012). ERA-Interim, however, tends to have a lower geopotential height and higher temperatures at 850 hPa. The MSLP from ERA-Interim and MERRA are on the same order of magnitude (Figures 3.11), but ERA-Interim produces a deeper pressure at sea level than both MERRA and NCEP. NCEP shows the largest deviations for all three variables from ERA-Interim and MERRA products, which is at least partly related to the coarser horizontal resolution. Validating the two nights for 9–11 June 2011 leads to similar conclusions. These differences motivate a climatological analysis of the differences in the synoptic-scale conditions between ERA-Interim and MERRA which is presented in Section 3.4.1.

3.3.3 NLLJs and dust emission in the Bodélé Depression

One of the hot spots for dust emission and the occurrence of NLLJs is the Bodélé Depression in Chad. During the BoDEX field campaign (Washington *et al.*, 2006) pilot balloon (PIBAL) measurements at Chicha (16.9° N, 18.5° E, Figure 2.3) document the vertical profile of wind speed every three hours for the period of 28 February to 13 March 2005. Although the applied single theodolite technique for tracking the balloon has uncertainties, the unique data from PIBAL are nevertheless a useful benchmark for evaluating NLLJs in ERA-Interim over this area.

Wind speed profile

Figure 3.12a shows the vertical profile of horizontal wind speed in ERA-Interim during BoDEx. The time series clearly indicates the presence of a NLLJ in every night, although the NLLJs on 1–2 March 2005 and 8–9 March 2005 are rather weak with less than 10 $\mathrm{ms^{-1}}$ in the NLLJ core. The core wind speed of the NLLJs in the other nights exceed 11 $\mathrm{ms^{-1}}$. The development of the strongest NLLJ in this

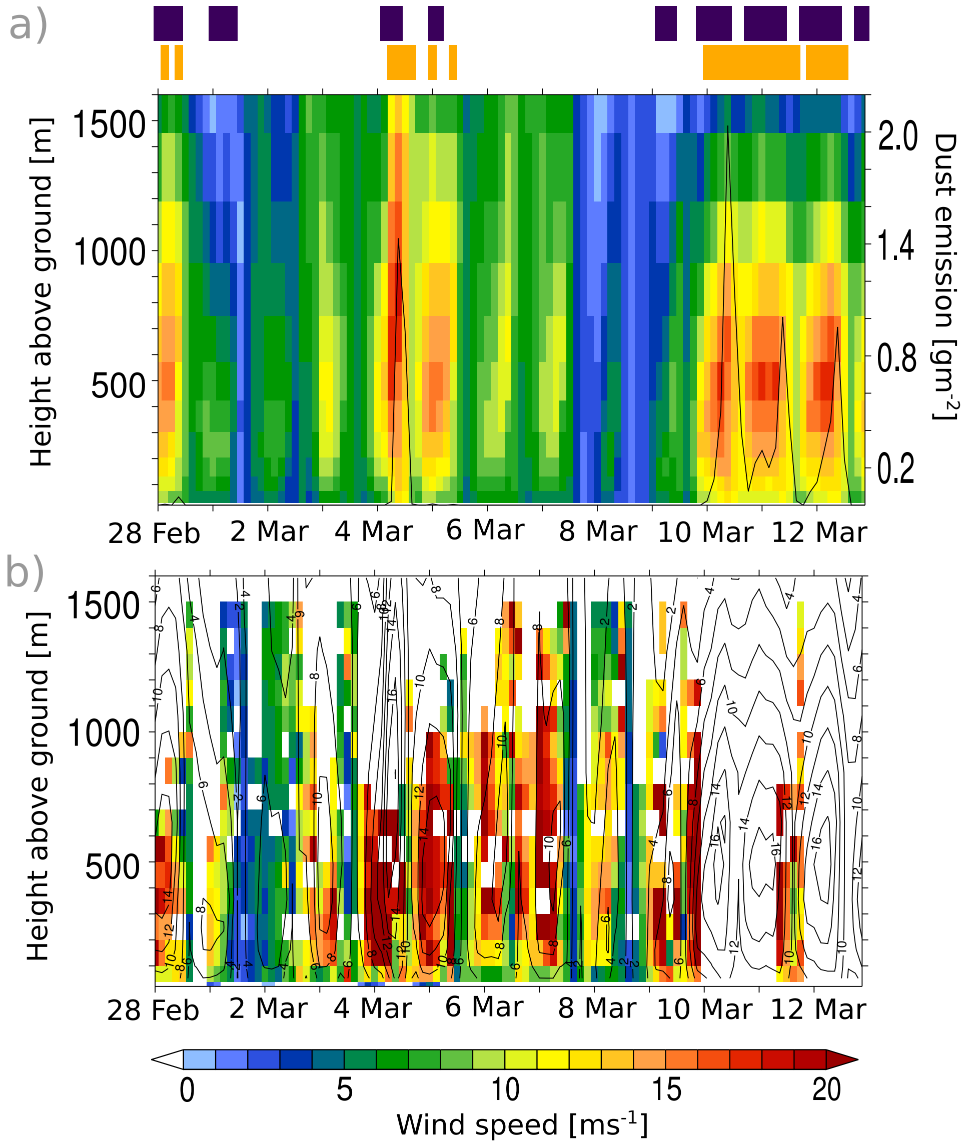

Figure 3.12: *Time series for the low-level profile of horizontal wind speed at Chicha for 28 February to 13 March 2005. (a) Horizontal wind speed (shaded) and time of automatic NLLJ detection (black bar) from ERA-Interim forecasts. Dust emission flux (contour) and time of DSA (orange bar) based on the dust model by Tegen et al (2002) and ERA-Interim forecasts, Figure and caption from Fiedler* et al. *(2013a) with permission of John Willey & Sons, Inc. (b) Horizontal wind speed from the pilot balloon observation from the BoDEX field campaign (shaded, data provided by M. Todd) and ERA-Interim forecasts (contours).*

time period was simulated for the 4 March 2005 with a core wind speed of 19 ms^{-1}. The same jet is a good example for the downward mixing of momentum from the jet level to the surface. The associated increase in near-surface wind speed from 6 ms^{-1} at night to 12 ms^{-1} during the morning of 4 March 2005 is apparent in Figure 3.12a.

The vertical structure of wind speed from ERA-Interim is remarkably similar to the profile observed with PIBAL shown in Figure 3.12b (Fiedler *et al.*, 2013a). The mean maximum wind speed is 17 ms^{-1} with a mean jet core height at roughly 400 m from PIBAL (Todd *et al.*, 2008). Qualitatively, the typical height of NLLJs is captured by ERA-Interim, although the vertical resolutions of the observation and the model do not enable a comparison of exact NLLJ heights. Maximum core wind speeds from PIBAL are 22 ms^{-1} for 6−7 March 2005, more than 25 ms^{-1} for 4 March and 9 March 2005 and potentially even larger values for 10−12 March 2005, when a strong dust storm prevented all measurements (Todd *et al.*, 2008). Compared to these values, the NLLJ core wind speed in ERA-Interim is systematically smaller, e.g. the maximum core wind speed in ERA-Interim is 19 ms^{-1} whereas PIBAL shows values exceeding 25 ms^{-1}. This underestimation of the wind speed by the model is in agreement with the result from Todd *et al.* (2008) for the regional model MM5. The MM5 experiment setup with the closest match to observed conditions underestimated the mean maximum wind speed in the jet at 6 UTC by roughly 15 %. ERA-Interim underestimates the NLLJ core wind speed by 24−50 % compared to PIBAL data at Chicha depending on the day. This larger underestimation by ERA-Interim relative to observations than the regional MM5 might be explained by different factors including the coarser resolution of ERA-Interim affecting the height of mountains, differences of physical parametrization schemes and the lack of tuning of ERA-Interim to match the regional conditions of the Bodélé Depression.

Dust emission

The offline dust emission model by Tegen *et al.* (2002) driven by ERA-Interim wind speed simulates dust emission on about half of the days in the BoDEx observation period (Fiedler *et al.*, 2013a). This occurrence frequency of dust emission events in the Bodélé Depression is in good agreement with the BoDEx field observations for 28 February until 4 March 2005 (Todd *et al.*, 2008) and the satellite observation for December 2003 to May 2004 (Koren *et al.*, 2006). These dust emissions occur mostly during the mid-morning in ERA-Interim and the observations by Todd *et al.* (2008) and Koren *et al.* (2006) which points to downward mixing of NLLJ momentum to the surface. In the first half of the BoDEx period, 0.5 $\mathrm{gm^{-2}}$ dust is emitted in the morning of the 28 February 2005 and 1.4 $\mathrm{gm^{-2}}$ of the 4 March 2005 based on the offline dust emission model driven with ERA-Interim wind speeds. These dust emissions occur simultaneously with NLLJs that are well detected by the automatic algorithm (Chapter 2), the occurrence of which are indicated by yellow and black bars in Figure 3.12a, respectively.

Particularly large amounts of dust aerosol are emitted during the mornings of and after 10 March 2005, when the rapid formation of a post frontal ridge over North Africa occurs (Todd *et al.*, 2008). The relatively strong horizontal pressure gradient between this Libyan high and the low pressure over the continent drives north-easterly trade winds over Chicha. The low-level wind speed is reinforced by channelling between the Tibesti and Ennedi Mountains. In combination with weakened frictional effects at night NLLJs form over the Bodélé Depression. ERA-Interim clearly simulates these NLLJs that are successfully identified by the automatic detection algorithm for 10−12 March 2005 (Figure 3.12a). These NLLJs are not documented in the PIBAL observation due to strong near-surface winds causing dust storms that prevented all measurements (Todd *et al.*, 2008). Such dust stroms associated with prevailing north-easterly winds are typical for the area as suggested for the entire of the winter-spring period of 2003−2004 by Koren *et al.* (2006). In contrast, the periods 1−3 March 2005 and 6−9 March 2005 are simulated as dust free in agreement with the observations by Todd *et al.* (2008). The study by Todd *et al.* (2008) links the lack of DSAs on these days to low pressure systems over the Mediterranean basin, disturbing the formation of strong north-easterly Harmattan winds that prevail during the remaining period (Todd *et al.*, 2008).

3.3.4 Discussion

The validation of NLLJs in ERA-Interim with radiosondes from field campaigns at different locations and seasons in North Africa suggests that the highest core wind speeds are underestimated by ERA-Interim. This is likely caused by the artificially increased mixing under stable stratification in the model. Sandu *et al.* (2013) show an underestimation of the strengths of inversions and NLLJ wind speeds due to tuning of the physical parameterisation scheme of ERA-Interim under European conditions. Moreover, the findings here are in agreement with underestimated NLLJ wind speeds in the operational analysis from ECMWF over Kansas for 23−26 October 1999 during the “Cooperative Atmosphere-Surface Exchange Study” (CASES-99, Steeneveld *et al.*, 2008). Analysis of the diurnal development of NLLJs in ERA-Interim and observations over North Africa points to the underestimation occurring throughout the night. This finding implies that nocturnal turbulence in ERA-Interim and, therefore, the calculated dust emission with the offline dust model by Tegen *et al.* (2002) might be overestimated at night. The diurnal cycle could be altered such that the mineral dust emission and the NLLJ contribution in Chapter 2 are underestimated during the mid-morning due to less available NLLJ momentum at sunrise.

Besides the vertical mixing of momentum weakening the acceleration of NLLJs in ERA-Interim, NLLJs may form in response to the presence of an aged and lifted cold pool (Heinold *et al.*, 2013). The missing parametrization of haboobs in ERA-Interim has been shown to cause an underestimation of the NLLJ wind speed when an haboob is observed at the same time as the NLLJ or earlier in the same night. Both further improvements of the parameterisation for stable stratification as well as the development of an haboob parameterisation are subject of ongoing research.

Quantifying the net effect of misrepresented NLLJ characteristics on dust emission is highly uncertain due to the parameterisation of dust emission as a non-linear function of the near-surface wind speed. A validation of NLLJs in ERA-Interim with a long-term observational data set over North Africa would be necessary to determine the uncertainty accurately, but such data are not available. The effect of nocturnal turbulence associated with NLLJs on the diurnal cycle of dust emission north of 25° N is, however, expected to be negligible in most months and source areas as other meteorological processes appear to generate dust-emitting peak winds more efficiently (Chapter 2) and will be addressed in Chapter 4. The time series of dust emission from the BoDEx field campaign, in the Bodélé Depression as a key region for simulating dust emission, is qualitatively captured by the dust emission model driven by near-surface winds from ERA-Interim. Further evaluation of the dust emission climatology derived with the model by Tegen *et al.* (2002) driven by ERA-Interim data will be performed in the following section.

Another aspect potentially causing a mismatch of observed and simulated NLLJ wind speeds is the synoptic-scale pressure gradient as a first-order driver of wind. The comparison of ERA-Interim forecasts with ERA-Interim re-analysis products for three case studies suggest that both are in reasonable agreement with differences on the order of +/-1 gpdm in single nights of June 2011 over West Africa. ERA-Interim is also similar to the higher resolved MERRA re-analysis but substantially different to NCEP. The investigation of the synoptic-scale differences shall be extended to continental and climatological scales for a more systematic assessment of re-analysis uncertainty for the near-surface wind speed in the following.

3.4 Climatology

3.4.1 Mean sea level pressure

Re-analysed MSLP from ERA-Interim, ERA-40 and MERRA are intercompared for the overlapping time period 1980−2001 to estimate the re-analysis uncertainty in the synoptic-scale conditions. The mean differences of MSLP between ERA-Interim and ERA-40 are on the order of +/- 1 hPa. The MSLP from MERRA, however, differs more from ERA-Interim with distinct temporal and spatial characteristics. These differences between ERA-Interim and the higher-resolved MERRA re-analysis are the focus in the following.

Figure 3.13a−b shows the MSLP of ERA-Interim and MERRA re-analysis for winter, respectively. The mean pressure pattern is dominated by the heat low between the equator and 10° N and a ridge over North Africa between 25° N and 35° N (Figure 3.13a). The horizontal pressure gradient in between drives the north-easterly Harmattan winds that prevail in this season (Chapter 1). Both products represent the general pattern in a similar way. However, the low pressure east of 20° E and South of 10° N is deeper in MERRA than in ERA-Interim at 18 UTC (Figure 3.13c). One part of this difference coincides with the Ethiopian Highlands and may reflect differences in the interpolation technique applied by the forecast centres to derive the MSLP, but the pattern grows in terms of spatial extent as the night progresses pointing to a systematic difference. At 0 UTC, MERRA simulates a deeper pressure of around 3 hPa east of 10° E and south of 15° N (Figure 3.13d). Areas further north away from mountains show no difference between both re-analysis products, which implies a stronger pressure gradient force exerted on the atmospheric flow over northern Sudan and southern Libya at mid-night in MERRA. This difference weakens slightly at 6 UTC (Figure 3.13e), but is even larger at 12 UTC (Figure 3.13f). At this time, pressure differences of 1.5−3 hPa are found across the entire of North Africa which can be linked to a different development of the daytime boundary layer in the models. The margin of these differences is pushed to areas over North Algeria, Libya and Sudan suggesting a smaller geostrophic wind in ERA-Interim than in MERRA. The temporal correlation of mostly 0.5 indicates little temporal coherence of meteorological conditions in both models in winter. This may be caused by temporally different development of disturbances in the re-analysis. It is, however, unclear which of the re-analysis products is closer to real conditions due to the lack of long-term observation records over most of the continent.

In March−May the heat low is deeper and lies further north compared to winter in both re-analysis products. MSLP values smaller than 1012 hPa are now found as far north as 25° N compared to 15° N in winter. The mean centre of high pressure

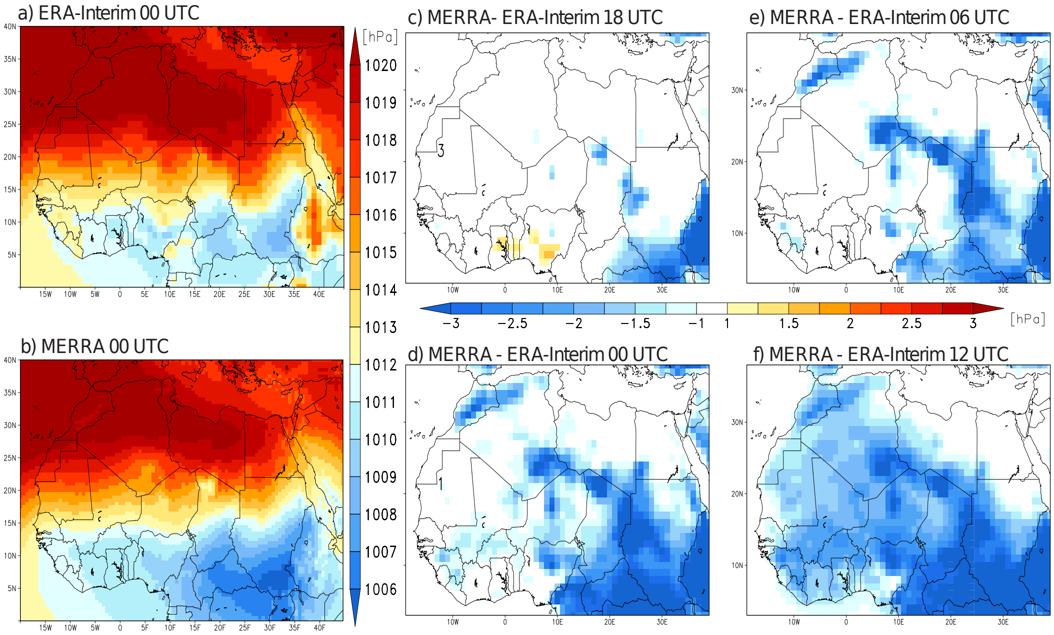

Figure 3.13: *Seasonal MSLP for December–February. Shows are (a) ERA-Interim re-analysis and (b) MERRA re-analysis at 0 UTC for 1980–2001 and mean difference of the MSLP of MERRA relative to ERA-Interim for (c) 18 UTC, (d) 0 UTC, (e) 6 UTC and (f) 12 UTC.*

is shifted to the Mediterranean basin causing an increased pressure gradient over wide areas of Algeria, Libya and Egypt that drives north-easterly Harmattan winds. The pattern of springtime differences between the two re-analysis data sets is comparable to winter differences. The Harmattan winds may therefore be weaker in ERA-Interim than in MERRA over the same areas as during winter. Also the mean pressure patterns and differences for September to November are similar to spring but with a weaker low and stronger high over the Mediterranean Sea.

Summertime conditions in North Africa are characterized by the Saharan heat low over West Africa seen at a mean location of 5–0° W and 22.5° N in Figure 3.14a–b. The Saharan heat low is deepest at 18 UTC with a core pressure below 1006 hPa in both MERRA and ERA-Interim re-analysis. Low MSLPs also dominate further to the east with a trough axis extending from the Arabian Peninsula over the Red Sea towards Sudan. The MSLP pattern is influenced by the complex terrain modifying the atmospheric flow through interaction with mountain barriers. The differences between MERRA and ERA-Interim are again similar to the differences described for winter (Figure 3.14c–f). The implications, however, are different due to the heat low position. The deeper core pressure south of 20° N and east of 10° E at night, results in a weaker horizontal pressure gradient force over parts of Sudan and Chad in MERRA compared to ERA-Interim. Contrary to this weaker synoptic-scale driver at the south-eastern margins of the heat low at night, a larger

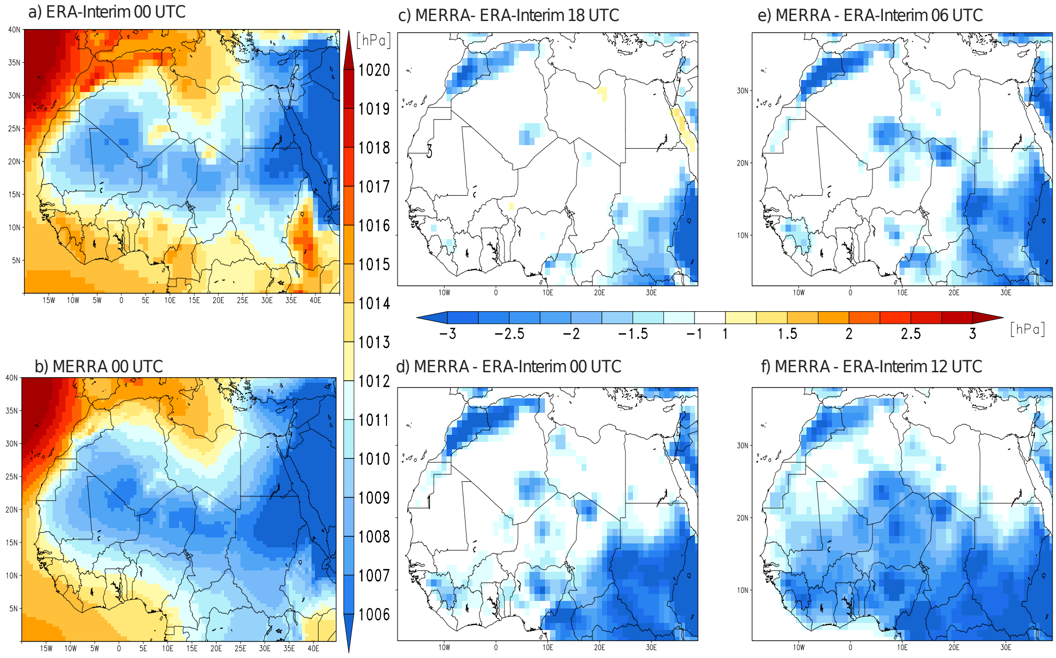

Figure 3.14: *Seasonal MSLP for June–August. Shown are (a) ERA-Interim re-analysis and (b) MERRA re-analysis at 0 UTC for 1980–2001, Differences of the mean climatology from MERRA relative to ERA-Interim are shown for (c) 18 UTC, (d) 0 UTC, (e) 6 UTC and (f) 12 UTC.*

horizontal pressure gradient is found along the northern margins over parts of Algeria and Libya at 12 UTC. The temporal correlation is better in summer than in winter. Particularly the north of the domain shows a temporal correlation of around 0.9 indicating good temporal agreement between both products. Again a different temporal development of the daytime boundary layer may cause the largest differences in MSLP at 12 UTC.

Mean statistical values for the inter-comparison of ERA-Interim and MERRA per season are shown in Figure 3.15. The mean spatial correlation ranges between 0.6 and 0.9 (Figure 3.15a). The highest values are found for summer during daytime, while the lowest correlation is found in spring at 6 UTC. The spatially averaged difference shows a tendency to overall smaller MSLPs in MERRA than in ERA-Interim (Figure 3.15b). The largest mean difference is found at mid-day with around -1.5 hPa. Route mean square differences (RMSD) between both re-analysis are similar at all times of day per season (Figures 3.15c). The largest RMSD is roughly 4 hPa for December to February and the smallest RMSD around 2.7 hPa occurs between June and August.

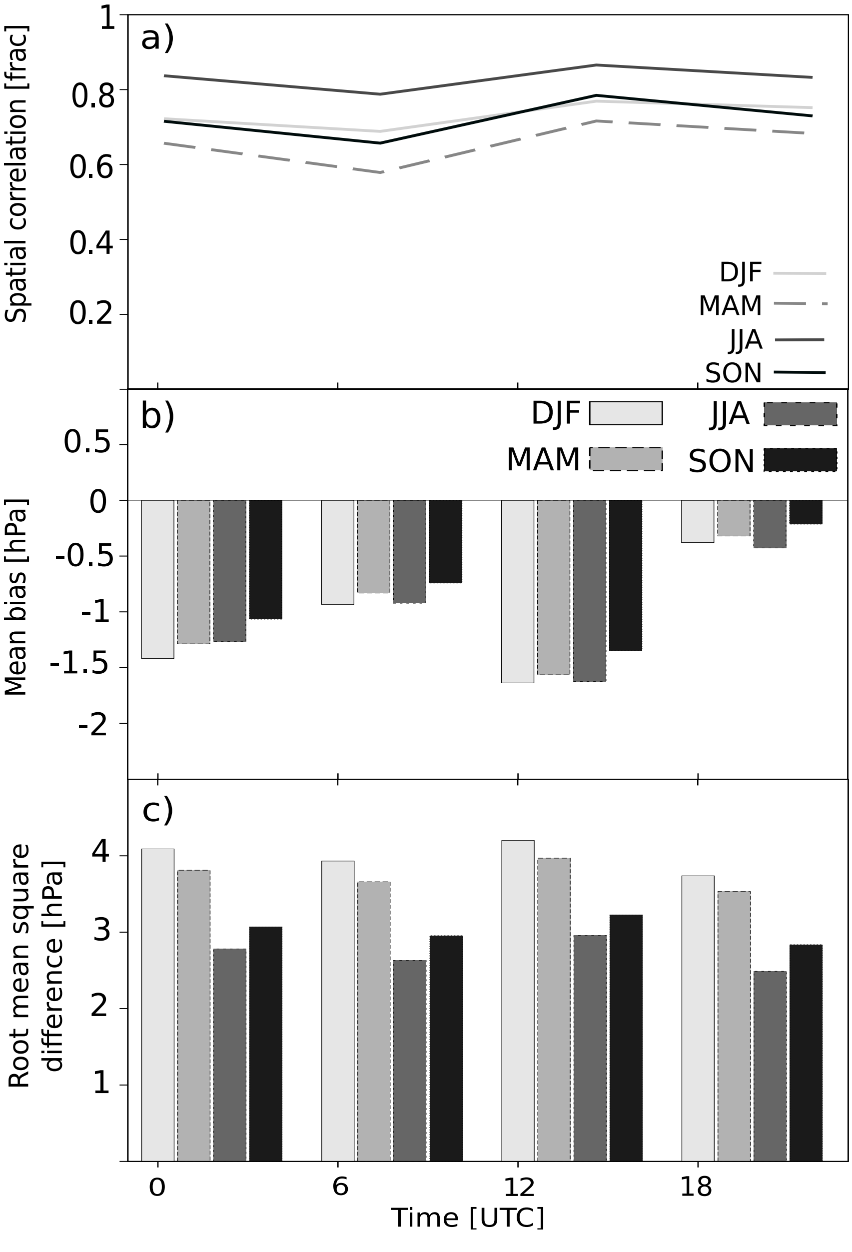

Figure 3.15: *Statistics for re-analysis intercomparison of MSLP. (a) Mean spatial correlation coefficient, (b) bias and (c) root mean square difference from MERRA compared to ERA-Interim assessed at different times of day and seasons temporally and spatially averaged for 1980−2001.*

3.4.2 Dust emission

[*] ERA-Interim winds are used to calculate dust emission over North Africa offline with the model by Tegen *et al.* (2002). The emissions shall be compared to observation in this section. Unfortunately a quantitative estimate for the emitted mass is currently unavailable from long-term observations over North Africa. As an alternative, the DSA frequency from satellite observations (Schepanski *et al.*, 2009, 2012, 2007) is used for a qualitative comparison of the number of dust emission events from the dust emission calculation in the period March 2006 to February 2010. The inter-annual variability of DSA frequency can be large (e.g. Schepanski *et al.*, 2009; Tegen *et al.*, 2013) so that the same time period is chosen from the model calculation for the comparison. Simulated dust emission events with fluxes exceeding $10^{-5}\,\mathrm{gm^{-2}s^{-1}}$ are taken into account only, as smaller amounts are unlikely to be detected by the instrument (e.g. Laurent *et al.*, 2010).

Figure 3.16 shows the annual mean DSA frequency from the dust emission calculation forced with meteorological fields from ERA-Interim (Fiedler *et al.*, 2013b). The DSA frequencies below 5 % compare well against the model simulation over large areas in the central Sahara. Maxima between the Hoggar and the Tibesti Mountains as well as over the Bodélé Depression with up to 35 % DSA frequency are also well represented. In the Bodélé Depression, the largest number of DSA events occurs between 03 and 9 UTC in the satellite product indicating the importance of NLLJ momentum mixing for dust emission discussed in Chapter 2. However, the high DSA frequencies from the model at the western coast of the continent are not seen in the satellite product (Figure 3.16). During spring and summer, the western coast may be influenced by moist air advected from the Atlantic Ocean. Atmospheric moisture can prevent dust detection in the satellite product (Brindley *et al.*, 2012), although the visual identification by Schepanski *et al.* (2012) might be less affected than an automatic algorithm (Ashpole & Washington, 2013). Also the tendency to larger DSA frequencies over the north compared to the south in the model simulation is not in agreement with the satellite DSA frequency. In winter and spring clouds associated with cyclones may obscure parts of the dust emission in observations along the northern margins of the desert (Figure 1.7), previously indicated by Schepanski *et al.* (2009). It is important to highlight that these differences of DSA frequency do not allow a conclusion on the quality of the dust emission

---

[*] Text passages and figures in the present section 3.4.2 are from my publication currently under review for the second stage in the Journal Atmospheric Chemistry and Physics with the intended title “How important are atmospheric depression and mobile cyclones for emitting mineral dust aerosol in North Africa?” following my publication “How important are cyclones for emitting mineral dust aerosol in North Africa?”, 13, 2013, pp. 32483−32528, in Atmospheric Chemistry and Physics Discussions distributed under the Creative Commons Public License (http://creativecommons.org/licenses/by/3.0/).

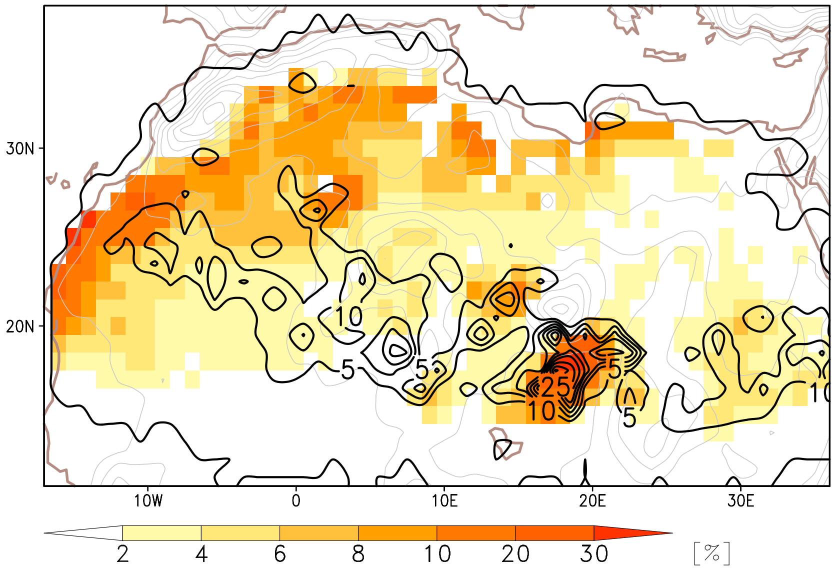

Figure 3.16: *DSA frequency based on satellite observations and ERA-Interim data. Annual mean DSA frequency based on the dust emission model by Tegen* et al. *(2002) driven by the near-surface wind speed and soil moisture from three-hourly ERA-Interim forecasts (shaded). Dust emission events larger than* $10^{-5}\,gm^{-2}s^{-1}$ *are considered only, as smaller dust amounts are unlikely to be detected in the satellite product (Laurent* et al.*, 2010). Black contours show the annually averaged DSA frequency derived from SEVIRI satellite observation by Schepanski* et al. *(2012, 2007) in steps of 5 %. The time period considered is March 2006 to February 2010 following the satellite observation. Grey contours show orography in steps of 200 m. Figure from Fiedler* et al. *(2013b).*

amount. The model can have higher DSA frequencies, but these events could be weaker than the detected source activations, and vice versa (Tegen *et al.*, 2013).

Since assessing the quality of the calculated emission amount with ERA-Interim data would be useful, these emissions are compared against a simulation with the dust model by Tegen *et al.* (2002) driven by near-surface wind speed from MERRA re-analysis. Figure 3.17 shows the seasonal climatology of the dust emission amount and the DSA frequency calculated from MERRA wind. Dust emission amounts are given in gm^{-2} per season in the following. The general pattern of the dust emission climatology derived from ERA-Interim (Figure 2.8 in Chapter 2) is reproduced, even though MERRA has a horizontally higher resolution. The most important dust emission maxima in winter and spring are here also the Bodélé Depression with more than $50\,\mathrm{gm}^{-2}$ and wide areas in North Africa with values around $30\,\mathrm{gm}^{-2}$ (Figures 3.17a–b). The frequency of DSA is particularly large in the Bodélé Depression with 20 %. Areas along the northern margins of the desert have DSA frequencies of 2-8 %, pointing to fewer but more intense dust storms. Summertime maxima of $10-40\,\mathrm{gm}^{-2}$ and DSA frequencies around 14 % are also situated over West Africa (Figure 3.17c). Autumn is characterized by generally low dust emission activity over most of the Sahara (Figure 3.17d).

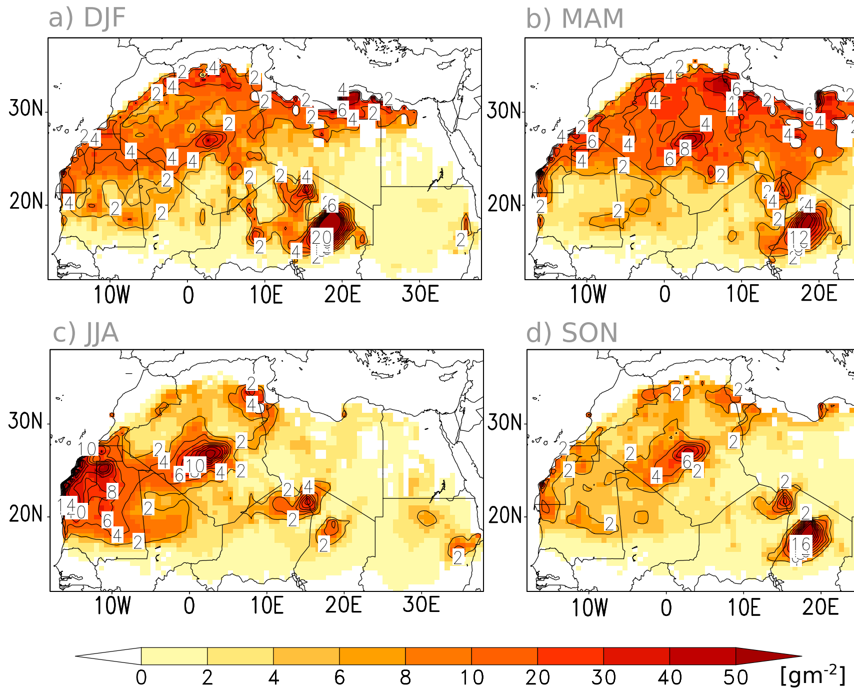

Figure 3.17: *Seasonal climatology of dust emission with MERRA winds. Dust emission amount (shaded) and dust emission frequency in percent (contours) for (a) December–February, (b) March–May, (c) June–August and (d) September–November for 1979–2010 based on the dust emission model by Tegen* et al. *(2002) driven by the near-surface wind speed from MERRA re-analysis without soil moisture effects.*

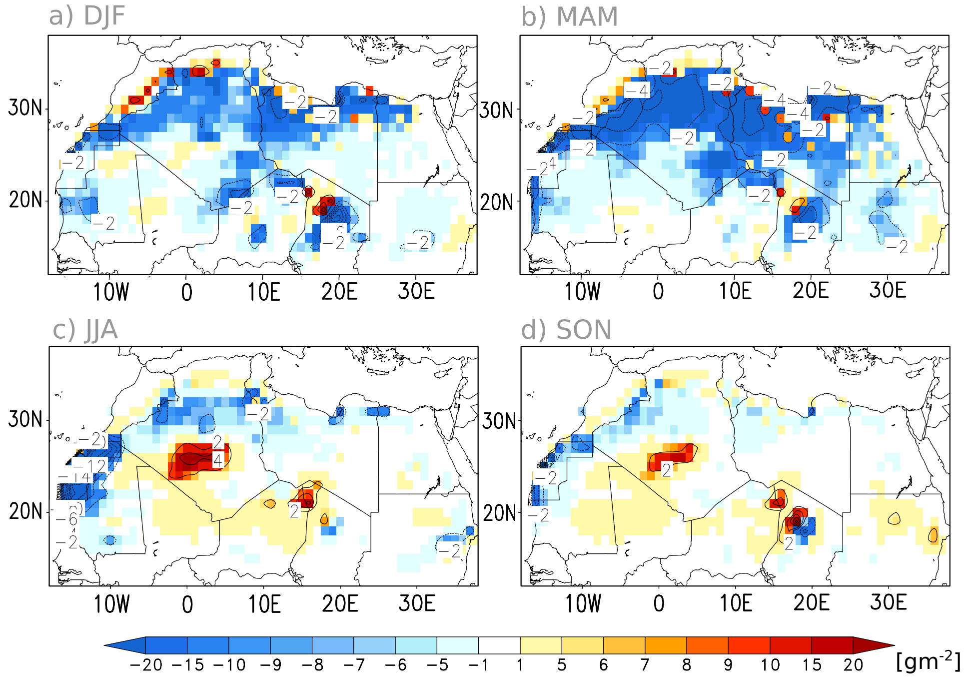

Figure 3.18: *Absolute differences of the dust emission climatologies. Shown are differences as MERRA minus ERA-Interim forecasts of the dust emission amount (shaded) and the DSA frequency in percent (contours) for (a) December–February, (b) March–May, (c) June–August and (d) September–November for 1979–2010 based on the dust emission model by Tegen* et al. *(2002) driven by the near surface wind speed from MERRA re-analysis and ERA-Interim forecasts without soil moisture.*

Differences between the dust emission climatologies using MERRA and ERA-Interim data are quantified in Figure 3.18. MERRA wind speeds produce less dust emission over North Africa by up to 20 gm^{-2} in winter and spring (Figures 3.18a$-$b). The activation frequency is smaller, particularly in spring when the number of DSAs is smaller by 2 %. These differences primarily over the north disagrees with the location of MSLP differences between both re-analysis products (Section 3.4.1). This points to the importance of deviations from the mean synoptic-scale conditions and processes at smaller scales for dust emission in the north (Chapter 4).

Interestingly the dust emission in the area of the North Atlantic ventilation is also smaller in the simulation with MERRA winds compared to ERA-Interim, namely by 4 % in spring and up to 14 % during summer (Figures 3.18b$-$c). Misrepresentations of surface properties in dust models are currently under discussion for this area where stony surface coverage, known as hammadas, is suggested to prevent dust emission that is not accurately represented in dust models (pers. comm. R. Washington, University of Oxford, 2013). The present results with re-analysis, however, suggests that the representation of the wind speed in the dust model is an important factor in this area. Further differences are the peak dust emissions in central Algeria that are more pronounced with MERRA than ERA-Interim in summer and autumn (Figures 3.18c$-$d). Here, the amount is larger by values around 10 gm^{-2} and the activation frequency higher by up to 4 %. The horizontal resolution may explain the larger values due to the complex terrain in this area that is better resolved by MERRA.

3.4.3 Near-surface wind speed

The differences in dust emission derived from ERA-Interim forecasts and MERRA re-analysis motivate a comparison of the representation of the 10m-wind speed in both data sets. Figure 3.19 shows the frequency distributions of the near-surface wind speed at different times of the day seasonally and spatially averaged for North Africa. ERA-Interim simulates the largest wind speeds during the day in both winter and summer (Figures 3.19a and d) in agreement with the expected diurnal cycle of the near-surface wind speed (Section 1.3.3). MERRA has more frequent wind speeds of 6$-$9 ms^{-1} in winter and summer that are typically sufficient for dust emission (Figures 3.19b and e). These winds occur primarily at night in MERRA pointing to even more frequent nocturnal events of downward momentum mixing than in ERA-Interim which has a artificially increased diffusion coefficient under stable stratification (Chapter 1). This larger number of wind speeds for dust emission at night is likely the cause for the larger dust emission over the northern areas of the continent in winter and in the west in summer. ERA-Interim has more frequent events at the upper end of the wind speed distribution above 11 ms^{-1} in both seasons for all times of day that are likely connected to strong dust emission events. These are not represented in MERRA despite its higher temporal and spatial resolution.

ERA-Interim forecasts are used instead of the re-analysis due to the temporally higher resolved wind speeds from the forecasts. The frequency distribution of the near-surface wind speed from the forecasts are compared to ERA-Interim re-analysis at 18 UTC, 00 UTC, and 06 UTC as spatial mean over North Africa in Figure 3.20. These times of day are chosen due to their importance for the NLLJ development. The result highlights that differences at the high end of the frequency distribution are negligible, which encourages the usage of ERA-Interim forecasts for model evaluation and process studies.

3.4.4 Discussion

Possible uncertainty of ERA-Interim in the synoptic-scale conditions, the derived dust emission and near-surface winds is estimated by comparison to different re-analysis products. Given the few observations available over North Africa for constraining the re-analysis products, the spatial patterns of the MSLP in MERRA and ERA-Interim are in reasonable agreement. The largest differences are found during mid-day but these likely have a small effect on the simulation of NLLJs. The midnight pressure gradient force is larger in MERRA over northern Sudan and southern Libya in winter and spring. Spring shows the smallest spatial correlation between both products pointing to differences in disturbances of the MSLP.

Calculating the dust emission climatology from both re-analysis shows smaller amounts with MERRA in the north of the continent and also in the Bodélé Depression from winter to spring, while the climatologies agree generally better in summer. An overestimation of the dust emission with winds from ERA-Interim is, however, unlikely as the overall dust emission computed with ERA-Interim lies at the lower end of the spectrum of dust emission estimates from models (Huneeus *et al.*, 2011). ERA-Interim is known to overestimate the nocturnal wind speed (Sandu *et al.*, 2013; Steeneveld *et al.*, 2008). Nocturnal wind speeds above the threshold for dust emission occur in MERRA even more frequently while the daytime wind speeds are smaller. This result is in agreement with Decker *et al.* (2012) showing that ERA-Interim agrees best with flux tower observations over land. Also the results by Ridley *et al.* (2014) point to an underestimation of the 10m-wind speed in

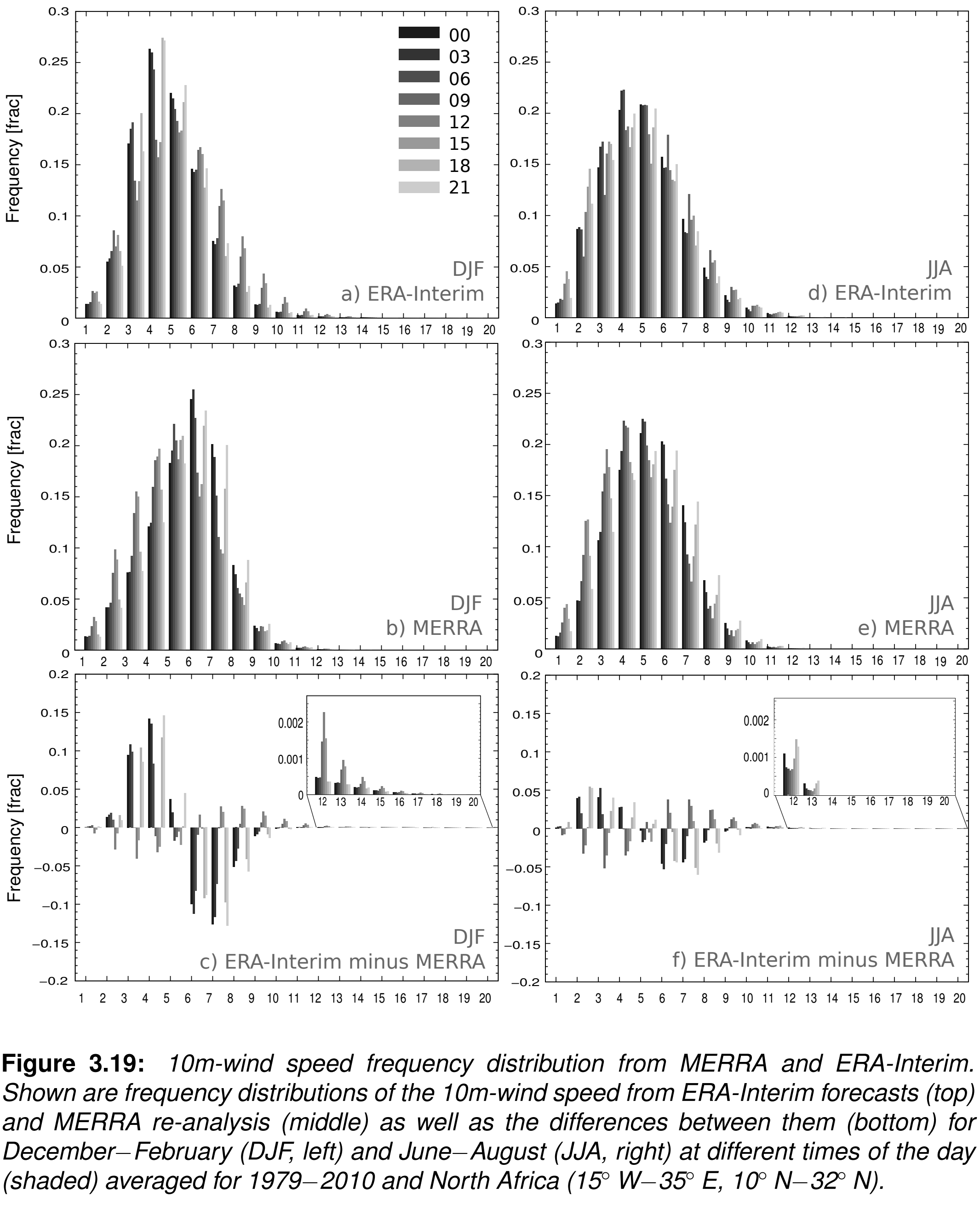

Figure 3.19: *10m-wind speed frequency distribution from MERRA and ERA-Interim. Shown are frequency distributions of the 10m-wind speed from ERA-Interim forecasts (top) and MERRA re-analysis (middle) as well as the differences between them (bottom) for December–February (DJF, left) and June–August (JJA, right) at different times of the day (shaded) averaged for 1979–2010 and North Africa (15° W–35° E, 10° N–32° N).*

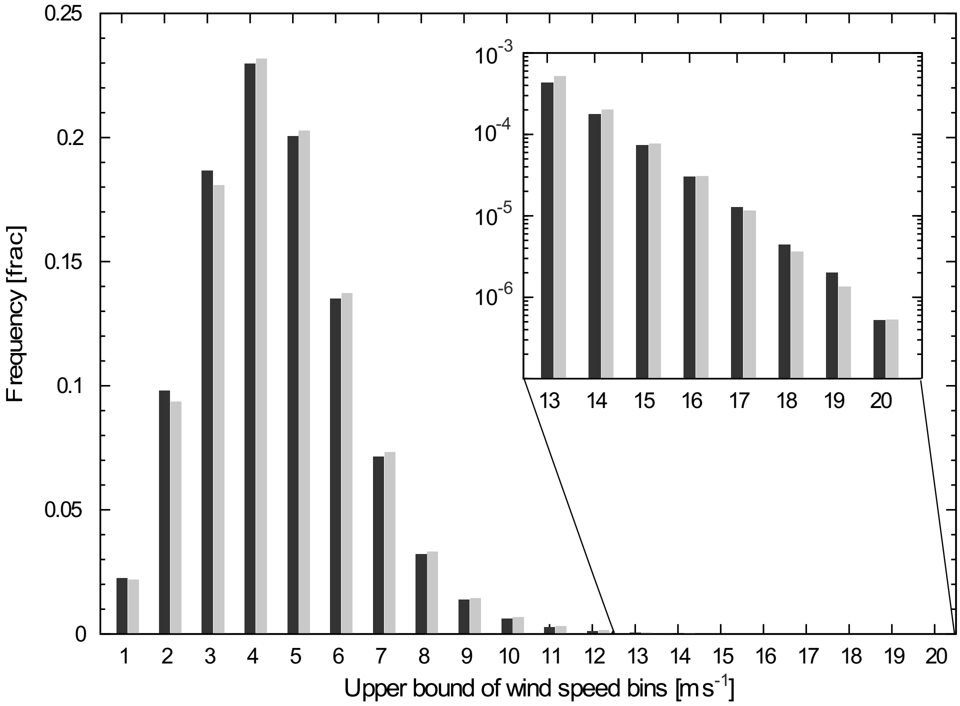

Figure 3.20: *10m-wind speed frequency distribution from ERA-Interim forecasts and re-analysis. Shown are values at 18 UTC, 00 UTC, and 06 UTC from ECMWF ERA-Interim six-hourly re-analysis (black) and three-hourly forecasts (grey) over North Africa for 1979–2010. Note the logarithmic scale in the zoom for the high end of the wind speed distribution, which is relevant for mineral dust emission. Figure from Fiedler* et al. *(2013a) with permission of John Wiley & Sons, Inc.*

MERRA resulting in too little dust emission over North Africa. Dust emission calculated with winds from ERA-Interim are therefore likely better than with MERRA. The temporally higher resolved wind speeds from ERA-Interim forecasts are used for the dust emission calculation in this thesis which is justified by a good agreement of the 12-hour forecasts with the re-analysis product (Fiedler *et al.*, 2013a). Both the MSLP and the wind speed distribution from the forecasts are close to the re-analysis from ERA-Interim.

3.5 Conclusions and recommendation

The ability of ERA-Interim for simulating NLLJs and dust emission is analyzed with case studies and climatological intercomparison of re-analysis in this chapter. The most important findings from the case studies are:

1. ERA-Interim forecasts reproduce NLLJs from radiosondes launched during AMMA (Redelsperger *et al.*, 2006) and Fennec (e.g. Marsham *et al.*, 2013b) successfully.
2. The largest wind speeds of NLLJs are underestimated by the model in agreement with the artificially increased vertical mixing in stably stratified boundary layers in the ECMWF forecast system (Sandu *et al.*, 2013). Particularly the wind speed of NLLJs connected to haboobs is underestimated which is not surprising given that haboobs are not parameterised in ERA-Interim.
3. Based on the comparison to the BoDEx field campaign (Todd *et al.*, 2008), the frequency of DSA, their general intensity classification, the frequency of NLLJ occurrence and the NLLJ height are well represented by the model chain used here.

Since the Bodélé Depression is a key region for simulating the dust emission in North Africa, the good performance of the model chain compared to BoDEx gives confidence in the dust emission climatology based on ERA-Interim calculated with the dust model by Tegen *et al.* (2002). The underestimation of the highest NLLJ wind speeds have implications for the dust emission associated with NLLJs shown in Chapter 2, but the net effect of the underestimation of high NLLJ wind speeds on dust emission is uncertain because of the non-linear dependency of dust emission on the near-surface wind. An underestimation of the upper end of the wind speed distribution of NLLJ wind speeds needs to be considered when the NLLJ process is evaluated in other atmospheric models based on ERA-Interim, e.g. HadGEM2-ES in Chapter 5.

The climatology of DSA frequency from satellite observation (Schepanski *et al.*, 2012) is compared against the model chain used here (Fiedler *et al.*, 2013b) indicating good agreement in the key region of the Bodélé Depression. DSA frequencies in the north and west of North Africa, however, differ, which may be partly caused by clouds and atmospheric moisture obscuring dust in the satellite product and partly due to limitations of the dust emission and winds in the model setup used (Brindley *et al.*, 2012; Schepanski *et al.*, 2009; Tegen *et al.*, 2013). It is important to underline that the DSA frequency does not allow a conclusion on the simulated emission amount, which is not available from observation. Alternatively different re-analysis products are compared leading to the following main results:

1. The synoptic-scale pressure gradient in ERA-Interim, ERA-40 and MERRA shows an overall good agreement during the night over most areas of North Africa.
2. The dust emission amount from calculations with MERRA and ERA-Interim winds differ in northern areas in winter and spring as well as the western coast in spring and summer.
3. Nocturnal 10m-wind speeds of $6-9\,\mathrm{ms}^{-1}$ occur more frequently in MERRA re-analysis than in ERA-Interim forecasts while wind speeds at the upper end of the distribution during the day are smaller and less frequent in MERRA.

The smaller dust emission with MERRA is likely due to its different diurnal cycle and smaller maximum wind speeds. ERA-Interim has been identified to have an artificially increased vertical mixing under stable stratification (Sandu *et al.*, 2013) that dominates at night. The number of nocturnal wind events above typical thresholds for dust emission onset is even larger in MERRA so that ERA-Interim likely gives a better estimate for the diurnal cycle of wind speed in agreement with Decker *et al.* (2012). In conclusion, the dust emission calculation with ERA-Interim likely gives a reasonable estimate with state-of-the-art tools for the entire of North Africa over the 32-year period.

CHAPTER 4

Dust emission associated with atmospheric depressions and mobile cyclones

4.1 Motivation

[*] A systematic analysis of mechanisms generating peak winds strong enough for mobilizing dust provides the basis for evaluating dust emission from atmospheric models. Chapter 2 investigated the importance of NLLJs for North African dust emission (Fiedler *et al.*, 2013a). The main meteorological driver for the largest dust emission amount of the continent that occurs north of 20° N between December and May (Fiedler *et al.*, 2013a), however, is not well quantified. During this time of year migrating and long-lived cyclones and Harmattan surges affect the region, but dust emission associated with them has not been estimated before. The aim of the present chapter is to reveal how much dust emission is linked to cyclones affecting North Africa.

The presence of soil moisture can have important implications for dust emission (Chapter 1). While precipitation amounts and therefore soil moisture are generally small in large areas of the Sahara, cyclones are an important source for rainfall in North Africa (Hannachi *et al.*, 2011) and may be able to moisten the soil sufficiently for increasing the threshold of dust emission onset. This soil moisture effect is predominantly expected for cyclones along the North African coast between December and May, and near-surface signatures of AEWs at the southern fringes of the Sahara desert between May and September. The magnitude of the soil moisture effect during cyclone passage is, however, not well quantified.

The present chapter provides the first climatological estimate of the mass of emitted dust aerosol associated with atmospheric depressions and migrating, long-lived cyclones in North Africa. The latter are herein a subset of atmospheric depres-

---

[*] Text passages and figures in the present chapter 4 are from my publication currently under review for the second stage in the Journal Atmospheric Chemistry and Physics with the intended title "How important are atmospheric depression and mobile cyclones for emitting mineral dust aerosol in North Africa?" following my publication "How important are cyclones for emitting mineral dust aerosol in North Africa?", 13, 2013, pp. 32483−32528, in Atmospheric Chemistry and Physics Discussions distributed under the Creative Commons Public License (http://creativecommons.org/licenses/by/3.0/).

sions. Depressions are defined as minima in the geopotential height at 925 hPa that are identified and tracked with an automatic algorithm. Minima in the field of geopotential height are termed cyclones if they migrate, live for more than two days, and have a decreasing core pressure at the beginning of their life cycle. The depression and cyclone tracks are combined with dust emission calculations driven by ECMWF ERA-Interim data. Details of the method are explained in Section 4.2. Section 4.3 presents the results for the climatology of depressions and cyclones for dust emission. Conclusions are drawn in Section 4.4.

4.2 Method

4.2.1 Depression and cyclone identification

The analysis uses the depression tracks over North Africa for 1989−2008 retrieved by Schepanski & Knippertz (2011). Schepanski & Knippertz (2011) investigate Sudano-Saharan depressions by using the tracking algorithm from Wernli & Schwierz (2006) with modifications for low latitudes. Threshold values are adapted and the original input fields of mean sea level pressure are replaced by the geopotential height at 925 hPa that represent North African conditions better. The automated algorithm determines minima relative to the adjacent grid cells and is applied to the ERA-Interim re-analysis with a horizontal resolution of 1° (Dee *et al.*, 2011). Even though the input data set is six-hourly, minima are identified daily at 0 UTC in order to avoid erroneous tracking caused by the large diurnal cycle of the geopotential height at low levels over North Africa (Schepanski & Knippertz, 2011). The influence of the time of day on a depression identification is shown by Maheras *et al.* (2001).

Once a minimum is identified, the corresponding area of the depression is determined by the closed contour that lies furthest away from the centre. The value of the contour interval is 4 gpm corresponding to about 0.5 hPa (Schepanski & Knippertz, 2011). Depressions are connected to a track if two consecutive positions lie within 1000 km. This criterion allows for a maximum speed of 11.6 ms^{-1} that is sufficient for the majority of systems in North Africa (Schepanski & Knippertz, 2011).

The investigation of depressions and migrating cyclones over North Africa presented here is broader than that by Schepanski & Knippertz (2011). Here, depressions are all identified minima in the geopotential height at 925 hPa without a geographical restriction. The selection of migrating cyclones from all identified depressions requires generalized criteria applicable for the entire domain and time period. Note that migrating cyclones include both near-surface signatures of AEWs and cyclones. Both are termed cyclones and identified by the following filter criteria that have to be fulfilled simultaneously:

1. Cyclones have to be identified in at least three consecutive nights reflecting a life time of 48 hours as the minimum time period for a complete life cycle of a cyclone. This assumption complies with life times given in the literature (Bou Karam *et al.*, 2010; Hannachi *et al.*, 2011).

2. Each cyclone has to propagate over a pre-defined horizontal distance between genesis and lysis. The mean propagation speed is defined as the maximum displacement during the life time of the system calculated from the range of longitudes and latitudes of centre positions. The threshold for the propagation speed is 5° per day corresponding to a mean cyclone speed of $5{-}6\,\mathrm{ms}^{-1}$. This generous criterion is well below migration speeds reported for cyclones over North Africa (Alpert & Ziv, 1989; Bou Karam *et al.*, 2010; Knippertz & Todd, 2010; Schepanski & Knippertz, 2011).

3. The propagation speed alone does not successfully exclude all identified cases of the Saharan heat low, the mean position of which migrates over time. In order to exclude most heat lows, the identified cyclones have to have a decreasing core pressure between the first and second night. This criterion reflects cyclogenesis and successfully reduces the number of identified cyclones in summertime West Africa. Tracks of filling cyclones in the Mediterranean region are also excluded by this criterion, particularly frequent in the east during spring. Sensitivity tests show that reducing the number of cyclones in the Mediterranean basin has a negligible effect on the dust emission coinciding with cyclones (Section 4.3.4). This suggests that filling cyclones with centres away from dust sources do not generate wind speeds sufficiently large for mobilizing dust.

4.2.2 Dust emission

Mineral dust emission is calculated for 1989−2008 with the dust emission model by Tegen *et al.* (2002) following the experiment setup from Fiedler *et al.* (2013a) and Heinold *et al.* (2013) also used in Chapter 2 (refer to Section 2.2.3). Here an additional experiment without soil moisture is run for estimating the effect of water in the top soil on dust emission.

Calculating the dust emission associated with depressions and cyclones requires the definition of an area affected by associated peak winds. The tracking algorithm determines an area for the grid boxes lying within the outermost closed contour of the geopotential height at 925 hPa at mid-night. This centre area is used for analysing the track density per season (Section 4.3.1 and 4.3.1). Dust emission, however, may occur in an area larger than the centre, e.g. near the fronts. In order to include these dust emissions in the climatology, a cyclone-affected area is approximated by a circle around the identified minimum in the geopotential height. This area is calculated at mid-night and used for selecting the three-hourly dust emission associated with the depression or cyclone between 15 UTC of the previous day and 12 UTC of the same day (Section 4.3.3 and 4.3.4). The radius of this circle is set to 10°, a value corresponding to a latitudinal distance of 964 km at 30° N. The choice of 10° is motivated by previous studies (e.g. Bou Karam *et al.*, 2010), the typical radius seen in Figure 1.7 and tested by sensitivity experiments. These show that even when the radius of the circle is doubled, the spatial pattern of the fraction of dust emission associated with cyclones shown in Section 4.3.4 is robust.

4.3 Results

4.3.1 Occurrence frequency of depressions and cyclones

Climatology of depressions

Figure 4.1 shows the seasonally averaged occurrence frequency of depressions identified by the algorithm. In winter, depressions are found over the Mediterranean basin during 4 % of the time (Figure 4.1a) corresponding to up to five depressions per winter. Maxima of similarly large depression occurrence frequencies lie to the south of the High Atlas and to the west of the Ethiopian Highlands (refer to Figure 4.4 for geographical terms). The origin of these depressions may be partly related to lee troughs that are associated with closed contours in the geopotential height at 925 hPa. In the case of the Ethiopian Highlands, the heat low that is located here during winter (Lavaysse *et al.*, 2009) may explain another large portion of identified depressions. The general location of depressions over the Mediterranean Sea and the lee maximum of the Atlas Mountains are in agreement with previous studies (Maheras *et al.*, 2001; Trigo *et al.*, 1999). The exact frequency and location of maxima, however, depend on the underlying data set and identification technique (e.g. Hannachi *et al.*, 2011; Hodges *et al.*, 2011; Maheras *et al.*, 2001, and references therein).

Depressions over the continent in spring are generally more frequent than in winter (Figure 4.1b). The maximum south of the High Atlas dominates the clima-

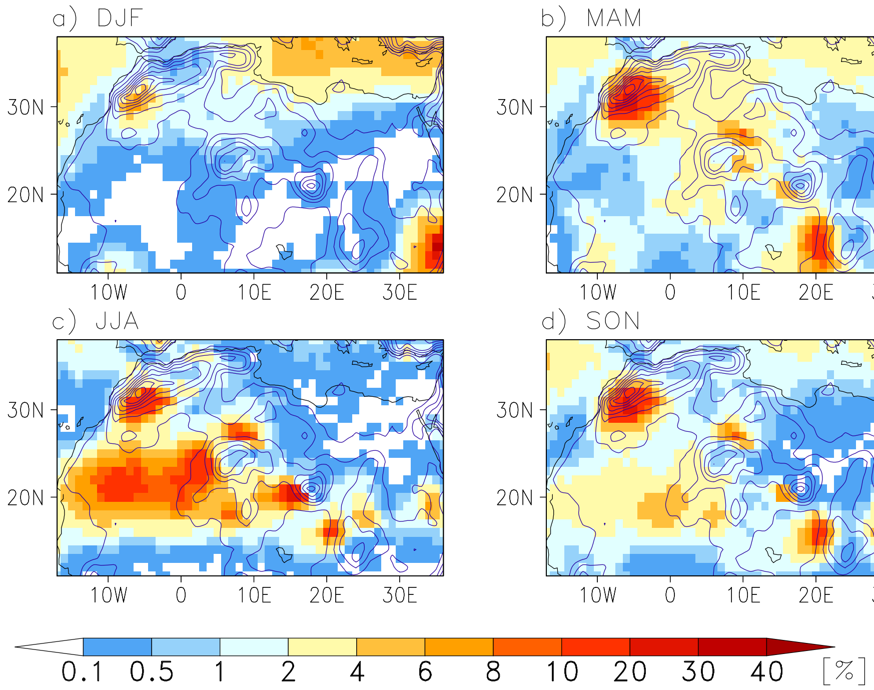

Figure 4.1: *Track density of all identified depressions. Climatology of the occurrence frequency of depressions for (a) December– February, (b) March–May, (c) June–August, and (d) September–November for 1989–2008 based on the depression centre defined by the outermost closed contour in the geopotential height at 925 hPa from the tracking algorithm (Section 4.2.1). Contours show orography in steps of 200 m. Figure from Fiedler* et al. *(2013b).*

tology in the north with occurrence frequencies of up to 30 % corresponding to ten depressions per spring. A secondary maximum can be identified at the northern side of the Hoggar Mountains with an occurrence frequency of up to 8 %. These two maxima agree with the formation of springtime cyclones from the literature, although the exact locations and frequencies differ (Hannachi *et al.*, 2011; Maheras *et al.*, 2001). Other studies for springtime North Africa find a single maximum for depressions (Trigo *et al.*, 1999). Reasons for these differences are the choice of a different data basis, time period, identification method, as well as the time of day due to the influence of the diurnal cycle of the net radiation budget on heat lows (Maheras *et al.*, 2001). Further maxima that can be related to lee troughs are found southwest of all mountains in the central Sahara due to the prevailing northeasterly Harmattan winds during this season. Maxima of the occurrence frequency in the vicinity of the Ethiopian Highlands and the Ennedi Mountains are, herein, particularly large with around 20 %.

Between June and August, occurrence frequencies of up to 20 % are found over West Africa (Figure 4.1c). Here, the Saharan heat low dominates the climatology while AEWs regularly influence the meteorological conditions (Lavaysse *et al.*,

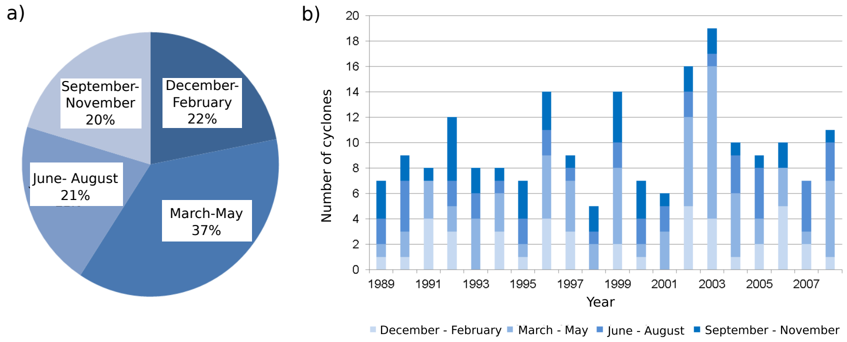

Figure 4.2: *Seasonal and interannual variations of long-lived and migrating cyclones. (a) Seasonal distribution of cyclones and (b) time series of cyclones in the sub-domain* $0^\circ-40^\circ$ *N and* 20° *W*-45° *E for 1989*–*2008. Figure from Fiedler* et al. *(2013b).*

2009; Luo *et al.*, 2004; Thorncroft & Hodges, 2000). Particularly the atmospheric depressions close and offshore of the West African coast point to the presence of AEWs. Similar track densities are found in the vicinity of mountains where the Saharan heat low influences the occurrence of depressions, predominantly at the Hoggar Massif (Lavaysse *et al.*, 2009).

The heat low over West Africa and the maxima near mountains in the central Sahara are also present in autumn but the relative importance changes (Figure 4.1d). In autumn, the frequency of depressions west of the Ethiopian Highlands is larger with up to 30 %, while the values over West Africa decrease to less than 6 %. This pattern is coherent with the shift of the heat low from West Africa towards the southeast near the equator (Lavaysse *et al.*, 2009). Heat lows and depressions in the vicinity of mountains seem to dominate the climatology of depressions throughout the year. Migrating cyclones and surface signatures of AEWs are investigated in the next section.

Climatology of cyclones

Migrating cyclones and surface signatures of AEWs are filtered as described in Section 4.2.1. The term cyclone is used for both types in the following. Cyclones regularly form over North Africa and the Mediterranean region, but the number of events is substantially smaller than the number of depressions. In the annual mean, ten cyclones occur in the sub-domain investigated, namely 0° to 40° N and 20° W to 45° E. Figure 4.2a shows the seasonal fraction of the total number of 196 cyclones that pass the filter. The analysis reveals that most of the cyclones form between March and May with 37 %. The remaining seasons have fewer events with roughly 20 % each.

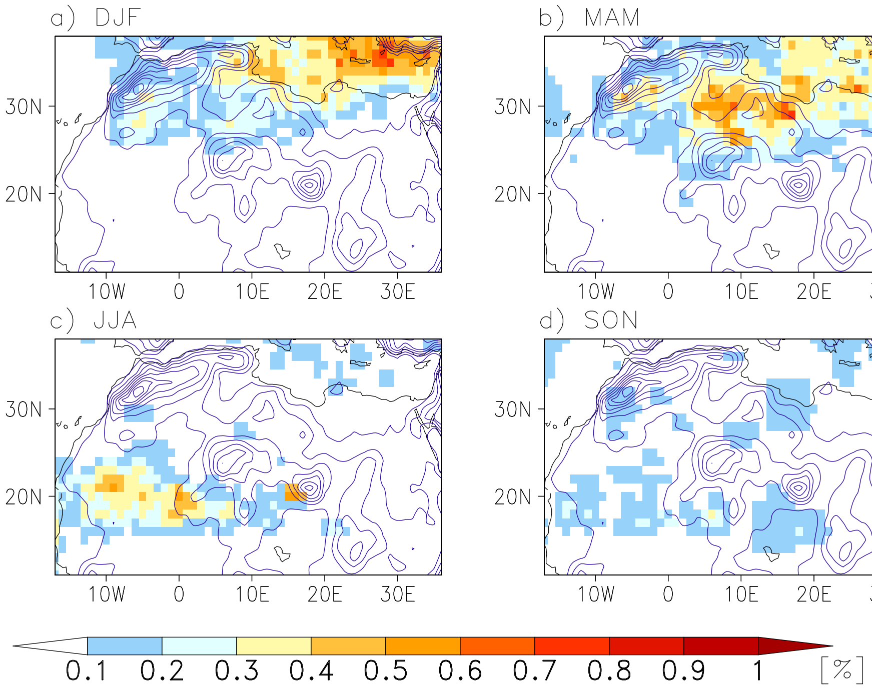

Figure 4.3: *Track density of long-lived and migrating cyclones. Climatology of the occurrence frequency of cyclones for (a) December– February, (b) March–May, (c) June–August, and (d) September–November for 1989–2008 based on the cyclone centre defined by the outermost closed contour in the geopotential height at 925 hPa from the tracking algorithm (Section 4.2.1). Contours show orography in steps of 200 m. Figure from Fiedler* et al. *(2013b).*

The time series of the total number of cyclones per year is shown in Figure 4.2b. The year-to-year variability of cyclone activity is relatively large with a factor three to four. The years with most identified events are 2003 with 19 cyclones, followed by 2002 with 16, 1996 and 1999 with 14 events each. The most inactive years are 1998, 2000, 2001 and 2007 with five to seven cyclones each. Most of this variability can be explained by the cyclone activity during spring. The year-to-year variability for this season is particularly large. Years with a large event number experience 6–12 cyclones, while years with low activity have one to three events between March and May.

Figure 4.3 shows the seasonal distribution of cyclone occurrence frequency in the 20-year period. The dominant cyclone track between December and February stretches from the Aegean Sea to Cyprus (Figure 4.3a). Some areas in this track have occurrence frequencies of up to 0.8 % corresponding to one cyclone every second year. Including filling cyclones doubles the number of cyclones passing the eastern Mediterranean. Few cyclones are situated over the African continent during winter. A maximum cyclone frequency of 0.4 % is limited to areas along the northern coast between Tunis, Tunisia, and Tobruk, Libya. The High Atlas is

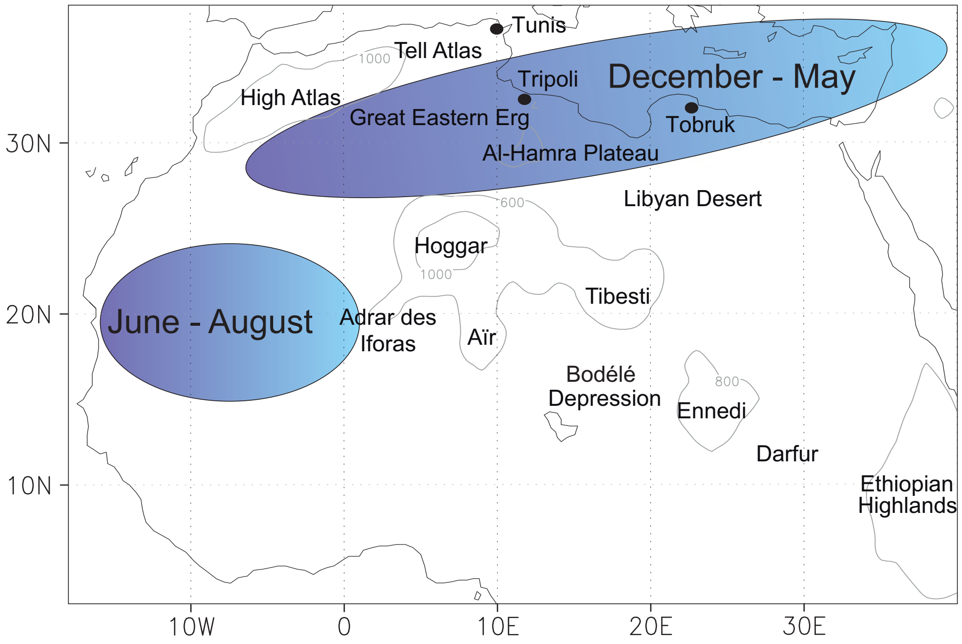

Figure 4.4: *Schematic overview on regions of most frequent cyclone occurrence. Contours show orography in steps of 200 m based on ERA-Interim. Geographical terms used in the text are indicated. Figure from Fiedler* et al. *(2013b).*

the region where lee depressions may lead to cyclogenesis. The present results indicate that only a few of these lee depressions develop into migrating and long-lived cyclones. Similar values are found north of the Great Eastern Erg, the south-eastern side of the Tell Atlas, Algeria and Tunisia, north of the Hoggar Mountains, Algeria, and south of the High Atlas Range, Morocco.

Between March and May, cyclones occur most frequently over North Africa (Figure 4.3b). Cyclones at the southern side of the High Atlas are identified in up to 0.5 % of the time between 1989 and 2008. Cyclones over areas of the Great Eastern Erg between the Tell Atlas Mountains and the Hoggar Massif, Tunisia and Algeria occur in up to 0.8 % of the time. This cyclone frequency is comparable to the cyclone track in the wintertime Mediterranean Sea (Figure 4.3a–b). The eastern side of the Al-Hamra Plateau, Libya, also shows a frequency around 0.8 %, which is consistent with the reported ideal conditions in this region (Alpert *et al.*, 1990; Pedgley, 1972).

The peak cyclone activity north of 25° N in winter and spring rapidly decreases as the year progresses (Figure 4.3c). Maxima of the track density are shifted from the north to West Africa where cyclones occur in up to 0.6 % of the time. These occur primarily over Mali and Mauritania around 20° N, a region known for frequent occurrence of AEW signatures at higher altitudes (Mekonnen *et al.*, 2006; Thorncroft & Hodges, 2000). Here, the cyclones are connected to AEWs that are strong enough to form a signature near the surface. Agustí-Panareda *et al.* (2010) suggest that AEWs are too weak in the ECMWF model over the eastern North Atlantic. This could imply that fewer AEWs are strong enough to be detected with the tracking algorithm used here. It is interesting that the track density peaks in the lee of mountains similar to the springtime maximum in the north. These maxima are situated at the western sides of the Tibesti, Aïr, and Adrar des Iforas mountains. The location suggests that the interaction of the flow with mountains aid the deepening and formation of closed contours in the geopotential height at 925 hPa. This result is in agreement with Bou Karam *et al.* (2009) who show that vortices form in the lee of mountain barriers during summer. Autumn shows the smallest cyclone activity with occurrence frequencies below 0.3 % (Figure 4.3d). The regions of most frequent cyclone occurrence are summarized in Figure 4.4. These are the northern fringes of North Africa between December and May and West Africa from June to August. The characteristics of the cyclones are investigated in the following.

4.3.2 Characteristics of cyclones

Figure 4.5 shows the life time and zonal displacement of the identified cyclones for areas north and south of 20° N over the continent. In the north, cyclogenesis occurs 56 times during the 20-year period, more than half of which form between March and May (32 cyclones). Most of these cyclones have their origin in the vicinity of the Atlas Mountains with 26 cyclones between 15° W and 10° E. Cyclones in the north frequently live for three days in spring (Figure 4.5a). Life times between five and seven days are similarly common for the season. Springtime cyclones predominantly follow eastward tracks in the north (Figure 4.5c). The migration distance is most often 30° to the east, closely followed by 20° and 10°. Some cyclones with eastward trajectories also form south of 20° N during spring (Figure 4.5d). Wintertime cyclones have a similar distribution of the migration direction. The prevailing eastward migration in the north is in agreement with previous studies (e.g. Alpert *et al.*, 1990; Hannachi *et al.*, 2011).

South of 20° N, the seasonality of cyclogenesis is different. Out of 50 cyclones forming here in total, 36 % occur between June and August followed by 26 % and 28 % in autumn and spring, respectively. Figure 4.5b shows the cyclone life time for the south. Here, the majority of cyclones are identified over three to four days. Summertime cyclones also live frequently for six days. The prevailing migration direction during summer and autumn is westwards by mostly $20-30^\circ$ (Figure 4.5d) that is consistent with the propagation of AEWs (Burpee, 1972; Thorncroft & Hodges, 2000).

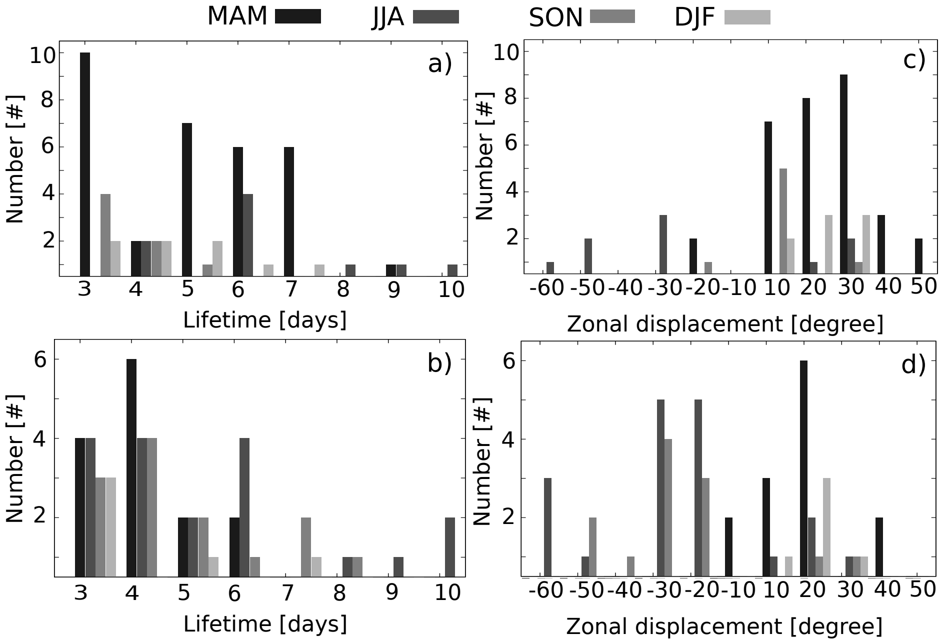

Figure 4.5: *Histograms of characteristics from long-lived and migrating cyclones. Cyclone life times for 1989–2008 forming (a) in the north (15° W–35° E, 20° N–32° N), and (b) in the south (15° W–35° E, 0° N–20° N); and zonal displacement of cyclone centres during their life time forming (c) in the north, and (d) in the south. Figure from Fiedler* et al. *(2013b).*

4.3.3 Dust emission associated with depressions

Annually and spatially averaged across dust sources of North Africa, 55 % of the dust emission is associated with atmospheric depressions. Regionally even larger fractions of dust emission coincide with depressions shown along with the occurrence frequency of depressions in Figure 4.6. Particularly areas in northern and western Africa have dust emission associated with depressions of up to 80 %. Since the influence of depressions on dust emission is limited to a radius of 10° (Section 4.2), nearby maxima of the depression occurrence frequency can be associated with them. For instance, the large dust emission amounts associated with depressions in the north and also close to the Ethiopian Highlands are associated with maxima in occurrence frequency. In contrast, dust emission in the northeast and west coincide with few depressions suggesting that these events are particularly intense.

The seasonal distribution of the dust emission fraction associated with atmospheric depressions is shown in Figure 4.7. Depressions coincide with 50 % of the dust emission in winter over most of North Africa (Figure 4.7a). Larger fractions are associated with depressions in Libya, Tunisia, and Sudan with values of up to 80 %. These maxima coincide with the frequent formation of depressions over the Mediterranean region and in the lee of the Ethiopian Highlands. The frequent

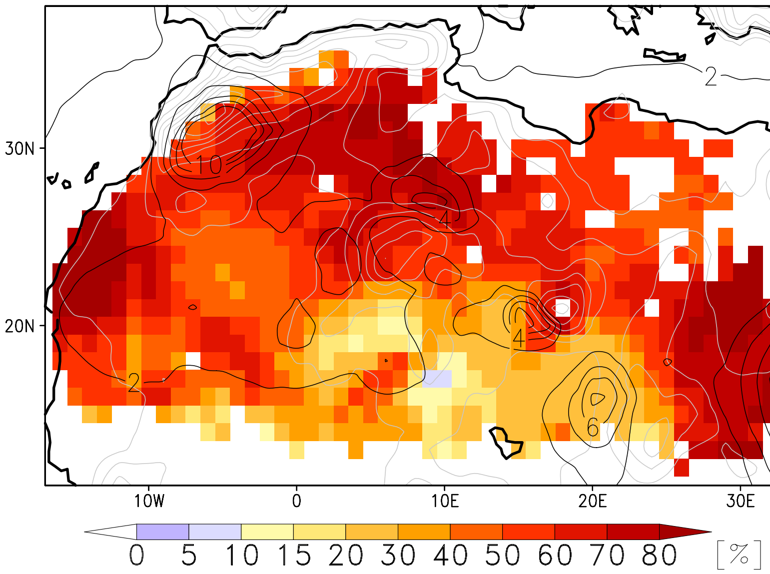

Figure 4.6: *Annual fraction of dust emission amount associated with depressions. Shown is the fraction of total dust emission associated with depressions in percent averaged for 1989–2008 (shaded). Dust emission within a radius of 10° from the depression centre is considered (Section 4.2). Black contours show the annually averaged occurrence frequency of depressions in steps of 2 %. Grey contours show orography in steps of 200 m. Figure from Fiedler* et al. *(2013b).*

formation close to the High Atlas is not associated with a dust emission maximum suggesting weak winds over the potential dust sources. The large fractions of dust emission in West Sahara occur away from a location with frequent depression formation pointing to rare but strong depressions. Spring shows even larger dust emission associated with depressions in wide areas to the north of 25° N and west of 10° E with up to 90 % (Figure 4.7b). These areas lie within or close to regions where depressions frequently form.

Depressions in summer are associated with up to 90 % of the dust emission across most of North Africa (Figure 4.7c). Depressions are abundant in this season. Most of them, particularly over West Africa, are likely Saharan heat lows given the spatio-temporal agreement with the climatology by Lavaysse *et al.* (2009). Areas of their frequent formation enclose most of the dust emission coinciding with them. In autumn, similarly large values are found along the northern and western margins of the continent, west of the Hoggar Massif and west of the Ethiopian Highlands (Figure 4.7d). The frequent formation of depressions within a radius of 10° coincides with these maxima. This large and widespread agreement between dust emission and depressions in summer is surprising as other dust-emitting processes have been suggested in the literature (e.g. Fiedler *et al.*, 2013a; Heinold *et al.*, 2013) and shall be briefly discussed here.

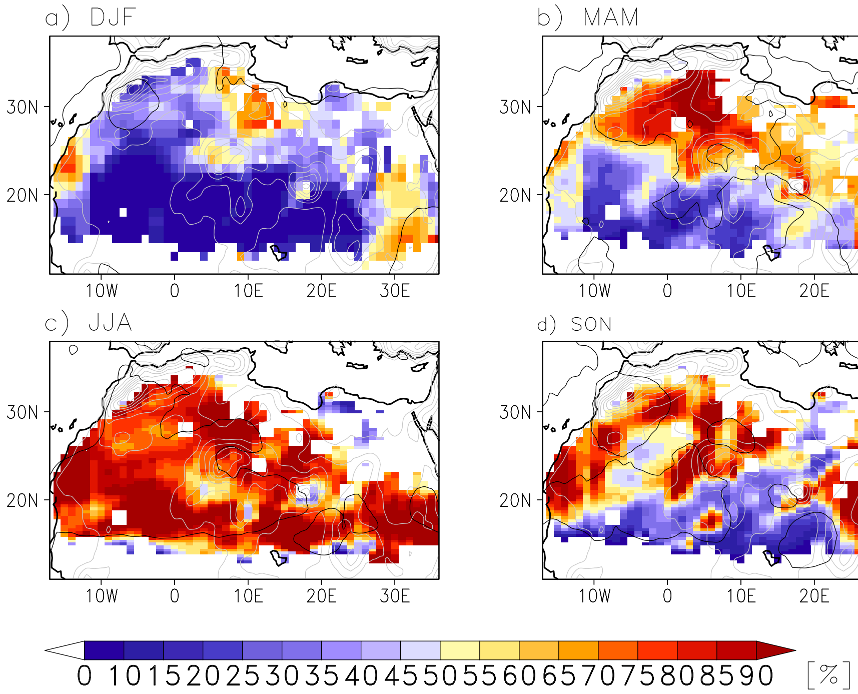

Figure 4.7: *Seasonal fraction of dust emission amount associated with depressions. Shown are fractions of total dust emission associated with depressions in percent for (a) December– February, (b) March–May, (c) June–August, and (d) September–November averaged for 1989–2008 (shaded). Dust emission within a radius of 10° from the depression centre is considered (Section 4.2). Areas within the black contour have an occurrence frequency of depression of more than 2 % (Figure 4.1). Grey contours show orography in steps of 200 m. Figure from Fiedler* et al. *(2013b).*

Estimating the dust emission amount associated with the heat low likely involves a number of mechanisms. Emissions can be directly caused by the horizontal pressure gradient around the heat low, but this alone may not always be sufficient to cause substantial dust mobilization. Mid-morning winds can be enhanced through the NLLJ mechanism (Fiedler *et al.*, 2013a), which depends on the horizontal pressure gradient around the heat low, but also on the diurnal evolution of the boundary layer. Using the NLLJ identification method from Fiedler *et al.* (2013a) to estimate the amount of dust emission associated with NLLJs within depressions results in an annual and spatial average of 12 %. Between March and October 12–16 % of the dust emission is associated with both phenomena, while values are below 10 % during the rest of the year. This result is in agreement with results from Chapter 2 showing frequent NLLJ formation along the margins of the Saharan heat low. Another process potentially embedded in depressions are haboobs, which are presumably not well represented in ERA-Interim data due to the physical parameterisation of moist convection. Dust emission coinciding with NLLJs and haboobs may also occur along with mobile and long-lived cyclones as a subset of depressions.

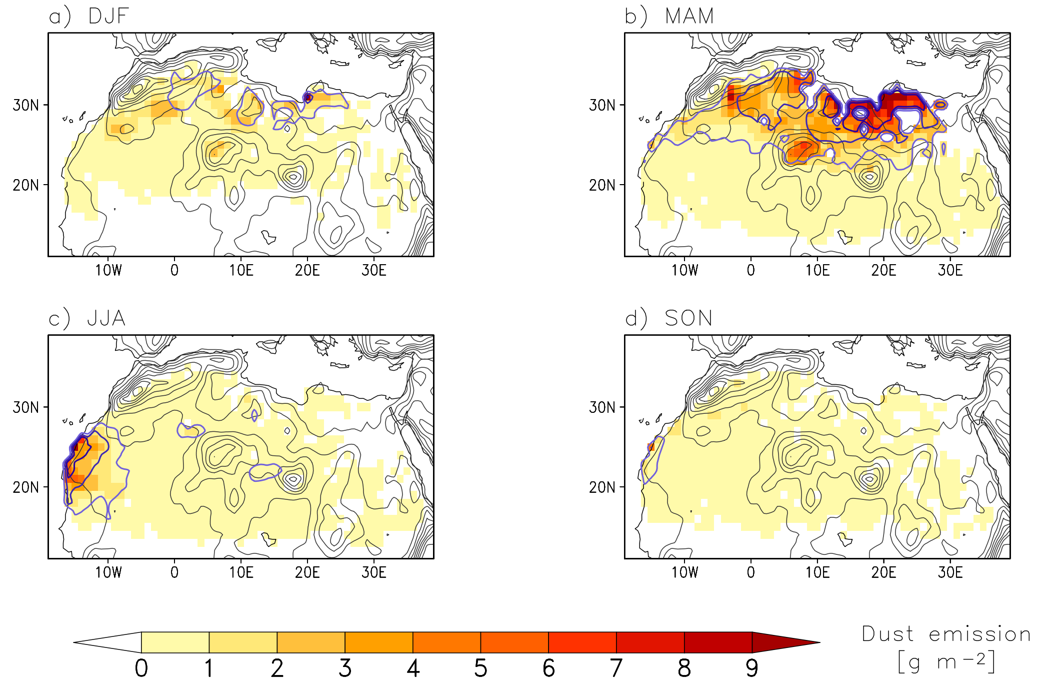

Figure 4.8: *Seasonal dust emission associated with long-lived and migrating cyclones. Shown are mean emissions (shaded) for (a) December– February, (b) March–May, (c) June–August, and (d) September–November averaged for 1989–2008. Black contours show orographic height in steps of 200 m. Blue contours show the number of intense dust emission events, defined by a flux larger than* 10^{-5} *gm*$^{-2}$*s*$^{-1}$ *following Laurent* et al. *(2010), in steps of three events. Figure from Fiedler* et al. *(2013b).*

4.3.4 Dust emission associated with cyclones

Seasonal climatology

The absolute emission amount associated with cyclones is shown first followed by the presentation of the fraction of associated dust emission. Figure 4.8 shows the seasonal total of dust emission and the number of intense emission events associated with cyclones averaged over the 20-year period. Intense emission is defined for fluxes greater than 10^{-5} gm^{-2}s^{-1} following Laurent *et al.* (2010). Across the continent and throughout the year, the seasonal total of dust emission within the cyclone-affected area (Section 4.2.2) is most frequently less than 1 gm^{-2}. Single regions and seasons, however, show distinct maxima of dust emission of up to 10 gm^{-2} north of 20° N. Between December and February, peak emissions near the Atlas and Hoggar Mountains as well as in Libya are 2–4 gm^{-2} (Figure 4.8a). Areas with more than three intense emission events per season lie mostly away from dust emission maxima. This points to moderate but frequent dust emissions in winter maxima, while rather small total emissions in some regions are generated by a few intense events.

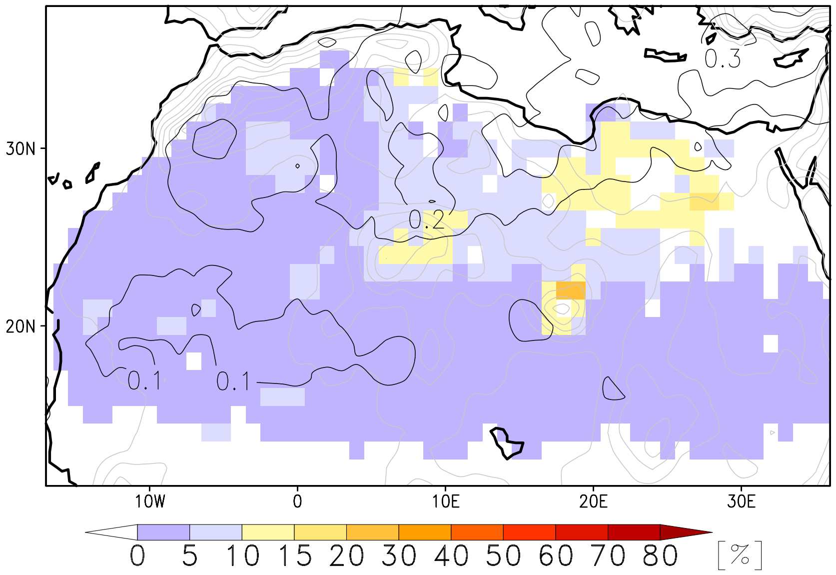

Figure 4.9: *Annual fraction of dust emission amount associated with cyclones. Shown is the fraction of total dust emission associated with long-lived and migrating cyclones in percent averaged for 1989–2008 (shaded). Dust emission within a radius of 10° from the cyclone centre is considered (see Section 4.2). Black contours show the annually averaged occurrence frequency of cyclones in steps of 0.1 percent. Grey contours show orography in steps of 200 m. Figure from Fiedler* et al. *(2013b).*

Springtime dust emission of 4–10 gm^{-2} associated with cyclones occur over a wider area (Figure 4.8b). The overall largest dust emission associated with cyclones are found in this season. Cyclones are particularly frequent then due to the large temperature contrast between land and sea which favours their development. Peak emissions coinciding with cyclones are found south of the Atlas Mountains, and west of the Libyan desert. More than three intense emission events occur over most of the region north of 20° N. Maxima of the emission amount coincide with more than six, in some areas even nine, intense emission events. This suggests that intense events substantially contribute to the largest emission amounts associated with springtime cyclones.

The findings change dramatically in summer when maximum emissions associated with cyclones are situated over West Africa with up to 6 gm^{-2} (Figure 4.8c) coinciding with more than six intense emission events. Here, surface signatures of AEWs may be deepest and cause the highest wind speeds (e.g. Thorncroft & Hodges, 2000). The coastal effect may be a contributing factor for strong winds in this region. In autumn, the number of intense emissions in the west is smaller with three events and the total dust emission associated with cyclones is smallest with typically less than 1 gm^{-2} (Figure 4.8d). This is in agreement with few cyclones identified for this season.

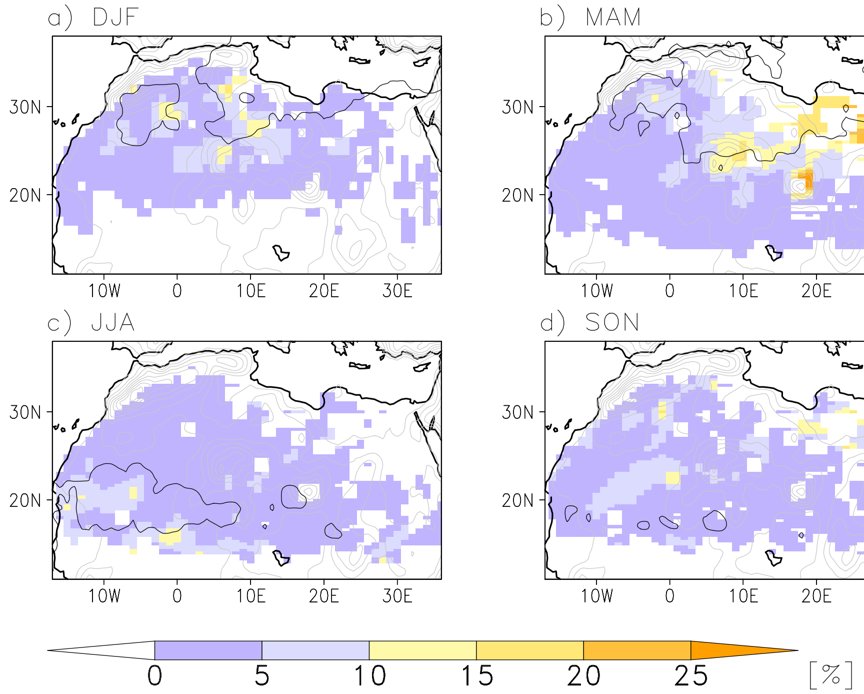

Figure 4.10: *Seasonal fraction of dust emission amount associated with cyclones. Shown are fractions of total dust emission associated with long-lived and migrating cyclones in percent for (a) December– February, (b) March–May, (c) June–August, and (d) September–November averaged for 1989–2008 (shaded). Dust emission within a radius of 10° from the cyclone centre is considered (Section 4.2). Areas within the black contour have an occurrence frequency of depression of more than 0.2 % (Figure 4.1). Grey contours show orography in steps of 200 m. Figure from Fiedler* et al. *(2013b).*

The fraction of the dust emission associated with migrating and long-lived cyclones relative to the total amount emitted per year is 4 % annually and spatially averaged over dust sources. Figure 4.9 shows the distribution of these fractions and the occurrence frequency of cyclones annually averaged. Single regions in the northeast have dust emission associated with cyclones exceeding 10 %. These regions are close to areas where cyclones occur most frequently.

The dust emission fraction is larger regionally in single seasons which are shown in Figure 4.10. From December to February, substantial dust emission fractions associated with cyclones occur in areas north of 20° N only, because of the limitation of cyclone tracks to northern locations (Figure 4.10a). The largest dust emission amounts associated with cyclones reach values of 5–15 % between 15° W and 15° E. Cyclones tracking over the eastern Mediterranean Sea in winter are not associated with large amounts of North African dust emission indicated by dust emission fractions below 5 % in regions east of 15° E. In spring, however, larger dust emissions of 10–25 % are associated with cyclones in this region (Figure 4.10b) when the main cyclone track shifts southwards onto the continent (Figure

4.3b). This is the overall largest area and magnitude of dust emission coinciding with cyclones in North Africa. Smaller areas with similar springtime fractions of dust emission lie to the south of the Atlas Mountains, northeast of the Hoggar Massif and in the Tibesti Mountains. These are within a distance of 10° from the areas of most frequent cyclone presence.

Between June and August, dust emission fractions in regions north of 25° N drop to values below 5 % while cyclones in isolated areas in Mali and Mauritania are associated with $5-15$ % of the dust emission amount (Figure 4.10c). Over West Africa, surface signatures of AEWs occur along 20° N and enclose these maxima of the dust emission fraction. Dust emission associated with cyclones remain similar in autumn but the spatial location of maxima changes (Figure 4.10d). The highest values of around 15 %, now, occur in the centre of the Sahara, the Western Great Erg and the Libyan Desert (Figure 4.10c$-$d). These occur away from areas of frequent cyclone passage suggesting that rare events are associated with relatively strong emission. It is, however, important to underline that the dust emission connected to cyclones is relatively small in autumn with typical totals below 1 gm^{-2}. This implies that, even though the relative importance is comparable to the north in winter and spring, the importance in terms of total dust mass is smaller (Figure 4.8d).

In light of the large relative importance of depressions for dust emission (Section 4.3.3), the overall fraction associated with migrating cyclones is small. Springtime depressions are associated with up to 90 % of dust emission in the lee of the High Atlas but considering migrating cyclones as a subset of depressions changes the fraction of dust emission to less than 15 % (compare Figure 4.7b and 4.10b). Over Libya, springtime dust emission associated with depressions are with values around 50 % also larger than the ones with cyclones with maxima around 25 %. Particularly in the lee of the Atlas Mountains the dust emission associated with cyclones is six times smaller than the amount associated with depressions. There are also no large and widespread dust emission associated with surface signatures of AEWs during summer.

Despite their coincidence with a small total dust emission amount in the north, intense emission fluxes are regularly associated with migrating cyclones in spring (Figure 4.10b). This aspect is analyzed further by defining a dust emission anomaly as the quotient of the dust emission associated with cyclones and the 20-year mean of the dust emission flux in the same month. Figure 4.11 shows this anomaly factor for both depressions and cyclones along with the dust emission flux spatially averaged across dust-emitting grid boxes. The largest dust emission fluxes occur between February and May with values larger than $1.5\cdot10^{-6}$ gm^{-2}s^{-1}. During this

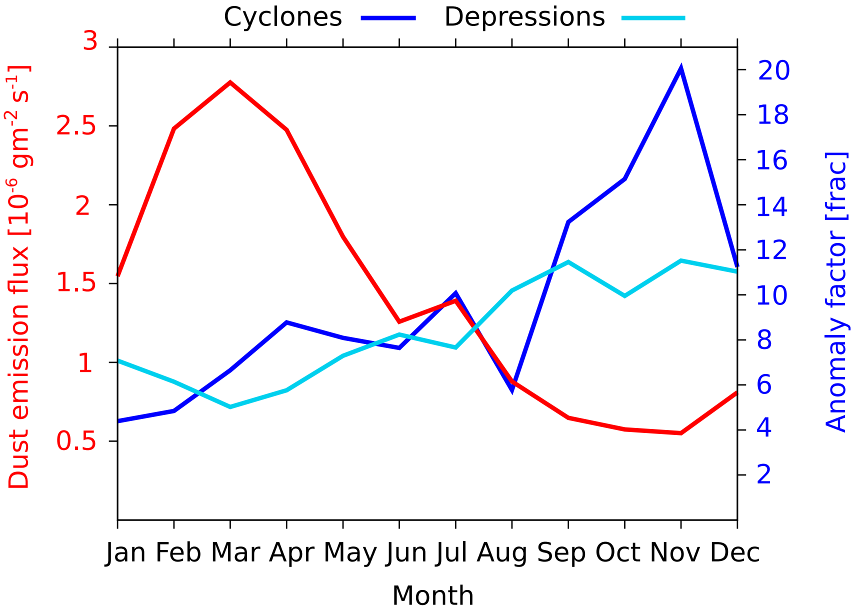

Figure 4.11: *Intensity of dust emission fluxes associated with long-lived, migrating cyclones and atmospheric depressions. Annual cycle of the dust emission flux associated with cyclones (red) and the anomaly factor of cyclones (blue) and depressions (cyan) averaged over dust-emitting grid boxes for 1989–2008. The anomaly factor is a measure of emission intensity and defined as the quotient of the dust emission flux associated with the cyclone/depression and the 20-year mean of the dust emission flux of the same month. Figure from Fiedler* et al. *(2013b).*

time of year the largest total dust emission occur over the north (Fiedler *et al.*, 2013a). The anomaly factor of cyclones during these months has values between four and eight, i.e. the dust emission associated with springtime cyclones is four to eight times larger than the long-term mean of the dust emission flux. From March to May, the anomaly factor of cyclones exceeds the values for depressions pointing to mobile cyclones as an important source for intense emission in spring, despite their rare occurrence.

The dust emission is generally smaller during summer with 0.7–1.3·10^{-6} gm^{-2}s^{-1} while the anomaly factors of cyclones increases to values of five to nine. During July the anomaly factor of cyclones is again larger than the one of depressions. Even larger anomaly factors of cyclones exceeding the values for depressions are found between September and November with up to 20, but both the dust emission flux and the number of cyclones is then smallest. These results underline that even though the total emission associated with migrating cyclones is rather small compared to the absolute emission in the north, the emission events during cyclone passage are particularly intense. For depressions, the emission intensity is more moderate throughout the year, but still clearly above the climatological mean.

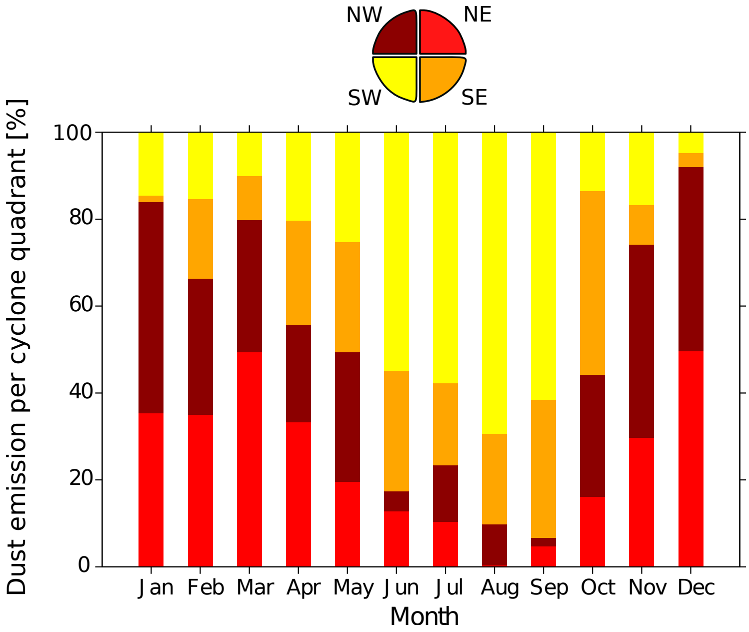

Figure 4.12: *Fraction of dust emission in quadrants of long-lived and migrating cyclones. Shown are monthly values averaged for the northern sub-domain (15° W–40° E and 20° N–40° N) and for 1989–2008. Figure from Fiedler* et al. *(2013b).*

Dependency on cyclone quadrant

The areas of largest dust emission amounts associated with cyclones reside close to maxima of cyclone tracks (Section 4.3.1). However, maxima of cyclones and dust emission (Figure 4.3 and 4.10) do not match perfectly due to two factors. On the one hand the location of peak winds within the cyclone-affected area is often away from the actual centre. On the other hand the parameterisation of dust sources restricts the region of active emission within the cyclone-affected area. The map of potential dust sources enables dust emission in most areas of North Africa so that the location of peak winds is expected to be the dominant factor. The spatial distribution of the dust emission within the cyclone-affected area is investigated in the following. Since the emitted mass associated with cyclones is relatively small south of 20° N in general (Section 4.3.4), only the northern sub-domain is taken into account. Here, dust emission is analyzed in four quadrants the position of which follow their geographical orientation depicted in Figure 4.12.

Figure 4.12 shows the annual cycle of the fraction of dust emission per quadrant of the cyclones north of 20° N spatially averaged. The results highlight that most dust is emitted in the northern quadrants with typical mean values of 30–55 % between November and March. In April, dust emission prevails in the northeast and southeast with about 30 % contribution each. Dust emission associated with cyclones in May is roughly equally distributed across the quadrants. June to September have clear maxima of dust emission in the southwest with 60−80 %. The total mass emitted between June and September, however, is smaller than at the beginning of the year. Cyclones in October have most dust emission in the southeast, but the integrated mass of dust emission is smallest during autumn (Figure 4.8d).

These results can be linked with the position of the highest wind speeds. In the case of a well-defined extra-tropical cyclone, the cold front typically lies to the west of the cyclone centre initially and moves towards the south and east thereafter. Peak winds, and therefore dust emission, are most likely at and behind the cool front as well as close to the cyclone centre due to the increased horizontal gradient of the geopotential height in these areas. Dust emission would primarily occur in the southwest initially, followed by prevailing emission in the southeast. At a later life stage, an extra-tropical cyclone typically forms an occlusion causing peak winds near the cyclone core. Dust emission may then form in all quadrants similarly. Integrated over the entire life time, most dust emission may be expected in southern quadrants if the cyclone has an extra-tropical character. While this is not found for the spatial average, examination of the spatial distribution of dust emission per quadrant reveals that areas south of the Atlas Mountains show indeed more than 50 % of the dust emission in the southwest or southeast quadrants between February and May. This distribution complies with the expectation for extra-tropical cyclones. However, the lack of a southern maximum in the spatial mean in winter and spring suggests that cyclones do not show typical characteristics of extra-tropical cyclones everywhere. Evaluating the spatial distribution of the dust emission per quadrant shows that dust emission in northern quadrants primarily occur in the central Sahara during spring. Here, the heat low lies typically to the south and relatively higher pressure northwards. This implies that instead of a classical frontal structure, a large horizontal gradient in the geopotential height occurs at the northern side of a large fraction of cyclones.

Summertime dust emission is mainly situated in the southwest of the cyclone centre in the spatial mean. Over West Africa, even larger emission fractions of up to 90 % occur in the southwest. The majority of cyclones during this season live particularly long and migrate westwards (Figure 4.5a,c) pointing to surface signatures of AEWs. The dominant quadrant during this time of year is well in agreement with the position of emission in front of the AEW trough where NLLJs are expected (Knippertz & Todd, 2010). The automated detection algorithm from Fiedler *et al.* (2013a) is used for estimating the mean fraction of dust emission within the cyclone-affected area that coincide with the occurrence of NLLJs. Figure 4.13a shows the fraction of dust emission within the cyclone-affected area that is associated with NLLJs for all areas north of 20° N. During summer, 10−20 % of dust emission are associated

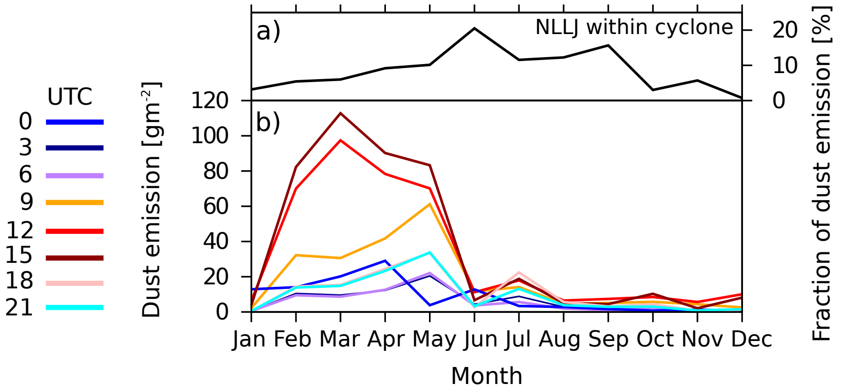

Figure 4.13: *Annual cycle of dust emission associated with cyclones. Monthly means of (a) the fraction of dust emission associated with long-lived and migrating cyclones and NLLJs and (b) the total dust emission associated with cyclones at different times of the day (colours). Values are spatially integrated over the northern sub-domain (15° W–40° E and 20° N–40° N) and monthly averaged over 1989–2008. NLLJ events are identified as in Fiedler* et al. *(2013a). Figure from Fiedler* et al. *(2013b).*

with NLLJs within the cyclone-affected area. Over parts of West Africa, the contributions from NLLJs to the dust emission associated with cyclones can be larger to up to 30 %. Another important driver for dust emission in association with AEWs are haboobs typically developing to the east of an AEW (Knippertz & Todd, 2010). Their missing physical parameterisation may cause an underestimation of the dust emission to the east of AEWs. The diurnal cycle of dust emission indicates driving mechanisms on a sub-daily scale that is analyzed next.

Diurnal cycle

Figure 4.13b shows the annual cycle of the total dust emission for different times of the day within the cyclone-affected area north of 20° N. Cyclones are associated with a substantial amount of mineral dust in late winter and spring. Maxima occur during mid-day with peaks of 90–110 gm^{-2} in March, and 70–90 gm^{-2} in May in contrast to values below 20 gm^{-2} between June and January (Figure 4.13b). The dust emission during the influence of cyclones has a diurnal cycle with a distinct maximum during the daytime. Emission at night has typical values around 10 gm^{-2} and never exceeds 30 gm^{-2} during spring (Figure 4.13b). At 9 UTC dust emission is often twice as large with maximum values of 60 gm^{-2} in May. Emissions at 12 and 15 UTC are even larger by a factor of two to four.

These diurnal differences for late winter and spring in the north can be explained by the development of the boundary layer in the context of the synoptic-scale conditions. Dust emission occurs when the momentum transport to the surface is sufficiently large to exceed the threshold for emission onset. Reduced stability during the day enables downward turbulent momentum transport, which increases the near-surface wind speed. This effect is expected to be largest, when the daytime boundary layer is sufficiently deep for reaching layers of high wind speed in the free troposphere. Strong winds prevail relatively close to the surface during cyclone passage in winter and spring. These cyclones form in a baroclinic zone between the warm (deep) North African air mass compared to the cold (shallow) air polewards. The contrast between the air masses causes a particularly strong thermal wind, i.e. an increase of the geostrophic wind with height in the lower troposphere. Along with typically deep daytime boundary layers over North Africa momentum from the free troposphere is efficiently transported towards the surface. In the Sahara, the boundary layer reaches a sufficiently large depth at or closely after mid-day (Culf, 1992), which coincides well with the mid-day peak of dust emission found here. The time of maximum dust emission is in agreement with the observation of suspended dust in cyclones shown in Figure 1.7.

The emission flux at 9 UTC in May, however, is almost as large as the mid-day values pointing to embedded NLLJs as a driving mechanism. Dust-emitting NLLJs are not frequently embedded in the cyclone-affected area with less than 10 % in winter and spring. This finding is well in agreement with the generally small dust emission amount associated with NLLJs during winter and spring in the north (Fiedler *et al.*, 2013a). The larger dust emission flux from cyclones at 9 UTC in May is, therefore, not predominantly linked to NLLJs. It seems most plausible that the momentum from the free troposphere is more efficiently mixed downwards in May than earlier in spring and winter. This is likely caused by a larger solar irradiation and longer days in late spring, aiding the development of the daytime boundary layer. NLLJs that can be embedded in AEWs are linked to 20 % of the dust emission in the cyclone-affected area in June and around 10 % in July and August.

Impact of soil moisture

While arid conditions prevail in North Africa, cyclones can produce rainfall that feeds soil moisture. The presence of soil moisture may weaken or suppress dust emission (Chapter 1). The magnitude of this effect is studied with two dust emission calculations with and without accounting for soil moisture, respectively (Section 4.2.2). Figure 4.14 shows the annual cycle of the fraction of dust emission suppressed by the presence of soil moisture along with the total dust emission when moisture is taken

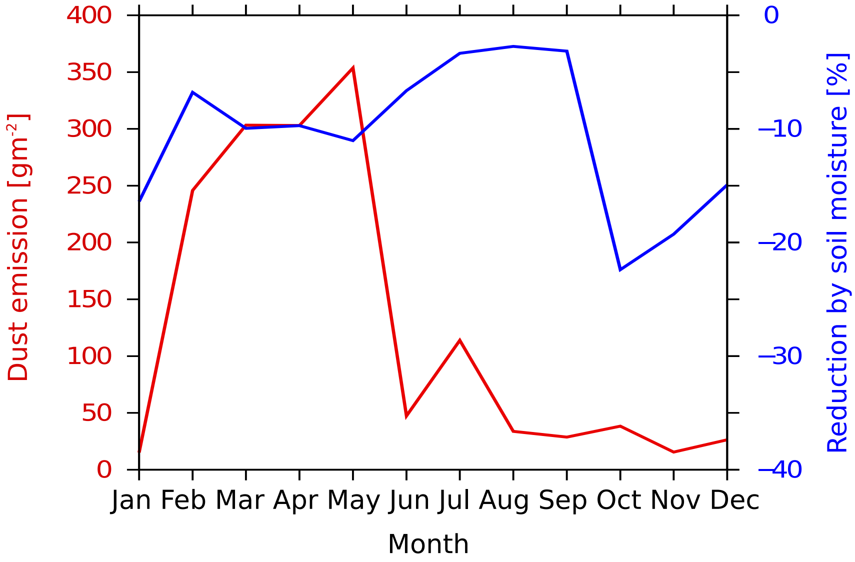

Figure 4.14: *Emission fraction associated with cyclones and weakened by soil moisture. Annual cycle of the total dust emission associated with long-lived and migrating cyclones (red) and the fraction of dust emission suppressed by soil moisture (blue). Values are spatially integrated over the northern sub-domain (15° W–40° E and 20° N–40° N) and monthly averaged over 1989–2008. Figure from Fiedler* et al. *(2013b).*

into account as a benchmark. During late winter and spring, the time when dust emission associated with cyclones show a clear maximum of 250–380 $\mathrm{gm^{-2}}$, soil moisture suppresses roughly 10 % of the dust emission spatially averaged across the north. Other months show values ranging from 5 % to 20 %, but the total dust emission is smaller than 100 $\mathrm{gm^{-2}}$ in July and smaller than 80 $\mathrm{gm^{-2}}$ during the rest of the year. It is interesting that the value for the emission reduction by soil moisture during cyclone passage for the 20-year period is of the same order of magnitude as the soil moisture effect for haboobs in a 40-day convection-permitting regional simulation for August 2006 (Heinold *et al.*, 2013) despite the underestimation of precipitation and soil moisture over West Africa in August 2006 by the ECMWF model (Agustí-Panareda *et al.*, 2010, and references therein).

4.4 Conclusions

The present chapter provides the first climatological estimate of the amount of dust emission associated with atmospheric depressions and mobile, long-lived cyclones over North Africa for 1989–2008. Atmospheric depressions are tracked following Schepanski & Knippertz (2011). While these depressions may be stationary or mobile with varying lifetimes, a subset of cyclones is defined which has to fulfil filter criteria, namely a certain horizontal displacement, a lifetime longer than 48 hours and a decreasing core pressure during the first day. The key findings from the depression and cyclone climatologies are:

1. Depressions are abundant over North Africa due to the frequent formation of lee troughs in spring and heat lows in summer with a maximum occurrence frequency of 40 %, while the occurrence frequency of cyclones is smaller by a factor of ten. This suggests that only few depressions become migrating and long-lived cyclones.

2. The cyclone climatology highlights that 37 % of cyclones affecting North Africa occur in spring. Their centres most frequently lie north of 20° N with a clear cyclone track stretching from south of the Atlas Mountains towards the eastern Mediterranean in agreement with previous studies (Alpert *et al.*, 1990; Hannachi *et al.*, 2011; Maheras *et al.*, 2001; Thorncroft & Hodges, 2000; Trigo *et al.*, 1999). Springtime cyclones predominantly migrate eastwards, and live for three to seven days. The year-to-year variability is largest during this season.

Dust emission is simulated as in Chapter 2 which show large values north of 20° N for December to May. Dust emission amounts are associated with depressions and cyclones within a radius of 10° from the centres. The highlights of the results are:

1. Depressions coincide with 55 % of the dust emission annually and spatially averaged over North African dust sources. Regionally and seasonally up to 90 % of the dust emission amount is associated with them. Embedded mechanisms such as the NLLJ, defined as in Chapter 2, coincide with 12 % of the dust emission associated with depressions annually and spatially averaged. This result is in agreement with findings from Chapter 2 (Fiedler *et al.*, 2013a) indicating that NLLJs form frequently along the margins of the Saharan heat low.

2. In contrast to depressions, migrating and long-lived cyclones are rare and associated with only 4 % of the dust emission annually and spatially averaged. The largest emission coinciding with cyclones occurs during spring over Libya and small areas south of the Atlas mountains with 15−25 %. Despite this small total fraction, their associated emission is particularly intense exceeding the climatological mean by a factor of four to eight which is larger than the anomaly factor for depressions in most months.

3. In summer, 5−15 % of the dust emission is associated with cyclones in isolated areas in West Africa. Here, AEWs amplify sufficiently to form near-surface signatures (Thorncroft & Hodges, 2000). The majority of the emissions within the cyclone-affected area is found in the southwestern quadrant, where northerly winds and potentially NLLJs occur (Knippertz & Todd, 2010). NLLJs coincide with 10−20 % of the monthly emissions associated with cyclones during summer while less than 10 % coincide with NLLJs and cyclones during the rest of the year. Larger dust emissions at the eastern side of AEWs would be expected, if haboobs were represented more realistically. Their missing parameterisation and the underestimated strength of AEWs in the ECMWF model (Agustí-Panareda *et al.*, 2010) probably lead to an underestimation of associated winds and dust emission.

4. Dust emission associated with springtime cyclones is substantially larger during mid-day than at night by a factor of three to five. This result suggests that the growth of the boundary layer into the baroclinic zone of the cyclone is important for generating dust-emitting winds.

5. The reduction of dust emission through soil moisture is on the order of 10 %.

6. Large parts of the climatological dust emission maximum between November and May north of 20° N shown in Chapter 2 (Fiedler *et al.*, 2013a) are not associated with depressions and cyclones investigated here. Harmattan surges developing in consequence of post cold frontal ridging are proposed as another mechanism capable of emitting large amounts of dust aerosol. This dust storm type will be subject of future work.

CHAPTER 5

Evaluation of dust emission in the Earth system model from the UK Met Office

5.1 Motivation

Studies on aerosol-climate effects and estimates of the atmospheric dust load are often based on a global aerosol-climate model (GACM). Inter-comparing the annual and monthly climatologies of mineral dust simulations from different models show large uncertainties (e.g. Huneeus *et al.*, 2011; Textor *et al.*, 2006). Global dust emission estimates range from 500 Tg to 4400 Tg per year for size bins mostly below 10 μm while the mean aerosol optical depth (AOD) has values of $0.02-0.035$ (Huneeus *et al.*, 2011, AeroCom for year 2000). North Africa as the globally largest dust source region is herein particularly important with estimates of the mineral dust emission varying between 400 Tg and 2200 Tg per year (Huneeus *et al.*, 2011).

Determining the dominant reason for the variety of dust emission simulations is rather complicated due to different processes involved and feedbacks within a coupled GACM. Textor *et al.* (2006) suggests that dust emission between models varies because of different wind speed distributions. The near-surface wind speed in a model represents the mean value of the grid box which are typically $100-200$ km wide in a GACM. This suggests that a coarser model resolution implies lower wind speeds. However, physical parameterisations account for sub-grid scale processes which can include resolution-dependent tuning factors. Also wind-generating meteorological processes may be represented differently. For instance, a model of coarser spatial resolution can have larger wind speeds than a higher resolution configuration, if the synoptic-scale pressure patterns differ (e.g. Marsham *et al.*, 2011).

A systematic approach is needed to understand model differences affecting dust emission. Here, the wind speed and dust emission from the Earth system model HadGEM2-ES are analyzed. Previous studies found that HadGEM2-ES produces global dust emissions at the upper end of the AeroCom range with 3311 +/- 227 Tg per year for particles smaller than 10 μm (Bellouin *et al.*, 2011; Huneeus *et al.*, 2011). The annual global dust emission amount by HadGEM2-ES for dust particle sizes of 0.03−30 μm is even larger with 8000 Tg per year (Bellouin *et al.*, 2011). The large dust load affects the model performance for AOD which agrees only well with station observations when mineral dust aerosol is absent (Bellouin *et al.*, 2011). Collins *et al.* (2011) and Woodward (2011) show that HadGEM2-ES produces substantially more dust aerosol than the atmosphere-only model version HadGEM2-A. African dust emission is overestimated over the Sahel, which is assigned to an increased fraction of bare soil due to vegetation die-back and higher near-surface wind speeds in the coupled model (Collins *et al.*, 2011).

Here, seasonal and diurnal differences of the wind speed for mineral dust emission in HadGEM2-ES are analyzed and compared against the climatology of ERA-Interim for a time period of 30 years. The historical simulation of HadGEM2-ES from the Coupled Model Intercomparison Project Phase Five (CMIP5) is chosen due to its usage in the AR5 of the IPCC. Since CMIP5 does not require data with hourly resolution as a standard output, the historical experiment for 1980−2010 was re-run by Nicolas Bellouin, University of Reading, for the purpose of this PhD work. This data set offers the opportunity to gain new insights into the performance of a GACM from the perspective of meteorological processes for dust emission. Compared to the coarser temporal resolution available from CMIP, this data set is unique for analysing processes on sub-daily scales over a climatological time period. The focus is set on the NLLJ as an important driver for dust emission (Chapter 2). In addition to HadGEM2-ES, results from the developmental model version HadGEM3-A are evaluated by comparing a free-running against a nudged simulation. These simulations with HadGEM3-A were run by Kirsty Pringle, University of Leeds for this PhD work and served also as the data basis for the trainee project of Master student Christian Weder, University of Hamburg, who was supervised in collaboration with Peter Knippertz.

5.2 Method

5.2.1 HadGEM2-ES

The Earth system model HadGEM2-ES is chosen for investigating the representation of dust emission and NLLJs for generating winds sufficiently large for emitting dust. HadGEM2-ES was developed at the UK Met Office (Bellouin *et al.*, 2011; Collins *et al.*, 2011; Martin *et al.*, 2011). It operates at a horizontal resolution of 1.875°x1.25° with 38 vertical levels up to 39 km. The coupled ocean has a horizontal resolution of 1° increasing to 1/3° towards the equator and 40 vertical layers. While the temporal integration in the atmospheric component has a time step of 30

Table 5.1: *Particle size distributions.*

Particle size bin	Woodward (2001)	Tegen *et al.* (2002)
1	0.0316$-$0.1 μm	0.1$-$0.288 μm
2	0.1$-$0.316 μm	0.0288$-$0.871 μm
3	0.316$-$1 μm	0.871$-$2.63 μm
4	1$-$3.16 μm	2.63$-$7.94 μm
5	3.16$-$10 μm	7.94$-$23.99 μm
6	10$-$31.6 μm	23.99$-$72.44 μm
7		72.44$-$218.77 μm
8		218.77$-$660.69 μm

minutes, the coupling to the ocean is hourly. The model is run with the historical CMIP5 setup (Bellouin *et al.*, 2011; Jones *et al.*, 2011) for the period 1980$-$2010 with hourly output of variables relevant for this PhD work.

Dust emission in HadGEM2-ES is calculated interactively every time step (30 min) with the dust emission scheme from Woodward (2001) and updates described in Woodward (2011). The parameterisation of dust emission is based on Marticorena & Bergametti (1995) where the horizontal dust emission flux $F_h^{Woodward}$ is calculated by

$$F_h^{Woodward} = 2.61\rho(1 - V_{frac})u_*^3 \left(1 + \frac{u_{*t}}{u_*}\right) \left(1 - \left(\frac{u_{*t}}{u_*}\right)^2\right) \frac{m_{rel}}{g}, \qquad u_* > u_{*t}. \tag{5.1}$$

The flux is calculated for nine particle size bins capturing 0.06$-$2000 μm and listed in Table 5.1. Here, ρ is the air density, V_{frac} the vegetation fraction, u_* the surface friction velocity, $u_{*,t}$ the threshold friction velocity, m_{rel} the relative mass of dust in the size bin and g the gravitational acceleration. The air density, friction velocity and vegetation fraction are interactively calculated in the model. Bagnold (1941) serves as the basis for the threshold friction velocities that are adapted to account for different spatial and temporal scales in HadGEM2-ES. The description of the effect of soil moisture follows Fécan *et al.* (1999) and is also adjusted to account for different scales. A global data set of the clay, silt and sand content with a horizontal resolution of 1° (Wilson & Henderson-Sellers, 1985) is used for deriving the relative mass m_{rel} under the assumption of size distributions. The vertical flux F_v is calculated for six particle size bins of up to 60μm with

$$F_v^{Woodward} = F_h^{Woodward} \cdot 10^{(13.6 f_c - 6)} \tag{5.2}$$

where f_c is the clay fraction of the grid box (Marticorena & Bergametti, 1995). The effect of surface roughness on dust emission has been omitted in Woodward (2001). Potential dust sources are parameterised following Ginoux *et al.* (2001) with a preferential source term S that depends on the surrounding orography:

$$S = \left(\frac{z_{max} - z}{z_{max} - z_{min}} \right)^3 \tag{5.3}$$

with the local altitude z and maximum (minimum) altitude z_{max} (z_{min}) in the surrounding area of less than 10^o distance. This parameterisation describes orographic sinks as preferential dust sources, but observations indicate that also other areas may emitt dust aerosol (compare Section 1.2.2).

5.2.2 Intercomparison

Climatologies of HadGEM2-ES are compared against ERA-Interim forecasts which serve as a benchmark. The ERA-Interim data gives a reasonable estimate for the past state for the atmosphere over North Africa (Chapter 3). Meteorological variables from the models are compared directly. However, conclusions from the direct comparison of the dust emission from HadGEM2-ES (H2ES-I) against the results of the dust emission model by Tegen *et al.* (2002) driven by ERA-Interim wind speeds (T-EI-O) would make it difficult to seperate the effect of wind speed and the dust parameterisation on the emitted amount. Although both parameterisation schemes are based on ideas proposed by Marticorena & Bergametti (1995), they use different soil libraries, potential dust sources, particle size distributions and tuning settings. The scheme by Tegen *et al.* (2002) uses eight particle size bins shifted towards larger particle radii (Table 5.1) which suggests a larger emission mass compared to the parameterisation by Woodward (2001). The saltation flux F_h^{Tegen} in Tegen *et al.* (2002) is calculated for these bins by:

$$F_h^{Tegen} = \frac{\rho}{g} u_*^3 \left[\left(1 + \frac{u_{*t}}{u_*} \right) \left(1 - \frac{u_{*t}^2}{u_*^2} \right) s \right], \qquad u_* > u_{*t}. \tag{5.4}$$

where s is the relative surface of the particle size. The vertical dust emission flux F_v^{Tegen} is:

$$F_v^{Tegen} = F_h^{Tegen} A_{eff} E_{moist} \alpha \tag{5.5}$$

with the effects of soil moisture E_{moist} and a particle-size dependent scaling parameter α that is set to 10^{-5} cm^{-1} in potential dust source. The reduction of emission by vegetation increase is considered in A_{eff} given by

$$A_{eff} = 1 - 4 \left(V_{max} f_{shrub} + V_{month} f_{grass} \right). \tag{5.6}$$

This factor decreases with a growing fraction of shrub f_{shrub} and maximum vegetation cover V_{max} as well as monthly varying vegetation V_{month} and fraction of grass f_{grass}. Soil types are based on Kaplan (2001) and vegetation cover is prescribed as monthly climatology from Tucker *et al.* (2005). Potential dust sources in the simulations with Tegen *et al.* (2002) are derived from the SEVIRI satellite product (Schepanski *et al.*, 2009, 2007) as areas with at least two observed dust emission events (Fiedler *et al.*, 2013a,b; Heinold *et al.*, 2013). The simulation with Tegen *et al.* (2002) use a roughness length of 0.001 cm in potential dust sources, motivated by otherwise missed emission from observed dust sources in complex terrain (pers. comm. B. Heinold, 2012).

Further uncertainties would result from the half hourly emissions online against three-hourly emission offline. In order to reduce uncertainties for the desired intercomparison of dust emission, the offline dust emission model by Tegen *et al.* (2002) is run with instantaneous 10m-wind speeds from HadGEM2-ES (T-H2ES-O). The results of T-H2ES-O are compared against the calculation with three-hourly instantaneous 10m-wind speeds from ERA-Interim forecasts (T-EI-O, details in Chapter 2). Instead of the six-hourly re-analysis product from ERA-Interim, the short-term forecasts are used due to the higher temporal resolution of three hours that is important for the diurnal cycle of dust emission. These forecasts are close to the re-analysis product at 18, 00 and 06 UTC (Chapter 3, Fiedler *et al.*, 2013a). Another offline dust emission calculation is driven with hourly instantaneous 10m-wind speeds from MERRA re-analysis (T-ME-O) as in chapter 3. The seasonal mean dust emission from T-ME-O is shown along with T-EI-O to illustrate the diversity of the best estimates of dust emission with state-of-the-art data sets. More detailed analysis of the diurnal cycle of dust emission from the calculations with MERRA is not shown for the purpose of validation because of the overestimation of near-surface wind speeds causing dust emission at night and the underestimation of wind speeds for dust emission during the day in MERRA (Chapter 3). An overview of the data sets used in this chapter is given in Table 5.2.

Soil moisture is not included in these offline calculations for ruling out the influence of different soil moisture fields of the models. The presence of soil moisture weakens dust emission along the southern margins of the Saharan desert between May and September and along the northern fringes of the continent between December and May (Chapter 4). Other external driving data sets for the offline dust model, e.g. potential dust sources, are chosen as previously (Fiedler *et al.*, 2013a). These are described in Chapters 1−2 and are the same for all offline calculations here. Dust emissions are calculated for the entire period of the HadGEM2-ES simulation (1980−2009). December 2000 and December 2005 are excluded from the

Experiment	Dust emission	Wind speed	Soil moisture	Time period
H2ES-I	interactive	HadGEM2-ES	yes	1980−2009
T-H2ES-O	offline	HadGEM2-ES	no	1980−2009
T-EI-O	offline	ERA-Interim forecasts	no	1980−2009
T-ME-O	offline	MERRA re-analysis	no	1980−2009
H3ES-I	interactive	HadGEM3-A	yes	2003−2007
H3ES-I-N	interactive	HadGEM3-A nudged	yes	2003−2007

Table 5.2: *Experiment overview used in this chapter. The interactive dust emission parameterisation scheme is described in Woodward (2011) and the offline dust emission model in Tegen* et al. *(2002). Nudging of H3ES-I-N is six-hourly with meteorological fields from ERA-Interim.*

presented analysis due to unrealistic large wind speeds of up to 130 ms^{-1} and missing data for some hours towards the end of the months in HadGEM2-ES. These winds are likely caused by unrealistic “gridpoint storms” leading to a model crash (pers. comm. N. Bellouin, University of Reading, 2014). Including these unrealistic wind speeds would cause an overestimation of the emitted mass in December by 30 % in T-H2ES-O illustrating the importance of realistic wind speeds for dust emission.

5.2.3 HadGEM3-A

The model performance of the developmental model version HadGEM3-A is also investigated for evaluating the progress of identified model differences between HadGEM2-ES and ERA-Interim. For HadGEM2-ES dust-emitting winds are evaluated with the aid of the offline dust emission model. While such an approach could have been chosen for winds from HadGEM3-A too, an analysis of HadGEM3-A winds in context with the interactive dust scheme would be beneficial for understanding the model behaviour as a whole. For the purpose of this validation two HadGEM3-A experiments are run and provided by Kirsty Pringle (University of Leeds, 2012): (1) a free-running model simulation (H3ES-I) and (2) an experiment where the potential temperature and the horizontal wind components are nudged six-hourly to ERA-Interim re-analysis (H3ES-I-N). The nudging is applied at model levels but likely not within the boundary layer (pers. comm. Sean Milton, 2014). The solution within the boundary layer is nevertheless influenced by the nudging of the free troposphere, e.g. by changes in the synoptic-scale pressure gradient that affects NLLJs. Both experiments provide hourly information for wind speed and dust emission for the time period 2003−2007. The atmosphere model version is based on the UM 7.7 Global Atmosphere 3.0 in which the boundary layer and convection parameterisation were updated compared to HadGEM2 (Bellouin *et al.*, 2013, and references therein). Especially the improved representation of the boundary layer is expected to have a positive effect on the modelled dust emission compared to HadGEM2-ES.

5.3 Evaluation of HadGEM2-ES

5.3.1 Dust emission intercomparison

Comparing the annually averaged dust emission amount shows substantial differences exceeding one order of magnitude. The largest emission amount is simulated by H2ES-I with an annual mean of 4067 Tg for particle sizes of 0.1−60 μm. About half of this emission amount is obtained with T-H2ES-O, namely 1947 Tg for particle radii of 0.1−660 μm. T-H2ES-O is five times larger than the dust mass emitted by T-EI-O with 425 Tg per year. Compared to T-ME-O with 280 Tg per year, the T-H2ES-O is even larger by about a factor of six.

Figure 5.1 shows the fraction of dust emission per season for H2ES-I and all offline dust emission calculations with the model by Tegen *et al.* (2002). T-EI-O produces 30 % of its annual dust emission between December and February, 40 % in March to May, 20 % in June to August and a minimum of 10 % between September and November. Dust emission in T-ME-O is coherent with this seasonal distribution of the total dust amount in winter and summer, but has relatively less emission in spring and larger values in autumn by roughly +/-10 % each. T-H2ES-O and H2ES-I should ideally lie within the spread between T-EI-O and T-ME-O of 10 % in spring and autumn and 5 % in winter and summer. The seasonal fraction of the H2ES-I shows good agreement for winter and lies within the spread for autumn and spring. The summertime emission fraction, however, is overestimated by 10 %. Looking at T-H2ES-O gives a rather different perspective on the model performance for simulating the seasonal fraction of dust emission. While the spring and autumn fractions from T-H2ES-O are within the re-analysis spread, the seasonal fractions for summer and winter in T-H2ES-O are under- and overestimated by 10 %, respectively. The different seasonal fractions from the intercomparison of H2ES-I and T-H2ES-O against T-EI-O underlines the influence of other factors than wind speed resulting from the different treatment of dust emission. In order to identify the regions with the largest differences, spatial patterns of the seasonal mean dust emission are analyzed next .

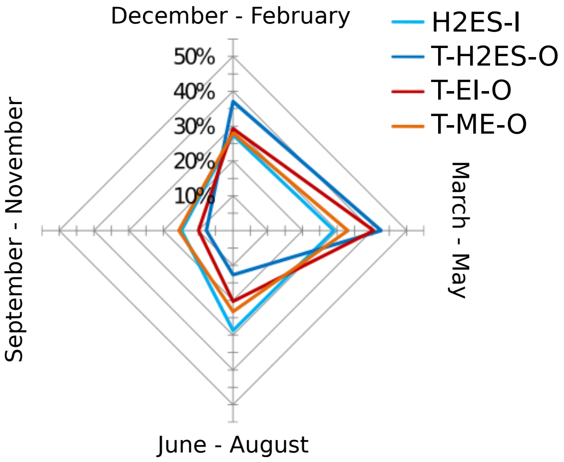

Figure 5.1: *Climatology of seasonal contributions to annual dust emission. Seasonal fraction of total dust emission for December–February, March–May, June–August and September–November based on online dust emission scheme from HadGEM2-ES (H2ES-I, light blue) and offline dust emission model driven by three-hourly 10m-wind speed from HadGEM2-ES (T-H2ES-O, dark blue), driven by three-hourly 10m-wind speed from ERA-Interim forecasts (T-EI-O, red) as well as hourly 10m-wind speeds from MERRA re-analysis (T-ME-O, orange) for 1980–2009.*

The dust emission is shown in Figure 5.2 averaged in gm^{-2} per season. In winter and spring, the largest dust emissions in H2ES-I are simulated for the southern fringes of the Saharan desert and parts of West Africa with seasonally 80–600 gm^{-2} (Figures 5.2a–b). These areas keep being active in the remaining months of the year, although peak emissions decrease to values below 100 gm^{-2} per season in most areas (Figures 5.2c–d). The dust emission from these areas in the Sahel are dominant in H2ES-I while little emission is produced in T-H2ES-O. This is associated with larger bare soil fractions due to vegetation die-back in H2ES-I caused by a precipitation deficit during the West African monsoon (Birch *et al.*, 2014; Collins *et al.*, 2011; Woodward, 2011). The small emission over parts of Mali and Mauritania in H2ES-I coincide with small values of the preferential source term used in the dust emission scheme by Woodward (2011). The Bodélé Depression is active throughout the year with maxima of up to 600 gm^{-2} between September and May. Northern margins of the Sahara have maximum dust emission amounts of up to 400 gm^{-2} in spring and summer (Figures 5.2b–c). Interestingly, dust emission in West Africa is larger in winter and spring with around 100 gm^{-2} per season than in summer. Summer is, however, the season when the maximum is expected over West Africa from T-EI-O and T-ME-O.

At a first glance, T-H2ES-O shows a similar annual cycle like H2ES-I (Figures 5.2e−h). The dust emission patterns, however, are smoother than in H2ES-I. Peak emissions are mostly reduced to values of 100−200 gm^{-2} in winter and spring (Figures 5.2e−f). Similar to H2ES-I, dust emission in the Bodélé Depression remain comparably large between September and May with maximum emissions of seasonally 400−600 gm^{-2}. The West African dust maximum in winter and spring is more pronounced in T-H2ES-O with seasonally 60−80 gm^{-2} over large areas in Mali, Mauritania and Algeria. Similar dust emissions are calculated for the northern fringes of the continent in winter that increases in some areas to seasonally 100−200 gm^{-2}. Maximum emissions between June and November are mostly smaller with 20−80 gm^{-2} (Figures 5.2g−h).

Compared to T-EI-O (Figures 5.2i−l), the dust emission in T-H2ES-O are substantially larger throughout the year. The larger dust emission is most apparent in winter and spring over large areas of West Africa (Figures 5.2i−j). Here T-H2ES-O has widespread emission of seasonally 200 gm^{-2} which is ten times larger than values in T-EI-O. Emissions in T-H2ES-O remain larger in summer and autumn with typically 60−100 gm^{-2} per season compared to mostly 10−40 gm^{-2} in T-EI-O (compare Figures 5.2g−h against 5.2k−l). T-ME-O is shown for providing an uncertainty estimate for the baseline dust emission. T-EI-O and T-ME-O show the same spatial patterns for each of the seasons, although the latter has smaller peak emission in springtime North Africa and summertime West Africa (more details in Chapter 3). These differences are, however, small compared to the differences found between T-EI-O and T-H2ES-O. Also the general level of the dust emission amounts in T-H2ES-O is closer to H2ES-I than to T-EI-O. This result indicates that the wind speeds used in the same dust emission model have a larger impact on the calculated dust emission amount than differences between dust emission parameterisations. Possible differences of meteorological processes for dust emission in T-H2ES-O and T-EI-O are investigated in the following.

5.3.2 Diurnal cycle of dust emission and 10m-wind speeds

The diurnal cycle of dust emission and 10m-wind speed provides first indications for the meteorological processes driving dust emission. Heinold *et al.* (2013) show that the downward mixing of momentum from NLLJs dominates the dust emission during the mid-morning while haboobs are the prevailing mechanism in the late afternoon and evening based on a 40-day convection permitting simulation for summertime West Africa. Nighttime emissions in these calculations are a mixture of

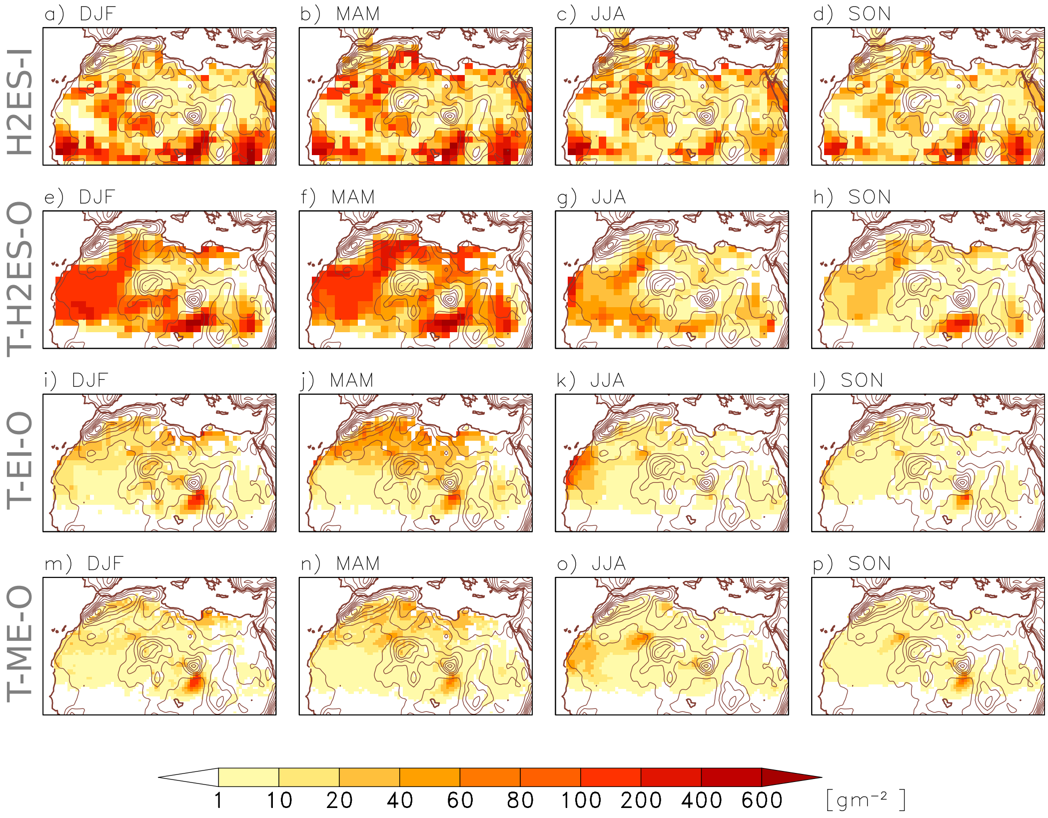

Figure 5.2: *Dust emission climatology. Seasonal mean dust emission for (from left to right) December–February, March–May, June–August and September–November based on (first row, H2ES-I) the online dust emission scheme from HadGEM2-ES, (second row, T-H2ES-O) offline dust emission model driven by three-hourly 10m-wind speed from HadGEM2-ES, (third row, T-EI-O) offline dust emission model driven by three-hourly 10m-wind speed from ERA-Interim forecasts and (forth row, T-ME-O) offline dust emission model driven by hourly 10m-wind speed from MERRA re-analysis for 1980–2009. Please note the non-linear scale for dust emission (shaded). Contours show the terrain height in steps of 200 m.*

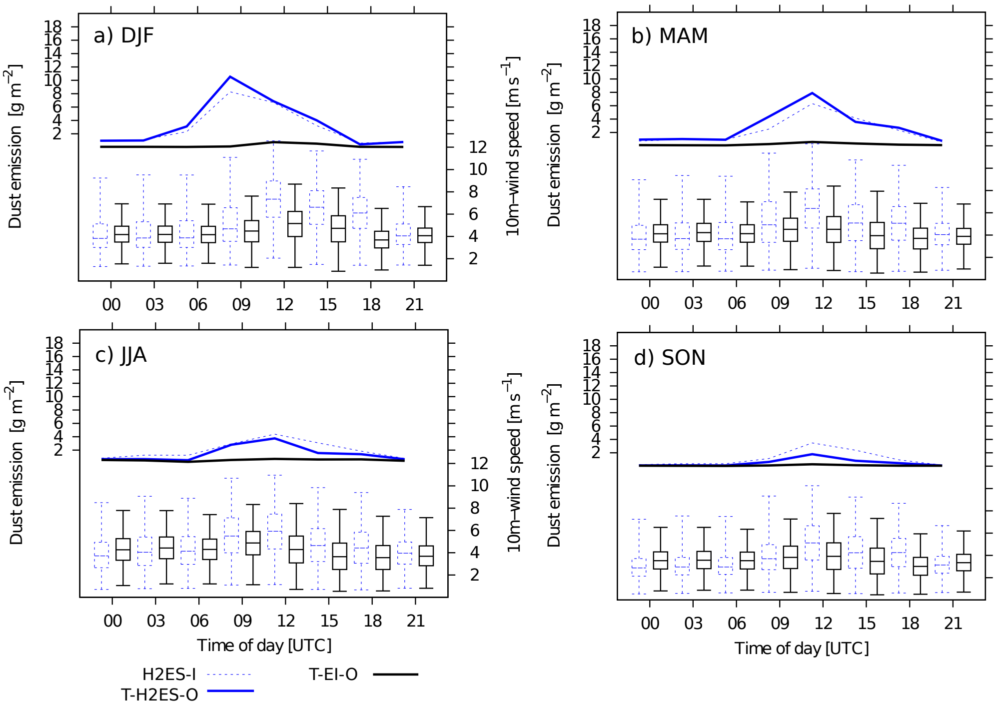

Figure 5.3: *Diurnal cycle of dust emission and 10m-wind speed per season in S1. Dust emission from HadGEM2-ES online (H2ES-I, dashed), HadGEM2-ES offline (T-H2ES-O, blue) and ERA-Interim forecasts offline (T-EI-O, black) at top. Box-and-whisker plots of the 10m-wind speed from HadGEM2-ES (dashed) and ERA-Interim (solid) at bottom. Figure shows three hourly values spatially averaged for sub-domain S1 as seasonal means for (a) December–February, (b) March–May, (c) June–August and (d) September–November for 1980–2009.*

both processes. The occurrence of haboobs is not expected in HadGEM2-ES because of the missing parameterisation of the momentum transport in convective downdrafts and underrepresentation of convective organization (Marsham *et al.*, 2013a). In HadGEM2-ES, dominating emission during mid-day and in the afternoon may rather be linked to the downward mixing of momentum from a layer of large wind speed in the free troposphere when the daytime boundary layer is sufficiently deep. Nighttime and morning emission are expected to be linked to the vertical mixing of momentum from NLLJs (Chapter 2, Fiedler *et al.*, 2013a). The diurnal cycle is used as an indication whether these mechanisms are responsible for larger dust emission in T-H2ES-O compared to T-EI-O.

Figure 5.3 shows the diurnal cycle of dust emission from H2ES-I, T-H2ES-O and T-EI-O as well as box-and-whisker plots of the near-surface wind speed from HadGEM2-ES and ERA-Interim forecasts seasonally averaged for 1980–2009 in the sub-domain S1 over West Africa. The geographical location of S1 is defined as in Chapter 2 and shown in Figure 2.5a. In this region, the differences in the dust emission between T-H2ES-O and T-EI-O are again larger than the differences between T-H2ES-O and H2ES-I. The largest differences of the dust emission between

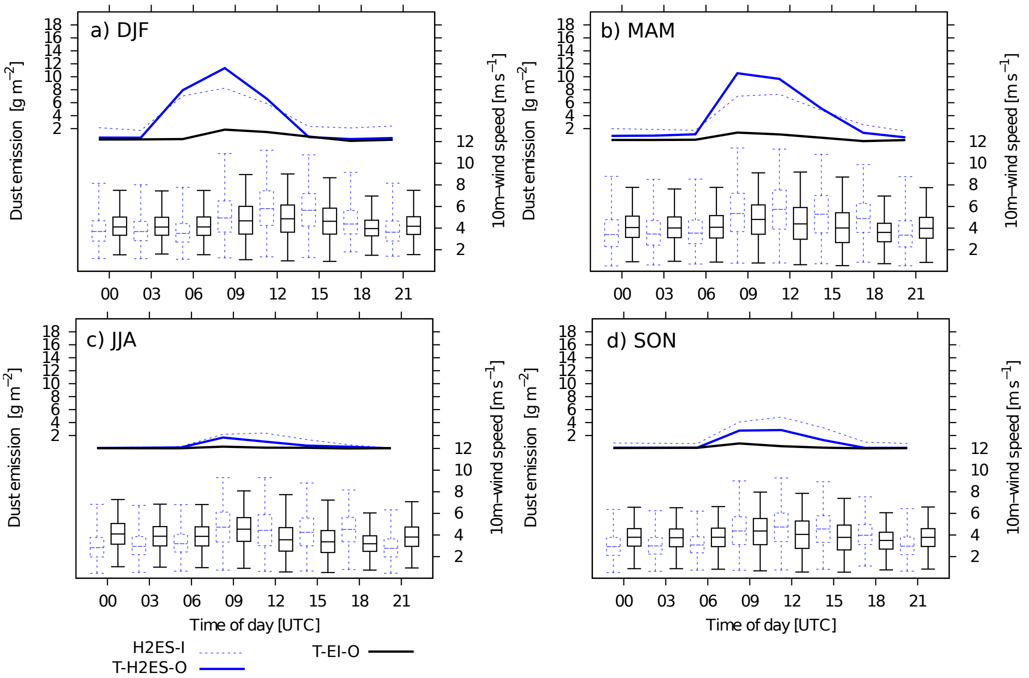

Figure 5.4: *As Figure 5.3 but for S3.*

T-H2ES-O and T-EI-O occur between December and May (Figure 5.3a–b). While T-H2ES-O has peak emissions of 8 gm^{-2} in spring and 12 gm^{-2} in winter, emission in T-EI-O do not have values larger than 2 gm^{-2} in both seasons. H2ES-I has dust emission closer to T-H2ES-O with lower values by up to 2 gm^{-2}. These peak dust emissions occur at 09 UTC in winter and 12 UTC in spring with prior increasing emissions beginning at 06 and 09 UTC, respectively. The diurnal variations in summer and autumn are similar with peaks in the morning, although the magnitude is generally below 4 gm^{-2} (5.3c–d). These mid-morning emissions point to NLLJs as driving mechanisms for dust emission.

Also the diurnal variations of the near-surface wind speed have a clear maximum during the morning and at mid-day, the former of which supports the hypothesis of NLLJs as driving mechanism for dust emission. The largest wind speeds, here shown by the 99%-percentile of the 10m-wind speed, are 11 ms^{-1} at 09 UTC and 12 ms^{-1} at 12 UTC in HadGEM2-ES, compared to 8 ms^{-1} at 12 UTC in ERA-Interim. These wind speeds are well above typical threshold velocities for dust emission. A perfect correlation between the wind speed and dust emission maxima, however, is not seen. For instance the largest wind speeds in HadGEM2-ES occur at 12 UTC, but the peak emission is earlier at 09 UTC. This can be due to surface properties that suppress dust emission in parts of the sub-domain, i.e. the high wind speeds at 12 UTC occur away from dust sources. As a result dust emission may not occur even if a sufficient wind speed is given in the grid box.

A similar diurnal cycle is found in the sub-domain S3 that encloses the Bodélé Depression shown in Figure 5.4 (compare Figure 2.5a for geographical location). Dust emissions are largest at 09 UTC in winter and spring with 12 $\mathrm{gm^{-2}}$ in T-H2ES-O, 8 $\mathrm{gm^{-2}}$ in H2ES-I and 3 $\mathrm{gm^{-2}}$ in T-EI-O (Figures 5.4a−b). The 99%-percentile of the wind speed in HadGEM2-ES at that time is 11 $\mathrm{ms^{-1}}$ spatially averaged. Maxima from HadGEM2-ES are also found at 09 and 12 UTC in summer and autumn, but the dust emission amount from T-H2ES-O does not exceed 2 $\mathrm{gm^{-2}}$ and 4 $\mathrm{gm^{-2}}$, respectively. ERA-Interim has less events at the upper end of the 10m-wind speed distribution and also T-EI-O has much smaller dust emission amounts than T-H2ES-O.

In summary, the mid-morning maxima of both the 10m-wind speeds and the dust emission from T-H2ES-O and H2ES-I in West Africa for December−February and the Bodélé Depression for December−August suggest that the NLLJ is a key driver for emission. Both regions have been identified for frequent NLLJ occurrence based on ERA-Interim (Fiedler *et al.*, 2013a). The NLLJ is further analyzed in the following Section 5.3.3. The mid-day maximum of dust emission and peak winds in springtime West Africa points to strong synoptic-scale pressure gradients in the lower troposphere which will be addressed in Section 5.3.4.

5.3.3 Representation of NLLJs

Occurrence frequency and associated dust emission

The diurnal cycle of dust emission and near-surface wind speed indicates that NLLJs play a role for dust emission. Using the automated NLLJ detection algorithm (Chapter 2) enables a more detailed analysis. The NLLJ occurrence frequency is defined as the percentage of nights showing a NLLJ. In the annual and spatial mean, the NLLJ occurrence frequency from HadGEM2-ES is 27 % that is remarkably close to 29 % found in ERA-Interim for 1980−2009. Figure 5.5 shows the spatial distribution for the occurrence frequency of NLLJs in HadGEM2-ES, in ERA-Interim and the difference between both climatologies. While both models show NLLJ occurrence hot spots with frequencies exceeding 30 % along a distinct band over the southern parts of the Sahara, NLLJ occurrence hot spots in HadGEM2-ES are shifted southwards and appear in a band that is narrower over West Africa than the one in ERA-Interim. Computing the difference between both models shows that NLLJs occur up to 12 % more frequently in southern West Africa in HadGEM2-ES. In contrast to the larger numbers of NLLJ events in the south, nights with NLLJs in the centre, north and west of North Africa are up to 20 % less frequent. Up to 20 %

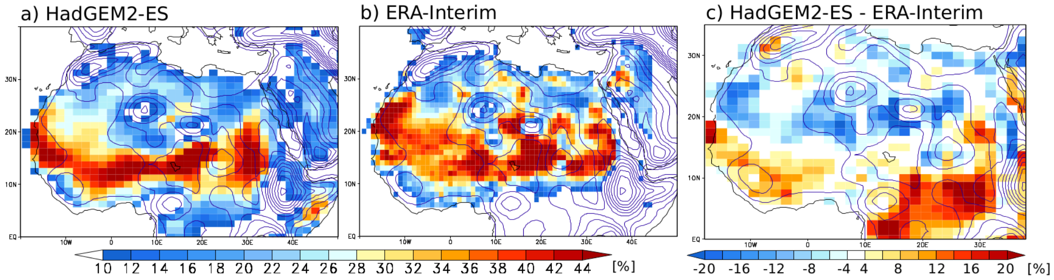

Figure 5.5: *Annual mean climatology of nocturnal low-level jets. Annual mean NLLJ occurrence frequency for (a) HadGEM2-ES, (b) ERA-Interim forecasts and (c) absolute difference of NLLJ frequency from HadGEM2-ES relative to ERA-Interim for 1980–2009.*

more NLLJ nights are found in central Africa. These differences, however, have no implication for dust emission because of the lack of dust sources near the equator.

The seasonal distributions are investigated to identify the time of largest differences. Figure 5.6 shows the seasonal distribution of NLLJ occurrence frequencies in HadGEM2-ES and the differences between HadGEM2-ES compared to ERA-Interim. During winter NLLJs occur more frequently over West Africa in HadGEM2-ES with typical differences of 4–20 % (Figure 5.6a). At the same time, areas in the central Sahara are characterised by less events. In spring, an underestimation compared to ERA-Interim is more widespread, when the west coast and northern parts of Africa have fewer events by -8 % to -20 %, but the Bodélé Depression shows more NLLJs by up to 10 % (Figure 5.6b).

Summertime West Africa shows fewer NLLJs in HadGEM2-ES, while areas further south have larger numbers of NLLJ nights (Figure 5.6c). More NLLJs are also detected over southern areas of Algeria and Libya in summer. At the same time fewer events are detected along the northern coast of Libya. This pattern strongly suggests a southward displacement of NLLJ hot spots along the margins of the Saharan heat low. The shift of the heat low and, therefore, the NLLJ hot spots, may be connected to the southward displaced monsoon in HadGEM2-ES (pers. comm. G. Martin, UK Met Office, 2013). The pattern of more NLLJ in the south and less in the north of West Africa is also found in autumn, but now accompanied by more NLLJ nights in the Bodélé Depression (Figure 5.6d).

The importance of NLLJs for dust emission in T-H2ES-O is measured by quantifying the dust emission amount associated with NLLJs. Figure 5.7 shows the fraction of dust emission in T-H2ES-O that coincides with NLLJs in HadGEM2-ES and the difference to T-EI-O. Particularly winter shows that 25–50 % of the dust emission is associated with NLLJs south of 25° N in T-H2ES-O (Figure 5.7a). Here, T-H2ES-O has larger fractions in western areas compared to T-EI-O by partly more than 30 % (Figure 5.7a). In the Bodélé Depression around 50 % of the emission

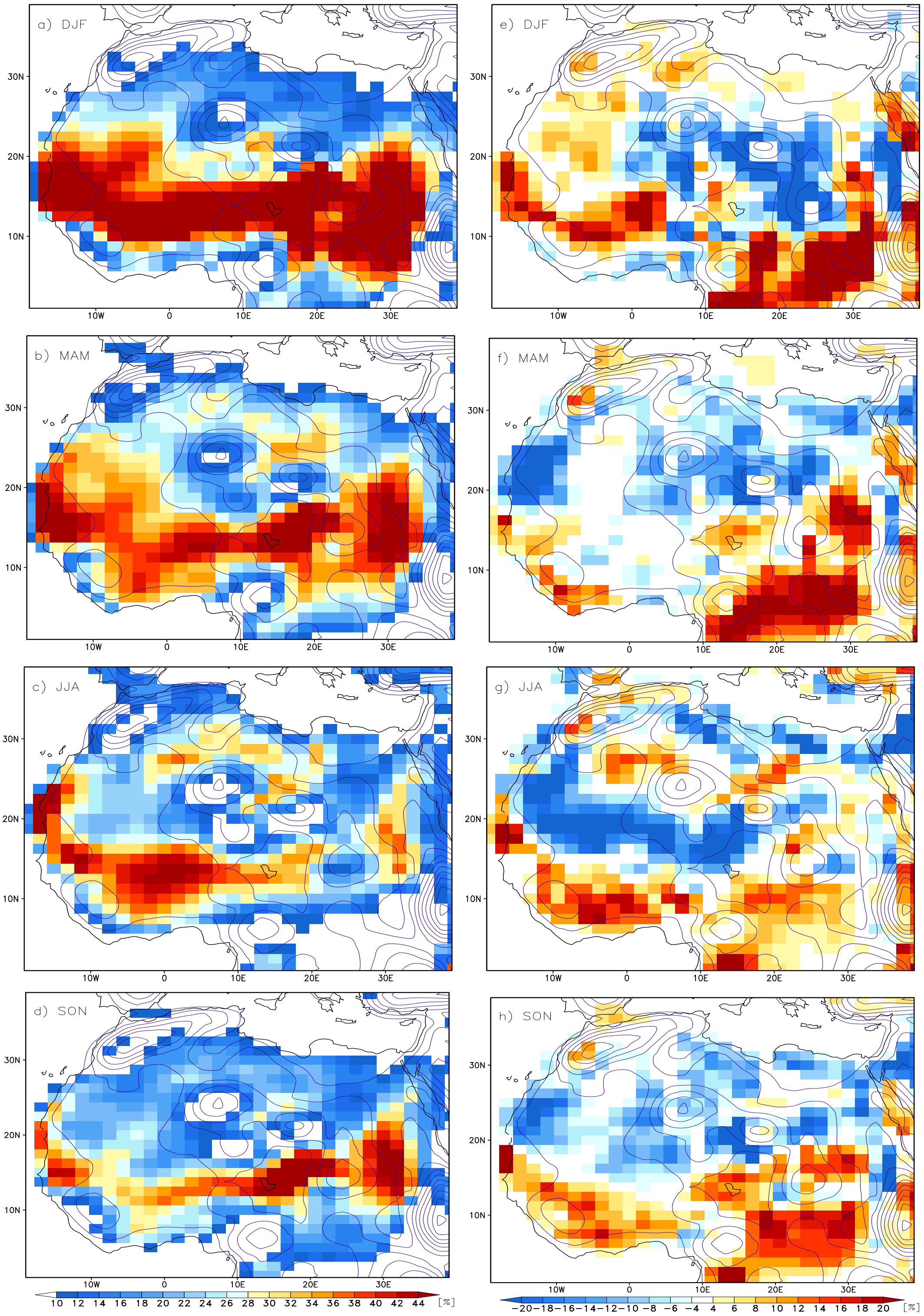

Figure 5.6: *Seasonal mean climatology of nocturnal low-level jets. Seasonal mean NLLJ occurrence frequency for (left, a–d) HadGEM2-ES and (right, e–h) absolute difference of NLLJ frequency from HadGEM2-ES relative to ERA-Interim for 1980–2009.*

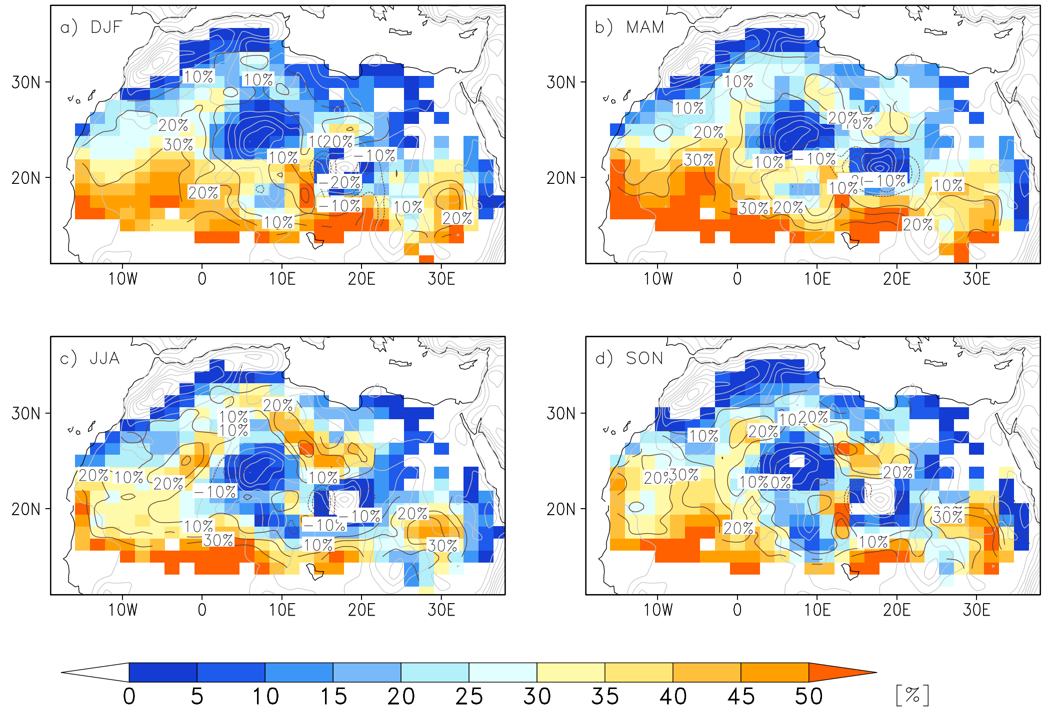

Figure 5.7: *Fraction of dust emission associated with NLLJs. Seasonal mean fraction of dust emission from T-H2ES-O associated with NLLJs for (a) December–February, (b) March–May, (c) June–August and (d) September–November 1980–2009.*

is associated with NLLJ in T-H2ES-O, which is of the same order of magnitude as in T-EI-O. The spatial distribution in spring is similar, but shows NLLJ contributions exceeding 50 % over larger areas in the south than in winter (Figure 5.7b). West Africa south of 20° N has again larger fractions by more than 30 % in T-H2ES-O than with T-EI-O. Dust emission associated with NLLJs increases to values larger than 25 % over most of the north in spring which is at least 10 % larger than in T-EI-O (Chapter 2). The spatial distribution in summer and autumn is similar to spring (Figure 5.7c–d). In Libya, 40 % of the dust emission is associated with NLLJs during summer which is typically by 20 % larger than in T-EI-O. Characteristic amounts of dust emission coinciding with NLLJs over West Africa in summer and autumn are 30 %, which is regionally larger by 10–20 % compared to T-EI-O.

In summary, NLLJs occur more frequently in HadGEM2-ES than in ERA-Interim in southern parts of West Africa throughout the year and in the Bodélé Depression in spring and autumn. Over West Africa, particularly south of 20° N, the fraction of dust emission associated with NLLJs is also larger in HadGEM2-ES. The more frequent number of NLLJs in HadGEM2-ES and the large contributions of NLLJs to dust emission in distinct regions of North Africa support the hypothesis that a different representation of NLLJs in HadGEM2-ES is a cause for larger dust emission during the mid-morning. It is herein interesting to understand whether this is an effect of more frequent NLLJ formation only or whether the wind speed and height of the NLLJ plays a role. The NLLJ characteristics are therefore analysed next.

NLLJ characteristics

The speed and height of NLLJs are important for the downward mixing of momentum to the surface. These variables are investigated for a thorough evaluation of the NLLJ in HadGEM2-ES for the two key regions S1 and S3 covering West Africa and the Bodélé Depression, respectively (compare Figure 2.5a for geographical location of sub-domains). Figure 5.8 shows the NLLJ core wind speed and height in HadGEM2-ES for these sub-domains. In S1, the median wind speed in the NLLJ core is around 11 ms^{-1} at the beginning of the night (Figure 5.8a). Between 21 UTC and 03 UTC their median core wind speed increases to 13 ms^{-1} and persists at this value until 06 UTC. Like in ERA-Interim, a nocturnal or near-morning wind speed maximum in the NLLJ core does not exist, which is consistent with artificially increased vertical mixing in both models (Chapter 1, Brown *et al.*, 2008, 2006; Sandu *et al.*, 2013). The median core wind speed in HadGEM2-ES, however, is larger by 2 ms^{-1} compared to ERA-Interim (compare Figure 2.5 in Chapter 2), probably at least partly related to a weaker enhancement of vertical mixing in HadGEM2-ES (Chapter 1, Brown *et al.*, 2008). The upper end of the wind speed distribution in the core of NLLJs has values of up to 23 ms^{-1}, which is higher than in ERA-Interim with 17 ms^{-1}. This upper end of the distribution is particularly important for dust emission due to the non-linear dependency on the wind speed. The distribution of core wind speeds in S3 shows an earlier increase of the median wind speed from 11 ms^{-1} at 18 UTC to 12.5 ms^{-1} at 22 UTC (Figure 5.8b). The highest value of the 99%-percentile in the early morning is, here, 22 ms^{-1}, therefore slightly lower than in West Africa, but substantially larger than in ERA-Interim with 18 ms^{-1} (Chapter 2).

While the NLLJ wind speed is shifted to higher values in HadGEM2-ES, the NLLJ core height is comparable between both models in S1 (Figure 5.8c). After a sharp decrease of NLLJ core heights in the first evening hours, HadGEM2-ES has median NLLJ heights around 250 m increasing to 350 m for 03−06 UTC. The height during the morning is of the same order of magnitude as the ERA-Interim long-term median for this region. The median NLLJ height in S3 with typically 450 m in HadGEM2-ES differs from ERA-Interim with 380 m (Figure 5.8d), but this difference is too small for being resolved by HadGEM2-ES with levels at 250 m, 410 m and 610 m a.g.l. It is interesting that the NLLJ height is not as sharply decreasing in the early evening in S3 as in S1. This difference is likely caused by a more advanced

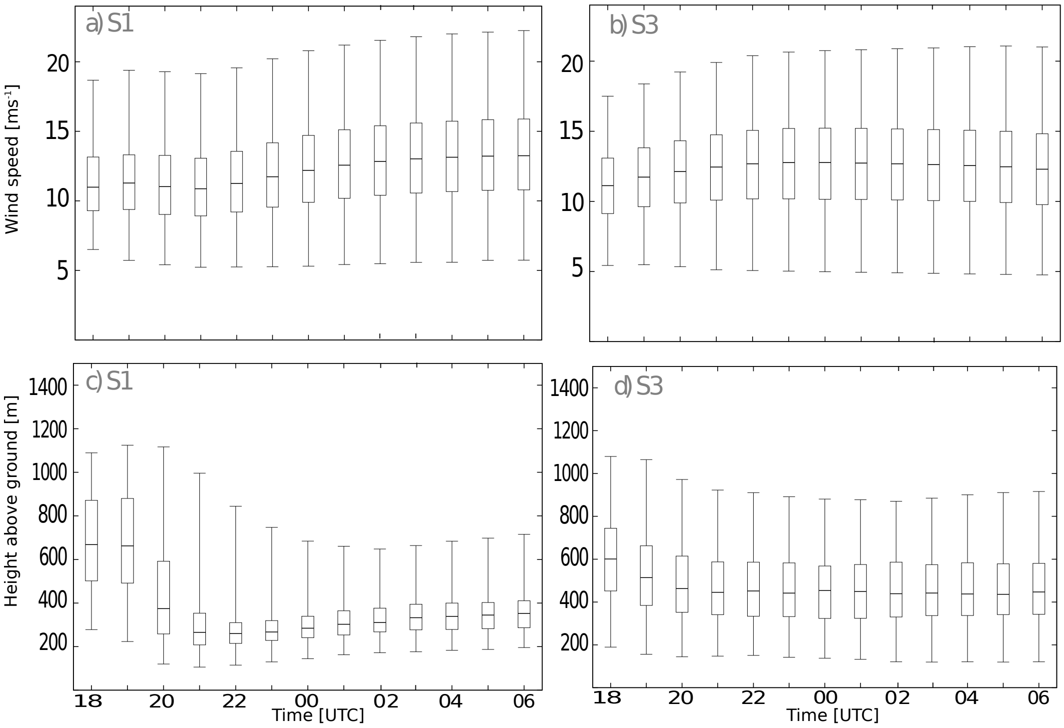

Figure 5.8: *Temporal development of NLLJ characteristics. Hourly box-and-whisker plots showing (from top to bottom) the 99%-, 75%-, 50%-, 25%- and 1%-percentiles of the LLJ core wind speed spatially averaged (a) for sub-domain S1 and (b) S3 and the NLLJ core height spatially averaged (c) for S1 and (d) S3 based on HadGEM2-ES 1989−2009.*

nocturnal development at 18 UTC in S3 located in the east of the continent. Here 18 UTC is about 19 local time (LT). In contrast, 18 UTC in the west is 17 LT which is too early for NLLJ formation over wide areas.

The nocturnal development suggests substantial differences of the NLLJ wind speed between ERA-Interim and HadGEM2-ES. Figure 5.9 shows the comparison of the NLLJ wind speed and height seasonally averaged for S1 and S3. In S1, the NLLJ wind speed is clearly larger in HadGEM2-ES (Figure 5.9a) while the height of the NLLJs is similar (Figure 5.9c). The largest median values of NLLJs in S1 occur in winter with 13 ms^{-1} at 320 m and gradually decrease in the following seasons to 11 ms^{-1} at 270 m in autumn. Compared to ERA-Interim, these median wind speeds are larger by 2−3 ms^{-1} while the 99%-percentiles of the NLLJ wind speed are even larger by up to 5 ms^{-1}. NLLJs in HadGEM2-ES occur at slightly higher altitudes by 50 m in spring and summer, but the coarse vertical resolution does not allow to distinguish between both models. S3 shows similarly large NLLJ wind speeds (Figure 5.9b) at similar altitudes of the NLLJ core (Figure 5.9d). Reasons for larger NLLJ wind speeds at similar altitudes in HadGEM2-ES may be due to model differences in the representation of synoptic-scale conditions and the stability in the nocturnal boundary layer which are investigated in the next two sections.

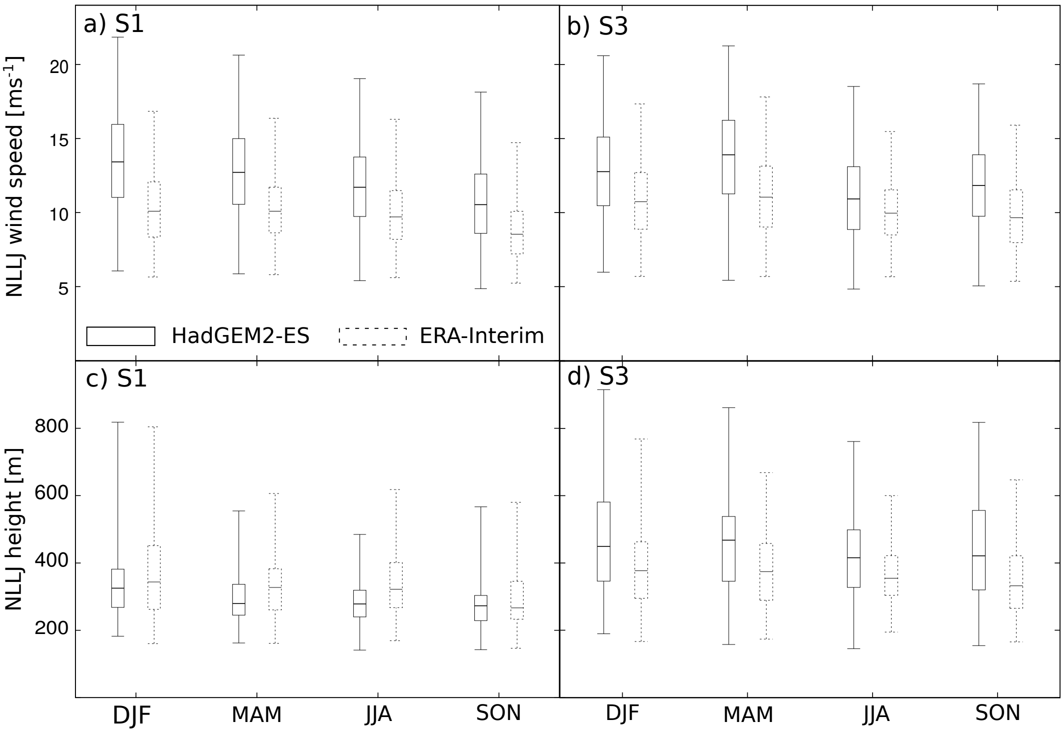

Figure 5.9: *Seasonal climatology of NLLJ characteristics. Box-and-whisker plots of the NLLJ core wind speed spatially averaged (a) for sub-domain S1 and (b) S3 and the NLLJ core height spatially averaged (c) for S1 and (d) S3 at 00 UTC based on HadGEM2-ES and ERA-Interim.*

5.3.4 Synoptic-scale conditions

The synoptic-scale conditions are compared by analysing the monthly mean geopotential height. The 925 hPa level is chosen as a representative height for the core of NLLJs in HadGEM2-ES. Figure 5.10 shows the monthly climatology of the geopotential height at this level at 00 UTC, the time of day when the re-analysis spread is smallest (Chapter 3) and when NLLJs occur. January to April is characterised by a ridge extending from the Azores towards northern Africa and the heat trough in the south. The horizontal pressure gradient across the continent is larger in HadGEM2-ES during these months and particularly strong in January and February (Figure 5.10a−b). As a result, the horizontal gradient of the geopotential height at 925 hPa is larger in HadGEM2-ES which has implications for the geostrophic wind as a first-order driver of the actual wind speed.

In order to quantify the contribution from differences in the synoptic-scale conditions between both models, the geostrophic wind at 925 hPa $|\vec{v_g}| = \sqrt{u_g^2 + v_g^2}$ is calculated from the geopotential height ψ and the latitude-dependent Coriolis parameter f following (e.g. Stull, 1988):

$$u_g = \frac{1}{f}\frac{\Delta\psi}{\Delta y} \qquad (5.7)$$

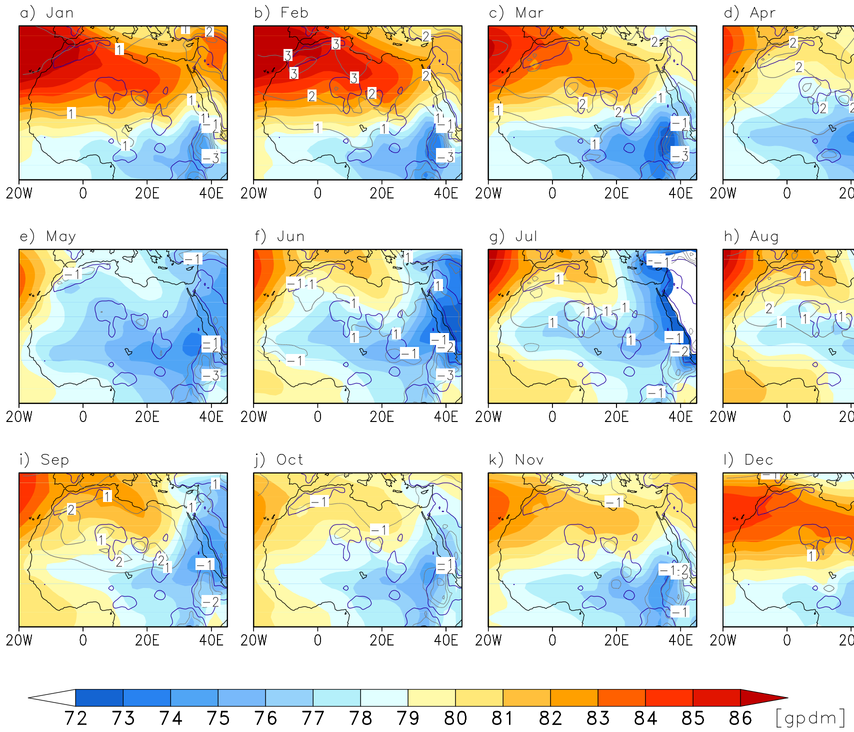

Figure 5.10: *Climatology of geopotential height at 925 hPa at 00 UTC. Monthly mean geopotential height at 925 hPa from HadGEM2-ES (shaded) and difference of HadGEM2-ES minus ERA-Interim re-analysis (contours) for 1989–2009. Note that 925 hPa lies below the surface in mountainous terrain causing differences between the model there.*

$$v_g = -\frac{1}{f}\frac{\Delta\psi}{\Delta x}. \tag{5.8}$$

Figure 5.11 shows the seasonal mean geostrophic wind at 925 hPa. At that level $|\vec{v_g}|$ is larger in HadGEM2-ES by up to 4 ms^{-1} over all southern sub-domains during winter (Figure 5.11a). Similarly, larger geostrophic winds are found during spring, but the spatial extent of areas with larger $|\vec{v_g}|$ in HadGEM2-ES is smaller. Since $|\vec{v_g}|$ is a strong control of the NLLJ wind speed, their larger values in HadGEM2-ES in S1 and S3 during winter and spring are likely causally related.

The conditions at 12 UTC shows similar results for these months. Differences in the geopotential height between HadGEM2-ES and ERA-Interim are larger than the spread in the re-analysed mean sea level pressure, although the spread amongst different re-analysis products is largest at mid-day (Chapter 3). The stronger geostrophic Harmattan winds at that time, consistent with a larger gradient in the geopotential height, likely cause the larger 10m-wind speeds and dust emission during mid-day in S1 and S3 during winter and spring in HadGEM2-ES.

May to September is dominated by the establishment of the heat low over West Africa (Figure 5.10e–i). The heat low is shifted southwards in HadGEM2-ES which is connected to a southward displaced West African monsoon system (pers. comm.

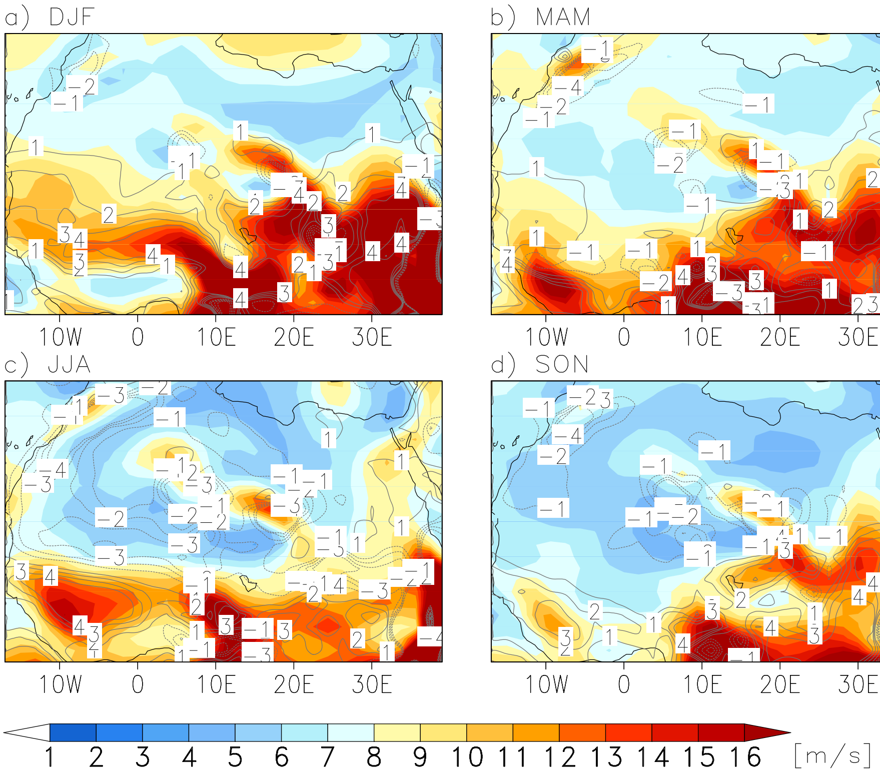

Figure 5.11: *Climatology of geostrophic wind at 925 hPa at 00 UTC. Seasonal mean geostrophic wind at 925 hPa from HadGEM2-ES (shaded) and difference of HadGEM2-ES minus ERA-Interim re-analysis (contours) for 1989–2009. Note that 925 hPa lies below the surface in mountainous terrain causing differences between the model there.*

G. Martin and C. Birch, UK Met Office, 2013). Along with the shift of the heat low the position of NLLJ occurrence hot spots along the margins change (compare Figure 5.6g). At the same time smaller geostrophic winds are found for HadGEM2-ES over most areas in the north and in the central Sahara, contrary to areas along the southern margins of the heat low with geostrophic wind speeds partly larger by 4 ms^{-1} (Figure 5.11c). Smaller values of $|\vec{v_g}|$ over most of S1 are not consistent with the larger NLLJ wind speeds in summer, so it is likely that mechanisms other than the synoptic-scale conditions dominate here. Similarly, S3 has not as large a model difference in $|\vec{v_g}|$ during summer as earlier in the year, so again other mechanisms are likely to contribute more to strong NLLJs.

From October onwards, the heat low retreats to the southeast while the ridge over the north strengthens again (Figure 5.10j−l). These conditions are similarly simulated by HadGEM2-ES and ERA-Interim forecasts. Since the mean pressure gradient over West Africa is not affected as much as at the beginning of the year, the geostrophic wind speed differences are smaller (Figures 5.11d). Only areas close to the wintertime heat low in the east and in the Bodélé Depression show larger geostrophic winds in HadGEM2-ES. Over West Africa, weaker boundary layer mixing under stable stratification in HadGEM2-ES (Brown *et al.*, 2008) may contribute more to the larger NLLJ wind speeds during summer and autumn which is analysed next.

5.3.5 Stability associated with NLLJs

In addition to the geostrophic wind, the strength of NLLJs is determined by the low-level stability and the potential momentum loss at the NLLJ level due to vertical mixing (Chapter 1 and 2). Figures 5.12 and 5.13 show the seasonally averaged diurnal cycle of stability characteristics associated with NLLJs for the sub-domains S1 and S3, respectively. The 1%-percentile of the vertical gradient of the virtual-potential temperature as a measure of the minimum stability below the NLLJ core is similar in both models due to the applied threshold for NLLJ detection. However, also the median is often similar in both models, particularly in S1 during spring from 21 to 06 UTC (Figure 5.12b). A small tendency towards larger nocturnal stability below the NLLJ core in HadGEM2-ES is found for S1 during summer and autumn (Figure 5.12c−d) and towards less stable conditions for S3 during winter and spring (Figure reffig:ri-stab-seas-MEa−b). The larger stability suggests a stronger frictional decoupling and therefore the possibility of developing larger NLLJ wind speeds despite the smaller geostrophic winds in this region and season. Weaker stability, however, could imply weaker winds in the NLLJ if all other conditions are similar,

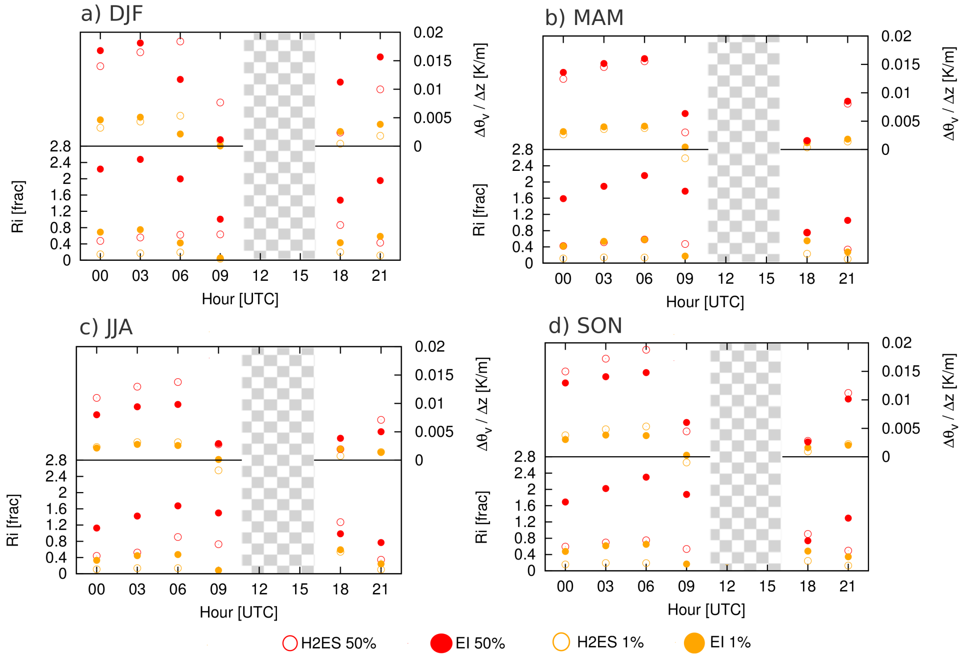

Figure 5.12: *Seasonal mean diurnal cycle of stability characteristics associated with NLLJs. Shown are the mean diurnal cycles for (a) December–February, (b) March–May, (c) June–August and (d) September–November for 1980–2009 of the 1 % (orange) and 50 % (red) percentiles for (top) the vertical gradient of the virtual potential temperature* $\Delta\theta_v/\Delta z$ *and (bottom) the gradient Richardson number Ri spatially averaged for NLLJ events in sub-domain S1 for HadGEM2-ES (empty circles) and ERA-Interim (filled circles). Values are calculated between the NLLJ core and the lowest model level. Sample sizes at 12 and 15 UTC are too small for a robust statistical analysis and therefore not shown.*

which contradicts the larger NLLJ wind speeds found for HadGEM2-ES in S3 at the beginning of the year. In this case the synoptic-scale conditions cause larger geostrophic winds that are particularly favourable for stronger NLLJs. It is interesting that both regions show larger stability in HadGEM2-ES during winter in the early morning. This implies that NLLJ may survive for a longer time in HadGEM2-ES before being weakened by turbulent mixing.

Vertical wind shear below the NLLJ level is taken into account by analysing the gradient Richardson number Ri, which describes the onset of turbulence and is defined in Section 1.3.5. Both sub-domains show substantially larger values of the median of Ri in ERA-Interim throughout the year (Figures 5.12 and 5.13). Since the differences in the stability below NLLJs are relatively small, the smaller Ri numbers in HadGEM2-ES give a strong indication that the vertical wind shear below NLLJs is much larger in HadGEM2-ES which is consistent with larger NLLJ wind speeds in HadGEM2-ES at similar heights. Based on S1 in spring, when the stability in both models agree particularly well, the vertical wind shear between the median NLLJ height and the ground is larger by 30 % in HadGEM2-ES (0.045 s^{-1}) compared to ERA-Interim (0.031 s^{-1}).

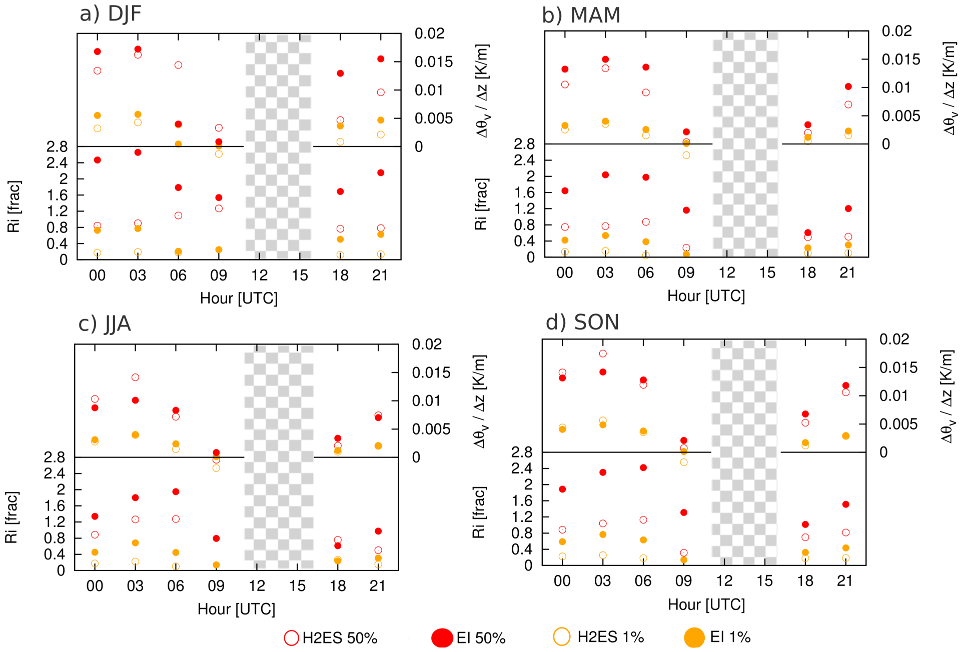

Figure 5.13: *As Figure 5.12 but for sub-domain S3.*

The 1%-percentile of Ri in HadGEM2-ES is mostly lower than in ERA-Interim suggesting that HadGEM2-ES is even more prone to nocturnal mixing during NLLJ events. Like in ERA-Interim, the vertical exchange coefficient for momentum in HadGEM2-ES is also artificially increased (Chapter 1, Brown *et al.*, 2008, 2006; Sandu *et al.*, 2013). This leads to an overestimation of vertical momentum mixing, weakening the NLLJ and increasing the near surface winds at night (Fiedler *et al.*, 2013a; Sandu *et al.*, 2013). These winds can also be large enough for nocturnal dust emission in T-H2ES-O (compare Figures 5.3 and 5.4). As a result the NLLJ accelerates to a certain speed and remains at that wind speed level during the night similar to ERA-Interim. The NLLJ core wind speed, however, is larger in HadGEM2-ES likely due to the smaller enhancement of the vertical mixing than in ERA-Interim (Brown *et al.*, 2008; Sandu *et al.*, 2013). This contributes to stronger NLLJs in HadGEM2-ES independent of the geostrophic wind speed, but the effect is expected to be larger where the geostrophic wind is also stronger.

5.3.6 Discussion

The Earth system model HadGEM2-ES is analysed regarding the simulation of dust emissions and NLLJs as driving mechanism. Dust emissions are calculated offline with the model by Tegen *et al.* (2002) which is driven with 10m-wind speeds from HadGEM2-ES (T-H2ES-O) and ERA-Interim forecasts (T-EI-O) for investigating the effect of wind speed on dust emission. The level of the dust emission amount from the interactive emission scheme in HadGEM2-ES (H2ES-I) is closer to the offline version T-H2ES-O than T-H2ES-O to T-EI-O, suggesting that the impact of the wind speed is larger than the choice of the dust emission parameterisation scheme. T-H2ES-O has substantially larger dust emission over North Africa compared to T-EI-O particularly in winter and spring. These differences of the emitted dust amount are particularly pronounced in West Africa and the Bodélé Depression where stronger winds are simulated compared to ERA-Interim. The origin of these larger wind speeds and dust emissions are addressed by evaluating the NLLJ frequency, their characteristics and the synoptic-scale conditions. The key findings of the evaluation from the two key regions, captured by the sub-domains S1 and S3, are summarized in Tables 5.3 and 5.4.

Sub-domain S1	DJF	MAM	JJA	SON
Difference of mean dust emission [gm^{-2}]	+10	+8	+3	+1
Time of wind speed maximum [UTC]	9	12	12	12
Difference of NLLJ occurrence frequency [%]	0 to +20	-20 to +20	-20 to +20	-20 to +20
Dust emission amount associated with NLLJs [%]	+20 to +30	+20 to +30	+10 to +20	+20 to +30
Difference of median of NLLJ wind speed [ms^{-1}]	+3	+2	+2	+2
Difference of 99%-percentile of NLLJ wind speed [ms^{-1}]	+5	+4	+3	+4
Difference of median Ri [frac]	+1	+1	+0.5	+1
Difference of geopotential height at 925 hPa	Stronger High	Stronger High	Shifted heat low	Shifted heat low
Difference of geostrophic wind [ms^{-1}]	+1 to +4	+1	-3 to +3	-1 to +2

Table 5.3: *Summary of findings for HadGEM2-ES in sub-domain S1 over West Africa. Modest (largest) overestimation of meteorological parameters of HadGEM2-ES compared against ERA-Interim and dust emission from T-H2ES-O against T-EI-O highlighted in yellow (red).*

Sub-domain S3	DJF	MAM	JJA	SON
Difference of mean dust emission [gm^{-2}]	+10	+10	+1	+2
Time of wind speed maximum [UTC]	9	9	9	9,12
Difference of NLLJ occurrence frequency [%]	-20 to 0	-14 to +14	-20 to +14	-20 to +20
Dust emission amount associated with NLLJs [%]	-20 to +10	-10 to +30	-10 to +30	+10 to +30
Difference of median of NLLJ wind speed [ms^{-1}]	+2	+3	+1	+2
Difference of 99%-percentile of NLLJ wind speed [ms^{-1}]	+3	+3	+3	+3
Difference of median Ri [frac]	+1	+0.5	+0.5	+1
Difference of geopotential height at 925 hPa	Stronger High	Stronger High	Shifted heat low	Shifted heat low
Difference of geostrophic wind [ms^{-1}]	up to +4	up to +4	-1 to +1	up to +3

Table 5.4: *As Table 5.3 but for sub-domain S3.*

S1 over West Africa

Sub-domain S1, situated over West Africa, shows clear evidence for larger dust emission in T-H2ES-O in winter due to a more frequent formation of NLLJs accompanied by stronger wind speeds in their core (Table 5.3). The results highlight that the horizontal gradient of the geopotential height at 925 hPa, a typical height for NLLJs, is substantially larger in HadGEM2-ES due to a stronger ridge stretching from the Azores High to northern Africa. The geostrophic wind is, therefore, larger in winter aiding the formation of stronger NLLJs and also stronger Harmattan winds during the day. The stronger geostrophic wind is likely the most important reason for larger NLLJ wind speeds in this region and season. In addition to the geostrophic winds, low-level static stability and the vertical wind shear are contributing factors to the NLLJ strength. The nocturnal vertical gradient of the virtual-potential temperature between the NLLJ core and the lowest level, as indicator for the static stability, agree well in both models. At the same time the vertical wind shear is larger in HadGEM2-ES due to the larger wind speeds in the NLLJ core. In results the gradient Richardson numbers are smaller and more often below the critical value for vertical mixing. These mixing events of NLLJ momentum likely contribute to higher nocturnal 10m-wind speeds and dust emission in HadGEM2-ES. The stronger geostrophic wind likely aids the wind speed in the NLLJ core to recover from the nocturnal momentum loss so that the NLLJ core wind speeds remain large during the entire night leading to substantial dust emission at the following morning (Table 5.3).

Conditions in spring over West Africa (Table 5.3) are similar regarding the dust emission associated with NLLJs, the NLLJ speed, the geopotential height and the geostrophic wind. Regions with larger NLLJ frequencies in HadGEM2-ES, however, are limited to southern West Africa while the centre shows little differences in NLLJ occurrence and areas along the coast show a reduction compared to ERA-Interim. The time of maximum emission and wind speed is also later at 12 UTC, suggesting that the downward mixing of momentum in the daytime boundary layer in spring is more important for producing the majority of dust emission than the stronger NLLJs. The Harmattan winds are also driven by the larger horizontal gradient in the geopotential height that is present throughout the day.

Summer is characterized by a shift of NLLJ occurrence hot spots due to the more southern position of the Saharan heat low in HadGEM2-ES. As a result large dust emission occurs over southern West Africa and a substantial fraction of this is associated with NLLJs in T-H2ES-O. NLLJs are stronger here like earlier in the year. Differences in the horizontal gradient of the geopotential height, however, are smaller in HadGEM2-ES than in ERA-Interim. The weaker artificial enhancement of the vertical mixing in the stable boundary layer in HadGEM2-ES compared to ERA-Interim (Brown *et al.*, 2008; Sandu *et al.*, 2013) may therefore have a larger net impact on the strength of NLLJs in summer. The spatial shift of NLLJs persists until September and vanishes with the retreat of the heat low from West Africa thereafter.

S3 enclosing the Bodélé Depression

The Bodélé Depression is one of the most active places for dust emission and is located in sub-domain S3. Here, T-H2ES-O shows larger dust emission compared to T-EI-O throughout the year, particularly in winter and spring when peak emissions at 9 UTC point to the importance of NLLJs (Table 5.4). NLLJ core wind speeds are particularly large in both seasons linked to stronger geostrophic winds which are due to a larger horizontal gradient in the geopotential height at 925 hPa in HadGEM2-ES. Interaction of the atmospheric flow with the Tibesti and Ennedi Mountains likely contributes to these larger geostrophic winds over the Bodélé Depression. NLLJs, however, occur less frequently in winter compared to ERA-Interim. This result is surprising as winter is the time of year when the channeling of the prevailing north-easterly Harmattan winds cause favourable conditions for NLLJ formation (Chapter 2, e.g. Fiedler *et al.*, 2013a; Todd *et al.*, 2008; Washington & Todd, 2005). It is plausible that the vertical shear below the larger geostrophic winds in winter leads to so much vertical mixing that the formation of NLLJs is prevented in some nights as discussed in Chapter 2.

From spring onwards, the NLLJ wind speed as well as the 9 UTC maximum in both dust emission and 10m-wind speed suggest that the NLLJ is important for dust emission (Table 5.4). The geostrophic winds in HadGEM2-ES are larger during spring and autumn, pointing to a substantial contribution from the synoptic-scale conditions. While the stability below the NLLJ core is remarkably similar in both models for those season, the gradient Richardson number is smaller in HadGEM2-ES and points to more nocturnal mixing events. Here, the larger geostrophic winds may again aid NLLJs to recover from the weakening effect of vertical momentum mixing during the night. The stronger geostrophic winds are likely the first-order driver of stronger NLLJs and associated dust emission. A contributing factor to stronger NLLJs is the weaker enhancement of mixing during stable stratification in HadGEM2-ES (e.g. Brown *et al.*, 2008).

In conclusion, the NLLJ is found to be a key driver for dust emission in T-H2ES-O. The stronger ridge over northern Africa in winter and the southward displaced heat low in summer result in other locations and strengths of NLLJs than in ERA-Interim. Particularly the larger geostrophic winds associated with the stronger ridge have a strengthening effect on NLLJs over West Africa in winter. Stronger NLLJs in summertime West Africa may rather result from an artificially increased mixing coefficient under stable stratification that is weaker compared to ERA-Interim (Brown *et al.*, 2008; Sandu *et al.*, 2013). Also NLLJs in the Bodélé Depression are affected by stronger synoptic-scale pressure gradients in HadGEM2-ES. Wintertime geostrophic winds might even be so strong that the associated vertical wind shear prevents the formation of NLLJs in some night.

5.4 Effect of nudging in HadGEM3-A

5.4.1 Dust emission amount

The results from the evaluation of dust emission in HadGEM2-ES motivate an analysis of the newer model version HadGEM3-A. A free-running experiment of HadGEM3-A (H3ES-I) is compared against a nudged model simulation (H3ES-I-N) for 2003−2007 with focus on the dust emission and synoptic-scale conditions which show the largest differences between HadGEM2-ES and ERA-Interim (Section 5.3). Figure 5.14 shows the seasonally and annually integrated dust emission mass from H2ES-I, H3ES-I and H3ES-I-N. Compared to an annual mean of 4164 Tg per year integrated over North Africa from H2ES-I for 2003−2007, H3ES-I shows substantially less emission with 2264 Tg per year. Using nudging in order to force the model to be closer to ERA-Interim re-analysis (H3ES-I-N) results in even smaller North African dust emission of 1853 Tg per year. These results imply that the total dust emission amount in the newer model version H3ES-I is substantially closer to H3ES-I-N representing atmospheric conditions close to ERA-Interim re-analysis. The same hierarchy of largest dust emission in H2ES-I and the smallest emission amount in H3ES-I-N is found for the seasonal totals of winter and summer, but surprisingly not during spring and autumn. In spring, the dust emission in H3ES-I-N is slightly larger than in H3ES-I. The opposite is true for autumn, but this season is the least active in terms of total emission. In the following section the wind speed is analysed as driver of dust emission in H3ES-I and H3ES-I-N.

5.4.2 Diurnal cycle of 10m-wind speed

The mean diurnal cycle of the 10m-wind speed for different seasons and the probability distribution of the 10m-wind speed at 09 UTC from both HadGEM3-A are

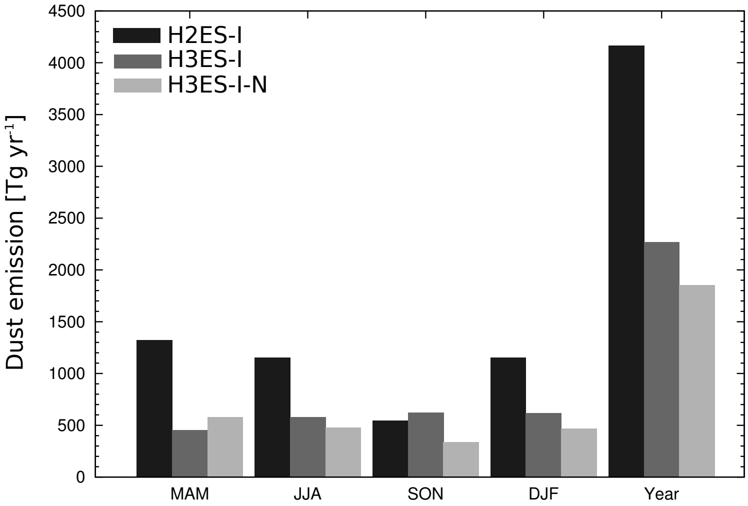

Figure 5.14: *Seasonal and annual total dust emission. Total dust emission amount for 2003–2007 from H2ES-I, H3ES-I and H3ES-I-N integrated over North Africa.*

shown in Figures 5.15 and 5.16 for the northern and southern sub-domains (as defined in Figure 2.5a), respectively. Mid-morning is the time of day when the effect of NLLJs on the near-surface wind speed and dust emission is expected to be largest (Section 2). Both model simulations show an increase in the mean 10m-wind speed in all seasons at the morning in all northern sub-domains (Figure 5.15a–c). In N1, the mean 10m-wind speed during spring is larger in H3ES-I-N while the opposite is the case in autumn (Figure 5.15a). Summer and winter in N1 show similar diurnal cycles so that the net effect on the annual mean diurnal cycle is small. The probability distribution at 9 UTC in N1 (Figure 5.15d) underlines, however, that dust-emitting wind speeds of 6–9 ms^{-1} occur more frequently in H3ES-I-N, but the highest winds of 10 ms^{-1} and above are less frequent. The mean diurnal cycle of wind speed in N2 (Figure 5.15b) shows similar results for spring and autumn, while the summertime wind speeds at night are comparable to the daytime values. Looking at the probability distribution highlights that H3ES-I-N produces generally more events with wind speeds above 3 ms^{-1} compared to H3ES-I (Figure 5.15e). In N3, mean mid-morning wind speeds are again large in spring but dust-emitting winds are simulated more often in H3ES-I-N above 9 ms^{-1} only (Figure 5.15f). The time of day points to differences of the NLLJ between both simulations.

The wind conditions for the southern sub-domains are shown in Figure 5.16. All southern sub-domains have the large daytime mean wind speeds in H3ES-I during winter, particularly in S1 and S2. As a result also the annual mean of the diurnal cycle is larger (Figure 5.16a–d). In all southern sub-domains, wind speed events above 6 ms^{-1} at 9 UTC occur more frequently in H3ES-I (Figure 5.16e–h), thus just opposite to the model comparison for the northern sub-domains. The larger wind

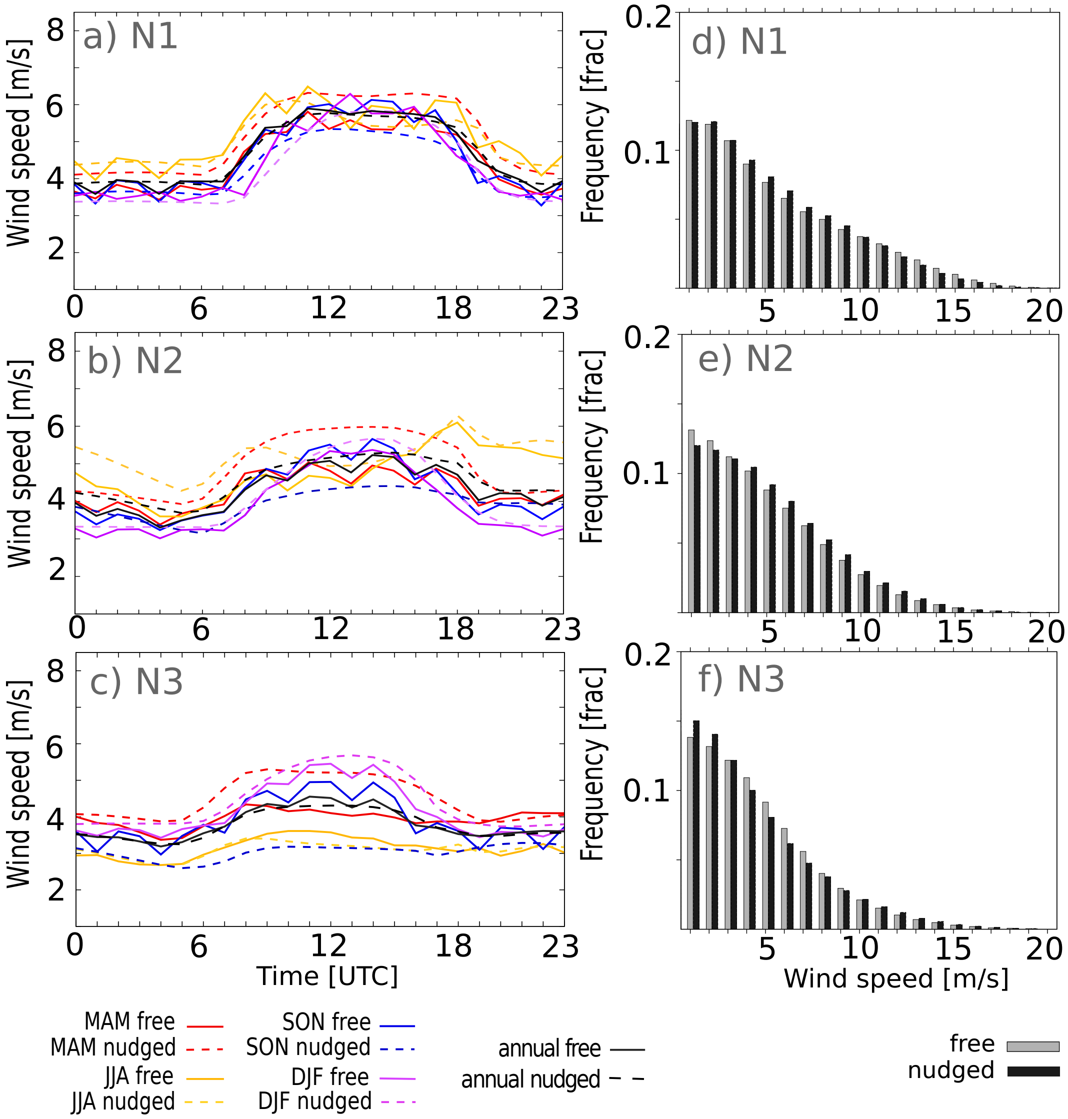

Figure 5.15: *Diurnal cycle of 10m-wind speed from HadGEM3-A. Hourly mean 10m-wind speed for different seasons and in the annual mean (a–c, left) as well as the probability density function of the 10m-wind speed at 09 UTC in the annual mean (d–f, right) from H3ES-I and H3ES-I-N for 2003–2007 spatially averaged for the northern sub-domains.*

speeds at 9 UTC in the south particularly over West Africa in winter and spring suggests similar synoptic-scale conditions in HadGEM3-A like in HadGEM2-ES. Whether a stronger ridge is still simulated in HadGEM3-A is investigated in the next section.

5.4.3 Mean sea-level pressure differences

The wind speed distributions suggest that differences in dust-emitting wind speeds occur between H3ES-I and H3ES-I-N. As differences in the geostrophic winds between HadGEM2-ES and ERA-Interim are identified as a main cause, the aim here is to reveal whether synoptic-scale conditions still differ in the newer model version HadGEM3-A. Figure 5.17 shows the seasonal MSLP in H3ES-I and the differences to H3ES-I-N. During winter the ridge stretching from the Azores High into northern Africa is stronger in H3ES-I (Figure 5.17a) similar to H2ES-I. The associated larger horizontal pressure gradient force can be linked to the larger wind speed seen in the southern sub-domains and the larger dust emission amounts of winter, while little difference is seen in the centre of the High over the north of the continent. Springtime is characterized by a the heat low over West Africa and high pressure over Europe that are both weaker in H3ES-I-N so that the mean horizontal gradient is not substantially different between both experiments (Figure 5.17b). At first sight this result appears inconsistent with the larger dust emission amount and wind speeds in H3ES-I-N for spring. Synoptic-scale variability may explain these differences which will be analysed further.

Summer shows a southward displaced heat low in H3ES-I similar to HadGEM2-ES (Figure 5.17c) likely contributing to the larger wind speeds over the southern areas. In autumn, the larger wind speeds over the south in H3ES-I are likely associated with the larger horizontal pressure gradient between the stronger high and the deeper heat low (Figure 5.17d).

The MSLP does not reflect the influence of atmospheric disturbances like extratropical cyclones and Harmattan surges (Chapter 1 and 4). Figure 5.18 shows the standard deviation of the MSLP as a first indication whether disturbances are of different importance in the experiments. In winter, the standard deviation of both simulations is in fair agreement over the central Sahara but shows some differences over southern North Africa (Figure 5.18a). Spring, however, has much larger standard deviations over the north in H3ES-I-N (Figure 5.18b). Deviations from the MSLP pattern may therefore play a more important role in H3ES-I-N for generating dust-emitting wind speeds in spring. Summer and autumn show larger standard

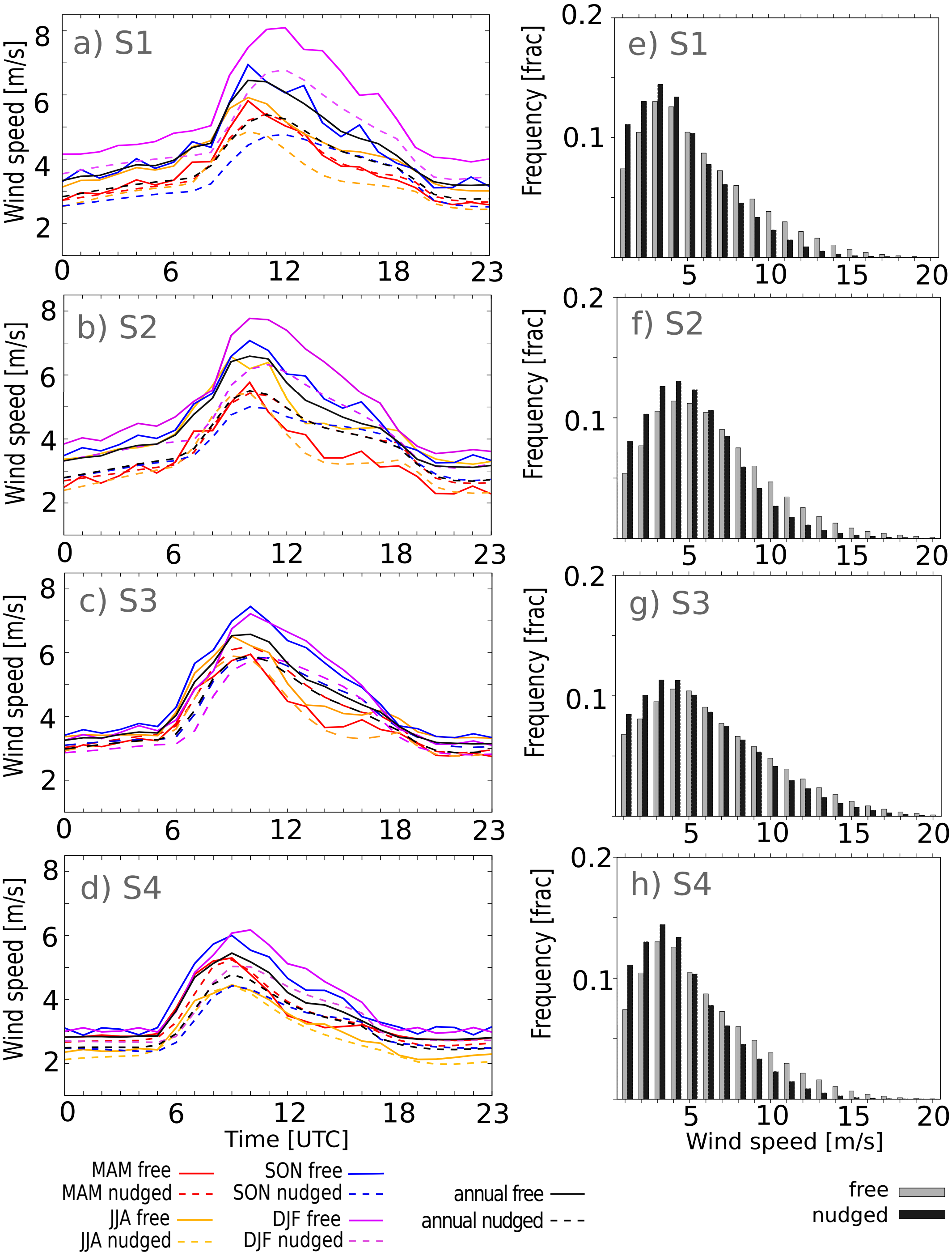

Figure 5.16: *As Figure 5.15 but for the southern sub-domains.*

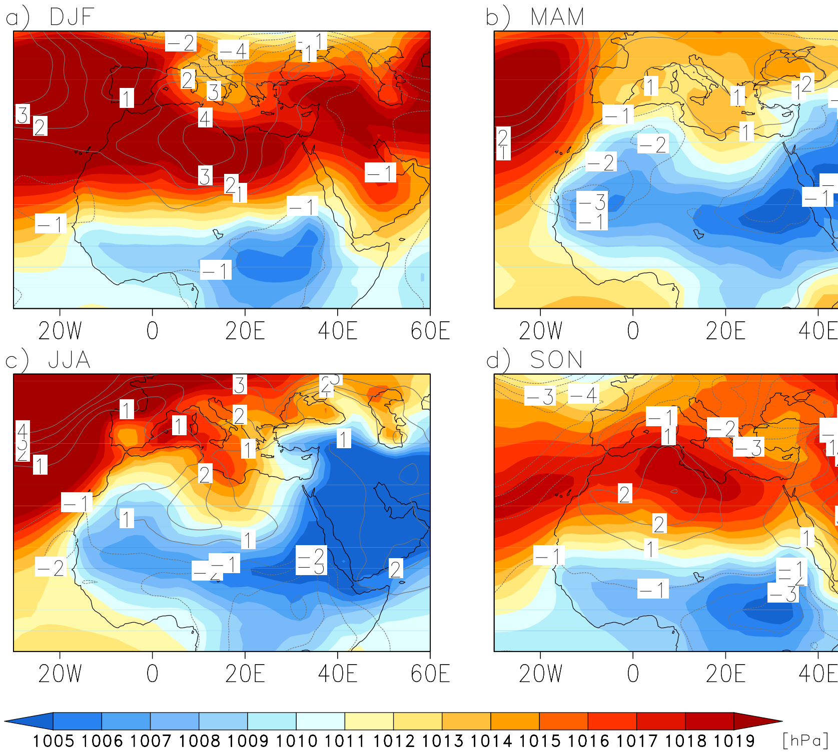

Figure 5.17: *Seasonal mean sea level pressure. Shown are H3ES-I (shaded) and the difference as H3ES-I minus H3ES-I-N (contours) for 2003–2007.*

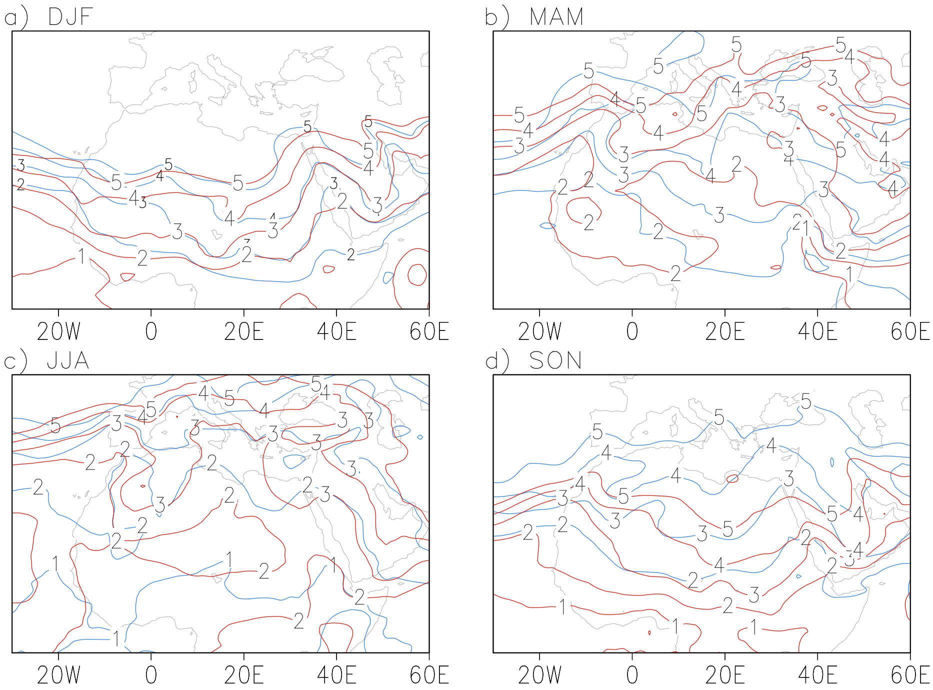

Figure 5.18: *Standard deviation of the MSLP. Shown are values at 00 UTC for different seasons in H3ES-I (red) and H3ES-I-N (blue) for 2003–2007.*

deviations in the MSLP in H3ES-I (Figure 5.18c–d) in addition to the larger horizontal gradient in the MSLP over southern sub-domains. These results for summer and autumn are in agreement with larger wind speeds in southern sub-domains (Figure 5.16) and larger seasonal dust emission in H3ES-I (Figure 5.14).

Both the mean horizontal gradient and the standard deviations in the MSLP are important for near-surface wind speeds in H3ES-I that are likely linked to the dust emission differences. Since these synoptic-scale conditions between H3ES-I and H3ES-I-N differ in a similar way as for HadGEM2-ES against ERA-Interim, the strength and position of NLLJs is likely similarly affected, the analysis of which is left for future investigations.

5.5 Conclusion

This chapter addresses the differences of dust-emitting winds between HadGEM2-ES and ERA-Interim. Dust emission with HadGEM2-ES winds is five and six times larger than the simulation with ERA-Interim and MERRA, respectively. Calculating the dust emission with the same dust emission model driven by wind speeds from two atmospheric models enables an isolation of the effect of wind speed on dust emission and subsequently a systematic investigation of the meteorological processes causing these winds. The key findings from HadGEM2-ES in the CMIP5 model setup for 1989–2009 are:

1. The downward mixing of NLLJ momentum is an important mechanism for dust emission in HadGEM2-ES in agreement with findings for the ERA-Interim climatology (Chapter 2, Fiedler *et al.*, 2013a). Annually and spatially averaged, the occurrence frequency of NLLJs is remarkably similar between both models, but the location of most frequent NLLJ formation shows distinct differences. For instance the NLLJ occurrence hot spots at the margins of the summertime heat low are shifted to the south consistent with the southward displaced heat low in HadGEM2-ES.

2. The wind speeds in the NLLJ core and near the surface as well as the dust emission amount are substantially larger with HadGEM2-ES winds, despite the coarser spatial resolution. More detailed analysis of the underlying reasons points to combinations of a weaker artificial enhancement of the vertical mixing in stable boundary layers and larger geostrophic winds at 925 hPa caused by a stronger ridge over northern Africa in HadGEM2-ES.

3. Over West Africa, the larger geostrophic winds in HadGEM2-ES are likely more important for the stronger NLLJs than the effect of stability from autumn to spring while the opposite is true during summer.

4. In the Bodélé Depression, the geostrophic winds during winter in HadGEM2-ES usually aid the occurrence of stronger NLLJs. However, the geostrophic wind may also become so large that the vertical wind shear prevents NLLJ formation in some nights.

While the parameterisation of the stable boundary layer was expected as a possible source for differences in dust emission investigated here, the stronger ridge over North Africa during winter relative to ERA-Interim is surprising. The developmental Earth system model HadGEM3-A is analyzed for investigating whether the representation of the synoptic-scale conditions for dust emission are improved in a newer model version. The main results are:

1. The dust emission amount in HadGEM3-A is much closer to dust emission with winds from ERA-Interim. Annually averaged the total dust emission from North Africa in HadGEM3-A is remarkably close to a simulation nudged to meteorological fields from ERA-Interim re-analysis. Comprehensive tuning of the dust emission in the new model version may explain the reduction of the dust emission amount in the free-running model (pers. comm. S. Woodward, UK Met Office, 2014).

2. The free-running experiment simulates more dust emission than the nudged simulation for most of the year, except in spring. The results point to larger wind speeds over the north in the nudged model during spring, but this is inconsistent with the smaller horizontal gradient in the MSLP in that season. Larger springtime winds may rather be caused by more synoptic-scale variability in the nudged experiment. Relevant processes during spring are cyclones, that are suggested as driver of particularly intense emission events, and also Harmattan surges (Chapter 4). The more detailed analysis of these differences are left for future investigations.

3. The stronger ridge over northern Africa in winter and the shifted heat low during summer persist in HadGEM3-A, likely affecting NLLJs in a similar way as in HadGEM2-ES. Dynamics over summertime West Africa are currently investigated at the UK Met Office (pers. comm. G. Martin and C. Birch, UK Met Office, 2014).

Weaknesses of the parameterisation of stable boundary layers are a known shortcoming of weather and climate models, further improvements of which are subject of ongoing research at the UK Met Office, ECMWF and elsewhere (e.g. Holtslag *et al.*, 2013; Sandu *et al.*, 2013). Future research on the reasons for differences of the ridge over northern Africa during winter between HadGEM2/3-ES and ERA-Interim would be useful for future model development leading to a better representation of meteorological processes. Since NLLJs and near-surface wind speeds depend on the pressure gradient force, any progress on representing the synoptic-scale conditions holds the potential to positively affect dust emission and therefore effects of dust aerosol in the Earth system.

CHAPTER 6

Synthesis

6.1 Scientific implication of this work

Dust aerosol is an important component of the Earth system, but state-of-the-art model estimates for dust emission show a large variety. While different meteorological processes are known to cause dust emission, their efficiency in terms of the emitted dust mass is poorly quantified. This work contributes to our understanding of the relative importance of processes for North African dust emission. Based on these findings, important dust-emitting processes can be evaluated in atmospheric models to help reducing the currently large uncertainties in dust modelling.

This PhD thesis provides the first-ever systematic investigation of North African dust emission amounts associated with NLLJs (Chapter 2), atmospheric depressions and mobile, long-lived cyclones (Chapter 4) from a climatological perspective. Based on ERA-Interim data from the ECMWF and with the aid of a newly developed detection algorithm for NLLJs, their occurrence frequencies, spatio-temporal characteristics and associated emission amounts are comprehensively analysed for the first time. Combining the climatology of emission associated with NLLJs and depressions illustrates the influence of the synoptic-scale conditions on NLLJs via their frequent formation along the margins of the Saharan heat low, previously observed over shorter time periods in single regions (Abdou *et al.*, 2010; Bain *et al.*, 2010; Parker *et al.*, 2005; Pospichal *et al.*, 2010). NLLJs are found to be embedded in AEWs, which has been suggested before in a case study (Knippertz & Todd, 2010), but is here climatologically estimated for the first time. In addition to NLLJs, mobile and long-lived cyclones over springtime North Africa have been proposed as a dust-emitting mechanism in the literature (Bou Karam *et al.*, 2010; Hannachi *et al.*, 2011; Schepanski & Knippertz, 2011; Schepanski *et al.*, 2009). Using ERA-Interim data and depression tracks at a near-surface atmospheric level, cyclones are found to have an overall small contribution to the total dust emission amount, but they coincide with particularly intense emission events (Chapter 4). These new climatologies of the relative importance of meteorological processes for dust emission in North Africa serve as a benchmark for identifying systematic behaviour in other atmospheric models for dust applications.

This thesis contributes to document model uncertainties with implication for North African dust emission. Validation with upper-air soundings points to an underestimation of the largest wind speeds in the core of NLLJs consistent with artificially increased mixing in the stable ABL of ERA-Interim (Sandu *et al.*, 2013), which likely affects dust emission (Chapter 3). NLLJs that form in response to haboobs are not well captured by ERA-Interim which is likely a general shortcoming of state-of-the-art coarse-resolution models with parameterised convection.

The statistical analysis of dust emission and wind speeds on sub-daily scales identifies systematic differences between the CMIP5 simulation of HadGEM2-ES and ERA-Interim (Chapter 5). These disagreements are likely associated with differences in the physical parameterisation of the stably stratified ABL and the position of the Saharan heat low in summer, but also with a disagreement in the strength of the mean ridge over northern Africa in winter. The associated changes in the synoptic-scale pressure gradients affect NLLJ characteristics and dust emission in HadGEM2-ES and are also found in HadGEM3-A. Adressing these differences in the synoptic-scale conditions during future model development will help to reduce uncertainties in North African dust emission. As a direct consequence, weather forecasts of dust storms in North Africa would become more accurate allowing better warnings to reduce adverse impacts of dust aerosol. Since this region is a dominant dust source, any improvements of the emission here could positively influence simulations of the atmospheric dust load and its effects in the entire of the Earth system.

6.2 Summary of main results

The major findings in response to the questions raised in Chapter 1 are summarized in the following.

1. **The importance of NLLJs for the mineral dust emission amount from North Africa has been quantified for the first time (Fiedler *et al.*, 2013a).**
    (a) Based on 32-years of ERA-Interim re-analysis, NLLJs occur in 29 % of the nights in the annual and spatial mean. The NLLJ climatology shows a distinct annual cycle with regional differences. Maxima of up to 80 % NLLJ frequency are found where low-level baroclinicity and orographic channels cause favourable conditions, e.g. over the Bodélé Depression, Chad, for November to February and along the Saharan heat low for April to September.

   (b) NLLJs have spatio-temporal varying characteristics with a median core height and wind speed of 350 m a.g.l. and 10 ms^{-1} spatially and temporally averaged. The nocturnal acceleration is relatively small most likely due to the artificially increased vertical mixing in stable boundary layers suggested by Sandu *et al.* (2013).

   (c) The near-surface wind speed distribution during the presence of NLLJs is shifted to larger values, but the highest values are less sensitive to the occurrence of NLLJs. These largest winds are likely caused by strong horizontal pressure gradients which would not allow a sufficient decoupling from surface friction for NLLJ formation.

   (d) Downward mixing of NLLJ momentum to the surface causes 15 % of mineral dust emission in the annual and spatial mean and can be associated with up to 60 % of the total dust amount in specific areas, e.g. in the Bodélé Depression and south of the Hoggar-Tibesti Channel. This is the first quantitative estimate for the dust emission amount associated with NLLJs in North Africa from a climatological perspective.

   (e) The dust emission associated with NLLJs is often larger during the mid-morning than during the night, but the fractions are likely influenced by the artificially increased boundary layer mixing. The sharp diurnal cycle of dust emission underlines the importance of using wind speed information with high temporal resolution as driving fields for dust emission models.

2. **Uncertainties of the baseline climatology regarding NLLJ characteristics and dust emission have been analysed highlighting the implications of artificially increased mixing in stably stratified ABLs (parts from Fiedler *et al.*, 2013a,b).**

   (a) ERA-Interim reproduces NLLJs over North Africa observed during AMMA and Fennec, but underestimates the largest core wind speed, particularly when associated with haboobs.

   (b) The DSA frequency over the Bodélé Depression from SEVIRI (e.g. Schepanski *et al.*, 2009) is well captured by the Tegen *et al.* (2002) model driven with ERA-Interim data. Regions to the north and west of North Africa show larger differences in the DSA frequencies, but these do not allow a conclusion on the calculated dust amount.

   (c) The spread in the MSLP from ERA-Interim, ERA-40 and MERRA re-analysis is smallest at night pointing to little uncertainty in the first-order driver of wind speed.

   (d) Differences in the dust emission amount calculated with MERRA and ERA-Interim winds are found in northern areas in winter and spring as well as along the western coast in spring and summer, but the wind speeds from MERRA are found to contain even more nocturnal wind events above typical emission thresholds than ERA-Interim.

   (e) Dust emission calculations with ERA-Interim winds likely give a better estimate than with high-resolved MERRA re-analysis, but the artificially increased mixing during stable stratification likely leads to an underestimation of the NLLJ strength.

3. **The dust emission amount associated with atmospheric depressions and cyclones has been estimated for the first time indicating their importance for the total emission amount and the emission intensity, respectively (Fiedler *et al.*, 2013b).**

   (a) Atmospheric depressions are abundant, e.g. over summertime West Africa. Only a small fraction of depressions develop into mobile and long-lived cyclones which are most frequent over northern regions of North Africa in spring.

   (b) Springtime cyclones predominantly migrate eastwards, and live for three to seven days.

   (c) Atmospheric depressions are associated with 55 % and cyclones with 4 % of the annually averaged dust emission from North Africa.

   (d) NLLJs are embedded at the margins of the Saharan heat low and associated with 12 % of the dust emission associated with atmospheric depressions during summer. Up to 20 % of the dust emission associated with AEW signatures coincide with embedded NLLJs.

   (e) Soil moisture has an overall small weakening effect on dust emission associated with cyclones and AEW signatures on the order of 10 %.

4. **Comparison of the Earth system model from the UK Met Office against ERA-Interim underlines considerable differences in dust emission associated with synoptic-scale conditions and NLLJs.**

   (a) The climatology of dust emission calculated with winds from the historical CMIP5 experiment with HadGEM2-ES differs from the dust emission simulated with ERA-Interim in terms of total amount, spatial and seasonal distribution.

(b) Using HadGEM2-ES winds to drive the dust model by Tegen *et al.* (2002) results in a five (six) times larger annually averaged dust emission amount compared to ERA-Interim (MERRA) due to stronger near-surface winds alone.

(c) HadGEM2-ES shows systematically larger wind speeds in the NLLJ core and a different seasonal distributions of their occurrence. The stronger wind speeds in the NLLJ core are likely associated with larger geostrophic winds and a weaker artificial enhancement of the vertical mixing in stable ABLs.

(d) The ridge over North Africa in winter is stronger in both HadGEM2-ES and a free-running experiment with HadGEM3-A, most likely driving larger winds in the NLLJ core and near the surface. HadGEM2/3-ES has a southward-displaced heat low in summer causing a spatial shift of NLLJs situated along the margins.

(e) Considerable differences in the synoptic-scale pressure gradients affect the dust emission amounts over North Africa. Addressing the origin of the synoptic-scale differences potentially aids further model improvements in order to decrease the model spread in dust emission.

6.3 Future research

This PhD thesis presents the first climatological estimates for the importance of NLLJ, atmospheric depressions and mobile, long-lived cyclones for the dust emission amount from North Africa. Future research regarding estimating the role of different meteorological processes for dust emission could include a long-term climatology of the dust emission amount associated with Harmattan surges which may be responsible for large dust emission in springtime North Africa (Chapter 4). In addition to strong Harmattan winds, haboobs are thought to be a key driver for summertime North Africa based on a 40-day convection permitting simulation (Heinold *et al.*, 2013). Since haboobs are currently not parameterised in atmospheric models, several years of wind speed data from a model experiment with explicit convection and sub-daily resolution would offer the possibility to estimate the dust emission amount associated with haboobs during all seasons and from a climatological perspective. Quantifying the emission associated with NLLJs in such a data set would also be interesting since aged cold pools may form NLLJs.

More quality-controlled observations from remote areas of the Saharan desert with sub-daily resolution are herein essential to validate model simulations better. The present availability of such observations is mostly restricted to single stations and short time periods.

Atmospheric models should be further improved regarding the simulation of NLLJs as an important driver of North African dust emission (Chapter 2). Current limitations for the representation of stably stratified ABLs need to be solved in order to overcome the underestimation of the largest NLLJ wind speed shown for ERA-Interim over North Africa in Chapter 3. While problems of modelling stable ABLs are known for decades, little progress has been made for better simulating NLLJs (Holtslag *et al.*, 2013). This is attributed to the physical parameterisation of the ABL but also to weaknesses of other model components, e.g. the parameterisation of the soil, surface and radiation (e.g. Holtslag *et al.*, 2013; Sandu *et al.*, 2013; Steeneveld *et al.*, 2006, 2008). Higher spatial resolution of models is suggested to improve the representation of stable ABLs but this does not entirely solve the problem (Steeneveld *et al.*, 2006; Svensson *et al.*, 2011) so that future research on the physical parameterisations is needed for simulating North African dust emission more realistically.

Physical parameterisations of the soil, the surface coverage, the orographic drag and mixing in the stable boundary layer have already been altered and the spatial resolution has been increased between the model version of ERA-Interim (cycle Cy31r2) and the currently operational forecast system (cycle Cy40r1)[*]. Therefore it would be interesting to study the climatology of NLLJs, particularly the NLLJ wind speed and the associated dust emission amount with a new re-analysis product from ECMWF in the future. Such a data set could serve as an even better benchmark for process evaluation in atmospheric models with dust applications. As a interim solution for dust applications, research on representing winds generated by the breakdown of NLLJs would be useful to estimate associated emission amounts.

In addition to the stably stratified ABL, the model evaluation of HadGEM2/3-ES (Chapter 5) highlights a stronger ridge over northern Africa compared to ERA-Interim which affects the strength of NLLJs, 10m-winds and dust emission. Future research should firstly focus on the underlying reasons for these synoptic-scale differences. Secondly, the improvement of the physical parameterisation of stable boundary layers in models will help to better simulate NLLJs and their effect on dust emission. Such developments hold the potential for further model improvements in the diurnal cycle of the near-surface wind speed. Thirdly, further research for improving dust emission include the representation of the particle size distributions,

---

[*] http://www.ecmwf.int/products/changes/ as of February 2014

potential dust sources, surface properties and dust entrainment without saltation (e.g. Klose & Shao, 2012; Menut *et al.*, 2005, 2013; Schepanski *et al.*, 2013).

Such improvements could contribute to reducing the model diversity of emission estimates for North Africa with possibly positive influence on the simulated atmospheric dust load and dust-aerosol effects in the Earth system model. The chosen approach of isolating the effect of winds on dust emission and subsequently analysing single meteorological processes generating these winds proved valuable for identifying model systematic behaviour in this thesis. Expanding the analysis to other regions and models in the future holds the potential to reduce the currently large diversity in global emission estimates.

References

ABDOU, K., PARKER, D.J., BROOKS, B., KALTHOFF, N. & LEBEL, T. (2010). The diurnal cycle of lower boundary-layer wind in the West African monsoon. *Quart. J. Roy. Meteor. Soc*, **136**, 66–76. 31, 33, 34, 52, 54, 173

ACKERMANN ET AL (2000). Reduction of tropical cloudiness by soot. *Science*, **288**, 1042–1047. 1

AGUSTÍ-PANAREDA, A., BELJAARS, A., CARDINALI, C., GENKOVA, I. & THORNCROFT, C. (2010). Impacts of Assimilating AMMA Soundings on ECMWF Analyses and Forecasts. *Weather & Forecasting*, **25**. 119, 132, 134

ALBRECHT, B. (1989). Aerosols, cloud microphysics and fractional cloudiness. *Science*, **245**, 1227–1230. 1

ALFARO, S.C. & GOMES, L. (2001). Modeling mineral aerosol production by wind erosion: Emission intensities and aerosol size distributions in source areas. *J. Geophys. Res*, **106**, 18075–18084. 11

ALLAN, R.P., WOODAGE, M.J., MILTON, S.F., BROOKS, M.E. & HAYWOOD, J.M. (2011). Examination of long-wave radiative bias in general circulation models over North Africa during May–July. *Quarterly Journal of the Royal Meteorological Society*, **137**, 1179–1192. 3

ALLEN, C.J.T. & WASHINGTON, R. (2014). The low-level jet dust emission mechanism in the central Sahara: Observations from Bordj-Badji Mokhtar during the June 2011 Fennec Intensive Observation Period. *Journal of Geophysical Research: Atmospheres*, **119**, 2990–3015. 74, 75

ALPERT, P. & ZIV, B. (1989). The Sharav cyclone: observations and some theoretical considerations. *J. Geophys. Res.*, **94**, 18495–18514. 20, 22, 113

ALPERT, P., NEEMAN, B.U. & SHAYEL, Y. (1990). Climatological analysis of Mediterranean cyclones using ECMWF data. *Tellus Series A*, **42**, 65. 21, 22, 68, 118, 119, 133

ANSMANN, A., TESCHE, M., KNIPPERTZ, P., BIERWIRTH, E., ALTHAUSEN, D. & CO AUTHORS (2008). Vertical profiling of convective dust plumes in southern Morocco during SAMUM. *Tellus*, **61B**. 27

ASHPOLE, I. & WASHINGTON, R. (2013). A new high-resolution central and western Saharan summertime dust source map from automated satellite dust plume tracking. *J. Geophys. Res. Atmos.*, **118**, 6981–6995. 102

BAAS, P., BOSVELD, F. & BALTINK, H.K. (2009). A Climatology of Nocturnal Low-level Jets at Cabauw. *J. Appl. Meteor. and Climat.*, **48**, 1627–1642. 28, 45, 56, 59

BAGNOLD, R.A. (1941). *The Physics of Blown Sands and Desert Dunes*. Methuen, New York. 137

BAIN, C.L., PARKER, D.J., TAYLOR, C.M., KERGOAT, L. & GUICHARD, F. (2010). Observations of the Nocturnal Boundary Layer Associated with the West African Monsoon. *Mon. Wea. Rev.*, **138**, 3142–3156. 31, 52, 173

BANTA, R., PICHUGINA, Y. & NEWSOM, R. (2003). Relationship between low-level jet properties and turbulence kinetic energy in the nocturnal stable boundary layer. *J. Atmos. Sci.*, **60**, 2549–2555. 28, 34, 45

BECHTOLD, P., KÖHLER, M., JUNG, T., DOBLAS-REYES, F., LEUTBECHER, M., RODWELL, M.J., VITART, F. & BALSAMO, G. (2008). Advances in simulating atmospheric variability with the ECMWF model: From synoptic to decadal timescales. *Quarterly Journal of the Royal Meteorological Society*, **134**, 1337–1351. 44

BELJAARS, A.C.M. & VITERBO, P. (1999). The role of the boundary-layer in a numerical weather prediction model. *Clear and cloudy boundary- layers*, Holtslag AAM, Duynkerke PG. (eds.) North Holland. 44

BELLOUIN, N., RAE, J., JONES, A., JOHNSON, C., HAYWOOD, J. & BOUCHER, O. (2011). Aerosol forcing in the Climate Model Intercomparison Project (CMIP5) simulations by HadGEM2-ES and the role of ammonium nitrate. *J. Geophys. Res*, **116**, D20206. 42, 135, 136, 137

BELLOUIN, N., MANN, G.W., WOODHOUSE, M.T., JOHNSON, C., CARSLAW, K.S. & DALVI, M. (2013). Impact of the modal aerosol scheme GLOMAP-mode on aerosol forcing in the Hadley Centre Global Environmental Model. *Atmospheric Chemistry and Physics*, **13**, 3027–3044. 141

BEN-AMI, Y., KOREN, I. & ALTARATZ, O. (2009). Patterns of North African dust transport over the Atlantic: winter vs. summer, based on CALIPSO first year data. *Atmos. Chem. Phys.*, **9**, 7867–7875. 2

BETTS, A.K. (1973). Non-precipitating cumulus convection and its parameterization. *Quart. J. Roy. Meteor. Soc*, **99**, 178–196. 37

BIRCH, C.E., PARKER, D., MARSHAM, J., COPSEY, D. & GARCIA-CARRERAS, L. (2014). A seamless assessment of the role of convection in the water cycle of the west african monsoon. *Journal of Geophysical Research: Atmospheres*, **119**, 2890–2912. 142

BLACKADAR, A. (1957). Boundary layer wind maxima and their significance for the growth of nocturnal inversions. *Bull. Amer. Meteor. Soc.*, **83**, 283–290. 27, 28, 30, 46, 56, 59

BLACKADAR, A.K. (1978). Modeling pollutant transfer during daytime convection. preprint. In *Fourth Symp. on Atmos. Turbulence. Diffusion and Air Quality. American Meteorological Society*, 443–447. 37

BLACKADAR, A.K. (1979). High-resolution models of the planetary boundary layer. *Advances in Environmental Science and Engineering*, **1**, 50–85. 37

BLEEKER, W. & ANDRE, M. (1951). On the diurnal variation of precipitation, particularly over central usa and its relation to large-scale orographic circulation systems. *Quart. J. Roy. Meteor. Soc.*, **77**, 260–271. 31

BONNER, W.D. (1968). Climatology of low level jet. *Mon. Wea. Rev.*, **96**, 833–850. 28, 45, 48

BONNER, W.D. & PAEGLE, J. (1970). Diurnal variations in boundary layer winds over the south-central United States in summer. *Mon. Wea. Rev.*, **97**, 735–744. 29

BOU KARAM, D., FLAMANT, C., KNIPPERTZ, P., REITEBUCH, O., PELON, J., CHONG, M. & DABAS, A. (2008). Dust emissions over the Sahel associated with the West African Monsoon inter-tropical discontinuity region: a representative case study. *Quart. J. Roy. Meteor. Soc*, **134**, 621–634. 18, 24

BOU KARAM, D., FLAMANT, C., TULET, P., TODD, M.C., PELON, J. & WILLIAMS, E. (2009). Dry cyclogenesis and dust mobilization in the intertropical discontinuity of the West African Monsoon: A case study. *Journal of Geophysical Research: Atmospheres (1984–2012)*, **114**. 119

BOU KARAM, D., FLAMANT, C., CUESTA, J., PELON, J. & WILLIAMS, E. (2010). Dust emission and transport associated with a Saharan depression: February 2007 case. *J. Geophys. Res.-Atmos.*, **115**, D00H27. 20, 22, 113, 114, 173

BOUCHER, O., RANDALL, D., ARTAXO, P., BRETHERTON, C., FEINGOLD, G., FORSTER, P., KERMINEN, V.M., KONDO, Y., LIAO, H., LOHMANN, U., RASCH, P., SATHEESH, S., SHERWOOD, S., STEVENS, B. & ZHANG, X. (2013). *Clouds and Aerosols. In: Climate Change 2013: The Physical Science Basis. Contribution of Working Group I to the Fifth Assessment Report of the Intergovernmental Panel on Climate Change*. Cambridge University Press, Cambridge, United Kingdom and New York, NY, USA. 1, 2

BOUET, C., CAUTENET, G., WASHINGTON, R., TODD, M., LAURENT, B., MARTICORENA, B. & BERGAMETTI, G. (2007). Mesoscale modeling of aeolian dust emission during the BoDEx 2005 experiment. *Geophys. Res. Let.*, **34**, L07812. 39

BRINDLEY, H., KNIPPERTZ, P., RYDER, C. & ASHPOLE, I. (2012). A critical evaluation of the ability of the Spinning Enhanced Visible and Infrared Imager (SEVIRI) thermal infrared red-green-blue rendering to identify dust events: Theoretical analysis. *J. Geophys. Res.*, **117**, D07201. 102, 110

BROWN, A., BEARE, R., EDWARDS, J., LOCK, A., KEOGH, S., MILTON, S. & WALTERS, D. (2008). Upgrades to the boundary-layer scheme in the met office numerical weather prediction model. *Boundary-Layer Meteorology*, **128**, 117–132. 36, 37, 151, 156, 158, 163, 164

BROWN, A.R., BELJAARS, A.C.M. & HERSBACH, H. (2006). Errors in parametrizations of convective boundary-layer turbulent momentum mixing. *Quarterly Journal of the Royal Meteorological Society*, **132**, 1859–1876. 37, 151, 158

BURPEE, R.W. (1972). The origin and structure of Easterly Waves in the lower troposphere of North Africa. *J. Atmos. Sci.*, **29**, 77–90. 18, 19, 119

CAKMUR, R.V., MILLER, R. & TORRESM, O. (2004). Incorporating the effect of small-scale circulations upon dust emissions in an atmospheric general circulation model. *J. Geophys. Res. - Atmos.*, **109**, D07201. 4, 38

CARSLAW, K.S., BOUCHER, O., SPRACKLEN, D.V., MANN, G.W., RAE, J.G.L., WOODWARD, S. & KULMALA, M. (2010). A review of natural aerosol interactions and feedbacks within the Earth system. *Atmos. Chem. Phys.*, **10**, 1701–1737. 2

CARSON, D.J. (1973). The development of a dry inversion-capped convectively unstable boundary layer. *Quart. J. Roy. Meteor. Soc*, **99**, 450–467. 37

CHIAPELLO, I., MOULIN, C. & PROSPERO, J. (2005). Understanding the long-term variability of African dust transport across the Atlantic as recorded in both Barbados surface concentrations and large-scale Total Ozone Mapping Spectrometer (TOMS) optical thickness. *J. Geophys. Res.*, **110**, D18. 6

CHOMETTE, O., LEGRAND, M. & MARTICORENA, B. (1999). Determination of the wind speed threshold for the emission of desert dust using satellite remote sensing in the thermal infrared. *Journal of Geophysical Research*, **104**, 31207–31215. 13

COLARCO, P., DA SILVA, A., CHIN, M. & DIEHL, T. (2010). Online simulations of global aerosol distributions in the NASA GEOS-4 model and comparisons to satellite and ground-based aerosol optical depth. *Journal of Geophysical Research: Atmospheres (1984–2012)*, **115**. 2

COLLINS, W., BELLOUIN, N., DOUTRIAUX-BOUCHER, M., GEDNEY, N., HALLORAN, P., HINTON, T., HUGHES, J., JONES, C., JOSHI, M., LIDDICOAT, S., MARTIN, G., O'CONNOR, F., RAE, J., SENIOR, C., SITCH, S., TOTTERDELL, I., WILTSHIRE, A. & WOODWARD, S. (2011). Development and evaluation of an Earth-System model - HadGEM2. *Geosci. Model Dev.*, **4**, 1051–1075. 2, 42, 136, 142

CORNELIS, W.M. & GABRIELS, D. (2003). The effect of surface moisture on the entrainment of dune sand by wind: an evaluation of selected models. *Sedimentology*, **50**, 771–790. 5

CROUVI, O., SCHEPANSKI, K., AMIT, R., GILLESPIE, A.R. & ENZEL, Y. (2012). Multiple dust sources in the Sahara Desert: The importance of sand dunes. *Geophys. Res. Let.*, **39**, L13401. 33, 46

CUESTA, J., EDOUART, D., MIMOUNI, M., FLAMANT, P., LOTH, C., GIBERT, F., MARNAS, F., BOUKLILA, A., KHAREF, M., OUCHENE, B., KADI, M. & FLAMANT, C. (2008). Multi-platform observations of the seasonal evolution of the Saharan atmospheric boundary layer in Tamanrasset, Algeria, in the framework of the African Monsoon Multidisciplinary Analysis field campaign conducted in 2006. *J. Geophys. Res.*, **113**, D00C07. 14

CUESTA, J., MARSHAM, J., PARKER, D. & FLAMANT, C. (2009). Dynamical mechanisms controlling the vertical redistribution of dust and the thermodynamic structure of the West Saharan atmospheric boundary layer during summer. *Atmos. Sci. Lett.*, **10**, 34–42. 3, 15, 18, 26

CULF, A.D. (1992). An application of simple models to sahelian convective boundary-layer growth. *Bound.-Lay. Meteorol.*, **58**, 1–18. 131

DE LONGUEVILLE, F., HOUNTONDJI, Y.C., HENRY, S. & OZER, P. (2010). What do we know about effects of desert dust on air quality and human health in West Africa compared to other regions? *Science of the total environment*, **409**, 1–8. 4

DECKER, M., BRUNKE, M.A., WANG, Z., SAKAGUCHI, K., ZENG, X. & BOSILOVICH, M.G. (2012). Evaluation of the Reanalysis Products from GFSC, NCEP and ECMWF Using Flux Tower Observations. *J. Climate*, **25**, 1916–1944. 93, 106, 110

DEE, D.P., UPPALA, S.M., SIMMONS, A.J., BERRISFORD, P., POLI, P., KOBAYASHI, S., ANDRAE, U., BALMASEDA, M.A., BALSAMO, G., BAUER, P., BECHTOLD, P., BELJAARS, A.C.M., VAN DE BERG, L., BIDLOT, J., BORMANN, N., DELSOL, C., DRAGANI, R., FUENTES, M., GEER, A.J., HAIMBERGER, L., HEALY, S.B., HERSBACH, H., HOLMA, E.V., ISAKSEN, L., KALLBERG, P., KÖHLER, M., MATRICARDI, M., MCNALLY, A.P., B. M. MONGE-SANZ AND, J.J.M., PARK, B.K., PEUBEY, C., DE ROSNAY, P., TAVOLATO, C., THEPAUT, J.N. & VITART, F. (2011). The ERA-interim reanalysis: configuration and performance of the data assimilation system. *Quart. J. Roy. Meteor. Soc.*, **137**, 553–597. 3, 41, 44, 76, 112

DUCE, R. (1995). *Aerosol forcing of Climate*, chap. Sources, distributions and fluxes of mineral aerosols and their relationship to climate, 43–72. John Wiley, New Work. 4

EMMEL, C., KNIPPERTZ, P. & SCHULZ, O. (2010). Climatology of convective density currents in the southern foothills of the Atlas Mountains. *J. Geophys. Res.*, **115**, D11115. 24

ENGELSTAEDTER, S. & WASHINGTON, R. (2007). Atmospheric controls on the annual cycle of north african dust. *J. Geophys. Res.*, **112**, D03103. 19

ENGELSTAEDTER, S., TEGEN, I. & WASHINGTON, R. (2006). North African dust emissions and transport. *Earth-Science Reviews*, **79**, 73–100. 2, 4, 5, 9, 12, 60

ESTOQUE, M.A. (1968). Vertical mixing due to penetrative convection. *J. Atmos. Sci.*, **25**, 1046–1051. 37

ETLING, D. (2008). *Theoretische Meteorologie: Eine Einführung*. Springer Berlin Heidelberg New York (German). 7, 8, 26

EVAN, A.T., FLAMANT, C., FIEDLER, S. & DOHERTY, O. (2014). An analysis of aeolian dust in climate models. *Geophysical Research Letters*. 2, 13

FARQUHARSON, J.S. (1939). The diurnal variation of wind over tropical Africa. *Quart. J. Roy. Meteor. Soc*, **65**, 165–184. 33, 54

FÉCAN, F., MARTICORENA, B. & BERGAMETTI, G. (1999). Parameterization of the increase of the aeolian erosion threshold wind friction velocity due to soil moisture for arid and semi-arid areas. *Ann. Geophys.*, **17**, 249–157. 5, 137

FIEDLER, S., SCHEPANSKI, K., HEINOLD, B., KNIPPERTZ, P. & TEGEN, I. (2013a). Climatology of nocturnal low-level jets over North Africa and implications for modeling mineral dust emission. *J. Geophys. Res.-Atmos.*, **118**. 9, 13, 34, 43, 47, 51, 53, 55, 56, 58, 60, 61, 62, 63, 65, 67, 74, 77, 78, 79, 80, 81, 82, 94, 95, 108, 109, 111, 113, 121, 122, 127, 129, 130, 131, 133, 134, 139, 145, 147, 158, 163, 170, 174, 175

FIEDLER, S., SCHEPANSKI, K., KNIPPERTZ, P., HEINOLD, B. & TEGEN, I. (2013b). How important are cyclones for emitting mineral dust aerosol in North Africa? *Atmospheric Chemistry and Physics Discussions*, **13**, 32483–32528. 21, 71, 102, 103, 110, 115, 116, 117, 118, 120, 121, 122, 123, 124, 125, 127, 128, 130, 132, 139, 175, 176

FINK, A. (2006). Das Westafrikanische Monsoonsystem. *Promet*, **32**, 114–122 (German). 16, 18, 24

FLAMANT, C., CHABOUREAU, J., PARKER, D., TAYLOR, C., CAMMAS, J., BOCK, O., TIMOUK, F. & PELON, J. (2007). Airborne observations of the impact of a convective system on the planetary boundary layer thermodynamics and aerosol distribution in the inter-tropical discontinuity region of the west african monsoon. *Quart. J. Roy. Meteor. Soc*, **133**, 1175–1189. 23, 24

FLANNER, M.G., ZENDER, C.S., RANDERSON, J.T. & RASCH, P.J. (2007). Present-day climate forcing and response from black carbon in snow. *Journal of Geophysical Research: Atmospheres*, **112**. 1

FOLKEN, T. (2006). 50 years of the monin-obukhov similarity theory. *Bound.-Lay. Meteorol.*, **119**, 431–447. 8

FORET, G., BERGAMETTI, G., DULAC, F. & MENUT, L. (2006). An optimized particle size bin scheme for modeling mineral dust aerosols. *J. Geophys. Res*, **111**, D17310. 7

GAMMO, M. (1996). Thickness of the dry convection and large-scale subsidence above deserts. *Bound.-Lay. Meteorol.*, **79**, 265–278. 26

GHIENNE, J., SCHUSTER, M., BERNARD, A., DURINGER, P. & BRUNET, M. (2002). The Holocene giant Lake Chad revealed by digital elevation models. *Quart. Int.*, **87**, 81–85. 9

GIANNAKOPOULOU, E. & TOUMI, R. (2012). The Persian Gulf summertime low-level jet over sloping terrain. *Quart. J. Roy. Meteor. Soc.*, **138**, 145–157. 28, 30

GILLETTE, D.A. (1999). A qualitative geophysical explanation for "hot spot" dust emitting source regions. *Contributions to Atmospheric Physics*, **72**, 67–77. 11

GILLETTE, D.A. & PASSI, R. (1988). Modelling dust emission caused by wind erosion. *J. Geophys. Res.*, **93**, 14,233–14,242. 3, 10

GINOUX, P., CHIN, M., TEGEN, I., PROSPERO, J., HOLBEN, B., DUBOVIK, O. & LIN, S.J. (2001). Sources and distributions of dust aerosols simulated with the GOCART model. *J. Geophys. Res.*, **106D**, 20255–20274. 4, 5, 6, 12, 138

GRAMS, C.M., JONES, S.C., MARSHAM, J.H., PARKER, D.J., HAYWOOD, J.M. & HEUVELINE, V. (2010). The Atlantic Inflow to the Saharan heat low: Observations and Modelling. *Quart. J. Roy. Meteor. Soc*, **136**, 125–140. 30, 52

GRIFFIN, D.W. (2007). Atmospheric Movement of Mircoorganisms in Clouds of Desert Dust and Implications for Human Health. *Clin. Microbiol. Rev.*, **20**, 459–477. 4

GRIFFIN, W.D., GARRISON, V.H., HERMAN, J.R. & SHINN, E.A. (2001). African desert dust in the Caribbean atmosphere: Microbiology and public health. *Aerobiologia*, **17**, 203–213. 4

GROSS, G. (2012). Numerical simulation of future low-level jet characteristics. *Meteorologische Zeitschrift*, **21**, 305–311. 28, 56

HANNACHI, A., AWAD, A. & AMMAR, K. (2011). Climatology and classification of Spring Saharan cyclone tracks. *Clim. Dyn.*, **37**, 473–491. 17, 20, 22, 111, 113, 114, 115, 119, 133, 173

HAYWOOD, J., FRANCIS, P., OSBORNE, S., GLEW, M., LOEB, N., HIGHWOOD, E., TANRE, D., MYHRE, G., FORMENTI, P. & HIRST, E. (2003). Radiative properties and direct radiative effect of Saharan dust measured by the C-130 aircraft during SHADE: 1. Solar spectrum. *Journal Geophys. Res.*, **108**, 8577. 3

HAYWOOD, J., ALLAN, R., CULVERWELL, I., SLINGO, T., MILTON, S., EDWARDS, J. & CLERBAUX, N. (2005). Can desert dust explain the outgoing longwave radiation anomaly over the Sahara during July 2003? *J. Geophys. Res.-Atmos.*, **110**. 3

HEINOLD, B., HELMERT, J., HELLMUTH, O., WOLKE, R., ANSMANN, A., MARTICORENA, B., LAURENT, B. & TEGEN, I. (2007). Regional modeling of Saharan dust events using LM MUSCAT: Model description and case studies. *J. Geophys. Res.*, **112**, D11204. 4

HEINOLD, B., TEGEN, I., SCHEPANSKI, K., TESCHE, M., ESSELBORN, M., FREUDENTHALER, V., GROSS, S., KANDLER, K., KNIPPERTZ, P., MÜLLER, D., SCHLADITZ, A., TOLEDANO, C., WEINZIERL, B., ANSMANN, A., ALTHAUSEN, D., MÜLLER, T., PETZOLD, A. & WIEDENSOHLER, A. (2011). Regional modelling of Saharan dust and biomass-burning smoke Part I: Model description and evaluation. *Tellus B*, **63**. 33, 49

HEINOLD, B., KNIPPERTZ, P., MARSHAM, J.H., FIEDLER, S., DIXON, N.S., K. SCHEPANSKI B. LAURENT, . & TEGEN4, I. (2013). The role of deep convection and nocturnal low-level jets for dust emission in summertimeWest Africa: Estimates from convection-permitting simulations. *J. Geophys. Res.-Atmos.*, **118**, 1–16. 9, 23, 25, 31, 32, 35, 83, 85, 97, 113, 121, 132, 139, 143, 177

HODGES, K.I., LEE, R.W. & BENGTSSON, L. (2011). A comparison of extratropical cyclones in recent reanalysis ERA-Interim, NASA MERRA, NCEP CFSR. and JRA-25. *J. Climate*, **24**, 4888–4906. 22, 114

HOLTON, J.R. (2004). *An introduction to dynamic meteorology*. Elsevier. 7, 8

HOLTSLAG, A., SVENSSON, G., BAAS, P., BASU, S., BEARE, B., BELJAARS, A., BOSVELD, F., CUXART, J., LINDVALL, J., STEENEVELD, G. *et al.* (2013). Stable Atmospheric Boundary Layers and Diurnal Cycles: Challenges for Weather and Climate Models. *Bull. Amer. Meteor. Soc.*, **94**, 1691–1706. 38, 73, 172, 178

HOMAR, V. & STENSRUD, D.J. (2004). Sensitivities of an intense Mediterranean cyclone: Analysis and validation. *Q. J. R. Meteorol. Soc.*, **130**, 2519–2540. 22

HOMAR, V., RAMIS, C. & ALONSO, S. (2002). A deep cyclone of African origin over the Western Mediterranean: diagnosis and numerical simulation. *Ann*, **20**, 93–106. 22

HOMAR, V., JANSÀ, A., CAMPINS, J., GENOVÉS, A. & RAMIS, C. (2007). Towards a systematic climatology of sensitivities of Mediterranean high impact weather: a contribution based on intense cyclones. *Nat. Hazards Earth Syst. Sci.*, **7**, 445–454. 22

HONG, S.Y. & PAN, H.L. (1996). Nonlocal boundary layer vertical diffusion in a medium-range forecast model. *Mon. Wea. Rev.*, **124**, 2322–2339. 37

HOPSCH, S.B., THORNCROFT, C.D., HODGES, K. & AIYYER, A. (2007). West African storm tracks and their relationship to Atlantic tropical cyclones. *J. Climate*, **20**, 2468–2483. 19

HOXIT, L.R. (1975). Diurnal variations in planetary boundary-layer winds over land. *Bound.-Lay. Meteorol.*, **8**, 21–38. 28

HUNEEUS, N., SCHULZ, M., BALKANSKI, Y., GRIESFELLER, J., PROSPERO, J., KINNE, S., BAUER, S., BOUCHER, O., CHIN, M., DENTENER, F., DIEHL, T., EASTER, R., FILLMORE, D., GHAN, S., GINOUX, P., GRINI, A., HOROWITZ, L., KOCH, D., KROL, M.C., LANDING, W., LIU, X., MAHOWALD, N., MILLER, R., MORCRETTE, J.J., MYHRE, G., PENNER, J., PERLWITZ, J., STIER, P., TAKEMURA, T. & ZENDER, C.S. (2011). Global dust model intercomparison in AeroCom phase I. *Atmos. Chem. Phys.*, **11**, 7781–7816. 2, 4, 13, 60, 106, 135

ISAKSEN, I., GRANIER, C., MYHRE, G., BERNTSEN, T., DALSØREN, S., GAUSS, M., KLIMONT, Z., BENESTAD, R., BOUSQUET, P., COLLINS, W., COX, T., EYRING, V., FOWLER, D., FUZZI, S., JÖCKEL, P., LAJ, P., LOHMANN, U., MAIONE, M., MONKS, P., PREVOT, A., RAES, F., RICHTER, A., ROGNERUD, B., SCHULZ, M., SHINDELL, D., STEVENSON, D., STORELVMO, T., WANG, W.C., VAN WEELE, M., WILD, M. & WUEBBLES, D. (2009). Atmospheric composition change: Climate–chemistry interactions. *Atmospheric Environment*, **43**, 5138 – 5192. 4

IVERSEN, J. & WHITE, B. (1982). Saltation threshold on Earth, Mars and Venus. *Sedimentology*, **29**, 111–119. 13

JICKELLS, T., AN, Z., ANDERSEN, K., BAKER, A., BERGAMETTI, G., BROOKS, N., CAO, J., BOYD, P., DUCE, R., HUNTER, K., KAWAHATA, H., KUBILAY, N., LAROCHE, J., LISS, P., MAHOWALD, N., PROSPERO, J., RIDGWELL, A., TEGEN, I. & TORRES, R. (2005). Global iron connections between desert dust, ocean biogeochemistry, and climate. *Science*, **308**, 67–71. 4

JOLLIFFE, I. & STEPHENSON, D., eds. (2003). *Forecast Verification - A Practitioner's Guide in Atmospheric Science*. John Wiley & Sons Ltd. 75, 76

JONES, C., MAHOWALD, N. & LUO, C. (2004). Observational evidence of African desert dust intensification of Easterly waves. *Geophys. Res. Let.*, **31**, L17208. 19

JONES, C., MAHOWALD, N. & LUO, C. (2003). The role of easterly waves on African desert dust transport. *J. Climate*, **16**, 3617–3628. 19

JONES, C.D., HUGHES, J.K., BELLOUIN, N., HARDIMAN, S.C., JONES, G.S., KNIGHT, J., LIDDICOAT, S., O'CONNOR, F.M., ANDRES, R.J., BELL, C., BOO, K.O., BOZZO, A., BUTCHART, N., CADULE, P., CORBIN, K.D., DOUTRIAUX-BOUCHER, M., FRIEDLINGSTEIN, P., GORNALL, J., GRAY, L., HALLORAN, P.R., HURTT, G., INGRAM, W.J., LAMARQUE, J.F., LAW, R.M., MEINSHAUSEN, M., OSPREY, S., PALIN, E.J., PARSONS CHINI, L., RADDATZ, T., SANDERSON, M.G., SELLAR, A.A., SCHURER, A., VALDES, P., WOOD, N., WOODWARD, S., YOSHIOKA, M. & ZERROUKAT, M. (2011). The HadGEM2-ES implementation of CMIP5 centennial simulations. *Geosci. Model Dev.*, **4**, 543–570. 137

KAHANA, R., ZIV, B., ENZEL, Y. & DAYAN, U. (2002). Synoptic climatology of major floods in the negev desert, israel. *Int. J. Climatol.*, **22**, 867–882. 22

KALNAY, E. & COAUTHORS (1996). The NCEP/NCAR 40-Year Reanalysis Project. *Bull. Amer. Meteor. Soc.*, **77**, 437–471. 41, 76

KALU, A. (1979). *Saharan dust*, chap. The African dust plume: its characteristics and propagation across West Africa in winter, 95–118. J. Wiley and Sons. 33

KAPLAN, J.O. (2001). Geophysical applications of vegetation modeling. Tech. rep., Lund University. 139

KARYDIS, V.A., KUMAR, P., BARAHONA, D., SOKOLIK, I.N. & NENES, A. (2011). On the effect of dust particles on global cloud condensation nuclei and cloud droplet number. *Journal Geophys. Res.*, **116**, D23204. 3

KAUFMAN, Y., KOREN, I., REMER, L., TANRE, D., GINOUX, P. & FAN, S. (2005). Dust transport and deposition observed from the Terra-Moderate Resolution Imaging Spectroradiometer (MODIS) spacecraft over the Atlantic Ocean. *J. Geophys. Res*, **110**, D10S12. 2

KLOSE, M. & SHAO, Y. (2012). Stochastic parameterization of dust emission and application to convective atmospheric conditions. *Atmospheric Chemistry and Physics Discussions*, **12**, 3263–3293. 179

KLOSE, M., SHAO, Y., M.K.KARREMANN & FINK, A. (2010). Sahel dust zone and synoptic background. *Geophys. Res. Let.*, **37**, L09802. 21

KNIPPERTZ, P. (2008). Dust emissions in the West African heat trough: the role of the diurnal cycle and of extratropical disturbances. *Meteorologische Zeitschrift*, **17**, 553–563. 9, 18, 19, 34, 43

KNIPPERTZ, P. & FINK, A.H. (2006). Synoptic and dynamic aspects of an extreme springtime Saharan dust outbreak. *Quart. J. Roy. Meteor. Soc.*, **132**, 1153–1177. 16, 20, 21, 22

KNIPPERTZ, P. & TODD, M. (2010). The central west Saharan dust hot spot and its relation to African easterly waves and extratropical disturbances. *J. Geophys. Res.-Atmos.*, **115**, D12117. 17, 18, 19, 21, 113, 129, 130, 134, 173

KNIPPERTZ, P. & TODD, M.C. (2012). Mineral dust aerosol over the sahara: Processes of emission and transport, and implifications for modeling. *Rev. Geophys.*, **RG1007**, 2011RG000362. 3, 14, 21

KNIPPERTZ, P., DEUTSCHER, C., KANDLER, K., MUELLER, T., SCHULZ, O. & SCHUETZ, L. (2007). Dust mobilization due to density currents in the Atlas region: Observation from the Saharan Mineral Dust Experiment 2006 field campaign. *J. Geophys. Res.*, **112**, D21109. 24

KNIPPERTZ, P., ANSMANN, A., ALTHAUSEN, D., MUELLER, D., TESCHE, M., BIERWIRTH, E., DINTER, T., MUELLER, T., VON HOYNINGEN-HUENE, W., SCHEPANSKI, K., WENDISCH, M., HEINOLD, B., KANDLER, K., PETZOLD, A., SCHUETZ, L. & TEGEN, I. (2009a). Dust mobilization and transport in the northern Sahara during SAMUM 2006 - a meteorological overview. *Tellus Ser. B - Chem. Phys. Meteor.*, **61**, 12–31. 20

KNIPPERTZ, P., TRENTMANN, J. & SEIFERT, A. (2009b). High-resolution simulations of convective cold pools over the northwestern Sahara. *J. Geophys. Res.-Atmos.*, **114**. 23, 24

KOCH, J. & RENNO, N. (2005). The role of convective plumes and vortices on the global aerosol budget. *Geophys. Res. Let.*, **32**, L18806. 27

KOCHA, C., TULET, P., LAFORE, J.P. & FLAMANT, C. (2013). The importance of the diurnal cycle of Aerosol Optical Depth in West Africa. *Geophysical Research Letters*, **40**, 785–790. 25

KOK, J. (2011). Does the size distribution of mineral dust aerosols depend on the wind speed at emission? *Atmos. Chem. Phys. Discuss.*, **11**, 19995–20012. 3, 11

KOREN, I. & KAUFMANN, Y. (2004). Direct wind measurements of Saharan dust events from Terra and Aqua satellites. *Geophys. Res. Let.*, **31**, L06122. 13, 39

KOREN, I., KAUFMAN, Y., WASHINGTON, R., TODD, M., RUDICH, Y., MARTINS, J. & ROSENFELD, D. (2006). The Bodele depression: A single spot in the Sahara that provides most of the mineral dust to the Amazon forest. *Environ. Res. Lett.*, **1**, 014005. 2, 9, 95, 96

KOTTEK, M., GRIESER, J., BECK, C., RUDOLF, B. & RUBEL, F. (2006). World map of the Koeppen-Geiger climate classification updated. *Meteorologische Zeitschrift*, **15**, 259–263. 6

LANDSEA, C., GRAY, W., MIELKE, P. & BERRY, K. (1992). Long-term variations of western sahelian monsoon rainfall and intense united-states landfalling hurricanes. *J. Climate*, **5**, 1528–1534. 19

LAURENT, B., MARTICORENA, B., BERGAMETTI, G., LÉON, J. & MAHOWALD, N. (2008). Modeling mineral dust emission from the sahara desert using new surface properties and soil database. *J. Geophys. Res.*, **113**, D14218. 2, 5, 6, 7, 9, 11, 13, 19, 49, 60

LAURENT, B., TEGEN, I., HEINOLD, B., SCHEPANSKI, K., WEINZIERL, B. & ESSELBORN, M. (2010). A model study of Saharan dust emission and distributions during the SAMUM-1 campaign. *J. Geophys. Res.*, **115**, D21210. 102, 103, 123

LAVAYSSE, C., FLAMANT, C., JANICOT, S., PARKER, D.J., LAFORE, J.P., SULTAN, B. & PELON, J. (2009). Seasonal evolution of the West African heat low: a climatological perspective. *Clim. Dyn.*, **33**, 313–330. 17, 18, 114, 115, 116, 121

LENSCHOW, D.H. & STANKOW, B.B. (1979). The rapid morning boundary-layer transition. *J. Atmos. Sci.*, **36**, 2108–2124. 33

LEROUX, S., HALL, N.M. & KILADIS, G.N. (2011). Intermittent african easterly wave activity in a dry atmospheric model: Influence of the extratropics. *Journal of Climate*, **24**. 18

LILLY, D.K. (1968). Models of cloud topped mixed layers under a strong inversion. *Quart. J. Roy. Meteor. Soc*, **94**, 292–309. 37

LOHMANN, U. & FEICHTER, J. (2005). Global indirect aerosol effects: A review. *Atmos. Chem. Phys.*, **5**, 715–737. 1, 3

LOTHON, M., SAID, F., LOHOU, F. & CAMPISTRON, B. (2008). Observation of the diurnal cycle in the low troposphere of West Africa. *Mon. Wea. Rev.*, **136**, 3477–3500. 31, 33, 47, 54

LOUIS, J., TIEDTKE, M. & GELEYN, J. (1982). A short history of the PBL parameterization at ECMWF. In *Proceedings of Workshop on boundary-layer parameterization.*, 59–79, ECMWF, Reading, UK. 44

LUO, C., MAHOWALD, N. & JONES, C. (2004). Temporal variability of dust mobilization and concentration in source regions. *J. Geophys. Res.*, **109**, D20202. 19, 116

MAHERAS, P., FLOCAS, H., PATRIKAS, I. & ANAGNOSTOPOULOU, C. (2001). A 40 year objective climatology of surface cyclones in the Mediterranean region: Spatial and temporal distribution. *Int. J. Climatol.*, **21**, 109–130. 20, 21, 22, 112, 114, 115, 133

MAHOWALD, N., BAKER, A., BERGAMETTI, G., BROOKS, N., DUCE, R., JICKELLS, T., KUBILAY, N., PROSPERO, J. & TEGEN, I. (2005). Atmospheric global dust cycle and iron inputs to the ocean. *Global Geochem. Cycle*, **19**, GB4025. 4

MAHOWALD, N.M. & LUO, C. (2003). A less dusty future? *Geophysical Research Letters*, **30**, n/a–n/a. 4

MARSHAM, J., PARKER, D., GRAMS, C., JOHNSON, B., GREY, W. & ROSS, A. (2008a). Observations of mesoscale and boundary-layer scale circulations affecting dust transport and uplift over the Sahara. *Atmos. Chem. Phys.*, **8**, 6979–6993. 18, 26, 27

MARSHAM, J., KNIPPERTZ, P., DICKSON, N., PARKER, D.J. & LISTER, G. (2011). The importance of the representation of deep convection for modeled dust-generating winds over West Africa during summer. *Geophys. Res. Let.*, **38**, L16803. 23, 34, 135

MARSHAM, J.H., PARKER, D., GRAMS, C., TAYLOR, C. & HAYWOOD, J. (2008b). Uplift of Saharan dust south of the inter-tropical discontinuity (itd). *J. Geophys. Res.*, **113**, D21102. 19

MARSHAM, J.H., DIXON, N.S., GARCIA-CARRERAS, L., LISTER, G.M.S., PARKER, D.J., KNIPPERTZ, P. & BIRCH, C.E. (2013a). The role of moist convection in the west african monsoon system: Insights from continental-scale convection-permitting simulations. *Geophysical Research Letters*, **40**, 1843–1849. 145

MARSHAM, J.H., HOBBY, M., ALLEN, C.J.T., BANKS, J.R., BART, M., BROOKS, B.J., CAVAZOS-GUERRA, C., ENGELSTAEDTER, S., GASCOYNE, M., LIMA, A.R., MARTINS, J.V., MCQUAID, J.B., O'LEARY, A., OUCHENE, B., OULADICHIR, A., PARKER, D.J., SACI, A., SALAH-FERROUDJ, M., TODD, M.C. & WASHINGTON, R. (2013b). Meteorology and dust in the central Sahara: Observations from Fennec supersite-1 during the June 2011 Intensive Observation Period. *J. Geophys. Res. - Atmos.*, **118**, 4069–4089. 74, 83, 109

MARTICORENA, B. & BERGAMETTI, G. (1995). Modelling the atmospheric dust cycle. 1: Design of a soilderived dust emission scheme. *J. Geophys. Res.*, **100**, 16,415–16,430. 3, 5, 7, 8, 10, 11, 12, 137, 138

MARTIN, G.M., BELLOUIN, N., COLLINS, W., CULVERWELL, I., HALLORAN, P., HARDIMAN, S., HINTON, T., JONES, C., MCDONALD, R., A.J, M., O'CONNOR, F., ROBERTS, M., RODRIGUEZ, J., WOODWARD, S., BEST, M., BROOKS, M., BROWN, A., BUTCHART, N., DEAR-DEN, C., DERBYSHIRE, S., DHARSSI, I., DOUTRIAUX-BOUCHER, M., EDWARDS, J., FALLOON, P., GEDNEY, N., GRAY, L., HEWITT, H., HOBSON, M., HUDDLESTON, M., HUGHES, J., INESON, S., INGRAM, W., JAMES, P., JOHNS, T., JOHNSON, C., JONES, A., JONES, C., JOSHI, M., KEEN, A., LIDDICOAT, S., LOCK, A., MAIDENS, A., MANNERS, J., MILTON, S., RAE, J., RIDLEY, J., SELLAR, A., SENIOR, C., TOTTERDELL, I., VERHOEF, A., VIDALE, P. & WILTSHIRE, A. (2011). The HadGEM2 family of Met Office Unified Model climate configurations. *Geosci. Model Dev.*, **4**, 723–757. 37, 42, 136

MAY, P.T. (1995). The Australian nocturnal jet and diurnal variations of boundary-layer winds over Mt. Isa in North-eastern Australia. *Quarterly Journal of the Royal Meteorological Society*, **121**, 987–1003. 28, 45

MEKONNEN, A., THORNCROFT, C.D. & AIYYER, A.R. (2006). Analysis of convection and its association with african easterly waves. *J. Climate*, **19**, 5404–5421. 18, 19, 118

MENUT, L., SCHMECHTIG, C. & MARTICORENA, B. (2005). Sensitivity of the sandblasting flux calculations to the soil size distribution accuracy. *Journal of Atmospheric and Oceanic Technology*, **22**, 1875–1884. 13, 179

MENUT, L., PEREZ, C., HAUSTEIN, K., BESSAGNET, B., PRIGENT, C. & ALFARO, S. (2013). Impact of surface roughness and soil texture on mineral dust emission fluxes modeling. *Journal of Geophysical Research: Atmospheres*, **118**, 6505–6520. 13, 179

MERCADO, L.M., BELLOUIN, N., SITCH, S., BOUCHER, O., HUNTINGFORD, C., WILD, M. & COX, P.M. (2009). Impact of changes in diffuse radiation on the global land carbon sink. *Nature*, **458**, 1014–1017. 1

MILLER, R., PERLWITZ, J. & TEGEN, I. (2004). Feedback upon dust emission by dust radiative forcing through the planetary boundary layer. *J. Geophys. Res*, **109**, D24209. 4

MILLER, S.D., KUCIAUSKAS, A.P., LIU, M., JI, Q., REID, J.S., BREED, D.W., WALKER, A.L. & MANDOOS, A.A. (2008). Haboob dust storms of the southern arabian peninsula. *Journal of Geophysical Research: Atmospheres (1984–2012)*, **113**. 24

MILTON, S.F., GREED, G., BROOKS, M.E., HAYWOOD, J., JOHNSON, B., ALLAN, R.P., SLINGO, A. & GREY, W.M.F. (2008). Modeled and observed atmospheric radiation balance during the West African dry season: Role of mineral dust, biomass burning aerosol, and surface albedo. *Journal of Geophysical Research: Atmospheres*, **113**. 77

MOULIN, C., LAMBERT, C..E., DAYAN, U.., MASSON, V.., RAMONET, M.., BOUSQUET, P.., LEGRAND, M., BALKANSKI, Y.J., GUELLE, W., MARTICORENA, B., BERGAMETTI, G. & DULAC, F. (1998). Satellite climatology of African dust transport in the Mediterranean atmosphere. *J. Geophys. Res*, **103**, 13137–13144,. 2, 22

NICHOLSON, S. (2000). The nature of rainfall variability over Africa on times scales of decades to millenia. *Global Planet Change*, **26**, 137–158. 17, 18

OKIN, G.S., MAHOWALD, N., CHADWICK, O.A. & P. ARTAXO, P. (2004). Impact of desert dust on the biogeochemistry of phosphorus in terrestrial ecosystems. *Global Biogeochem. Cycle*, **18**, GB2005. 4

PARKER, D., BURTON, R., DIONGUE-NIANG, A., ELLIS, R., FELTON, M., TAYLOR, C., THORNCROFT, C., BESSEMOULIN, P. & TOMPKINS, A. (2005). The diurnal cycle of the West African monsoon circulation. *Quart.J. Roy. Meteor. Soc.*, **131**, 2839–2860. 28, 31, 52, 173

PARKER, D.J., FINK, A., JANICOT, S., NGAMINI, J., DOUGLAS, M., AFIESIMAMA, E., AGUSTI-PANAREDA, A., BELJAARS, A., DIDE, F., DIEDHIOU, A., LEBEL, T., POLCHER, J., REDELSPERGER, J., THORNCROFT, C. & WILSON, G. (2008). The AMMA radiosonde program and its implications for the future of atmospheric monitoring over Africa. *Bull. Amer. Meteor. Soc.*, **89**, 1015–1027. 73

PEDGLEY, D. (1972). Desert depression over northeast Africa. *Meteorol. Mag.*, **101**, 228–244. 118

PETERS, M. & TETZLAFF, G. (1988). The structure of West African squall lines and their environmental moisture budget. *Meteorol. Atmos. Phys.*, **39**, 74–84. 18, 24

PINCUS, R. & BAKER, M. (1994). Effect of precipitation on the albedo susceptibility of clouds in the marine boundary layer. *Nature*, **372**, 250–252. 1

POSPICHAL, B., KARAM, D.B., CREWELL, S., FLAMANT, C., HUENERBEIN, A., BOCK, O. & SAID, F. (2010). Diurnal cycle of the intertropical discontinuity over West Africa analysed by remote sensing and mesoscale modelling. *Quart. J. Roy. Meteor. Soc.*, **136**, 92–106. 31, 45, 52, 173

PRIGENT, C., TEGEN, I., AIRES, F., MARTICORENA, B. & ZRIBI, M. (2005). Estimation of the aerodynamic roughness length in arid and semi-arid regions over the globe with ers scatterometer. *J. Geophys. Res.*, **110**, D09205. 12

QUAAS, J., MING, Y., MENON, S., TAKEMURA, T., WANG, M., PENNER, J.E., GETTELMAN, A., LOHMANN, U., BELLOUIN, N., BOUCHER, O., SAYER, A.M., THOMAS, G.E., MCCOMISKEY, A., FEINGOLD, G., HOOSE, C., KRISTJANSSON, J.E., LIU, X., BALKANSKI, Y., DONNER, L.J., GINOUX, P.A., STIER, P., GRANDEY, B., FEICHTER, J., SEDNEV, I., BAUER, S.E., KOCH, D., GRAINGER, R.G., KIRKEVAG, A., IVERSEN, T., SELAND, O., EASTER, R., GHAN, S.J., RASCH, P.J., MORRISON, H., LAMARQUE, J.F., IACONO, M.J., KINNE, S. & SCHULZ, M. (2009). Aerosol indirect effects - general circulation model intercomparison and evaluation with satellite data. *Atmos. Chem. Phys.*, **9**, 8697–8717. 2

RACZ, Z. & SMITH, R.K. (1999). The dynamics of heat lows. *Q. J. R. Meteorol. Soc.*, **125**, 225–252. 17, 87

REDELSPERGER, J.L., THORNCROFT, C.D., DIEDHIOU, A., LEBEL, T., PARKER, D.J. & POLCHER, J. (2006). African Monsoon Multidisciplinary Analysis: An International Research Project and Field Campaign. *Bulletin of the American Meteorological Society*, **87**, 1739. 73, 109

REINFRIED, F., TEGEN, I., HEINOLD, B., SCHEPANSKI, K., CUBASCH, U., HUEBENER, H. & KNIPPERTZ, P. (2009). Simulations of convectively-driven density currents in the Atlas region using a regional model: Impacts on dust emission and sensitivity to horizontal resolution and convection schemes. *Journal Geophys. Res.*, **114**, D08127. 3, 24

Ridley, D.A., Heald, C.L. & Prospero, J.M. (2014). What controls the recent changes in African mineral dust aerosol across the Atlantic? *Atmospheric Chemistry and Physics Discussions*, **14**, 3583–3627. 106

Rienecker, M.M., Suarez, M.J., Gelaro, R., Todling, R., Bacmeister, J., Liu, E., Bosilovich, M.G., Schubert, S.D., Takacs, L., Kim, G.K., Bloom, S., Chen, J., Collins, D., Conaty, A., da Silva, A., Gu, W., Joiner, J., Koster, R.D., Lucchesi, R. & Molod, A. (2011). MERRA: NASA's Modern-Era Retrospective Analysis for Research and Applications. *Journal of Climate*, **24**, 3624 – 3648. 41, 76

Rife, D.L., Pinto, J.O., Monaghan, A.J., Davis, C.A. & Hannan, J.R. (2010). Global Distribution and Characteristics of Diurnally Varying Low-Level Jets. *J. Climate*, **23**, 5041–5064. 28, 45, 52, 54

Rosenfeld, D., Rudich, Y. & Lahav, R. (2001). Desert dust suppressing precipitation: A possible desertification feedback loop. *PNAS*, **98**, 5975–5980. 3

Samelson, R.M. & Barbour, P.L. (2007). Low-Level Jets, Orographic Effects, and Extreme Events in Nares Strait: A Model-Based Mesoscale Climatology. *Mon. Wea. Rev.*, **136**, 4746–4759. 28, 31

Sandu, I., Beljaars, A. & Balsamo, G. (2012). Experience with the representation of stable conditions in the ECMWF model. In *Workshop on Diurnal cycles and the stable boundary layer, 7-10 November 2011*, Shinfield Park, Reading. 44, 66

Sandu, I., Beljaars, A., Bechtold, P., Mauritsen, T. & Balsamo, G. (2013). Why is it so difficult to represent stably stratified conditions in numerical weather prediction (NWP) models? *Journal of Advances in Modeling Earth Systems*. 36, 37, 38, 73, 80, 83, 90, 96, 106, 109, 110, 151, 158, 163, 164, 172, 174, 175, 178

Schepanski, K. & Knippertz, P. (2011). Soudano-Saharan depressions and their importance for precipitation and dust: a new perspective on a classical synoptic concept. *Quarterly Journal of the Royal Meteorological Society*, **137**, 1431–1445. 20, 22, 112, 113, 132, 173

Schepanski, K., Tegen, I., Todd, M., Heinold, B., Bönisch, G., Laurent, B. & Macke, A. (2009). Meteorological processes forcing Saharan dust emission inferred from MSG-SEVERI observations of subdaily dust source activation and numerical models. *J. Geophys. Res.*, **114**, D10201. 4, 5, 9, 19, 20, 21, 24, 25, 28, 31, 33, 34, 35, 43, 46, 49, 54, 64, 68, 69, 102, 110, 139, 173, 175

SCHEPANSKI, K., I.TEGEN & MACKE, A. (2012). Comparison of satellite based observations of Saharan dust source areas. *Remote Sensing of Environment*, **123**, 90–97. 9, 10, 21, 42, 49, 102, 103, 110

SCHEPANSKI, K., FLAMANT, C., CHABOUREAU, J.P., KOCHA, C., BANKS, J.R., BRINDLEY, H.E., LAVAYSSE, C., MARNAS, F., PELON, J. & TULET, P. (2013). Characterization of dust emission from alluvial sources using aircraft observations and high-resolution modeling. *Journal of Geophysical Research: Atmospheres*, **118**, 7237–7259. 9, 13, 35, 179

SCHEPANSKI, K., KNIPPERTZ, P., FIEDLER, S., TIMOUK, F. & DEMARTY, J. (2014). The sensitvity of nocturnal low-level jets and near-surface winds over the Sahel to resolution, initial conditions and boundary-layer setup. *submitted to Q. J. Roy. Met.*. 38

SCHEPANSKI, K., TEGEN, I., LAURENT, B., HEINOLD, B. & MACKE, A. (2007). A new Saharan dust source activation frequency map derived from MSG-SEVIRI IR-channels. *Geophys. Res. Let.*, **34**. 9, 12, 21, 23, 49, 102, 103, 139

SCHMECHTIG, C., MARTICORENA, B., CHATENET, B., BERGAMETTI, G., RAJOT, J.L. & COMAN, A. (2011). Simulation of the mineral dust content overWestern Africa from the event to the annual scale with the CHIMERE-DUST model. *Atmos. Chem. Phys.*, **11**, 7185–7207. 2, 3, 4, 9, 13, 14, 19, 39, 60

SCHULZ, M., PROSPERO, J.M., BAKER, A.R., DENTENER, F., ICKES, L., LISS, P.S., MAHOWALD, N.M., NICKOVIC, S., GARCÍA-PANDO, C.P., RODRÍGUEZ, S. *et al.* (2012). Atmospheric transport and deposition of mineral dust to the ocean: implications for research needs. *Environmental science & technology*, **46**, 10390–10404. 4

SHAO, Y. (2001). A model for mineral dust emission. *J. Geophys. Res.*, **106**, 20239–20254. 11

SHAO, Y. (2008). *Physics and Modeling of wind erosion*. Springer, 2nd edn. 26

SHAO, Y., RAUPACH, M. & FINDLATER, P. (1993). Effect of saltation bonbardment on the entrainment of dust by wind. *J. Geophys. Res.*, **98**, 12,719–12,726. 3

SHAO, Y., WYRWOLL, K.H., CHAPPELL, A., HUANG, J., LIN, Z., MCTRAINSH, G.H., MIKAMI, M., TANAKA, T.Y., WANG, X. & YOON, S. (2011). Dust cycle: A emerging core theme in eaerth system science. *Aerolian research*, **2**, 181–204. 4, 5, 10, 11, 15

SLINGO, A., ACKERMAN, T.P., ALLAN, R.P., KASSIANOV, E.I., MCFARLANE, S.A., ROBINSON, G.J., BARNARD, J.C., MILLER, M.A., HARRIES, J.E., RUSSELL, J.E. & DEWITTE, S. (2006). Observations of the impact of a major Saharan dust storm on the atmospheric radiation balance. *Geophys. Res. Let.*, **33**. 16

SOKOLIK, I. & TOON, O. (1996). Direct radiative forcing by anthropogenic airborne mineral aerosols. *nature*, **381**, 681–683. 3

STANELLE, T., VOGEL, B., VOGEL, H., BAEUMER, D. & KOTTMEIER, C. (2010). Feedback between dust particles and atmospheric processes over West Africa during dust episodes in March 2006 and June 2007. *Atmos. Chem. Phys.*, **10**, 10771–10788. 4

STEENEVELD, G.J., VAN DE WIEL, B.J.H. & HOLTSLAG, A.A.M. (2006). Modeling the Evolution of the Atmospheric Boundary Layer Coupled to the Land Surface for Three Contrasting Nights in CASES-99. *Journal of the Atmospheric Sciences*, **63**, 920 – 935. 38, 178

STEENEVELD, G.J., MAURITSEN, T., DE BRUIJN, E.I.F., VILÈ-GUERAU DE ARELLANO, J., SVENSSON, G. & HOLTSLAG, A.A.M. (2008). Evaluation of Limited-Area Models for the Representation of the Diurnal Cycle and Contrasting Nights in CASES-99. *Journal of Applied Meteorology & Climatology*, **47**, 869 – 887. 38, 96, 106, 178

STENSRUD, D. (2007). *Parameterization schemes. Keys to understanding Numerical Weather Prediction Models*, chap. Planetary boundary layer and turbulence parameterization, 138–181. Cambridge University Press. 26, 36, 37

STENSRUD, D.J. (1996). Importance of Low-Level Jets to Climate: A review. *J. Climate*, **9**, 1698–1711. 27, 28, 30, 45, 47

STEVENS, B. & FEINGOLD, G. (2009). Untangling aerosol effects on clouds and precipitation in a buffered system. *Nature*, **461**, 607–613. 1

STIER, P., KINNE, S., KLOSTER, S., VIGNATI, E., WILSON, J., GRANZEVELD, L., TEGER, I., WERNER, M., BALKANSKI, Y., SCHULZ, M., BOUCHER, O., MINIKIN, A. & PETZOLD, A. (2005). The aerosol-climate model ECHAM5-HAM. *Atmos. Chem. Phys.*, **5**, 1125–1156. 9

STULL, R. (1993). Review of non-local mixing in turbulent atmospheres: transilient turbulence theory. *Bound.-Layer Meteor.*, **62**, 21–96. 37

STULL, R.B. (1988). *An Introduction to Boundary Layer Meteorology*. Kluwer. 26, 27, 28, 33, 36, 153

SUTTON, L. (1925). Haboobs. *Quarterly Journal of the Royal Meteorological Society*, **51**, 25–30. 24

SVENSSON, G., HOLTSLAG, A., KUMAR, V., MAURITSEN, T., STEENEVELD, G., ANGEVINE, W., BAZILE, E., BELJAARS, A., BRUIJN, E., CHENG, A., CONANGLA, L., CUXART, J., EK, M., FALK, M., FREEDMAN, F., KITAGAWA, H., LARSON, V., LOCK, A., MAILHOT, J., MASSON, V., PARK, S., PLEIM, J., SÖDERBERG, S., WENG, W. & ZAMPIERI, M. (2011). Evaluation of the Diurnal Cycle in the Atmospheric Boundary Layer Over Land as Represented by a Variety of Single-Column Models: The Second GABLS Experiment. *Boundary-Layer Meteorology*, **140**, 177–206. 38, 178

TAKEMI, T., YASUI, M., ZHOU, J. & LIU, L. (2006). Role of boundary layer and cumulus convection on dust emission and transport. *J. Geophys. Res.-Atmos.*, **111**, D11203. 27

TANAKA, T. & CHIBA, M. (2006). A numerical study of the contributions of dust source regions to the global dust budget. *Global Planet Change*, **52**, 88–104. 5

TEGEN, I. & FUNG, I. (1994). Modeling of mineral dust in the atmosphere: Sources , transport, and optical thickness. *J. Geophys. Res.*, **99**, 22897–22914. 7

TEGEN, I. & SCHEPANSKI, K. (2009). The global Distribution of Mineral Dust. *IOP: Conf. Series: Earth and Environmental Science*, **7**, 012001. 2, 9, 12

TEGEN, I., HARRISON, S., KOHFELD, K., PRENTICE, I., COE, M. & M. HEIMANN (2002). Impact of vegetation and preferential source areas on global dust aerosols: Results from a model study. *J. Geophys. Res.*, **107**, 4576. 3, 4, 9, 10, 11, 12, 13, 42, 49, 60, 77, 95, 97, 102, 103, 104, 109, 113, 137, 138, 139, 140, 141, 158, 175, 177

TEGEN, I., WERNER, M., HARRISON, S.P. & KOHFELD, K.E. (2004). Relative importance of climate and land use in determining present and future global soil dust emission. *Geophysical Research Letters*, **31**. 13

TEGEN, I., SCHEPANSKI, K. & HEINOLD, B. (2013). Comparing two years of Saharan dust source activation obtained by regional modelling and satellite observations. *Atmospheric Chemistry and Physics*, **13**, 2381–2390. 102, 103, 110

TEXTOR, C., SCHULZ, M., GUIBERT, S., KINNE, S., BALKANSKI, Y., BAUER, S., BERNTSEN, T., BERGLEN, T., BOUCHER, O., CHIN, M., DENTENER, F., DIEHL, T., EASTER, R., FEICHTER, H., FILLMORE, D., GHAN, S., GINOUX, P., GONG, S., GRINI, A., HENDRICKS, J., HOROWITZ, L., HUANG, P., ISAKSEN, I., IVERSEN, I., KLOSTER, S., KOCH, D., KIRKEVÅG, A., KRISTJANSSON, J.E., KROL, M., LAUER, A., LAMARQUE, J.F., LIU, X., MONTANARO, V., MYHRE, G., PENNER, J., PITARI, G., REDDY, S., SELAND, Ø., STIER, P., TAKEMURA, T. & TIE, X. (2006). Analysis and quantification of the diversities of aerosol life cycles within AeroCom. *Atmospheric Chemistry & Physics*, **6**, 1777–1813. 135

THORNCROFT, C.D. & HODGES, K. (2000). African Easterly Wave Variability and Its Relationship to Atlantic Tropical Cyclone Activity. *J. Climate*, **14**, 1166–1179. 18, 19, 116, 118, 119, 124, 133, 134

THORNCROFT, C.D., HALL, N.M.J. & KILADIS, G.N. (2008). Three-dimensional structure and dynamics of African Easterly Waves. Part III: Genesis. *J. Atmos. Sci.*, **65**, 3596–3607. 18, 19

TODD, M., ALLEN, C., BART, M., BECHIR, M., BENTEFOUET, J., BROOKS, B., CAVAZOS-GUERRA, C., CLOVIS, T., DEYANE, S., DIEH, M., ENGELSTAEDTER, S., FLAMANT, C., GARCIA-CARRERAS, L., GANDEGA, A., GASCOYNE, M., HOBBY, M., KOCHA, C., LAVAYSSE, C., MARSHAM, J., MARTINS, J., MCQUAID, J., NGAMINI, J.B., PARKER, D., PODVIN, T., ROCHA-LIMA, A., TRAORE, S., WANG, Y. & WASHINGTON, R. (2013). Meteorological and dust aerosol conditions over the Western Saharan region observed at Fennec supersite-2 during the Intensive Observation Period in June 2011. *Journal of Geophysical Research: Atmospheres*. 17, 74, 85, 87, 90

TODD, M.C., WASHINGTON, R., RAGHAVAN, S., LIZCANO, G. & KNIPPERTZ, P. (2008). Regional model simulations of the Bodele low-level jet of northern Chad during the Bodélé Dust Experiment (BoDEx 2005). *J. Climate*, **21**, 995–1012. 28, 31, 33, 38, 45, 50, 54, 73, 95, 96, 109, 163

TOMPKINS, A., CARDINALI, C., MORCRETTE, J. & RODWELL, M. (2005). Influence of aerosol climatology on forecasts of the African Easterly Jet. *Geophys. Res. Lett.,*, **32**, L10801. 4

TRIGO, I.F., DAVIES, T.D. & BIGG, G.R. (1999). Objective Climatology of Cyclones in the Mediterranean Region. *J. Climate*, **12**, 1685–1696. 21, 22, 114, 115, 133

TRIGO, I.F., BIGG, G.R. & DAVIES, T.D. (2002). Climatology of Cyclogenesis Mechanisms in the Mediterranean. *Mon. Wea. Rev.*, **130**, 549–569. 21, 22

TROEN, I. & MAHRT, L. (1986). A simple model of the atmospheric boundary layer: sensitivity to surface evaporation. *Bound.-Layer Meteor.*, **37**, 129–148. 37

TUCKER, C.J., PINZON, J.E., BROWN, M.E., SLAYBACK, D.A., PAK, E.W., MAHONEY, R., VERMOTE, E.F. & EL SALEOUS, N. (2005). An extended avhrr 8-km ndvi dataset compatible with modis and spot vegetation ndvi data. *International Journal of Remote Sensing*, **26**, 4485–4498. 139

TWOMEY, S. (1974). Pollution and the planetary albedo. *Atmos. Environ.*, **8**, 1251–1256. 1

UPPALA, S.M., KÅLLBERG, P.W., SIMMONS, A.J., ANDRAE, U., BECHTOLD, V.D.C., FIORINO, M., GIBSON, J.K., HASELER, J., HERNANDEZ, A., KELLY, G.A., LI, X., ONOGI, K., SAARINEN, S., SOKKA, N., ALLAN, R.P., ANDERSSON, E., ARPE, K., BALMASEDA, M.A., BELJAARS, A.C.M., BERG, L.V.D., BIDLOT, J., BORMANN, N., CAIRES, S., CHEVALLIER, F., DETHOF, A., DRAGOSAVAC, M., FISHER, M., FUENTES, M., HAGEMANN, S., HÓLM, E., HOSKINS, B.J., ISAKSEN, L., JANSSEN, P.A.E.M., JENNE, R., MCNALLY, A.P., MAHFOUF, J.F., MORCRETTE, J.J., RAYNER, N.A., SAUNDERS, R.W., SIMON, P., STERL, A., TRENBERTH, K.E., UNTCH, A., VASILJEVIC, D., VITERBO, P. & WOOLLEN, J. (2005). The ERA-40 re-analysis. *Quarterly Journal of the Royal Meteorological Society*, **131**, 2961–3012. 76

VAN DE WIEL, B., MOENE, A., STEENEVELD, G., BAAS, P., BOSVELD, F. & HOLTSLAG, A. (2010). A Conceptional view on Inertial Oscillations and Nocturnal Low-Level Jets. *J. Atmos. Sci.*, **67**, 2679–2689. 29, 30, 59

VAN DE WIEL, B., MOENE, A., HARTOGENSIS, O., DE BRUIN, H. & HOLTSLAG, A. (2003). Intermittent turbulence in the stable boundary layer over land. Part III: A classification for observations during CASES-99. *J. Atmos. Sci.*, **60**, 2509–2522. 33

WARNER, T. (2004). *Desert Meteorology*. Cambridge University Press. 5, 6, 7, 22

WASHINGTON, R. & TODD, M. (2005). Atmospheric controls on mineral dust emission from the Bodele depression, Chad: the role of the low-level jet. *Geophys. Res. Let.*, **32**, L17701. 9, 28, 31, 34, 43, 46, 50, 68, 163

WASHINGTON, R., TODD, M., ENGELSTAEDTER, S., MBAINAYEL, S. & MITCHELL, F. (2006). Dust and the low-level circulation over the Bodele Depression. *J. Geophys. Res.-Atmos.*, **111**, D03201. 28, 31, 42, 74, 93

WERNLI, H. & SCHWIERZ, C. (2006). Surface Cyclones in the ERA-40 Dataset (1958–2001). Part I: Novel Identification Method and Global Climatology. *J. Atmos. Sci.*, **63**, 2486–2507. 112

WHITEMAN, C., BIAN, X. & ZHONG, S. (1997). Low-Level Jet Climatology from Enhanced Rawinsonde Observations at a Site in the Southern Great Plains. *J. Appl. Meteor.*, **36**, 1363–1376. 28, 45

WILSON, M.F. & HENDERSON-SELLERS, A. (1985). A global archive of land cover and soils data for use in general circulation climate models. *Journal of Climatology*, **5**, 119–143. 137

WINSTANLEY, D. (1972). Sharav. *Weather*, **27**, 146–160. 2, 17, 20, 22

WOODWARD, S. (2001). Modeling the atmospheric life cycle and radiative impact of mineral dust in the Hadley Centre climate model. *J. Geophys. Res.- Atmos.*, **106**, 18155–18166. 10, 11, 13, 14, 137, 138

WOODWARD, S. (2011). Mineral dust in HadGEM2. Technical Note 87, Hadley Centre. 136, 137, 140, 142

ZENDER, C., MILLER, R. & TEGEN, I. (2004). Quantifying mineral dust mass budgets: Terminology constraints and current estimates. *EOS Trans AGU*, **85**, 509–512. 5

ZHANG, D.L. & ANTHES, R.A. (1982). A high-resolution model of the planetary boundary layer - sensitivity tests and camparison with SESAME-79 data. *J. Appl. Meteor.*, **21**, 1594–1609. 37

ZHANG, D.L. & ZHENG, W.Z. (2004). Diurnal cycle of surface winds and temperatures as simulated by five boundary layer parameterizations. *J. Appl. Meteor.*, **43**, 157–169. 37, 38

ZHANG, K., O'DONNELL, D., KAZIL, J., STIER, P., KINNE, S., LOHMANN, U., FERRACHAT, S., CROFT, B., QUAAS, J., WAN, H., RAST, S. & FEICHTER, J. (2012). The global aerosol-climate model ECHAM-HAM, version 2: sensitivity to improvements in process representations. *Atmospheric Chemistry and Physics*, **12**, 8911–8949. 49

ZHAO, C., LIU, X., LEUNG, L.R., JOHNSON, B., MCFARLANE, S.A., GUSTAFSON, W.I., JR., FAST, J.D. & EASTER, R. (2010). The spatial distribution of mineral dust and its shortwave radiative forcing over North Africa: modeling sensitivities to dust emissions and aerosol size treatments. *Atmos. Chem. Phys.*, **10**, 8821–8838. 4